UNIVERSITAT DE BARCELONA

Departament d'Astronomia i Meteorologia

The structure and dynamics of clusters and the H I content of spiral galaxies

Memòria presentada per
Maria Teresa Sanchis Estruch
per optar al grau de
Doctora en Física
Barcelona, octubre de 2003

Programa de Doctorat d'Astronomia i Meteorologia

Bienni 1998–2000

Memòria presentada per **Maria Teresa Sanchis Estruch** per optar al grau de Doctora en Física

Directors de tesi

Dr. Eduard Salvador Solé

Dr. Josep Maria Solanes Majúa

Contents

Resum de la tesi: Estructura i dinàmica dels cúmuls i el contingut d'H I de les galàxies espirals

1. Introducció

L'origen i evolució de les galàxies ha estat una qüestió a resoldre des de l'establiment de la seqüència de Hubble (Hubble 1926, 1927) i el posterior descobriment que les galàxies de diferents tipus no estan homogèniament distribuïdes a l'espai, sinó que es presenten segregades segons la seua morfologia (Hubble & Humason 1931; Abell 1958; Morgan 1961). A l'univers proper, les galàxies de tipus primerenc (el·líptiques i lenticulars) es troben fonamentalment en regions d'elevada densitat com ara els centres dels cúmuls, mentre que les galàxies de tipus tardiu (espirals i irregulars) són característiques d'entorns poc densos. Nombrosos autors han estudiat aquesta segregació morfològica per tal d'esbrinar els paràmetres físics que caracteritzen la distribució inhomogènia de les galàxies de diferents tipus (Oemler 1974; Dressler 1980; Salvador-Solé, Sanromà, & Rdz. Jordana 1989; Whitmore & Gilmore 1991, entre d'altres). Aquests paràmetres físics donen evidències sobre els processos involucrats en la formació i possible evolució de les galàxies, contribuint al debat entre els defensors de la idea que les galàxies presenten morfologies diferents segons l'entorn on es van formar (Sandage, Freeman, & Stokes 1970; Silk 1978; Bardeen et al. 1986; Dekel & Rees 1987; Evrard, Silk, & Szalay 1990) i aquells que proposen que les galàxies evolucionen al llarg de la seqüència de Hubble. El paradigma evolutiu va rebre importància pel descobriment de l'anomenat efecte Butcher-Oemler (Butcher & Oemler 1978, 1984): els cúmuls a gran desplaçament cap al roig tenen una fracció de galàxies blaves major que els cúmuls propers. Més recentment, gràcies a la nova generació de telescopis d'alta resolució, capaços de distingir la morfologia de les galàxies en cúmuls llunyans, hem obtingut una visió més acurada d'aquest efecte: Conforme s'observa enrera en el temps, la fracció d'espirals en cúmuls augmenta amb z en detriment de la de lenticulars, mentre que la fracció d'el·líptiques roman constant (Couch et al. 1994; Dressler et al. 1994; Wirth, Koo, & Kron 1994; Dressler et al. 1997; Oemler, Dressler, & Butcher 1997; Smail et al. 1997; Fasano et al. 2000). La formació estelar també evoluciona, augmentant amb z (Poggianti et al. 1999; Balogh et al. 1999). Segons el paradigma actualment acceptat, les galàxies el·líptiques (i potser les lenticulars més brillants) es van formar abans de la virialització dels cúmuls rics i evolucionen passivament des d'aleshores (Ellis et al. 1997), mentre que una fracció important de lenticulars (aproximadament el 50%) és generada a partir de la transformació morfològica de les espirals (Dressler et al. 1997). Diferents mecanismes han estat proposats per tal d'explicar aquesta evolució de les galàxies: escombrat del gas causat per interaccions directes galàxia-galàxia (Spitzer & Baade 1951), per la pressió cinètica del medi intracumular (Gunn & Gott 1972), per viscositat o per conducció tèrmica (Cowie & Songaila 1977; Nulsen 1982), interaccions de marea o fins i tot fusions (Toomre 1972), interacció gravitatòria (Byrd & Valtonen 1990; Valluri 1993) o assetjament galàctic (Moore, Katz, & Lake 1996).

En qualsevol cas, per tal d'entendre les propietats de les galàxies és necessari estudiar la física de les interaccions galàctiques amb el medi dins del context del paradigma jeràrquic de formació galàctica (White & Rees 1978) on les galàxies es desenvolupen a dins d'halos de matèria fosca que creixen jeràrquicament des de petites a grans escales. Cole (1991), Lacey & Silk (1991) i White & Frenk (1991) van ser els primers en abordar models de formació galàctica dins d'aquest context general. Aquests treballs van donar pas als anomenats Models Semi-analítics, els quals segueixen el creixement dels halos de matèria fosca i utilitzen, al si d'aquests halos, receptes analítiques per descriure la complicada física dels barions (veure per ex. Kauffmann, White, & Guiderdoni 1993; Lacey et al. 1993; Somerville & Primack 1999; Hatton et al. 2003, per citar alguns treballs). Seguint l'esperit d'aquests models semi-analítics, el nostre grup de recerca, liderat pel Dr. Eduard Salvador-Solé, està desenvolupant un nou model de formació jeràrquica i evolució de galàxies totalment analític que incorpora aspectes fins ara només parcialment inclosos als models semi-analítics existents, com ara una descripció consistent de l'estructura interna de galàxies de diferents tipus, la inclusió de forats negres massius centrals i de les principals interaccions entre galàxies: truncament per marea, fricció dinàmica, fusions i escombrat per pressió cinètica del medi intracumular.

Per tal de discernir entre les abundants teories d'evolució galàctica en cúmuls i contrastar les prediccions dels models de formació jeràrquica de galàxies és necessari realitzar observacions en diferents entorns dels paràmetres físics que caracteritzen les galàxies al llarg de la seqüència de Hubble (Roberts & Haynes 1994). Aquestes observacions en cúmuls propers han mostrat que les galàxies en cúmuls es diferencien de les de camp en que presenten deficiència d'hidrogen neutre (H I) (veure per ex. Solanes et al. 2001) i una disminució de la formació estelar (Koopmann & Kenney 2002; Gavazzi et al. 2002; Lewis et al. 2002), mentre que el contingut en gas molecular (traçat pel CO) sembla no dependre de l'entorn (Stark et al. 1986; Kenney & Young 1989). Aquestes característiques, a més de la presència de discs d'H I truncats al centre dels cúmuls (Cayatte et al. 1990; Bravo-Alfaro et al. 2000), assenyalen les interaccions amb el medi intracumular com a les principals responsables del canvi de morfologia de les galàxies espirals. Aquesta evidència observacional ve confirmada per treballs teòrics com el de Solanes & Salvador-Solé (1992), els quals van explicar la concentració actual de galàxies de tipus S0 en cúmuls seguint la transformació d'espirals a lenticulars causada per l'escombrat per pressió cinètica del medi intracumular a partir d'una distribució no segregada de galàxies. Simulacions hidrodinàmiques (Abadi, Moore, & Bower 1999; Quilis, Moore, & Bower 2000; Schulz & Struck 2001; Vollmer et al. 2001) han provat també l'eficiència de les interaccions amb el medi intracumular en escombrar l'hidrogen neutre i truncar la formació estelar.

A més d'observacions, per tal d'obtindre una visió completa del marc en el qual les galàxies es formen i evolucionen, és també necessari conèixer les propietats dels halos de matèria fosca on les galàxies resideixen i el paper que aquests halos juguen en la determinació de la morfologia d'aquestes. Models dinàmics de cúmuls, com el model de caiguda esfèrica (Gunn & Gott 1972), el mètode de Jeans (Binney & Tremaine 1987) o el model basat en càustiques (Regős & Geller 1989), entre d'altres, proporcionen valuoses informacions sobre la massa, el perfil de densitat i la distribució de velocitats dels halos de matèria fosca i per tant permeten obtindre una visió global dels processos de formació i evolució d'estructures lligats a la matèria fosca i la lluminosa.

1.1 Motivació d'aquesta tesi

Per tal d'entendre l'abast i l'efectivitat de les condicions existents als cúmuls en la inducció de l'evolució de les galàxies és fonamental caracteritzar la distribució d'H I dels cúmuls. El disc d'hidrogen neutre és el component menys gravitatòriament lligat de les galàxies. Per aquest motiu resulta molt afectat per l'agressiu entorn dels cúmuls i per tant és un indicador ideal del tipus d'interaccions que provoquen canvis morfològics a les galàxies. Malgrat que l'escombrat de l'hidrogen neutre impedeix la formació de gas molecular, la matèria primera dels estels, encara no està del tot clar com la manca d'hidrogen neutre afecta la formació estelar (Kennicutt 1998), doncs els resultats existents fins a l'actualitat indiquen que el contingut d'H_2 de les galàxies dels cúmuls és similar al de les de camp (veure, per exemple, Kenney & Young 1989). A més, els discs d'H I són molt més extensos que els discs estelars (Cayatte et al. 1994). Només recentment s'han trobat evidències d'una connexió entre el contingut d'H I de les galàxies espirals i el seu ritme de formació estelar (Gavazzi et al. 2002). Si es confirmen, aquestes evidències proporcionarien el lligam entre el gas neutre, la formació estelar i la subsegüent evolució del color i la lluminositat, que condueixen en darrer terme les galàxies a patir canvis morfològics.

Per investigar el contingut d'H I del cúmuls de galàxies i veure com està afectat per la dinàmica i l'entorn dels mateixos és molt útil tindre no només la informació usual sobre quantitats projectades, sinó a més la distribució 3D. El cúmul de Virgo, el més proper i ric, és un candidat excel·lent per a el·laborar mapes 3D de la distribució espacial de les propietats de les galàxies dels cúmuls. Existeix una gran quantitat de dades disponibles a la literatura sobre posicions, distàncies i velocitats de les seues galàxies. A més, tenim accés al Catàleg General d'Arecibo, un catàleg privat mantingut per Martha P. Haynes i Riccardo Giovanelli a la universitat de Cornell. Aquest catàleg conté una gran quantitat de dades d'H I de galàxies d'aquest i d'altres cúmuls que ens permeten abordar aquest projecte.

Malgrat que la importància de les interaccions amb el medi intracumular en l'evolució de les galàxies sembla suficientment establerta, encara queden qüestions sense resoldre. Als cúmuls, tant l'H I com el ritme de formació estelar són menors que en el camp fins a 2 radis del virial del centre. Aquest fet sembla difícil de compatibilitzar amb l'acció de les interaccions amb el medi intracumular, doncs aquestes són efectives només en les regions més centrals i denses dels cúmuls. No obstant això, les galàxies deficients en H I es troben en òrbites més radials que les no deficients (Dressler 1986; Giraud 1986; Solanes et al. 2001), la qual cosa explicaria que galàxies tan allunyades del centre hagueren patit els efectes d'interaccions amb el medi intracumular. En efecte, una espiral movent-se a través del medi intracumular (MIC) calent perdrà el seu gas si la pressió exercida per aquest medi ($\rho_{\rm MIC}V^2$, on V és la velocitat de la galàxia respecte al MIC) és major que la força gravitatòria que lliga la galàxia. Segons això, per tal que l'escombrat siga efectiu, les galàxies han de passar a prop del centre del cúmul a grans velocitats. Llavors, és possible trobar la majoria de galàxies deficients en H I lluny del centre del cúmul després d'haver-lo travessat a grans velocitats (Vollmer et al. 2001). No obstant això, encara no està clar fins a quines distàncies es poden trobar galàxies deficients en H I. Saber-ho tindria profundes implicacions en el nostre coneixement de l'escala temporal d'evolució galàctica, doncs informaria sobre quant de temps poden mantenir la seua morfologia galàxies amb una manca important d'hidrogen neutre. Per tal d'investigar aquestes qüestions necessitem modelitzar la cinemàtica de les galàxies caient al potencial del cúmul, travessant-lo i reemergent. Un factor crucial per a aquesta modelització és la massa del cúmul, doncs aquest paràmetre determina la dinàmica de tot el sistema. Models com el formalisme de Jeans ens poden proporcionar la massa del virial dels cúmuls a partir de l'estudi de la seua distribució de velocitats. Aquest mètode es basa, però, en l'anàlisi de quantitats projectades i assumeix que els cúmuls són esfèricament simètrics i estan relaxats, mentre que els cúmuls reals no són així (Wang & Ulmer 1997; Biviano, Durret, & Gerbal 1996). Per tant, és necessari determinar la validesa d'aquest mètode investigant els efectes de la caiguda de matèria, no esfericitat, no virialització i projecció en l'estimació dels paràmetres dinàmics dels cúmuls.

El treball descrit en aquesta tesi ha donat com a resultat cinc articles en revistes amb arbitratge (tres publicats i dos encara en procés d'arbitratge):

- "The 3D structure of the Virgo cluster region from Tully-Fisher and H I data" Solanes, J. M., Sanchis, T., Salvador-Solé, E., Giovanelli, R., & Haynes, M. P., 2002, *Astronomical Journal*, 124, 2440.
- "Are the H I-deficient galaxies on the outskirts of Virgo recent arrivals?" Sanchis, T., Solanes, J. M., Salvador-Solé, E., Fouqué, P., & Manrique, A. 2002, *Astrophysical Journal*, 580, 164.
- "The origin of H I-deficient galaxies on the outskirts of the Virgo cluster. I. How far can galaxies bounce out of clusters?" Mamon, G. A., Sanchis, T.,

Salvador-Solé, E., & Solanes, J. M. 2003. Enviat a l'*Astronomy & Astrophysics.*

- "The origin of H I-deficient galaxies on the outskirts of the Virgo cluster. II. Companions, and uncertainties in distances and deficiencies" Sanchis, T., Mamon, G. A., Salvador-Solé, E., & Solanes, J. M. 2003. Enviat a l'*Astronomy & Astrophysics.*
- "How reliable is the kinematical evidence for dark matter: the effects of non-sphericity, substructure and streaming motions" Sanchis, T., Łokas, E. L., & Mamon, G. A. 2003, *Monthly Notices of the Royal Astronomical Society*, en premsa.

A més, durant la realització d'aquesta tesi he colaborat en els següents articles en revistes amb arbitratge:

- "Structure, mass and distance of the Virgo cluster from a Tolman-Bondi model" Fouqué, P., Solanes, J. M., Sanchis, T., & Balkowski, C. 2001, *Astronomy & Astrophysics*, 375, 770.
- "On the origin of the inner structure of halos" Manrique, A., Raig A., Salvador-Solé, E., Sanchis, T., & Solanes, J.M. 2003, *Astrophysical Journal*, 593, 26.

2. L'estructura 3D de la regió del cúmul de Virgo[1]

L'estructura tridimensional de la regió de Virgo ha estat analitzada incorporant a les dades sobre posició i velocitats de les galàxies espirals, dades sobre el contingut d'hidrogen neutre d'aquestes galàxies. La proximitat del cúmul de Virgo facilita la recollida d'un gran nombre d'observacions de la línia de 21 cm així com de distàncies a galàxies mesurades amb el mètode de Tully-Fisher (TF) (Tully & Fisher 1977). Per al nostre estudi ens vam centrar en aquelles galàxies espirals situades en la regió delimitada en coordenades per $12^{\rm h} \leq$ AR $\leq 13^{\rm h}$ i $0^\circ \leq$ Dec. $\leq +25^\circ$ (referides a l'equinocci B1950) i en velocitats pel valor màxim de 3000 km s^{-1}, el qual aïlla la regió de Virgo en velocitats.

---

[1] En aquesta secció comentem els resultats més importants del Capítol 3.

Les dades d'hidrogen neutre utilitzades provenen en gran majoria del Catàleg General d'Arecibo i en una petita fracció del catàleg de Huchtmeier & Richter (1989) i del *Lyon-Meudon Extragalactic Database* (LEDA). Per mesurar la deficiència d'H I de les galàxies vam utilitzar un estimador independent de la distància a la galàxia en qüestió, donades les incerteses en aquesta darrera quantitat.

Pel que fa a les distàncies TF, aquestes han estat recollides de la literatura, concretament dels treballs de Ekholm et al. (2000), Federspiel, Tammann, & Sandage (1998), Fouqué et al. (1990), Gavazzi et al. (1999), Kraan-Korteweg, Cameron, & Tammann (1988), Mould, Aaronson, & Huchra (1980), Pierce & Tully (1988) i Yasuda, Fukugita, & Okamura (1997). Donat que aquests 8 catàlegs poden contenir dades inconsistents entre sí, vam realitzar un procés d'homogeneïtzació dels catàlegs per calcular la distància d'una galàxia a partir de les diferents estimacions de cada catàleg. A més, vam incloure al nostre catàleg 7 galàxies amb distància mesurada amb cefeides provinents del treball de Freedman et al. (2001) amb observacions del Telescopi Espacial Hubble. Un cop realitzat el procés d'homogeneïtzació i d'haver rebutjat galàxies amb velocitats de rotació menors que 100 km s^{-1} per tal de disminuir els possibles errors en distància, vam obtindre un catàleg final amb 161 galàxies amb mesures en principi acurades de coordenades, velocitats, distància i deficiència d'hidrogen.

Analitzant aquest catàleg hem obtingut la distribució tridimensional de la deficiència d'H I i l'hem comparada amb la distribució en l'espai de fases (posició i velocitat) de les galàxies. A més, hem examinat en detall la possibilitat suggerida per Solanes et al. (2001) que, a banda de la concentració principal de galàxies deficients al voltant del centre del cúmul (definit com la posició de M87), podrien existir altres concentracions de galàxies deficients associades a grups perifèrics. A la figura 1, podem veure com es distribueixen a la volta celest les galàxies espirals de Virgo per diferents rangs de distàncies. En aquesta figura, s'observen tres concentracions de galàxies deficients corresponents a distàncies entre 15 i 20 Mpc, entre 10 i 15 Mpc i entre 25 i 30 Mpc. A més, podem veure com la majoria de galàxies llunyanes es concentren al quadrant oest, mentre que a la part est només trobem galàxies fins a 25 Mpc.

Mitjançant l'anàlisi realitzat, hem arribat a les següents conclusions, les quals, malgrat la presència d'importants errors en les mesures de distància, proporcionen una visió global de l'estructura tridimensional del cúmul correcta a grans trets:

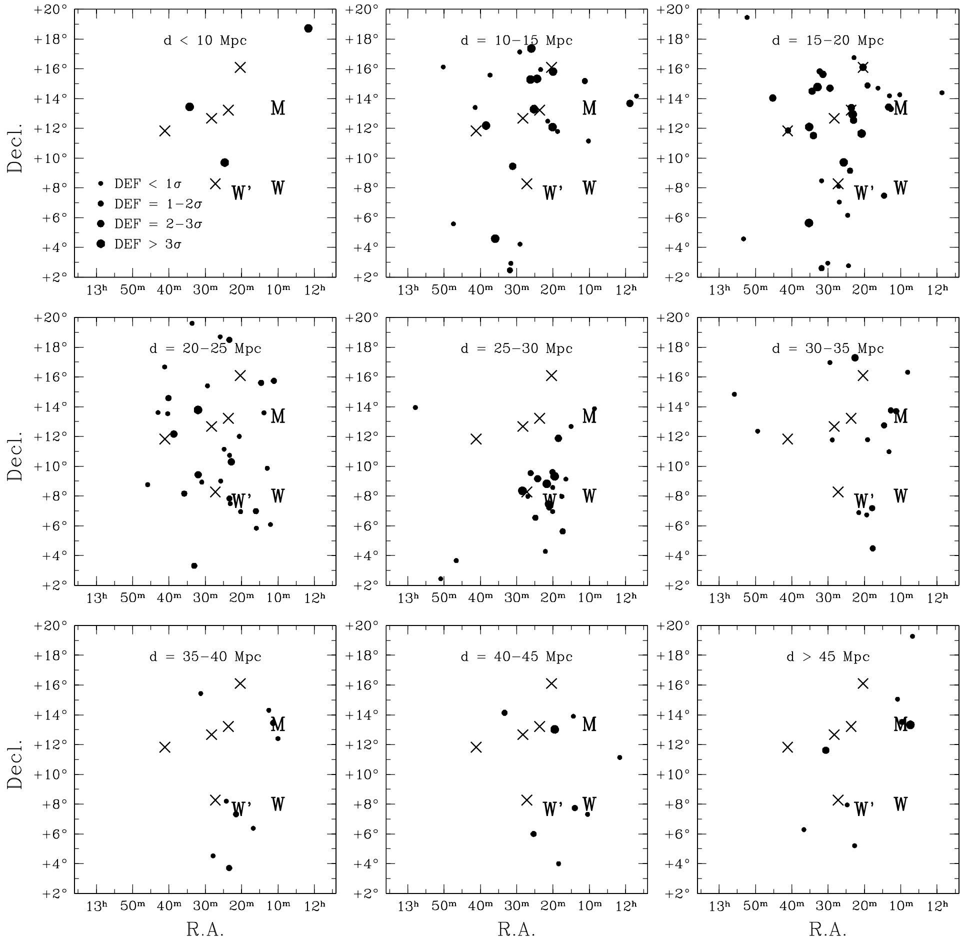

Figura 1: Distribució sobre la volta celest de les galàxies espirals de Virgo per diferents rangs de distàncies. La mida dels símbols indica la deficiència d'H I de les galàxies. La posició de cinc galàxies dominants està marcada amb creus (de dalt cap a baix: M100, M86, M87, M60 i M49). També s'indica la posició de les regions W, W' i M.

- Confirmem resultats previs que indicaven que la distribució d'espirals en el cúmul de Virgo és molt allargada seguint la línia de visió. Les galàxies associades a aquesta regió tenen distàncies que van des de 10 fins a més de 50 Mpc. La distribució projectada d'aquestes galàxies sembla no obstant relativament compacta, amb una extensió típica de només 10 Mpc. La proporció amplada-profunditat és doncs aproximadament 1:4 amb una forta variabilitat est-oest. Els objectes més llunyans es concentren al quadrant oest, mentre que a la meitat est es troben molt poques galàxies amb distàncies majors que 25 Mpc. L'estructura filamentària de Virgo sembla dividir-se en dues branques al voltant de la regió W' (situada darrere del centre del cúmul, segons es troba definida a de Vaucouleurs 1961).

- La distribució de galàxies espirals amb una deficiència d'hidrogen significativa també es caracteritza per presentar una gran profunditat al llarg de la línia de visió. Les galàxies més deficients tendeixen a concentrar-se al llarg de la branca superior de la distribució de galàxies espirals, la qual està aproximadament alineada amb l'eix principal del cúmul de Virgo.

- En els primers 4 Mpc al voltant de M87, la deficiència d'H I mesurada decreix monòtonament conforme augmenta la distància al centre del cúmul, en concordança amb el comportament observat a d'altres cúmuls deficients (Solanes et al. 2001). A més, a la regió de Virgo s'identifiquen zones amb deficiència de gas neutre significativa situades a grans distàncies del centre del cúmul i lluny de la regió on es concentra el gas intracumular calent.

- Mentre que el pic principal de la distribució de deficiència d'H I prové de nombroses galàxies deficients en la zona del centre del cúmul amb distàncies entre 16 i 22 Mpc, altres pics importants estan associats a algunes galàxies properes ($d \lesssim 15$ Mpc) que s'allunyen del cúmul a grans velocitats i al que sembla un grup compacte darrera del cúmul format per galàxies amb distàncies entre 25 i 30 Mpc, la majoria de les quals tenen velocitats similars a la velocitat mitjana del cúmul. Aquest possible grup estaria situat a la mateixa posició que la regió clàssica W'. A més, hem comprovat que el pic de deficiència visible al mapa projectat de Virgo al voltant de la regió M (Ftclas, Struble, & Fanelli 1984) prové en realitat de galàxies a distàncies molt diferents alineades per atzar al llarg de la línia de visió i sense connexió física.

- En concordança amb els resultats de Dale et al. (2001), res a la nostra anàlisi suggereix que les mesures de distància pel mètode de Tully-Fisher siguen incertes per als objectes molt deficients.

3. Model dinàmic de la regió de Virgo[2]

Donat que al nostre anàlisi de la distribució de deficiència d'hidrogen neutre al cúmul de Virgo vam trobar un nombre significatiu de galàxies deficients a grans

---

[2] En aquesta secció comentem els resultats més importants del Capítol 4.

distàncies del centre del cúmul, hem desenvolupat un model dinàmic del cúmul per tal d'explicar la posició al diagrama distància-velocitat d'aquestes galàxies. El nostre objectiu era comprovar si aquestes galàxies deficients en les zones perifèriques haurien pogut travessar el centre del cúmul en el passat i haver perdut el seu gas amb interaccions amb el dens medi intracumular allí existent.

Per poder modelitzar el camp de velocitats al voltant del cúmul de Virgo incloent-hi òrbites amb rebot (aquelles que passen pel centre del cúmul i tornen a eixir), vam implementar un model amb massa puntual pel col·lapse esfèric d'un fluid de pressió nul·la. Així, la solució del problema no es limita a la deducció clàssica del camp de velocitats dels objectes fins que cauen al centre per primer cop, sinó que els càlculs s'estenen més enllà fins que les galàxies recol·lapsen un altre cop. Les galàxies són tractades com partícules test movent-se sota el potencial gravitatori creat per una massa puntual, ignorant els efectes provinents del creuament de capes. Amb aquestes aproximacions, el camp de velocitats resultant al voltant del cúmul de Virgo depèn només de 4 paràmetres: l'edat de l'univers t_0, la massa de la partícula puntual que genera el potencial gravitatori $M_{\rm VIC}$, la distància del centre del cúmul $R_{\rm VIC}$ i la velocitat d'aquest centre $V_{\rm VIC}$. Només 3 d'aquests 4 paràmetres són independents.

Donat el diagrama distància-velocitat de les galàxies del nostre catàleg, vam ajustar els paràmetres del model. Per fer-ho, vam utilitzar aquelles galàxies que defineixen la branca que tendeix asimptòticament a seguir la llei de Hubble a grans distàncies del centre del cúmul. Aquestes galàxies ofereixen nombrosos avantatges: no estan afectades pels efectes del creuament de capes, presenten un gran rang de posicions i velocitats que permet constrènyer millor els paràmetres del model i les prediccions del model per a aquests objectes no depenen de la distància angular de les galàxies al centre del cúmul. No obstant això, les mesures de les quals disposem no permeten ajustar tots tres paràmetres alhora, així que vam decidir fixar $V_{\rm VIC}$, la magnitud millor coneguda a la literatura, i ajustar $M_{\rm VIC}$ i $R_{\rm VIC}$. El t_0 resultant ens permet jutjar la validesa dels nostres resultats.

A la figura 2 podem veure el diagrama distància-velocitat de la regió de Virgo. Aquest diagrama mostra les característiques esperades: un relació distància-velocitat inicialment creixent davant del cúmul, una ampla regió central amb la màxima dispersió de velocitats i una part final de velocitats creixents, tendent asimptòticament a la llei de Hubble local. Superposades trobem les corbes (per diferents distàncies angulars al centre del cúmul) definides pels paràmetres del model dinàmic que mi-

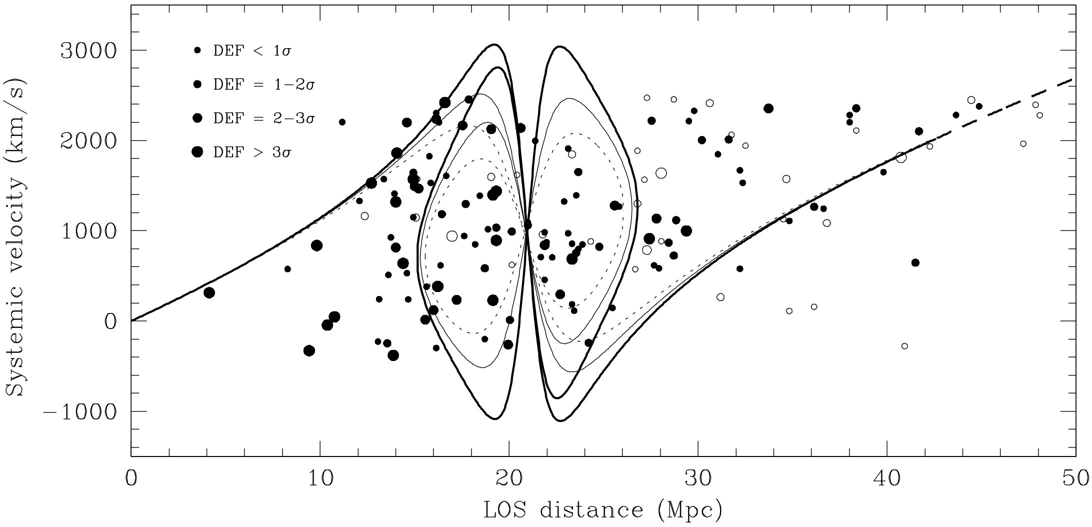

Figura 2: Velocitat en funció de la distància per a les espirals de Virgo. Les corbes mostren les velocitats predites per a una distància angular al centre del cúmul $\theta = 4°$ (gruixuda), $\theta = 6°$ (fina) i $\theta = 8°$ (puntejada). Les galàxies amb distàncies incertes (símbols en blanc) van ser excloses de l'ajust dels paràmetres. El paràmetre DEF mesura la deficiència d'H I en unitats de la desviació estàndard mitjana pels objectes en el camp ($= 0.24$).

llor s'ajusten a les branques asimptòtiques: $M_{\rm VIC} = 2.8 \times 10^{15}$ M$_\odot$ i $R_{\rm VIC} = 21.0$ Mpc, valors que, juntament amb la velocitat $V_{\rm VIC}$ fixada a 980 km s^{-1}, impliquen $t_0 = 13.5$ Gyr. Malgrat que l'ajust dels paràmetres s'ha realitzat només amb algunes galàxies, la solució trobada explica la posició al diagrama de moltes de les galàxies al voltant del cúmul de Virgo i suggereix que el possible grup deficient al darrere del cúmul (a distàncies $\sim$ 28 Mpc i velocitats $\sim$ 1000 km s^{-1}) es troba a prop del punt de retorn després d'haver passat pel centre del cúmul.

A més a més, vam explorar la possibilitat que aquest grup deficient estiguera caient per primer cop cap al centre del cúmul. Introduint aquestes galàxies al conjunt de les galàxies de la branca asimptòtica que utilitzàvem per ajustar els paràmetres del model, vam trobar que el millor ajust corresponia als següents paràmetres: $M_{\rm VIC} = 1.8 \times 10^{15}$ M$_\odot$ i $R_{\rm VIC} = 20.2$ Mpc, els quals impliquen $t_0 = 14.0$ Gyr.

Tant en el cas de considerar el grup deficient darrera del cúmul en primera caiguda o havent passat ja pel centre del cúmul, els paràmetres obtinguts amb l'ajust del model dinàmic són raonables i comparables als obtinguts a la literatura. Mentre que la massa obtinguda $\sim$ 10^{15} M$_\odot$ és major que les estimacions de la massa del cúmul de Virgo basades en l'emissió de raigs-X o en el teorema del virial (les quals donen valors de l'ordre de 10^{14} $M_\odot$), els nostres valors són similars als obtinguts amb modelitzacions del camp de velocitats del Supercúmul Local (Tully & Shaya 1984; Fouqué et al. 2001). Les distàncies al centre del cúmul obtingudes estan inscrites també dins de l'interval de distàncies a Virgo que podem trobar a la literatura ($\sim$ 16–24 Mpc). A més, les nostres solucions impliquen edats de l'univers d'acord amb el resultat recentment obtingut amb l'experiment WMAP (Spergel et al. 2003).

Els nostres resultats indiquen que, malgrat que altres possibilitat no han estat descartades, no podem rebutjar la hipòtesi que algunes galàxies deficients en la perifèria del cúmul de Virgo hagen travessat en el passat el centre del cúmul i perdut allà el gas per la pressió cinètica del medi intracumular. De confirmar-se aquest resultat, tindria fortes implicacions si considerem que galàxies que van perdre el seu gas fa més de 4 Gyr podrien mantenir la seua morfologia intacta durant aquest llarg període de temps. De tota manera, en les dues possibilitats considerades, trobem encara un significatiu nombre de galàxies que no encaixen en les prediccions dels models dinàmics. Aquestes discrepàncies podrien ser en part degudes a les aproximacions utilitzades al nostre model de massa puntual. A més a més, malgrat que per l'ajust del model vam rebutjar les galàxies amb distància més incerta, els errors en distància podrien ser més grans que els estimats, la qual cosa explicaria també la posició discordant d'algunes galàxies al diagrama distància-velocitat.

4. L'origen de la deficiència d'H I de les galàxies en la perifèria del cúmul de Virgo[3]

L'existència d'algunes galàxies discordants al diagrama distància-velocitat (veure la figura 2) ens va portar a estudiar més detalladament el camp de velocitats al voltant dels cúmuls. En primer lloc vam utilitzar tant càlculs analítics com simulacions numèriques d'halos de matèria fosca (realitzades per Hatton et al. 2003 per al seu model de formació jeràrquica de galàxies) per determinar la distància màxima al centre del cúmul a la qual podem trobar objectes que l'hagen travessat. Ambdós mètodes condueixen a que aquesta màxima distància ha de ser més petita que 2.5

---

[3] En aquesta secció comentem els resultats més importants dels Capítols 5, 6 i 7.

vegades el radi del virial del cúmul r_{100} (definit com el radi en el qual la densitat mitjana del cúmul és 100 vegades la densitat crítica de l'univers). Per tal de poder comparar aquest resultat amb les observacions al cúmul de Virgo, vam calcular el seu radi del virial a partir del perfil de densitat inferit d'observacions de raigs-X del cúmul per Schindler, Binggeli, & Böhringer (1999), obtenint un valor de 1.65 Mpc. Aquest valor resulta massa petit per a que les galàxies deficients en la perifèria hagen travessat el cúmul, donats valors raonables de la distància al centre.

Per tal d'estimar aquesta distància al centre del cúmul de Virgo i identificar més precisament l'entorn de les galàxies deficients, vam fer una compilació (similar a l'exposada a la Secció 2) de dades de coordenades, distància i velocitats de galàxies de tipus primerenc, doncs, en principi, aquestes galàxies tracen millor el centre del cúmul degut a la segregació morfològica existent als cúmuls (veure introducció). Les dades de distàncies provenen dels treballs de Gavazzi et al. (1999), Young & Currie (1995), Tonry et al. (2001), Jensen, Tonry, & Luppino (1998), Neilsen & Tsvetanov (2000) i Kundu & Whitmore (2001). Amb la inclusió de les el·líptiques, observem una concentració d'aquestes galàxies al voltant de 17 Mpc, que coincideix amb la distància de M87.

Hem construït rèpliques del cúmul utilitzant els halos de matèria fosca de les simulacions. Donat que el cúmul de Virgo consta d'una component massiva central al voltant de M87 i els subgrups al seu voltant són força menys massius que aquesta component, vam decidir utilitzar per simular el cúmul els halos de matèria fosca que estigueren més aïllats. Després d'una anàlisi del grau d'aïllament dels halos més massius de la simulació, vam trobar que l'halo més aïllat era l'halo més massiu de les simulacions amb $M_{100} = 1.7 \times 10^{15}$ $M_{\odot}$ i $r_{100} = 3.2$ Mpc. Donada la diferència entre aquests paràmetres i els del cúmul de Virgo, vam realitzar un procés d'escalat de les simulacions per posar-les en unitats comparables al cúmul de Virgo. Després d'aquest procés d'escalat, vam obtenir el camp de velocitats que mostrem a la figura 3 superposat amb el camp de velocitats observat.

La figura 3 indica que el camp de velocitats definit per les galàxies observades és força diferent del que segueixen les partícules de matèria fosca de l'halo en la simulació. No obstant això, veiem que el centre de l'halo coincideix amb la posició del màxim de densitat de galàxies i que la dispersió de velocitats de l'halo coincideix amb la de les galàxies en la part central del cúmul. Aquests factors ens fan pensar que tant la distància escollida al centre del cúmul (17 Mpc) com el procés de reescalat

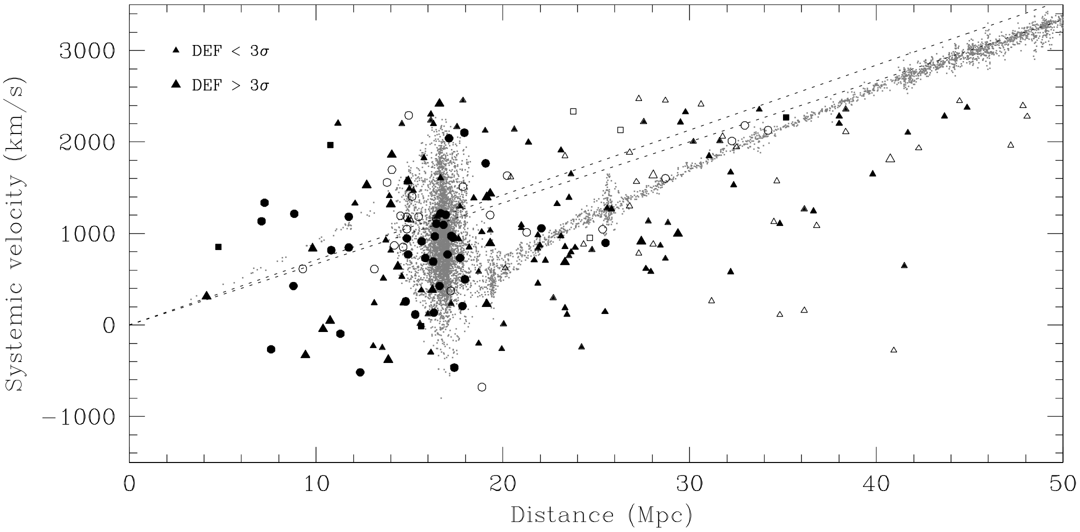

Figura 3: Diagrames distància-velocitat simulat i observat. Els punts representen el camp de velocitats traçat per les partícules en la simulació cosmològica de N-cossos. Les galàxies del cúmul de Virgo estan superposades. Els cercles i els triangles representen galàxies de tipus primerenc i tardiu respectivament. La mida dels triangles indica la deficiència d'H I de les espirals en unitats de la desviació estàndard mitjana pel objectes en el camp. Els quadrats representen galàxies espirals sense dades de deficiència d'H I. Els símbols en blanc indiquen galàxies amb estimacions de distància incertes. Les línies a traços mostren el flux de Hubble no pertorbat per $H_0 = 66.7$ i $70\,\mathrm{km\,s^{-1}\,Mpc^{-1}}$, respectivament.

són correctes i que les diferències entre ambdós diagrames (l'observat i el definit per les simulacions) són degudes a errors en l'estimació de les distàncies, doncs els errors en velocitat són negligibles. En construir el catàleg de galàxies espirals amb dades TF de distància, vam utilitzar 8 catàlegs amb un error relatiu mitjà del 18% (veure Secció 2). Per estudiar la influència d'aquest error en el camp de velocitats, mostrem de nou a la figura 4 el diagrama distància-velocitat, afegint-hi aquest cop a les partícules de matèria fosca errors relatius en distància gaussians amb una mitjana del 20%. Com es pot veure en aquest nou diagrama la posició de la majoria de galàxies correspon a posicions de partícules de matèria fosca. Això ens fa pensar que l'error relatiu en distància al nostre catàleg té una mitjana del 20% o superior i que galàxies deficients aparentment allunyades del centre del cúmul podrien trobar-se en realitat més a prop i haver sofert interaccions amb el medi intracumular que hagueren escombrat el seu contingut gasós.

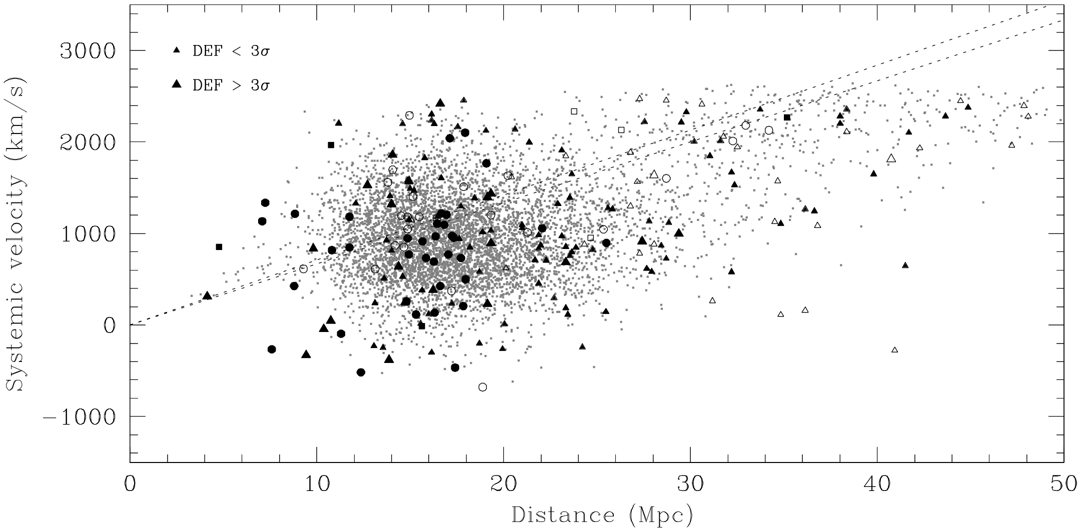

Figura 4: El mateix que a la figura 3, però incorporant a les partícules de matèria fosca errors relatius gaussians en distància amb una mitjana del 20%.

A més d'aquesta possibilitat, hem investigat si les galàxies deficients aparentment allunyades del centre del cúmul es troben en entorns de densitat elevada o tenen companys propers i són susceptibles per tant d'haver perdut el seu hidrogen neutre per interaccions de marea. També hem indagat la possibilitat d'una sobreestimació de la deficiència d'H I deguda a que galàxies de tipus S0 hagen estat classificades incorrectament com a Sa.

5. Els efectes d'elongació, subestructura i no virialització en l'anàlisi dinàmic dels cúmuls[4]

Després d'haver utilitzat un model de col·lapse esfèric que ens ha permès, entre d'altres coses, obtenir una estimació de la massa del cúmul de Virgo, hem abordat el mètode d'estudi de les propietats dinàmiques dels cúmuls basat en l'equació de Jeans. Aquest mètode permet obtindre, a partir de l'anàlisi dels moments de la distribució de velocitats projectades sobre la línia de visió, la massa, el perfil de densitat i l'anisotropia de la distribució de velocitats. L'anàlisi de Jeans assumeix un sistema esfèric en equilibri. A l'interior dels cúmuls, però, existeix matèria no virialitzada, per exemple matèria caient cap al cúmul per primer cop o petits grups en procés de

---

[4] En aquesta secció comentem els resultats més importants del Capítol 8.

virialització. A més, els cúmuls no són esfèricament simètrics (Binggeli 1982; Wang & Ulmer 1997). A sobre, en analitzar la cinemàtica de partícules projectades sobre la volta celest, no es pot saber si les partícules analitzades corresponen vertaderament a la zona interior al radi del virial.

Per tal d'estudiar la influència d'aquests efectes tradicionalment negligits en la determinació de les propietats dinàmiques dels cúmuls de galàxies, vam escollir els 10 halos més massius de les simulacions a N-cossos de Hatton et al. (2003). Primerament vam caracteritzar aquests halos, calculant la seua massa del virial M_{100}, el seu radi del virial, el factor de concentració c (que determina el seu perfil de densitat en el cas que aquest segueixi el perfil de densitat de Navarro, Frenk, & White 1997), l'anisotropia de la distribució de velocitats β i els tres eixos principals dels halos.

Seguidament, amb cadascun dels halos vam simular observacions de les velocitats projectades al llarg de la línia de visió tal i com es fa quan s'observen cúmuls de galàxies. Per tal de poder estudiar els efectes de la no esfericitat dels halos, vam escollir per cada halo 3 observadors diferents, tots tres a la mateixa distància a l'halo però cadascun en una direcció diferent: al llarg de l'eix principal de l'halo, a 45° o a 90° respecte a aquest eix. Aleshores vam mesurar les velocitats de les partícules de l'halo en funció de les distàncies projectades al centre tal i com un observador ho faria. Mitjançant aquestes dades, vam rebutjar les partícules que clarament no pertanyien a l'halo (seguint el mètode emprat per Kent & Gunn 1982; Łokas & Mamon 2003). Amb les partícules restants vam definir dues famílies: una formada per totes les partícules i una altra formada per només aquelles partícules que realment es trobaven a dins de l'esfera de radi r_{100} al voltant de l'halo. Per cadascun d'aquests dos grups vam estimar, en funció de la distància projectada al centre de l'halo, els moments de les velocitats projectades al llarg de la línia de visió: la mitjana, la dispersió, el biaix i la curtosi. Malgrat l'existència de molt soroll a les nostres estimacions degut a la presència de subestructura i de les diferències entre els 10 halos, vam comprovar que en tots els casos els moments calculats no diferien substancialment d'un grup a l'altre.

Tot seguit vam aplicar l'anàlisi de Jeans als moments calculats per al grup amb totes les partícules (el grup que realment un observador utilitzaria donat que no podria determinar quines partícules pertanyen a la zona virialitzada). La solució de l'equació de Jeans depèn de 3 paràmetres: M_{100}, c i β que s'ajusten amb les

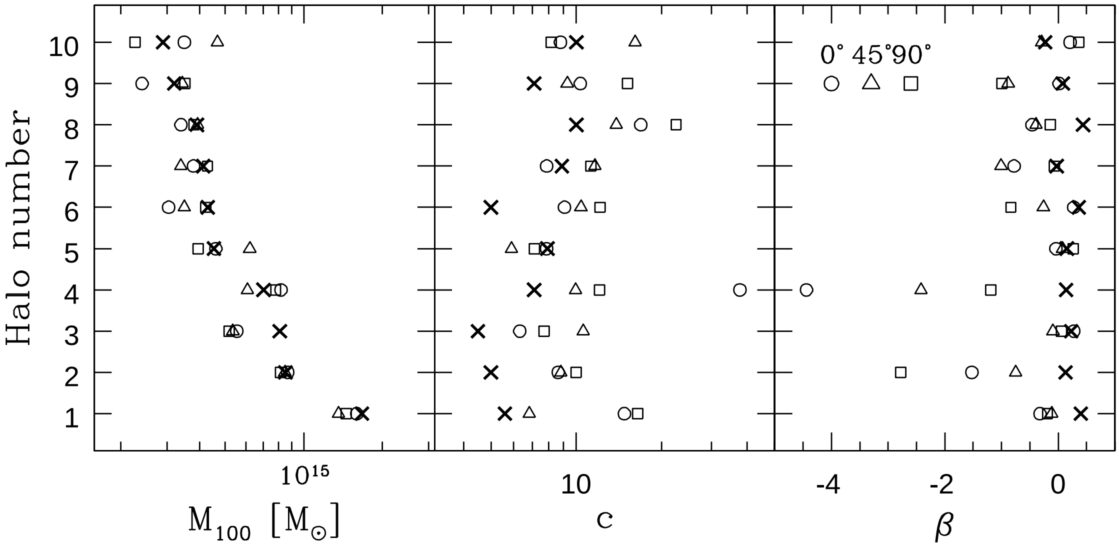

Figura 5: Valors ajustats (amb dades projectades) de la massa del virial M_{100}, el paràmetre de concentració c i l'anisotropia β dels 10 halos per les 3 direccions d'observació respecte a l'eix principal de cada halo: 0° (cercles), 45° (triangles) i 90° (quadrats). Els valors reals estan marcats amb creus.

dades mesurades de dispersió i curtosi de les velocitats projectades al llarg de la línia de visió. Els resultats obtinguts per als 10 halos i les 3 direccions d'observació es poden veure a la figura 5. Com es pot veure en aquesta figura, la massa del virial dels halos pot ser reproduïda satisfactòriament independentment de la forma de l'halo. El paràmetre de concentració resulta sobreestimat, mentre que l'anisotropia obtinguda és sovint més tangencial que la real.

En realitat, quan s'estudien cúmuls, el nombre de galàxies és molt inferior al nombre de partícules de matèria fosca a les simulacions, de manera que els errors de mesura dels moments de la distribució de les velocitats projectades al llarg de la línia de visió són majors (almenys un ordre de magnitud). Per veure com aquests errors afecten la determinació dels paràmetres dinàmics dels cúmuls, hem mesurat per cada halo els moments de la distribució de velocitats per un grup de 400 partícules escollides a l'atzar. Aquest nombre de partícules és similar al nombre usual de galàxies utilitzades en l'estudi de cúmuls reals (veure per ex. Łokas & Mamon 2003). Amb aquests moments mesurats vam realitzar el mateix ajust de M_{100}, c i β exposat anteriorment.

A la taula 1 mostrem la mitjana i la desviació estàndard de les diferències en-

Taula 1: Resultats de l'ajust

Nombre de	$\Delta \log M_{100}$		$\Delta \log c$		$\Delta\beta$	
partícules	mitjana	σ	mitjana	σ	mitjana	σ
Totes	–0.03	0.09	0.20	0.18	–0.78	1.04
400	–0.07	0.10	0.08	0.24	–0.20	0.48

tre els paràmetres ajustats ($\log M_{100}$, $\log c$, i β) i els valors mesurats. En aquesta taula podem veure que, amb 400 partícules, el paràmetre de concentració resulta menys sobreestimat, mentre que s'obté una anisotropia menys tangencial. Aquest comportament de c i β es pot entendre si considerem que, com ja hem mencionat, amb només 400 partícules els errors són molt més grans. Quan la curtosi és molt negativa, uns errors petits poden forçar l'ajust dels paràmetres cap a valors de β petits, la qual cosa s'ha de compensar amb factors de concentració grans per tal de reproduir la dispersió de velocitats.

A més, trobem que els errors en la determinació dels paràmetres són similars per als dos casos (totes les partícules de matèria fosca o només 400 partícules escollides a l'atzar). Aquest resultat ens indica que les variacions físiques degudes a la subestructura i a la diferent forma que presenta cada halo dominen respecte al soroll estadístic.

6. Conclusions

Aquesta tesi està centrada en les implicacions que la dinàmica dels cúmuls té en el contingut d'H I de les galàxies. Per una banda hem analitzat els efectes dels moviments de caiguda en la quantitat de gas neutre a les galàxies en la perifèria dels cúmuls. S'ha prestat una atenció especial als errors en l'estimació de distàncies en l'anàlisi del patró de caiguda en les zones externes dels cúmuls. A més, hem estudiat la dinàmica de la regió interna d'aquests sistemes, analitzant els efectes d'una incompleta virialització en la determinació de les propietats cinemàtiques dels cúmuls, les quals són un factor crucial per la possible pèrdua d'H I de les seues galàxies.

La determinació de l'origen de la deficiència d'H I de les galàxies en cúmuls requereix dades fiables de la seua posició i cinemàtica. Amb les incerteses actuals, hem sigut capaços d'obtindre una visió general de la distribució tridimensional de les galàxies del cúmul de Virgo. Aquesta distribució indica la presència de galàxies deficients en H I a la perifèria del cúmul, amb algunes al punt de retorn després d'haver travessat el centre. Això explicaria la presència de galàxies escombrades fins a una distància $\sim 2r_{100}$, la nostra estimació del radi màxim de rebot, mentre que l'extensió del medi intracumular revelada pels mapes de raigs-X és d'aproximadament un radi del virial. A més, hem mostrat que, tractant adequadament els errors en distància, és possible estimar masses i distàncies a cúmuls mitjançant models dinàmics de caiguda. D'altra banda, hem comprovat com la presència de no esfericitat, subestructura i moviments de caiguda no permet una determinació precisa de la cinemàtica i l'estructura interna dels cúmuls. Malgrat aquests efectes, hem mostrat que és possible obtindre una estimació acceptable de la seua massa del virial, l'anisotropia de la distribució de velocitats i el factor de concentració.

1 Introduction

The origin and evolution of galaxies has been an open question from the very moment the Hubble sequence was established (Hubble 1926, 1927), and the subsequent discovery that galaxies of different types are not homogeneously distributed in the sky, but show a morphological segregation (Hubble & Humason 1931; Abell 1958; Morgan 1961; and more recently, Giovanelli, Haynes, & Chincarini 1986; Andreon et al. 1996). In the near universe (i.e. at $z \sim 0$), early-type galaxies (ellipticals and lenticulars) are found mostly in high density regions such as cluster cores, whereas late-type galaxies (spirals and irregulars) tend to reside in looser environments. Many authors have studied this morphological segregation in order to unearth the main physical quantities governing this inhomogeneous distribution of galaxy types (e.g. Oemler 1974; Dressler 1980; Salvador-Solé, Sanromà, & Rdz. Jordana 1989; Whitmore & Gilmore 1991). These physical quantities could give important clues about the processes involved in the formation and possible evolution of galaxies and thus shed light on the longstanding “nature vs. nurture” debate: do galaxies present different morphologies according to the environmental conditions found at formation (e.g. Sandage, Freeman, & Stokes 1970; Silk 1978; Bardeen et al. 1986; Dekel & Rees 1987; Evrard, Silk, & Szalay 1990) or do they evolve along the Hubble sequence?

The evolutionary scenario received important support from the finding of the so-called Butcher-Oemler effect (Butcher & Oemler 1978, 1984): high redshift clusters have a larger fraction of blue galaxies than nearby clusters. Now, in the era of high resolution astronomy, we have become capable of disentangling galaxy morphologies in distant clusters, earning a much more accurate view of this effect: as one observes back in time, the spiral fraction in clusters rises with z at the expenses of the S0 fraction, while the elliptical fraction remains constant (Couch et al. 1994; Dressler et al. 1994; Wirth, Koo, & Kron 1994; Dressler et al. 1997; Oemler, Dressler, &

Butcher 1997; Smail et al. 1997; Fasano et al. 2000). The star formation rate also evolves, growing with increasing z (Poggianti et al. 1999; Balogh et al. 1999). The currently accepted scenario is one in which ellipticals (and perhaps the brightest S0's) are formed before the virialization of rich clusters at large z's and evolve passively ever since (Ellis et al. 1997), while an important fraction ($\sim 50\%$) of the S0 population is generated from the morphological transformation of spirals (e.g. Dressler et al. 1997). Several mechanisms have been suggested to be responsible for such morphological changes on the disk population. These include collisional gas removal by direct galaxy-galaxy encounters (Spitzer & Baade 1951), ram pressure stripping by interactions with the hot intracluster medium (Gunn & Gott 1972), viscous stripping and thermal conduction (Cowie & Songaila 1977; Nulsen 1982), tidal interactions or even mergers (Toomre 1972), galaxy-cluster gravitational interaction (Byrd & Valtonen 1990; Valluri 1993) or galaxy harassment (Moore, Katz, & Lake 1996).

In any case, to understand the observed properties of galaxies it is necessary to study the physics of galaxy interactions with their environment within the cosmological context of the hierarchical scenario for galaxy formation (White & Rees 1978) where galaxies develop inside dark matter halos growing hierarchically from small to large-scales. Cole (1991), Lacey & Silk (1991), and White & Frenk (1991) were the first ones to model the process of galaxy formation in this general context. These works were the seed for the so-called Semi-Analytic Models (SAM's) that follow the growth of dark matter halos (using Montecarlo realizations of the extended Press-Schechter model or by means of N-body simulations) and apply analytic recipes to model the complicated physics of baryons (see e.g. Kauffmann, White, & Guiderdoni 1993; Lacey et al. 1993; Somerville & Primack 1999; Hatton et al. 2003, to name only a few). In the spirit of these SAM's, our research group led by Dr. Eduard Salvador-Solé is currently developing a new, fully analytical, model of hierarchical galaxy formation and evolution that incorporates aspects so far only partially included by existing SAM's, such as fully motivated initial conditions, a consistent description of the internal structure of galaxies of different morphological types, the inclusion of central massive black holes and of the main interactions among galaxies: tidal truncation, dynamical friction, mergers, and ram pressure stripping.

Further constraints on the processes governing galaxy evolution in clusters and on the predictions of the models of hierarchical galaxy formation also come from observations in different environments of the physical parameters characterizing galaxies along the Hubble sequence (Roberts & Haynes 1994). If we want to obtain observational evidence to unmask the possible evolutionary mechanisms present in clusters, it is necessary to carry on studies in a statistically significant number of clusters of varying density and richness to disentangle which environmental conditions can play a role in the evolution of galaxies. Studies of this kind in nearby clusters have shown that galaxies in clusters differ from their field counterparts in their H I deficiency (see e.g. Solanes et al. 2001) and reduced star formation (Koopmann & Kenney 2002; Gavazzi et al. 2002; Lewis et al. 2002), while the molecular gas content (as traced by the CO) seems to be invariant with environment (Stark et al. 1986; Kenney & Young 1989). These characteristics, together with the presence of truncated H I disks in the center of clusters (Cayatte et al. 1990; Bravo-Alfaro et al. 2000), seem to favor interactions with the intracluster medium (ICM) as the main mechanism responsible for the changes of morphology in spirals. This observational evidence is supported by theoretical works, such as the one performed by Solanes & Salvador-Solé (1992), who explained the present concentration of S0's in clusters by following the transformation of spirals to lenticulars caused by ram pressure stripping from an initially non-segregated distribution of disk galaxies, and by hydrodynamical simulations (Abadi, Moore, & Bower 1999; Quilis, Moore, & Bower 2000; Schulz & Struck 2001; Vollmer et al. 2001), which proved the efficiency of the ICM in removing the neutral hydrogen disks and truncating star formation.

In addition to observations, and in order to have a complete view of the framework in which galaxies form and evolve, it is also necessary to know accurately the properties of dark matter halos in which galaxies reside and the role they play in determining the morphology of galaxies. Dynamical models of clusters, such as the spherical infall model (Gunn & Gott 1972), the Jeans approach (Binney & Tremaine 1987) or the caustic model (Regős & Geller 1989), among others, provide valuable information about the mass, density profiles and velocity distribution of dark matter halos, and complete the general picture of the formation and evolution of structures linking dark and luminous matter.

1.1 Motivation of this thesis

In order to understand the extent and effectiveness of the cluster environment in fueling the evolution of galaxies, the characterization of the H I distribution of cluster members plays a key role. The neutral hydrogen disk is the less gravitationally bound component of galaxies. It is therefore greatly affected by the aggressive environmental conditions present in clusters and thus an ideal indicator of the kind of interactions leading galaxies to experience morphological changes. Although the removal of the neutral hydrogen reservoir may prevent the formation of new molecular gas, reducing star formation as suggested by Guiderdoni & Rocca-Volmerange (1985), it is not yet clear how the lack of neutral hydrogen affects stellar formation (Kennicutt 1998) given that H I reservoirs extend significantly farther than the stellar disk (Cayatte et al. 1994). Although most observations indicate that the H_2 content of cluster galaxies is similar to that found in the field (see e.g. Kenney & Young 1989), the first evidences of a connection between the H I content of spiral galaxies and their star formation rate have recently been found (Gavazzi et al. 2002). If confirmed, these evidences would provide the missing link among neutral gas, star formation and subsequent color and luminosity evolution, leading ultimately to morphological changes.

To investigate the H I content of clusters and how it is affected by their dynamics and environmental conditions, it is very helpful to gather not only abundant data on projected quantities, but also on intrinsic (3D) ones. The Virgo cluster, the nearest rich large-scale galaxy concentration, is probably the best place to elaborate 3D maps of the spatial distribution of cluster properties. There is already a large amount of available data in the literature on positions, distances and velocities of its galaxies. Moreover, we have access to the Arecibo General Catalog, a private dataset maintained by Martha P. Haynes and Riccardo Giovanelli at the Cornell University, containing a huge amount of H I data for galaxies in this and others clusters that allow us to undertake this project.

As already mentioned, there are important reasons to suspect that ICM interactions play a crucial role in the evolution of galaxies. However, open questions still remain. Both H I content and star formation rate have been found to be depressed up to around 2 viral radii (e.g. Solanes et al. 2001; Lewis et al. 2002), what seems to be too large a distance given that ICM interactions are assumed to be effective only in the most central and densest parts of clusters. Nevertheless, the finding that H I-deficient galaxies are on more radial orbits that their non-deficient counterparts (Dressler 1986; Giraud 1986; Solanes et al. 2001) seems to overcome this difficulty. In effect, a spiral moving through the hot ICM will lost its gas if the pressure exercised by the intergalactic medium ($\rho_{\mathrm{ICM}}\, V^2$, where V is the velocity of the galaxy with respect to the ICM) is larger than the gravitational restoring force of the galaxy. Thus, for ram pressure to be effective, galaxies must pass through or near the cluster cores at high velocities. Therefore, it is reasonable to find most H I-deficient galaxies away from the cluster center after a passage through the dense core at high velocities (Vollmer et al. 2001). However, it is still not clear how far from the center we can expect to find H I-deficient galaxies resulting from interactions with the ICM. This would have serious implications in our knowledge of the time scale for galaxy evolution, as it would tell us how long galaxies with an important dearth of neutral hydrogen can maintain its morphology. To investigate this issue in detail, it is necessary to model the kinematics of galaxies falling into the cluster potential well, crossing the center and reemerging. A crucial factor for such a modeling is the mass of the cluster, as it determines the dynamics of the whole system. Methods such as the Jeans formalism can provide us with the virial mass of clusters from the study of their velocity distribution. This method, however, relies on the analysis of projected quantities and supposes clusters to be spherically symmetric and in steady-state, whereas real clusters are not (e.g. Wang & Ulmer 1997; Biviano, Durret, & Gerbal 1996). It is therefore necessary to determine its reliability by investigating the effects of infalling matter, non-sphericity, non-virialization and projection on the estimation of the dynamical parameters of clusters.

1.2 This work and related publications

The outline of this thesis is as follows. In the next chapter, we present antecedents of the two main issues that will be treated in this work, i.e., observations of H I deficiency in clusters and dynamical models of clusters. In Chapter 3, we infer the three-dimensional galaxy distribution of the Virgo cluster together with the distribution of H I deficiency. In Chapter 4, we model the Virgocentric velocity field, deriving an extension of the Tolman-Bondi model, with the aim of determining the dynamics of H I-deficient galaxies. Next, in Chapter 5, we use cosmological N-body simulations complemented by analytical arguments to estimate the maximum radius that galaxies can achieve after crossing the core of a cluster. Given that the positions of some galaxies in the Virgo cluster are apparently incompatible with our predictions, we use again, in Chapter 6, N-body simulations to study the role of errors in distance in deforming the Virgocentric velocity field and affecting the fitting of the parameters of Tolman-Bondi models. In Chapter 7, we further investigate the origin of the lack of neutral hydrogen of the outlying H I-deficient Virgo galaxies. Finally, Chapter 8 focuses again in the modeling of the internal dynamics of clusters, but this time to study not individual trajectories of galaxies but global quantities that we can infer from these models, such as the mass of clusters, their velocity anisotropy or their density profile. The former N-body simulations are used here to study the effects of non-sphericity, substructure and streaming motions in reproducing the structure and internal kinematics of clusters of galaxies by means of the analysis of their velocity distribution through the Jeans analysis. A summary, general conclusions and future perspectives are presented in the last chapter.

The work described in this thesis has given rise to five papers in refereed journals (two of them still under revision):

- *Chapter 3:* "The 3D structure of the Virgo cluster region from Tully-Fisher and H I data" Solanes, J. M., Sanchis, T., Salvador-Solé, E., Giovanelli, R., & Haynes, M. P. 2002, *Astronomical Journal*, 124, 2440.
- *Chapter 4:* "Are the H I-deficient galaxies on the outskirts of Virgo recent arrivals?" Sanchis, T., Solanes, J. M., Salvador-Solé, E., Fouqué, P., & Manrique, A. 2002, *Astrophysical Journal*, 580, 164.
- *Chapter 5:* "The origin of H I-deficient galaxies on the outskirts of the Virgo cluster. I. How far can galaxies bounce out of clusters?" Mamon, G. A., Sanchis, T., Salvador-Solé, E., & Solanes, J. M. 2003. Submitted to *Astronomy & Astrophysics.*
- *Chapters 6 and 7:* "The origin of H I-deficient galaxies on the outskirts of the Virgo cluster. II. Companions and uncertainties in distances and deficiencies" Sanchis, T., Mamon, G. A., Salvador-Solé, E., & Solanes, J. M. 2003. Submitted to *Astronomy & Astrophysics.*
- *Chapter 8:* "How reliable is the kinematical evidence for dark matter: the effects of non-sphericity, substructure and streaming motions" Sanchis, T., Łokas, E. L., & Mamon, G. A. 2003, *Monthly Notices of the Royal Astronomical Society*, in press.

In addition, during the realization of this thesis, I have collaborated in the following papers:

- "Structure, mass and distance of the Virgo cluster from a Tolman-Bondi model" Fouqué, P., Solanes, J. M., Sanchis, T., & Balkowski, C. 2001, *Astronomy & Astrophysics*, 375, 770.
- "On the origin of the inner structure of halos" Manrique, A., Raig, A., Salvador-Solé, E., Sanchis, T., & Solanes, J. M. 2003, *Astrophysical Journal*, 593, 26.

where we further investigate both the structure of the Virgo cluster by means of a Tolman-Bondi model and the inner structure of dark matter halos.

2 Historical overview

2.1 H I observations in clusters of galaxies

Since its detection in 1951, the 21-cm line of neutral hydrogen has provided astronomers with a fundamental tool for unveiling the effects of the environment on galaxies. The H I content of a galaxy indicates the strength of the interactions suffered by galaxies according to their surrounding environment (Haynes, Giovanelli, & Chincarini 1984). Therefore, the investigation of the neutral hydrogen content of galaxies provides fundamental clues for understanding their evolution.

2.1.1 Early work

At the beginning of the 80's, when large scale observations of neutral hydrogen in clusters became commonplace, a series of papers by Sullivan and coworkers (Sullivan et al. 1981; Schommer, Sullivan, & Bothun 1981; Bothun, Schommer, & Sullivan 1982a,b) based on observations performed in 9 clusters reached the conclusion that most spirals in clusters present H I contents comparable to galaxies in the field.

Two main problems in these early works hampered, however, the determination of the amount of neutral hydrogen of galaxies and the comparison of the H I content of galaxies in high density environments with those in the field (Haynes et al. 1984). On one hand, the very definition of H I content. The direct estimator, the H I mass, is a distance-dependent quantity affected by the (still nowadays) large uncertainties in distance estimates. Alternative measures such as the hydrogen mass to luminosity ratio used by Sullivan and coworkers have a residual dependence on luminosity, which may affect the analysis of samples affected by the Malmquist bias (Haynes et al. 1984), and is highly dependent of galaxy type, whose determination is not entirely reliable and subject to variations from one investigator to another. On the contrary, the hydrogen mass to optical diameter ratio proposed by Haynes & Giovanelli (1984) has a lesser dependence on morphological type and distance (the latter through a residual dependence on optical diameter). The other main source of uncertainty when trying to determine if a galaxy has an abnormal quantity of neutral hydrogen is the requirement of an unbiased and complete observational sample of isolated galaxies to compare with.

Early attempts of defining a reference sample for the H I content of galaxies by Balkowski (1973) and Roberts (1975) consisted on the compilation of mainly nearby isolated galaxies, which had the problem of being sometimes members of groups or pairs and thus were susceptible of having disturbed H I contents. Haynes & Giovanelli (1984) using objects in the Catalog of Isolated Galaxies by Karachentseva (1973) defined the first reliable standards of H I content for disk galaxies as a function of their diameter and morphological type. These standards allowed Giovanelli & Haynes (1985), from a much larger dataset than that of Sullivan and coworkers, to conclude that spirals in the core of dense clusters present high H I deficiencies, whereas only loose clusters (such as the ones studied by Sullivan and coworkers) have normal H I contents. Giovanelli & Haynes (1985) and subsequent works using their data (Dressler 1986; Magri et al. 1988; Valluri & Jog 1991) tried to find relations between the H I deficiency present in cluster galaxies and other cluster physical parameters. These relations could help to identify the process(es) responsible for the H I deficiency. Although these investigations argued in favor of an ongoing interaction between spiral disks and their environments, it was not possible to unambiguously identify the underlying mechanism(s). A correlation between the degree of deficiency and the X-ray luminosity was detected (Giovanelli & Haynes 1985), which appeared to favor interactions with the hot intracluster medium as responsible for the lack of neutral hydrogen. However, no clear correlation between the relative velocity of galaxies with respect to the cluster and their H I deficiency was found (Giovanelli & Haynes 1985; Dressler 1986; Magri et al. 1988). Moreover, the analysis of Valluri & Jog (1991) suggested the existence of a correlation between optical size and H I deficiency, which would argue in favor of tidal encounters among galaxies.

2.1.2 The Virgo cluster

Given its proximity and richness the Virgo cluster is an excellent candidate for quantifying the effects of the environment on the properties of galaxies, i.e. to distinguish the characteristics of galaxies in dense aggressive regions such as clusters from those in low density zones away from clusters and groups. As we have discussed at length in previous sections, the H I content is the most important characteristic that allows exploring the effect of cluster dynamics on galaxy evolution.

The first survey investigating the H I content of galaxies in the Virgo cluster was performed in the 60's by Robinson & Koehler (1965). Their data, as analyzed by Davies (1968), conducted already to the conclusion that Virgo cluster spirals are deficient in neutral hydrogen with respect to field galaxies. However, the small number of galaxies observed by Robinson & Koehler and the fact that their observations were limited in both position and velocity, a limitation which could result in an underestimation of H I masses, did not allow an unambiguous confirmation of the H I deficiency of galaxies in the cluster.

In the 70's, three major works pursued the study of the H I content of the Virgo cluster. On one side, Davies & Lewis (1973) and Huchtmeier, Tammann, & Wendker (1976) observed mainly late type spirals and found the average H I content of Virgo spirals to be about 1.7 smaller than the corresponding to galaxies in the field. As argued by Bottinelli & Gouguenheim (1974) and even Huchtmeier et al. (1976), these results were nevertheless doubtful because of the dependence of the luminosity of the estimator used to measure the H I content. On the other hand, Krumm & Salpeter (1979a,b) focused on S0's and early-type spirals, showing that these objects inside the Virgo cluster present also H I deficiency. Later works relying on larger samples confirmed that Virgo galaxies present a dearth of neutral hydrogen (Chamaraux, Balkowski, & Gérard 1980; Giovanardi et al. 1983; Giovanelli & Haynes 1983; Helou, Hoffman, & Salpeter 1984; Haynes & Giovanelli 1986).

In order to unambiguously identify the mechanism(s) responsible for the H I deficiency present in the core of the cluster, more detailed observations were necessary to disentangle among the effects in the H I distribution of each of the processes suggested as the cause of gas removal. Although some trends, such as the decrease of H I diameter towards the center of the cluster, had already been pointed out by single-dish measurements with the Arecibo antenna for the nearest galaxies (Giova-

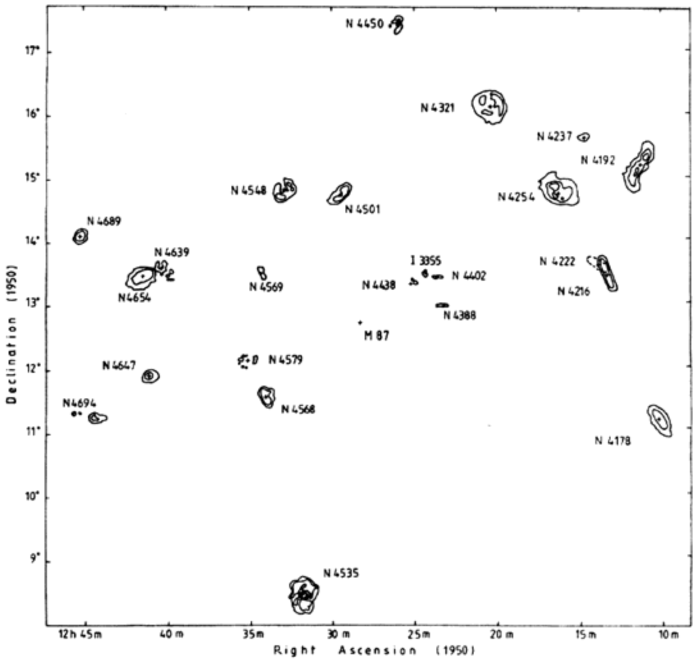

Figure 2.1: Integrated neutral hydrogen maps of the brightest spirals in the Virgo Cluster center. The center of the cluster is marked with a cross at the position of M87. *Note:* Taken from Cayatte et al. (1990)

nardi et al. 1983; Giovanelli & Haynes 1983; Haynes & Giovanelli 1986), it was not until the development of high-resolution images of the H I distribution obtained by aperture synthesis telescopes that it was possible to fully visualize the details of the distribution of neutral gas disks of galaxies. Warmels (1988) with the Westerbork Synthesis Radio Telescope and Cayatte et al. (1990) with NRAO's Very Large Array (VLA) identified the different features showed by the H I distribution of disk galaxies in the Virgo Cluster. They found strong asymmetries in the gas distribution of H I-deficient galaxies as well as truncated H I disks and central H I depressions in earlier spirals. In particular, Cayatte et al. (1990) showed how galaxies in the central part of the cluster have H I disks significantly smaller than their optical disks. We can see this trend in figure 2.1, taken from their paper.

Analyzing Warmels' data, Valluri & Jog (1990) proposed collisional gas removal by direct galaxy-galaxy encounters (Spitzer & Baade 1951) occurring in infalling groups in the cluster outskirts as the most plausible mechanism able to explain the deficiency of neutral hydrogen in the inner disks of spiral galaxies and the fact that the molecular gas content and its distribution show normal trends even in severely

H I-deficient galaxies (Stark et al. 1986; Kenney & Young 1989). In a follow-up study, Cayatte et al. (1994) classified Virgo spiral galaxies according to their H I extent as compared to the size of their optical disk $D_{\mathrm{H}}/D_{\mathrm{o}}$ (normalized for every Hubble type). They suggested that most H I-deficient galaxies placed deep into the cluster core had suffered the effects of ram pressure stripping, presenting small $D_{\mathrm{H}}/D_{\mathrm{o}}$ ratios and a sharp decline in their H I distribution. On the other hand, galaxies placed farther away from the cluster core presented higher $D_{\mathrm{H}}/D_{\mathrm{o}}$ ratios than central galaxies and smaller H I deficiencies (although noticeable across the whole disk) and thus were assumed to have undergone transport processes, such as turbulent viscosity or thermal conduction, since these processes affect the entire face of galaxies and not only the outer parts as ram pressure stripping does. Their results then argued against the importance of tidal stripping or direct encounters between galaxies to account for the deficiency in Virgo contrarily to the results of Valluri & Jog (1990).

2.1.3 Recent results

The great revolution brought by observations of clusters at high redshift, providing direct evidence of the evolution of galaxies with z, has put the debate on the physical mechanisms governing galaxy evolution again in the headlines of astronomical research, pushing H I observations back to the main interests of astronomers, especially those relying on aperture synthesis telescopes, as they allow obtaining detailed maps of the H I distribution. Apart from Virgo, other clusters have been recently imaged: Hydra (McMahon 1993), Ursa Majoris (Verheijen 1996), A2670 (van Gorkom 1996), A262 (Bravo-Alfaro et al. 1997) and Hercules (Dickey 1997). Specially interesting are the results of Bravo-Alfaro et al. (2000) in the Coma cluster, the richest of the nearby clusters, which confirm previous findings that H I poor galaxies are concentrated towards cluster centers, with optical disks extending beyond H I disks.

This renewed interest in the H I content of spirals in clusters led Solanes et al. (2001) to review and update the properties of H I-deficient galaxies in clusters. With 1900 spirals in the field of 18 nearby clusters and using new Malmquist bias-free estimates of the H I mass standards for isolated galaxies (Solanes, Giovanelli, & Haynes 1996), they found that 12 of the 18 cluster under study were deficient in neutral hydrogen, with deficient galaxies extending up to 2 Abell radii. These authors also investigated the possible connections between H I content and other global properties of H I-deficient clusters. Contrarily to the tendency suggested by Giovanelli & Haynes (1985), no clear correlation between the X-ray luminosity and the degree of H I deficiency was found. On the other hand, it was shown that early spiral types present higher rates of H I deficiency than late types, even when the effects of morphological segregation (which would leave earlier types in more central and aggressive environments) are taken into account, in agreement with previous results by Guiderdoni & Rocca-Volmerange (1985) and Dressler (1986). Findings that early type spirals often exhibit central H I depressions and holes in their H I distribution (Broeils & van Woerden 1994; Cayatte et al. 1994), which could amplify the effectiveness of ram pressure (Moore, Quilis, & Bower 1999), appear to support this result. Moreover, no trend between H I content and optical diameter was found contrarily to the claims by Valluri & Jog (1991) based on a smaller sample and a biased deficiency estimator. Finally, the existence of an orbital segregation of disk galaxies according to their gas content, as suggested by Dressler (1986) and Giraud (1986), was confirmed: H I-poor objects move along more eccentric orbits than gas-rich objects. This finding is consistent with dark matter simulations of hierarchical clustering (e.g. Ghigna et al. 1998), which show that the orbital distribution of substructure halos has a median value of apocentric to pericentric distances of 6:1, being circular orbits rather rare. Overall, these results, taken in its totality, favor ram pressure stripping as the main agent of gas removal.

The large amount of data accumulated in the Virgo cluster also allowed Solanes et al. (2001) to study the effects of the environment in the H I content of Virgo galaxies in much more detail. These authors did a two-dimensional map of the gas deficiency in the central cluster region, a copy of which we present in figure 2.2. In this figure, we can see several structures: the zone with the maximum gas deficiency coincides with the main density enhancement known as Cluster A (Binggeli, Popescu, & Tammann 1993), a double system comprising the subclusters centered on the giant ellipticals M87 and M86. Apart from this central maximum, we can see up to 5 deficiency enhancements, which seem related to the Cluster B around M49 to the South (Binggeli et al. 1993), around M100 to the North, around M59 and M60 to the East and finally, around two background concentrations, the M cloud in the northwest and the W group in the southwest. The possible existence of highly H I-deficient galaxies at large projected distances of the main body of the cluster and apparently connected to it by gas deficient zones, together with the previous result that deficient galaxies exhibit highly eccentric orbits, suggested the possibility that galaxies in these deficient zones away from the cluster core could have already ex-

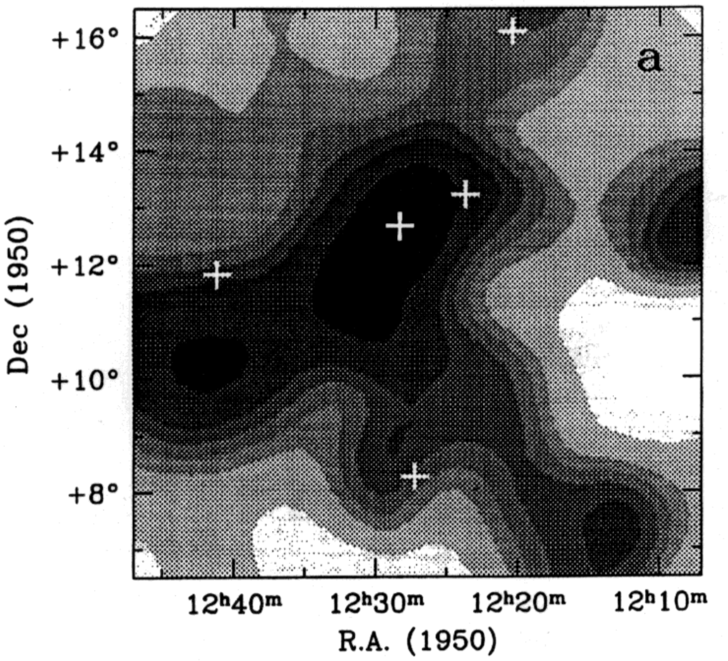

Figure 2.2: Gray-scale image of the sky distribution of the H I deficiency in the central region of the Virgo Cluster. The darkest regions in the maps correspond to the most deficient zones. The position of five dominant galaxies are marked by crosses (top to bottom: M100, M86, M87, M60, and M49). The peak value of H I deficiency is located near the position of M87. *Note:* Taken from Solanes et al. (2001)

perienced a high-velocity passage through the Virgo core, which could have affected their gas content. In order to study this intriguing possibility and its implications on the origin of the H I deficiency of Virgo cluster galaxies, dynamical models of the velocity field drawn by cluster galaxies are necessary to determine the kinematics of H I-deficient objects and verify if their positions in the phase space diagram are compatible with an early passage through the cluster core.

2.2 Dynamical models of clusters

2.2.1 Infall models

Within this category we include models that describe the dynamical history of clusters, following the trajectories of their components, usually idealized as mass shells.

Hence, these are models that study the radial component of the orbits of individual objects, so they are useful to investigate if H I deficient galaxies could have lost its gas in an early passage through the cluster core.

Motivated initially by the aim of determining the physical parameters of the universe, such as Ω_0 and the deceleration parameter q_0, many works began studying in the 70's the dynamical effects of a concentration of matter on a otherwise expanding homogeneous universe. The most general approach was to model spherical condensations with purely radial flow in an expanding Friedmann-Robertson-Walker background universe (Gunn & Gott 1972) to predict a connection between the infall peculiar velocity of galaxies and the density parameter of the universe (Silk 1974). Peebles (1976) used a linearized version of the spherical infall model, and therefore only valid in the outer parts of a density enhancement, which he modeled with a radial profile following $\rho(r) \propto (1 + Ar^{-\alpha})$, where r is the distance to the center of the density peak. He found that peculiar velocities in the outskirts of this mass distribution should be proportional to $r^{-(\alpha-1)}$.

Two main problems rendered the application of the spherical infall model to the inner parts of clusters difficult. On one hand, the treatment of shell-crossing, i.e. when two shells, one still expanding and the other one already on infall, meet and thus the energy of each individual shell is not conserved. On the other, the problem of the singularity at the center of the mass distribution, where velocities diverge. In a series of papers, Silk, Wilson and Olson (Silk & Wilson 1979a,b; Olson & Silk 1979) addressed these problems and extended the spherical infall scenario to the inner parts of clusters introducing, for a variety of initial conditions, the idea of an exchange of potential energy between two crossing shells. They avoided the problem of the singularity at the center of the mass distribution by introducing a reflecting surface near the origin. In a follow-up study, Hoffman, Olson, & Salpeter (1980) and Hoffman & Salpeter (1982) used parametric solutions to Newton's equations to avoid the problem of the singularity at the center (and thus the reflecting surface needed by Olson & Silk 1979). They treated shell crossing as Silk & Wilson. However, when using Newton's equations, shells arrive to very small radii, which can produce unphysical very large exchanges of potential energy. They had thus to introduce a length parameter to control the energy exchange at small radii. Furthermore, they incorporated the transformation of radial velocities into orbital velocities by violent relaxation, converting a fixed fraction of the initial radial kinetic energy of the shells into orbital kinetic energy. As a result of this transformation of energy, this model produces an inner core in the density profile of the cluster. With this model, they obtained a mass of Virgo inside 6° of 4×10^{14} $M_\odot$. Capelato et al. (1982) also derived a method for inferring the velocity field around a cluster from the observed velocity dispersion, applicable to the inner parts of the cluster.

When the works cited above were published, both distance estimators were not fully developed and the amount of data was small. So most of them tested the validity of their modeling comparing the predicted velocity distribution with that of observed galaxies. Once larger samples of galaxies with more accurate distances became available, it was possible to compare velocity-distance diagrams with results from dynamical models. Tully & Shaya (1984) used velocity and distance observations in the Virgo Southern extension in the framework of an infall model neglecting shell crossing. They found that most spirals were falling into the cluster for the first time. They tried different mass-age models, as the age of the Universe (t_0) was still not well known. Their data were consistent with a point mass of 7.5×10^{14} $M_\odot$. In a follow-up study to take into account galaxies that had already crossed the center of the cluster, Giraud (1986) used 107 galaxies in the Virgo area to investigate the orbits of H I-deficient galaxies and the velocity-distance relation in Virgo. He found that the residual velocity of galaxies as a function of the projected radius was consistent with radial orbits only for H I-deficient galaxies. Although his estimations of distances were rather inaccurate, with a dispersion of 0.46 magnitudes, he found that positions in the velocity-distance diagram of H I-deficient galaxies were compatible with a rebound orbit for a mass-age model with $M \sim 5 \times 10^{14}$ $M_\odot$ and $t_0 \sim 12$ Gyr. Teerikorpi et al. (1992) used exact Tolman-Bondi solutions valid also in the inner parts of a spherical mass distribution. They did not use a point mass model but a model with a density excess proportional to $r^{-\alpha}$. With better distances and a larger sample than Tully & Shaya (1984), they found an overall good fit to the Tolman-Bondi model but also some galaxies expanding away from the cluster, contrarily to the conclusions of Tully & Shaya (1984) and in concordance with the proposal of Giraud (1986). Subsequent work based on more extensive datasets by Ekholm & Teerikorpi (1994), Ekholm (1996), Ekholm et al. (1999), and Ekholm et al. (2000) (as well as Hanski et al. 2001, for the Piscis-Perseus supercluster) refined this method reaching the conclusion that the distance to Virgo should be between $20 - 24$ Mpc and its mass $\sim 1.5 \times 10^{15}$ $M_\odot$.

An application of the Tolman-Bondi model as defined by Teerikorpi et al. (1992) and subsequent work can be found in Fouqué et al. (2001), where we used this model

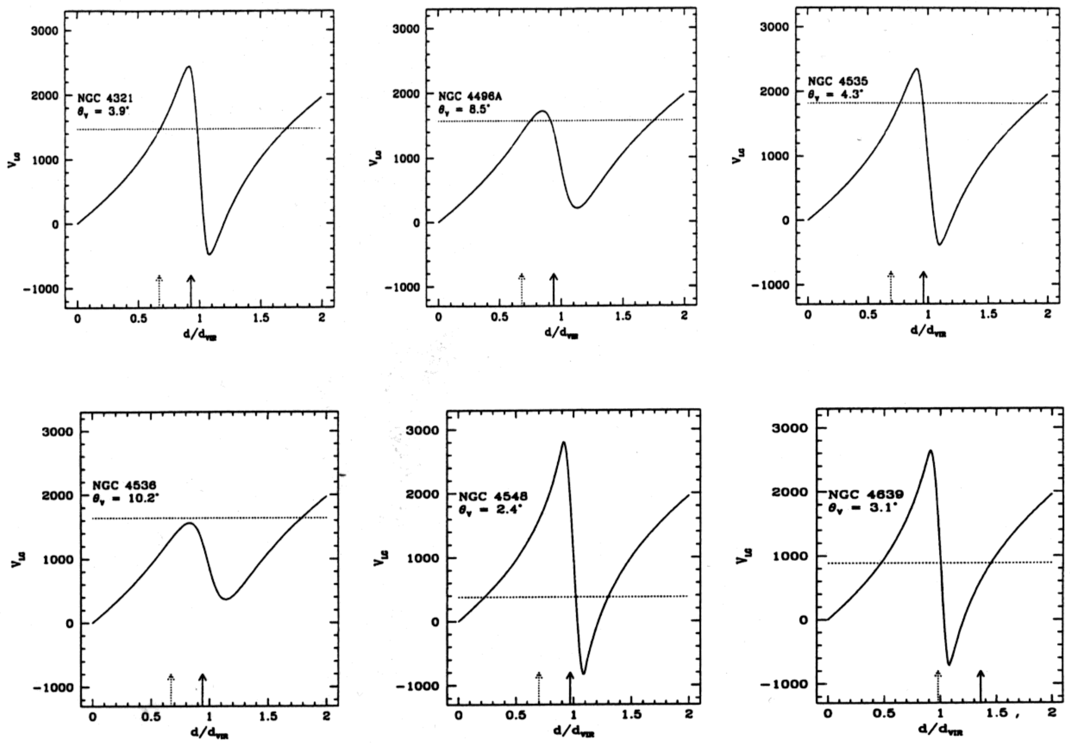

Figure 2.3: Tolman-Bondi model for the six galaxies with Cepheid distances. The dotted line corresponds to the recession velocity of the galaxy, while the arrows mark the expected distance ratio if $d_{\rm VIR} = 15.4Mpc$ (solid arrow) or $d\ _{rmVIR} = 21.5Mpc$ (dotted arrow). *Note:* Taken from Fouqué et al. (2001)

to constrain the Virgo cluster mass and its distance. We made use of the fact that for each galaxy, its angular-distance to the Virgo center of mass completely defines the shape of a Tolman-Bondi "S-curve" in the velocity-distance (in units of the distance to Virgo) diagram, for a given choice of model parameters (i.e. the observed Virgo cluster velocity in the Local Group reference frame, the Virgocentric infall velocity of the Local Group, the Virgocentric density profile and the deceleration parameter of the background homogeneous universe; see equations 4.1-4.6 in Chapter 4). Therefore, given the velocity of a galaxy in the Local Group reference frame, there are three possible distance ratios of the galaxy to Virgo, two corresponding to a galaxy falling into the cluster from the front or from behind and one corresponding to a galaxy in the core of the cluster. In order to obtain a value for the distance to the center of Virgo, we used 6 Virgo galaxies whose distance where known from measures of the Cepheid period-luminosity relation (Freedman et al. 2001). From the Tolman-Bondi "S-curves" and the velocity of these galaxies, we selected the most plausible distance ratios by choosing the values closest to the assumed Virgo distance of 16 Mpc (Gavazzi et al. 1999) and, as we had also measures of the H I deficiency of these galaxies, taking into account that a true member of the cluster has a higher probability to be gas deficient than a galaxy falling into the cluster for the first time (see Section 2.1). In figure 2.3, we show the velocity-distance diagram with the Tolman-Bondi “S-curve” (obtained with the parameters of Ekholm et al. 1999) for the 6 Cepheid galaxies. Given the known distances of these 6 galaxies and the ratio between the distance to each galaxy and the distance to the cluster obtained from the Tolman-Bondi model, we inferred a distance to the Virgo cluster of 15.4 Mpc. This value allowed us to estimate that the mass enclosed within 6° around the cluster (see equation 4.12) has a value of 1.2×10^{15} $M_\odot$.

2.2.2 Structural models

This category encompasses methods that do not follow the dynamical history of clusters but infer their structural properties from global kinematical parameters, such as velocity moments, the velocity anisotropy or caustic shapes, measured at a given time (i.e. at $z = 0$).

One of the methods that can be used to extract information on the dynamical state of clusters consists on the identification of the caustics (surfaces with a characteristic “trumpet” or “diamond” shape) defined by galaxies around clusters in redshift space, first discussed by Kaiser (1987) within the framework of the spherical infall model. This method is valid at intermediate distances (i.e. outside the virialized region but also outside the linear regime characteristic of larger cluster-centric distances). Regős & Geller (1989) extended the work of Kaiser (1987) and showed that the shape and size of caustics are defined by the mass of the system and could be used to estimate Ω_0. However, van Haarlem et al. (1993) and van Haarlem & van de Weygaert (1993) found that the observed caustics were smeared out, making it difficult in practice to identify their location, while model caustics are very sharp. This was attributed to deviations from sphericity and to the contribution of substructure in the infalling material. Two works tried to solve this difficulty: Vedel & Hartwick (1998) suggested an alternative procedure to extract the information contained in redshift diagrams based on a maximum likehood technique. They used a superposition of a systematic component following the spherical infall model and a noise component chosen to represent the effects of small-scale substructure and observational errors. This method needs, however, observations from several clusters to obtain reliable results of the mass profile of clusters. On the other hand, Diaferio (1999) presented an operational method for extracting the mass profile from the redshift space distribution of galaxies within real clusters based on the results of Diaferio & Geller (1997), who using N-body simulations showed that the amplitude of caustics is related to the local escape velocity and is therefore a measure of the cluster gravitational potential. Later applications of the results of Diaferio & Geller (1997) can be found, for instance, in Geller, Diaferio, & Kurtz (1999), Drinkwater, Gregg, & Colless (2001), and Rines et al. (2002).

Another method of estimating the dynamical properties of clusters consists on the analysis of the spatial distribution and kinematics of its galaxies through the Jeans equation (see Biviano 2002, for a review), which has been applied to elliptical galaxies (e.g. Binney & Mamon 1982), clusters of galaxies (e.g. Kent & Gunn 1982; Merritt 1987; Solanes & Salvador-Solé 1990), as well as to globular clusters (e.g. Merrifield & Kent 1990). This method dates back to Zwicky (1933, 1937) and Smith (1936) who estimated the masses of the Coma and Virgo clusters using the virial theorem. The virial theorem method was refined by The & White (1986) who introduced the surface-term correction, which has been used lately by Carlberg et al. (1997b), Girardi et al. (1998) and Girardi & Mezzetti (2001). The traditional Jeans approach assumes a non-rotating system with spherical symmetry in equilibrium (see Binney & Tremaine 1987). Under these circumstances, the Jeans equation provides the mass profile of the object under study from the density profile, the radial velocity dispersion and the anisotropy. The use of the Jeans equations therefore requires dealing with 3D density and velocity dispersion profiles that could be inferred from the observed projected 2D profiles. The scarcity of data in clusters of galaxies makes it difficult, however, to adopt this approach. Instead, it is quite common to follow the inverse approach, i.e. adopt ad-hoc forms for the three-dimensional profiles (density and velocity dispersion profiles), which are then projected to constrain the involved parameters by comparison with the observed moments of the velocity distribution. However, the solutions obtained in this way are intrinsically degenerated, so it is not possible to constrain simultaneously the mass and the anisotropy profile only from the observed line-of-sight velocity dispersion (see e.g. King 1972; Bailey 1982; Merrifield & Kent 1990; Merritt 1987). One possible way to break this degeneracy is by modeling not only the second moment of the velocity distribution of galaxies, but also higher orders (Merritt 1987; Merritt & Saha 1993; Łokas & Mamon 2003). Moreover, in order to increase the size of galaxy samples and reduce the noise of data, it is customary to deal with composite clusters formed by grouping data of several clusters (after normalization with respect to the virial radius for distances and velocity dispersion for velocities), extracted from catalogs such as the ESO Nearby Abell Cluster Survey ENACS (Mazure et al. 2000; Biviano et al. 2003), the Canadian Network for Observational Cosmology CNOC (Carlberg, Yee, & Ellingson 1997a; Carlberg et al. 1997b; van der Marel et al. 2000; Carlberg et al. 2001) and the Two Degree Field Galaxy Redshift Survey 2dFGRS (Biviano & Girardi 2003). Although these composite clusters are, by construction, spherically symmetric, the Jeans approach has the problem that real clusters are generally not (Binggeli 1982; Wang & Ulmer 1997). Moreover, there have been claims of the existence of rotational motions in clusters (Biviano et al. 1996; Dupke & Bregman 2001) and of systems still in the phase of collapse or not fully virialized. It is therefore interesting to study the contribution of these effects usually neglected when performing the Jeans analysis of clusters. Tormen, Bouchet, & White (1997) where the first to address this question by means of cosmological N-body simulations. They focused only on the inaccuracy of the estimation of cluster masses due to an incomplete virialization. They found that the dispersion between masses inferred by the Jeans analysis and real ones was less than 20%. A more detailed analysis of the effects of infalling matter, non-sphericity, non-virialization and projection will be addressed in this work.

For the sake of completeness, we would finally like to mention two other methods that, although do not involve analysis of kinematical data of clusters (i.e. positions and velocities of their components), are also useful for estimating their mass profiles and therefore characterizing their dynamical state. One is based on gravitational lensing (see e.g. recent applications in Dahle, Hannestad, & Sommer-Larsen 2003; Gavazzi et al. 2003) and cannot be applied to nearby clusters. The other one is based on the assumption that the hot X-ray emitting intracluster gas is in hydrostatic equilibrium (see e.g. Demarco et al. 2003; Ettori, De Grandi, & Molendi 2002).

3 The 3D structure of the Virgo cluster region from Tully-Fisher and H I data

3.1 Introduction

Solanes et al. (2001) examined the possible connections between gas deficiency and the properties of both the underlying galaxies and their environment in the fields of eighteen nearby clusters. The main motivation was to gain insight into the mechanisms responsible for the atomic gas depletion. While no clearly discriminating circumstances were found among those clusters which show significant H I deficiency and those which do not, this work definitely confirmed previous findings (e.g., Giovanelli & Haynes 1985; Haynes & Giovanelli 1986; Magri et al. 1988) that in H I-deficient clusters the proportion of gas-poor spirals increases monotonically towards the center. Moreover, Solanes et al. clearly demonstrated, as first suggested by Dressler (1986), that H I-deficient objects move on orbits more radial than those of their gas-rich counterparts. This result made a strong case for the ram pressure stripping of the spirals by the hot X-ray emitting intracluster medium as the most likely process responsible for the gas deficiencies observed in rich cluster environments.

The wealth of 21-cm data gathered for the Virgo region in Solanes et al. (2001) also made it possible to examine the distribution in two-dimensional space of the neutral gas deficiency in the Virgo central area. The sky distribution of H I deficiency was found to be in overall agreement with the radial pattern characteristic of rich clusters, showing that the maximum depletion occurred at the cluster center. But quite unexpectedly, the same map of the H I deficiency pattern, a variation of which is produced here as figure 3.1, also revealed peripheral groups of galaxies with a dearth of atomic hydrogen but found in areas where the density of X-ray luminous gas is very low, raising into question the feasibility that the ram pressure of the ICM was responsible for the observed H I deficiency. However, the two-dimensional nature of the H I map did not allow to unambiguously state the existence of such gas deficient zones away from the cluster center, as they could be produced by a chance superposition along the line-of-sight of galaxies with a lack of neutral hydrogen but without any physical connection among them. It became thus evident the necessity of recovering three-dimensional information for a complete picture of the H I distribution in the cluster and a further understanding of the influence of the cluster environment in the evolution of galaxies.

In this chapter, we conduct a further investigation into the nature of and conditions within the three-dimensional structure of the Virgo region, by incorporating into the analysis the H I content of its spiral population. The proximity of the region under study facilitates the gathering of a large number of 21-cm single-dish observations, which we complement with a large number of Tully-Fisher (hereafter TF) distance estimates (Tully & Fisher 1977) also reported in the literature. Section 3.2 presents a catalog of 161 galaxies with good H I and TF distance measurements. After reviewing in Section 3.3 the manner in which the H I deficiency is calculated, our galaxy sample is used in the following two sections to discuss, first the radial pattern of H I deficiency, and then its spatial distribution in the Virgo region. We conclude with a summary and some remarks in Section 3.6.

3.2 Observational data

3.2.1 Galaxy selection

The backbone of the present study is the complete spiral sample taken from the *Virgo Cluster Catalog* (Binggeli, Sandage, & Tammann 1985, hereafter VCC) by Yasuda, Fukugita, & Okamura (1997, hereafter YFO97) to study the Virgo cluster using the B-band TF relation. The YFO97 sample has been supplemented by data from seven other studies of the Virgo cluster, likewise presenting TF distance estimates at various wavelengths. Table 3.1 lists the different sources of TF distances for Virgo

Table 3.1: TF Datasets Contributing to the Present Sample

		Number of galaxies	
Source	Acronym	Total	Selected
Yasuda, Fukugita, & Okamura 1997	YFO97	246	165
Mould, Aaronson, & Huchra 1980	MAH80	23	21
Pierce & Tully 1988	PT88	34	34
Kraan-Korteweg, Cameron, & Tammann 1988	KCT88	128	84
Fouqué et al. 1990	Fou90	178	145
Federspiel, Tammann, & Sandage 1998	FTS98	132	129
Gavazzi et al. 1999	Gav99	75	72
Ekholm et al. 2000	Ekh00	96	52

objects included in the present work, along with the number of galaxies included in our catalog. These datasets include virtually all spiral galaxies used to date in the application of the TF relation to study the Virgo region.

For the current purpose, we have selected from the original catalogs listed in table 3.1 only galaxies with heliocentric radial velocities below the well-defined gap near 3000 km s^{-1} that neatly isolates the Virgo region in redshift space (Binggeli, Popescu, & Tammann 1993). In addition, we have focused on galaxies located in the region bounded by $12^{\mathrm{h}} \leq$ R.A. $\leq 13^{\mathrm{h}}$ and $0° \leq$ Decl. $\leq +25°$ (throughout the chapter equatorial coordinates are referred to the B1950.0 equinox), which encompasses the VCC survey boundary and is centered on the classical Virgo I cluster (de Vaucouleurs 1961). Thus, wherever we use the terminology “Virgo cluster region”, it should be kept in mind that objects located in the “Virgo Southern Extension” (Tully 1982) or Virgo II cluster, i.e., with Decl. $< +5°$, are indeed largely excluded. Note that our selection procedure also implies that all the galaxies included in our sample (even those classified as background objects in VCC) are expected to have peculiar motions influenced by the central mass concentration of the cluster.

Our initial selection of Virgo galaxies includes a total of 198 objects, which we summarize in table A.1 in Appendix A. This table contains, among other information, the distance moduli to each galaxy given in the eight TF studies on which our investigation is based. For seven of these galaxies, we also list their Cepheid distances given in the final results from the Hubble Space Telescope Key Project to measure the Hubble constant by Freedman et al. (2001) corrected for the effects of metallicity.

3.2.2 Homogenization of the distances to individual galaxies

Since our compilation of TF distances was built from eight datasets that contain sometimes inconsistent data, the average of the measurements available for each object does not necessarily provide the best estimate of the galaxy distances. We thus have attempted first to reduce the data to a homogeneous system by eliminating systematic differences among the different sources. We have carried out this task by means of a recursive procedure applied separately to each of the eight Virgo datasets listed in table 3.1 and composed of the following steps:

(i) For each dataset, we take only those galaxies which also have distance measurements in any of the other seven datasets and calculate for each of those objects the arithmetic mean of all their distance estimates, as well as the standard deviation of the individual measurements.

(ii) Then, using only the galaxies in the chosen catalog which have multiple distance measurements, we determine the linear regression of the individual distances against the average values, applying a 3σ clipping to remove those points which deviate significantly from the regression line. The regression coefficients are then recalculated and the 3σ rejection procedure is repeated until no more galaxies are rejected. Once a datum is flagged as highly deviant, it retains this status for the rest of the procedure.

(iii) The regression coefficients calculated at the end of step (ii) are used to transform all distance measurements of the dataset under scrutiny, including those not listed elsewhere, into the system of mean distances defined by the sample members with multiple observations.

The standardization to the mean values affects each dataset differently. So once steps (i), (ii), and (iii) have been performed for the eight source catalogs (excluding the data already flagged as most deviant), the procedure is repeated again until all the corrections become negligible. Convergence to a homogeneous system of mean distances is achieved in only a few cycles.

When *all* the distance measurements available for an individual object show residuals inconsistent with the regression lines, we ascribe this to a possible source misidentification and accordingly exclude the galaxy from the calculations. This seems to be the case of the galaxies V0975 and V1678, with only two distance measurements each that disagree beyond allowed uncertainty. We have also excluded from the homogenization process the seven galaxies with Cepheid distances: V0596, V1375, V1555, V1562, V1615, V1943, and N4725. For these galaxies we use the Cepheid measurements and their quoted errors.

The distances obtained with the procedure described above and their associated 1σ uncertainties are listed in the last column of table A.1. The rms error of the individual distance moduli is 0.29 mag, which translates to an uncertainty of about 13% in the redshift-independent distance measurements. This means that for an individual galaxy at, say, 20 Mpc, we expect a typical error in the distance of ~ 2.5 Mpc. This implies a sufficient level of accuracy in the measurement of individual distances to allow us to explore the gross features of the three-dimensional structure of the Virgo cluster.

3.2.3 The 21-cm sample

For the homogenization of the distance moduli, we have taken all the galaxies listed in two or more of the source TF catalogs (i.e., with multiple distance measures), regardless of their Hubble type, in order to minimize the impact of statistical “shot noise”. Since irregular and bulge-dominated galaxies may give, however, unreliable TF distances and/or H I content measurements, we re-examined the morphologies of the galaxies and picked up only those with Hubble types ranging from $T = 1$ (Sa) to $T = 9$ (Sm), as given in the *Third Reference Catalogue of Bright Galaxies* (de Vaucouleurs et al. 1991).

The principal source for the H I line fluxes is the *Arecibo General Catalog* (hereafter AGC), which contains an extensive compilation of 21-cm-line measurements collected from a large number of sources. Among the galaxies with a clear spiral morphology, there are 15 for which the AGC did not provide useful data, including 2 galaxies that overlap with obvious optical companions and 3 non-detections. We found H I flux measures for 9 of these objects in *A General Catalog of* H I *Observations of Galaxies* (Huchtmeier & Richter 1989) and in the *Lyon-Meudon*

Extragalactic Database (LEDA, nowadays HyperLEDA). All the observational values have been corrected for the effects of random pointing errors, source extent, and internal H I absorption following Haynes & Giovanelli (1984), except the nine non-AGC fluxes and the only non-detection, V0522, which have been corrected only for internal H I self-absorption and assigned an 'H' flag in the final dataset.

The AGC is also adopted as the source of other observational parameters required by our study, such as the equatorial coordinates of the galaxies, their visual optical diameters, which are involved in the determination of the H I deficiency (see next section), and their heliocentric radial velocities, which we transform to systemic velocities, $v_{\rm sys}$, by referring them to the kinematic frame of the Local Group, taken equal to 308 km s^{-1} towards $(l, b) = (105°, -7°)$ (Yahil, Tammann, & Sandage 1977).

On the other hand, for the H I-line width, a parameter of lesser importance in this investigation, the heterogeneity of the measures contained in the AGC prompted us to adopt instead the inclination-corrected values of the line width at 20% level of the line-profile peak, $W_{20}^{\rm c}$, listed in YFO97. For most of the galaxies that concern us here, these authors provide a set of observations standardized into line widths measured at the Arecibo circular feed following a similar process to that carried out here with the distance moduli. For galaxies not included in the YFO97 sample, we use the values of W_{20} and inclination quoted in LEDA, except for the galaxy V1043, not listed in either of these two catalogs, for which we adopt the corresponding measurements by MAH80 (measurements other than from YFO97 are flagged 'W' in the final dataset). Furthermore, we have excluded spiral galaxies with $W_{20}^{\rm c} \leq 100$ km s^{-1} to reduce the error induced from turbulent disk motion. We do not impose an inclination cut because this parameter does not play any explicit role in our investigation (remember that, for most of the galaxies in our dataset, we are adopting values of the line width already corrected for inclination). Nevertheless, objects with $i < 45°$ in LEDA are warned with an 'i' flag in our final catalog.

After all these selections, we end up with a sample of 161 spiral galaxies with reliable H I content and distance data, hereafter called the "21-cm sample", which is used below to assess the spatial distribution of the neutral gas deficiency in the Virgo cluster region. As stated in Section 3.3.1, the scatter of the best fitting TF template for the 161 galaxies is 0.41 mag. Hence, the uncertainty in the distance modulus of the individual galaxies in this dataset is comparable to the scatter of

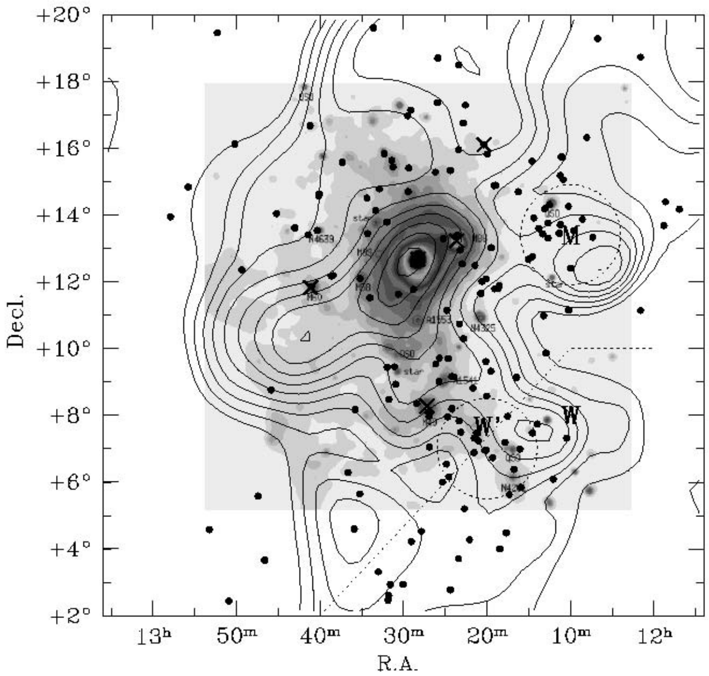

Figure 3.1: Distribution in celestial coordinates of the 161 members of the 21-cm sample. The contour map of the *distance-independent* H I deficiency parameter is reproduced from Solanes et al. (2001) A grey-scaled version of the X-ray image of the central cluster region in the ROSAT all-sky-survey in the hard energy band is overlaid. The background W, W′, and M subgroups are delineated by dotted lines. The sky positions of five dominant galaxies are marked by crosses (top to bottom: M100, M86, M87, M60, and M49).

the most accurate TF template relations currently available.

All the parameters relevant to our investigation are listed in table A.2 in Appendix A, where we have included two different measurements of the H I deficiency and the absolute B-magnitude of the galaxies, $M^{\mathrm{c}}_{B_{\mathrm{T}}}$, calculated from their total apparent corrected B-magnitude listed in LEDA and our distance estimate. The sky distribution of the members of the 21-cm sample is presented in figure 3.1 (five galaxies with extreme values of declination have been omitted for a better overall impression).We have reproduced the contour map of the *distance-independent* H I deficiency parameter from Solanes et al. (2001). This contour map has been generated using a straightforward extension of the adaptive kernel technique described in Silverman (1986). Note that the contours are generated from all the 287 spirals with a neutral content measure listed in the AGC within the area depicted by the figure, not only with the 161 members of which we have reliable distance estimates. In order to visualize the density of the ICM, we have overlaid a grey-scaled version of the X-ray image of the central cluster region in the ROSAT all-sky-survey in the hard (0.4–2.4 keV) energy band. For a better understanding of the structure of the Virgo cluster, we show the position in the sky of background subgroups from Binggeli et al. (1993) as well as for five dominant galaxies (M100, M86, M87, M60, and M49). We can see from this figure that the projected location of M87 coincides with the peak of the H I deficiency and of the X-ray emission.

3.3 The diagnosis of H I deficiency

H I deficiency is often quantified by the parameter $< DEF >$ defined as

$$< DEF > = \langle \log M_{\rm HI}(D_{\rm opt}, T) \rangle - \log M_{\rm HI} \ , \tag{3.1}$$

(e.g., Chamaraux et al. 1980; Haynes & Giovanelli 1984; Solanes et al. 1996), where $M_{\rm HI}$ is the H I mass of the galaxy in solar units, and the angular brackets on the right of the equal sign indicate the expected value of this quantity inferred from a sample of field galaxies of the same *optical* linear diameter $D_{\rm opt}$ and morphological type T. The neutral hydrogen mass, in turn, is calculated from the expression

$$M_{\rm HI} = 2.36 \times 10^5 d^2 F_{\rm HI}, \tag{3.2}$$

where d is the observed radial distance of the object in Mpc and $F_{\rm HI}$ represents the corrected H I flux density integrated over the profile width in units of Jy km s^{-1}. The most recent determinations of the expectation values for the H I mass as a function of the size and morphology of the galaxies are given in Solanes et al. (1996) in the form of linear regressions that imply power law relationships of the type $M_{\rm HI} \propto D_{\rm opt}^n$, with the values of n oscillating between about 1.7 for Sc's and 1.2 for earlier spiral types.

For the present study, however, we need to use a calibrator for the neutral gas deficiency not tied to the distance to the galaxies. Given that the $M_{\rm HI} - D_{\rm opt}$ relationships do not deviate substantially from a constant H I surface density, especially for the latest spiral types, it is reasonable to adopt the distance-independent approximation to equation (3.1) based on the difference of the logarithms of the expected and observed values of this latter quantity

$$\mathrm{DEF} = \langle \log \overline{\Sigma}_{\mathrm{H\,I}}(T) \rangle - \log \overline{\Sigma}_{\mathrm{H\,I}} \;, \tag{3.3}$$

where $\overline{\Sigma}_{\mathrm{H\,I}}$ is the mean *hybrid* H I surface density, which can be calculated directly from the ratio of the observables $F_{\mathrm{H\,I}}$ and the apparent optical diameter of the galaxy, a^2_{opt}, given in arcmin (see also Solanes et al. 1996). The adopted values for $\langle \log \overline{\Sigma}_{\mathrm{H\,I}}(T) \rangle$ are: 0.24 units for Sa, Sab; 0.38 for Sb; 0.40 for Sbc; 0.34 for Sc; and 0.42 for later spiral types.

The values of H I deficiency for the galaxies of the 21-cm sample calculated using the two definitions given above are listed in columns (4) and (5) of table A.2 —to gauge the numerical values, they can be compared with the overall scatter of 0.24 units shown by field galaxies (Solanes et al. 1996). A brief glance at the figures shows that the two measurements are indeed very close for most galaxies. Hence, statistical measurements of the H I deficiency that rely on values of DEF taken from subsets of objects not segregated according to size should give unbiased estimates of this property. We have checked in our sample the statistical agreement of both of those H I deficiency estimates. This can be visualized in figure 3.2 where we plot the value of $< DEF >$ versus DEF for each galaxy in our sample. A linear model fitted to the data by assuming errors only on $< DEF >$ gives $< DEF >= 0.03 + 0.97$ DEF, with a scatter of 0.126 units.

The error in $< DEF >$ resulting from the propagation of the uncertainty in the distance modulus (see Section 3.2.2) is equal to 0.079 units for an Sb galaxy, much smaller than the model scatter shown in figure 3.2. This means that a substantial portion of the error budget of this H I deficiency estimate can be attributed exclusively to the uncertainty of the galactic distances.

3.3.1 Possible bias of H I deficiency in the distance

Before going into the analysis of the 3D structure of the Virgo Cluster Region, we have to consider a potential problem with the determination of TF distances from H I line widths, first brought into consideration by Guhathakurta et al. (1988) and Teerikorpi et al. (1992). It consists in the possibility that gas stripping can reduce the size of the H I disks to radii smaller than the turnover of the rotation curve (see, e.g., Cayatte et al. 1994). This would produce objects that are too

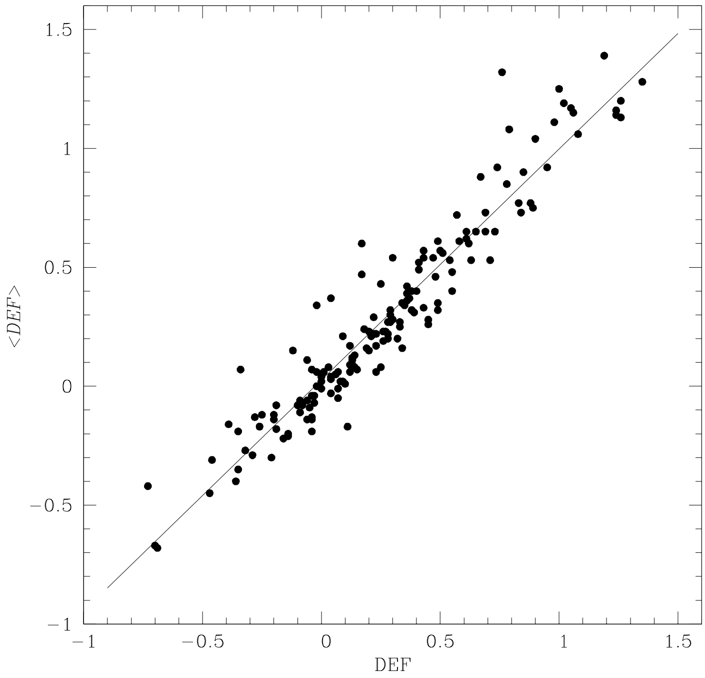

Figure 3.2: Comparison between the two alternative measures of H I deficiency defined in the text. Superposed on the data points is the regression line obtained assuming errors only on $< DEF >$.

luminous for their line width, therefore resulting in TF distances that are artificially underestimated. Possible evidence of this effect has been cited in the Virgo cluster studies by Fukugita, Okamura, & Yasuda (1993), YFO97, and FTS98, though no environmental dependences on TF distance determinations have been found in more distant clusters (Giovanelli et al. 1997; Dale et al. 2001) using combined H I and optical rotation width datasets.

We have investigated the possible alteration of distance resulting from atomic gas deficiency in our Virgo data by inspecting the positions of the members of the 21-cm sample on the $M^{c}_{B_{\rm T}}$-logW^{c}_{20} plane (i.e., the TF relation) according to their H I deficiency. The TF relation for the 161 spirals included in this data set is displayed in figure 3.3. The two lines show the linear regression of the data excluding H I-deficient objects (i.e., those with DEF $\geq 2\sigma$), identified in the figure by a starred symbol. The equations of the fits are: $M^{c}_{B_{\rm T}} = -6.75\,\log W^{c}_{20} - 2.55$ and $\log W^{c}_{20} = -0.13 M^{c}_{B_{\rm T}} - 0.05$. More importantly, the number of gas-poor galaxies on each side of the regression lines is about the same. Similar behaviors are obtained when the threshold for the exclusion of the H I-deficient objects is increased up to 3 and 4σ (the latter

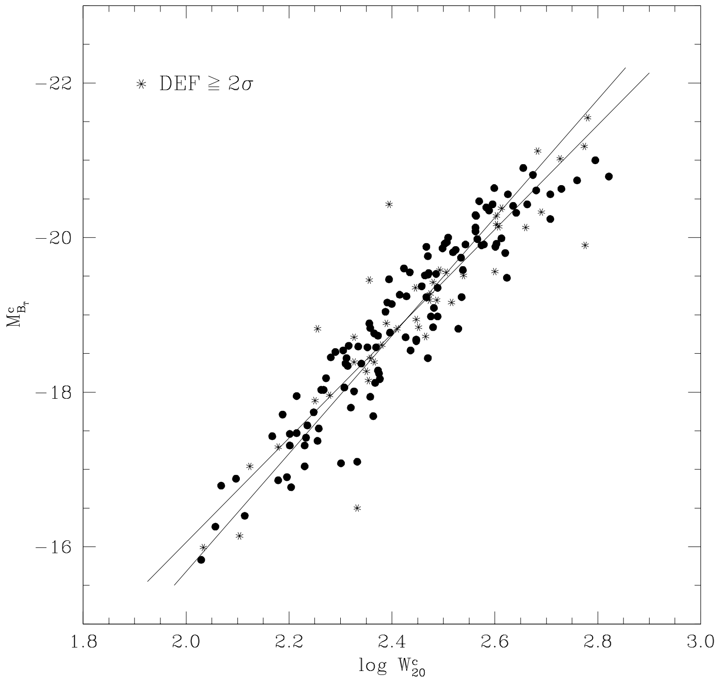

Figure 3.3: TF relation for the members of the 21-cm sample. The two straight lines correspond to the direct and inverse linear regressions of the data. Filled circles denote spirals with DEF $< 2\sigma$, while asterisks represent objects with larger H I deficiencies, which have been excluded from the fits.

value implying roughly a factor 10 decrement in the H I mass), with regression lines obeying equations almost identical to the former ones. These results are consistent with a scenario in which the gas deficiency does not have any noticeable effect on the distance estimates, even for the objects most severely depleted in their interstellar H I gas. This conclusion is also supported by the observation that, for the data points corresponding to the most H I-deficient galaxies, the values of $< DEF >$ do not appear to be systematically lower than those calculated from the distance-independent parameter DEF.

The absence of systematic deviations from the mean values of the TF relation with increasing gas deficiency suggests that, in any event, the value of the distance underestimates that could affect our most H I-deficient galaxies should be commonly smaller than the rms residual about the regression line, which has a value of 0.41 mag (i.e., should be lower than 19%). We note that this scatter is only slightly larger than the values around 0.35 mag found in TF templates based on the combination of measurements in many clusters (e.g., Gav99, Dale et al. 1999) and fully comparable to the intrinsic scatter of 0.43 mag found by Sakai et al. (2000) for nearby galaxies with Cepheid distances. A more accurate quantification of the effects of H I deficiency on TF distances should be obtained from extensive comparison of rotation curves at radio wavelengths in different galactic environments for spirals of specific morphological subsets.

3.4 The H I deficiency in Virgo

Numerous studies (e.g., Giovanelli & Haynes 1985; Haynes & Giovanelli 1986; Magri et al. 1988; Cayatte et al. 1994; Bravo-Alfaro et al. 2000) reveal that gas-poor galaxies tend to be more abundant in the centers of rich galaxy clusters than in their periphery. Virgo is less rich and younger than the classical Abell clusters and is characterized by a lower X-ray luminosity and larger spiral fraction than Coma-like clusters. Probably as a result, although it does contain a substantial fraction of H I-deficient galaxies (e.g., Haynes & Giovanelli 1986; Solanes et al. 2001; see also below), the degree of H I deficiency is not observed to increase towards the center as dramatically as in other rich clusters. However, because of its proximity, even strongly gas-poor galaxies remain detected, allowing precise determination of higher degrees of the H I deficiency, whereas in more distant clusters only lower limits to this parameter can be derived.

The contour map of H I deficiency shown in figure 3.1 illustrates that the maximum of the gas deficiency distribution coincides with the position of the central cD galaxy, M87, where the projected galaxy and intracluster gas densities are also the highest. But this map also reveals other zones of significant deficiency at sky positions dominated by background subclumps which lie at substantial clustercentric distances.

3.4.1 Radial pattern

The first lines of evidence that there is an excess of highly deficient galaxies on the outskirts of the Virgo cluster are presented here by means of figures 3.4 and 3.5. Figure 3.4 shows the values of DEF for the 161 members of the 21-cm sample as a function of their line-of-sight (LOS) distance, *d*. Horizontal error bars represent

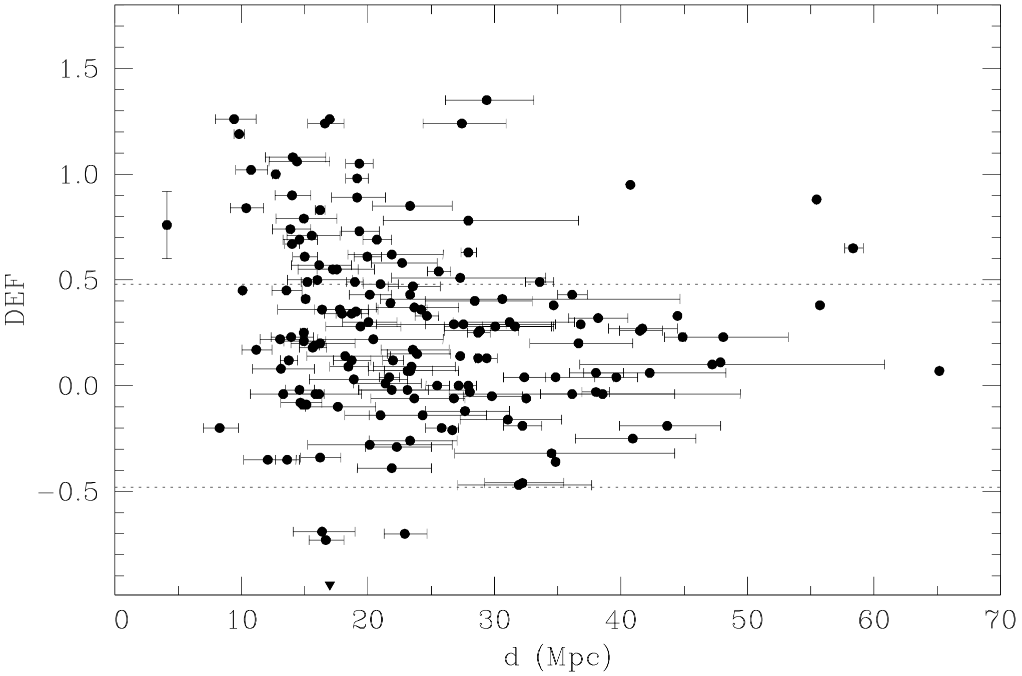

Figure 3.4: Individual values of DEF for the 161 members of the 21-cm sample as a function of the LOS distance. Dotted lines show 2 times the standard deviation shown by the values of this parameter in field galaxies. The filled triangle marks the distance to M87 quoted in LEDA. The vertical error bar in the point closest to us shows an estimate of the typical uncertainty of the individual values of DEF.

the 1σ uncertainties of the distances quoted in the literature with respect to the calculated mean values. We also show an estimate of the typical uncertainty of the individual values of DEF expected from random errors in the determination of the observables $a^2_{\rm opt}$, $F^{\rm c}_{\rm DEF}$, and T, that enter in the calculation of this parameter. This diagram illustrates that most of the galaxies with substantial deficiencies in the Virgo cluster region are localized in a broad range of projected distances, which stretches from about 10 to 30 Mpc along the LOS. A few more gas deficient objects lie beyond 40 Mpc.

By transforming the sky positions of the galaxies and their LOS distances to rectangular coordinates, we can also inspect the behavior of the H I deficiency as a function of the *three-dimensional* radial distance, r, from the center of Virgo. We adopt the standard identification of the cluster center at the position of M87, at a distance modulus of 31.11 mag quoted in LEDA, which translates to a LOS distance of 16.7 Mpc. The results are shown in figure 3.5, where we adopt two different rep-

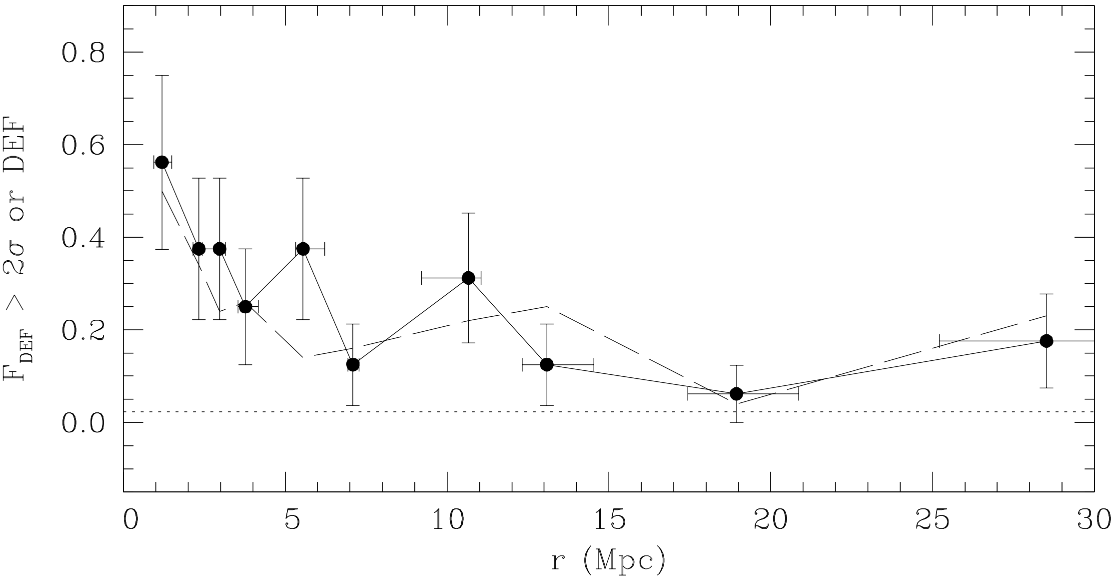

Figure 3.5: Run of the fraction of spirals with DEF $> 2\sigma$ with three-dimensional radial distance from the center of the Virgo cluster. Vertical error bars correspond to 1σ confidence Poisson intervals. The horizontal dotted line is the expectation value of $F_{\rm DEF}$ for field spirals if DEF follows a Gaussian distribution. The long-dashed curve illustrates the radial run of the medians of the binned number distributions in the measured DEF.

resentations of the radial run of the H I deficiency: one based on the parameter $F_{\rm DEF}$ used in Solanes et al. (2001), which measures the relative populations of deficient and normal spirals, and the other based directly on the averaged values of DEF. In both cases the data have been binned into annuli containing 16 galaxies per ring, with the final bin having 17, in order to increase the statistical weight of the scarcer low- and high-distance objects.

We see that, for $r \lesssim 4$ Mpc, the radial behavior of the gas deficiency is consistent with the pattern exhibited by the composite sample of 11 H I-deficient clusters investigated previously in Solanes et al. (2001) (see figure 3.6 taken from that paper): it decreases almost monotonically towards normalcy with increasing distance from the cluster center. But at greater Virgocentric distances this tendency is broken by a series of secondary maxima, more conspicuous in the radial run of $F_{\rm DEF}$ because of its higher sensitivity to localized enhancements, caused by regional enhancements of gas deficiency where this parameter reaches values several times larger than —and clearly inconsistent with— the field expectation (~ 2–3%). Besides, as illustrated in figure 3.4, the spirals on the Virgo cluster outskirts are not only more likely to be

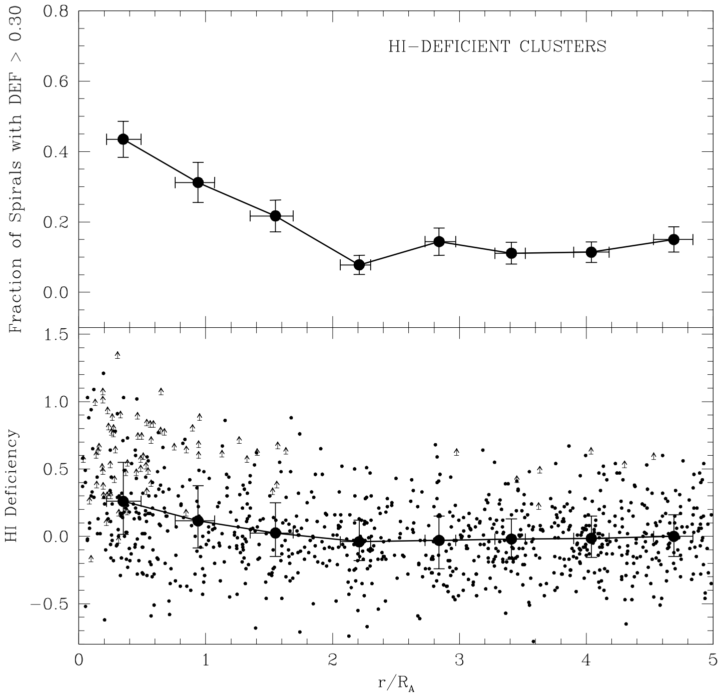

Figure 3.6: *Top:* HI-deficient fraction in bins of projected radius from the cluster center for the superposition of all the HI-deficient clusters but Virgo. Vertical error bars correspond to 1σ confidence Poisson intervals. The abscissas show medians and quartile values of the bins in radial distance. *Bottom:* same as in upper panel for the measured HI deficiency. Displayed are the medians and quartiles of the binned number distributions in HI deficiency. Dots show HI deficiency for individual galaxies while arrows identify estimated lower limits for non-detections. *Note:* Taken from Solanes et al. (2001)

deficient in H I than field objects, but they also reach gas deficiencies typical of the cluster core. The reader, however, should be aware of the fact that this same sort of careful analysis of H I deficiency at large clustercentric distances has not been performed on other clusters. So, it is not unfeasible that the differences in the radial pattern can be explained simply by the bias that arises from Virgo's proximity which leads to (a) much larger number of 21-cm observations, (b) more stringent values of DEF, and (c) more accurate TF distance estimates.

Further inspection of figure 3.4 (see also Section 3.5.1) reveals that the central peak in the radial pattern of the H I deficiency is the result of the accumulation of highly deficient galaxies in the interval of LOS distances ranging from ~ 16 up to 22 Mpc. This range coincides essentially with the distribution of the bright ellipticals associated with the cluster core (Neilsen & Tsvetanov 2000). The second local maxima visible in the radial run of $F_{\rm DEF}$ is produced by galaxies with extreme deficiencies at $d \lesssim 15$ Mpc, while the peak most distant from the cluster core obeys to several gas-deficient objects at LOS distances between about 25 and 30 Mpc. As we show in the next section, this latter enhancement of H I deficiency might be related to one of the classical background clouds of the Virgo cluster region.

Previous studies by Fukugita et al. (1993), YFO97, and FTS98, among others, have shown that the Virgo spiral distribution is strongly elongated along the LOS. The impressions obtained above from the distribution of H I deficiency, although crude, provide further evidence for the large depth in LOS distance of the Virgo spirals, which we now see that is also reflected in the gaseous deficiency. Hence, in contrast to what it is commonly assumed, it seems that not all the H I-poor objects in the Virgo region reside in the neighborhood of the cluster core.

3.4.2 Correlation with recessional velocities

The most frequently discussed gas removal mechanism that depends on the ICM density is ram pressure sweeping (Gunn & Gott 1972; Quilis et al. 2000; Vollmer et al. 2001). For a given galaxy, the stripping efficiency relies both on the density of the hot intracluster gas and on the square of the relative velocity of the galaxy with respect to the latter (actually, it is only the component in the direction normal to the disk that matters). Suggestive indication that it is a density that correlates with gas deficiency is provided by the radial nature of the deficiency pattern in the core of rich clusters (see Solanes et al. 2001) which, as shown above, it is also reproduced in the center of the Virgo cluster region. However, attempts to unearth further evidence of ram pressure stripping by seeking possible correlations between H I depletion and velocity relative to the cluster are severely limited, not only by projection effects arising from the poor correlation between the unknown space velocities of the galaxies with the one component that can be measured (see, e.g., Giovanelli & Haynes 1985; Haynes & Giovanelli 1986; Magri et al. 1988), but also because in some cases the effects of the galaxy-ICM interaction are observed only *after* the closest passage of the galaxies to the cluster center (Vollmer et al. 2001).

The inclusion of 2D or 3D positional information increases notably the sensitivity of the tests. In Solanes et al. (2001), this approach served to demonstrate that spirals

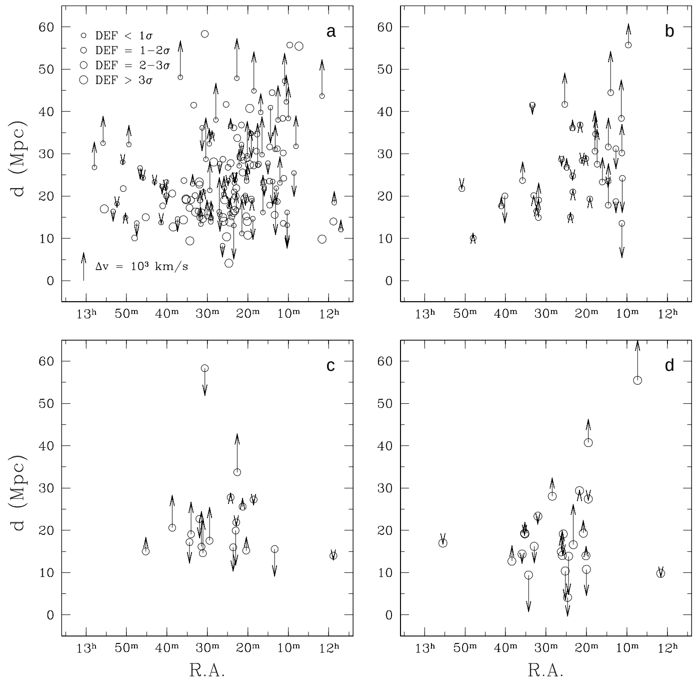

Figure 3.7: The distribution of the observed relative recessional velocities for different intervals of H I deficiency. The horizontal axis shows the position of the galaxy in R.A. while the vertical axis shows its LOS distance in Mpc. The size and orientation of the arrows indicates the radial velocity relative to the systemic cluster recessional velocity. Panel (a) depicts all data points but only the velocities for non-H I-deficient galaxies (DEF $< 1\sigma$). In the rest of panels, the H I-deficient galaxies are separated according to specific ranges of deficiency: (b) DEF $= 1$–2σ, (c) DEF $= 2$–3σ, and (d) DEF $> 3\sigma$.

devoid of gas follow more eccentric orbits than the gas-rich objects in the central regions of H I-deficient clusters. However, in the dynamically young Virgo cluster, where the galaxy orbits are not yet fully settled, no correlation was found between the gas deficiency and the orbital parameters of the spirals. A similar exercise is reproduced here in figure 3.7 for a much more spatially extended dataset. This figure shows the radial velocities of the galaxies in our 21-cm sample relative to the Virgo systemic velocity —for this parameter we choose the typical value of 980 km s^{-1} (e.g., Teerikorpi et al. 1992)— plotted as a function of their right ascension and LOS distance for different intervals of H I deficiency. Two galaxies with $d > 65$ Mpc have been excluded from the figure. As in the previous study of the central Virgo region, the inspection of the different panels does not reveal any clear connection between the kinematics of the galaxies and their gas contents. An indication exists that the galaxies with DEF $= 2$–3σ closest to the cluster core have preferentially higher relative velocities. This impression, however, is not corroborated by the objects with the highest gas deficiencies. The only clear trait, consistently repeated in the four panels, is the coherence in sign and in magnitude of the relative velocities of the galaxies located at large Virgocentric distances, suggesting collective motions that still retain a memory of the Hubble expansion: galaxies behind the Virgo core ($d \gtrsim 30$ Mpc) tend to move far away at high speed, while almost all galaxies in front of this region ($d \lesssim 15$ Mpc) exhibit substantial radial movements toward us. The feasibility of a scenario in which the galaxies at large Virgocentric distances are deficient from having traversed the cluster core earlier will be explored in the next chapter.

The inclusion of spatial coordinates perpendicular to the LOS in the present graphical analysis serves to emphasize additionally the marked east-west asymmetry in the depth of the galaxy distribution. In the western half of the Virgo cluster region, most galaxies have LOS distances spread throughout the range from 10 to 50 Mpc, whereas, in the eastern half, few objects are seen at distances larger than 25 Mpc. Interestingly enough, West & Blakeslee (2000) also detected a tendency for the brightest elliptical galaxies located in the western region of the Virgo cluster to be more distant than those on the eastern side. In contrast, as evident in figure 3.1, the X-ray emission of the cluster core is more extended towards the eastern side.

3.5 The structure of the Virgo region

Some progress toward a precise determination of the complex structure of the Virgo cluster region is now beginning to emerge from distance measurement methods capable of determining individual galaxy distances to a precision comparable to the inter-group separations. Recent studies relying on TF, surface brightness fluctuations, or fundamental plane distance measurement techniques (e.g., YFO97; Gav99; Neilsen & Tsvetanov 2000; Fouqué et al. 2001) have produced quite an elaborate set of substructures and opened a debate on the original group membership assignments of numerous galaxies. In essence, however, they have confirmed the robustness of the original subdivision inferred from imaging and recessional velocity data (e.g., de Vaucouleurs 1961; VCC; Binggeli et al. 1993) that splits the Virgo I cluster region essentially in two major central subclusters and three peripheral groups (cf. figure 3.1). The largest galaxy concentration dominates the northern part of the

Virgo region and coincides with the brightest giant elliptical, M87, which also appears to be the center of the X-ray emission (Böhringer et al. 1994). This main subunit, which will be referred to here as the M87 subcluster, is supposed to trace the cluster core, which might not be virialized (Binggeli et al. 1993; Böhringer et al. 1994; Schindler, Binggeli, & Böhringer 1999). Another giant elliptical, M49, marks the center of the other major Virgo galaxy concentration, hereafter the M49 subcluster, located southwards from the M87 subcluster. The M49 subcluster appears to be connected towards the southwest with the W′ and W background clouds (de Vaucouleurs 1961), forming a continuous chain that extends up to roughly twice the distance of the M87 subcluster (interestingly enough, a tenuous bridge of X-ray luminous gas can be seen in Figure 3.1 connecting the M49 subcluster with the W′/W cloud region). Finally, in the northwest and at about the distance of the W cloud, there is another well-defined background cloud named M (Ftclas, Struble, & Fanelli 1984).

3.5.1 Spherical coordinates

Let us see now whether the main substructures of the Virgo region that we have just enumerated bear any relationship with any of the maxima observed in the radial pattern of the H I deficiency. For this, we use the tomographic presentation of the sky distribution of the members of the 21-cm sample shown in figure 3.8 which partitions the galaxies into 9 segments of TF distance. Every panel encompasses a range of LOS distances of 5 Mpc, except for the first and last ones which encompass, respectively, all the objects with $d < 10$ Mpc and with $d > 45$ Mpc. The size of the symbols informs us about the H I deficiency of the galaxies measured in units of the mean standard deviation for field objects ($= 0.24$). Again for a better visualization of the structure of the Virgo cluster we show the position in the sky of background subgroups from Binggeli et al. (1993) as well as the main galaxies of the cluster.

It is seen clearly that the center of gravity of the H I deficiency distribution moves from north to south as the distance increases, consistently following the structure of the Virgo cluster described above. The major concentration of H I-deficient spirals is seen in the distance range of 15–20 Mpc encircling the position of M87. Numerous gas-deficient objects are detected also in the panels corresponding to the distance ranges of 10–15 Mpc and 25–30 Mpc. In the latter, these galaxies are essentially concentrated between the southern edge of the M49 subcluster and the W′/W cloud

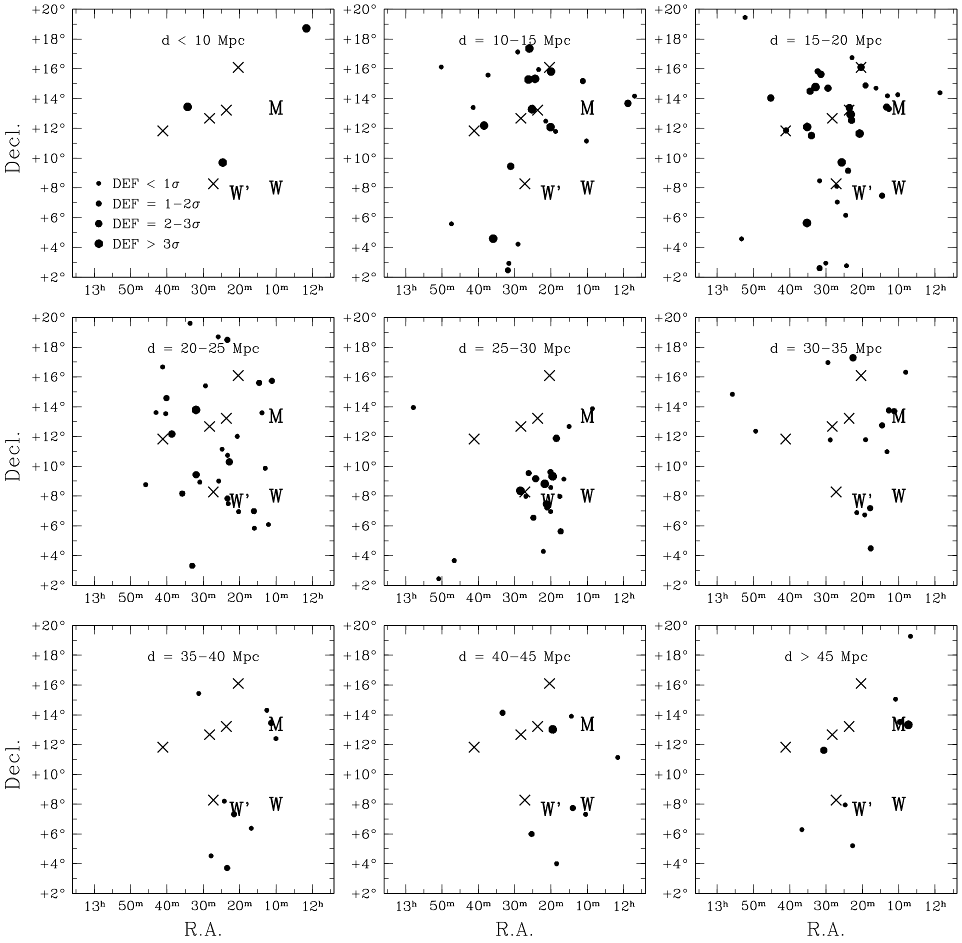

Figure 3.8: Sky distribution of the Virgo spirals for specific ranges of the LOS distance. The size of the symbols correlates with the H I deficiency of the galaxies. Crosses and uppercase letters have the same meaning as in figure 3.1.

region, while in the former they tend to be located to the north of M87. Some of the gas poor galaxies in the near distance slice could be former companions of M86 ejected at high speeds to relatively high clustercentric distances because of the falling of this subclump into the cluster (Solanes et al. 2001; Vollmer et al. 2001). The intermediate range of $20 < d < 25$ Mpc is composed mainly of galaxies with moderate neutral gas deficiencies spread more or less uniformly over all the sky. Although the uncertainties in the distance estimates do not permit a neat separation of the different Virgo substructures, it is interesting to note that the majority of the objects in the H I-deficient galaxy clustering seen at 25–30 Mpc also have systemic velocities not dissimilar from those of the M87 subcluster (see tables A.1 and A.2), in agreement with the original definition of the W′ cloud given in VCC (note that the W cloud is underrepresented in TF datasets). On the other hand, the marginal indications of a galaxy enhancement in the NW of the 30–35-Mpc-distance slice might correspond to the M cloud, given that the candidate galaxies exhibit systemic velocities around 2000 km s^{-1}. Beyond 35 Mpc, galaxies become progressively scarce, although with an apparent tendency to reside in the peripheral W and M cloud regions. This picture is consistent with the claims that the W and M background clouds of Virgo are twice as far away as its central subunits, with the W$'$ cloud being somewhat closer (e.g., Binggeli, Tammann, & Sandage 1987; YFO97; Gav99). A final glance at figure 3.8 also shows that the gas-deficient enhancement around the region of the M cloud (see figure 3.1) is indeed the result of the chance superposition along the line-of-sight of several spirals with substantial gas deficiency, but located at very different distances and without any physical connection.

3.5.2 Cartesian coordinates

A complementary characterization of the spatial structure of the Virgo region can be inferred from the projected distributions of the spiral galaxies into the three main planes of the cartesian three-dimensional space visualized in figure 3.9. In the plots, the xy-plane is taken parallel to the equatorial plane (Decl. = 0°), with the x- and y-axis pointing to R.A. = 12 and 18 hr, respectively, and the z-axis pointing to the north. In this coordinate system, the yz-plane is nearly perpendicular to the line-of-sight to M87, i.e., it is roughly a tangent plane to the celestial sphere. The spherical coordinates have been transformed into linear coordinates at the distance of the individual galaxies listed in table A.2. As in previous figures, the symbol sizes are directly proportional to the H I deficiency of the galaxies and the large cross marks the position of M87.

This figure allows one to appreciate the true aspect of the spiral and H I distributions in the Virgo region. One remarkable feature of the galaxy distribution is that at large radial distances ($\gtrsim$ 25–30 Mpc) it appears to split into two branches in the vertical direction of the xz-plane, which is roughly perpendicular to the plane of the Local Supercluster. The fact that the z-axis is nearly perpendicular to the line-of-sight suggests that this galaxy arrangement is not an artifact produced by the uncertainty in the radial distances affecting for the most part the x direction. Notice also that the upper branch, which goes through M87 and embraces the deficient

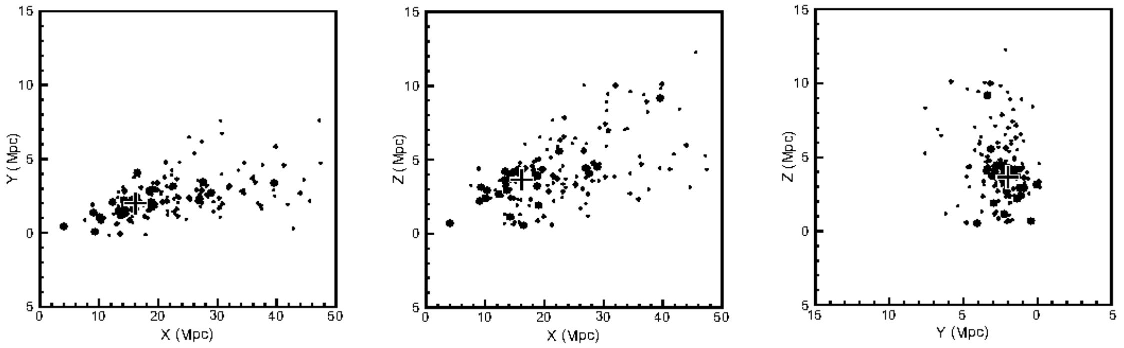

Figure 3.9: Distribution of the Virgo spirals in the three main planes of the rectangular equatorial coordinate system. The xy-plane corresponds to Decl. = 0°, the x- and y-axis point to R.A. = 12 and 18 hr, respectively, and the z-axis points to the north. As in figure 3.8, the symbol size indicates the relative degree of H I deficiency. The large cross in each panel marks the position of M87.

objects having the most extreme radial distances, contains nearly all the galaxies with strong H I depletions, i.e., those with DEF $> 2\sigma$, or equivalently, with at least a factor three reduction in the H I mass.

Given the linear arrangements of the spiral galaxies detected above it is worth studying their possible relationship with other filamentary features believed to exist in this region. The most important is the "principal axis" defined by the brightest elliptical galaxies in the northern half of the Virgo cluster (Arp 1968). West & Blakeslee (2000) argued that these objects indeed have a remarkably collinear arrangement in three dimensions that can be traced to larger scales, where it appears to join a filamentary bridge of galaxies connecting Virgo to the rich cluster A1367, which together with its close neighbor the Coma cluster (A1656) form part of the "Great Wall" (de Lapparent, Geller, & Huchra 1986). As these authors stress, the principal axis of Virgo also appears to mark the general direction of the orientations of the elliptical galaxies, of the distributions of both the dwarf ellipticals and the hot X-ray-emitting intracluster gas, and even of the jet emanating from M87. All these lines of evidence lead them to suggest that the formation of the Virgo cluster, and of its brightest member galaxies, might have been driven by infall of material along the Virgo-A1367 filament.

Figure 3.10 is a variation of figure 4 in West & Blakeslee (2000). It reproduces the distribution of our 21-cm sample in the xz-plane, i.e., the middle panel of figure 3.9, together with the distribution of the brightest Virgo ellipticals calculated

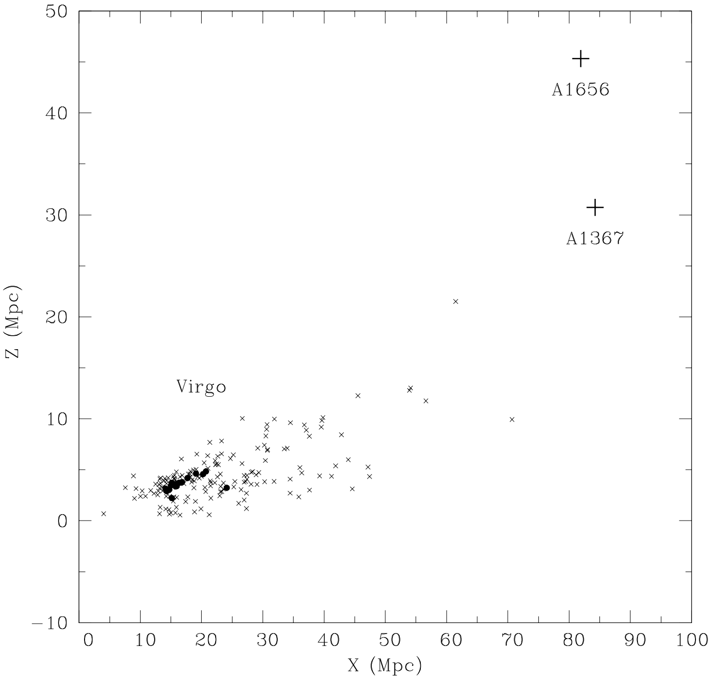

Figure 3.10: Distribution of the spirals (small crosses) and bright ellipticals (solid circles) of the Virgo cluster region in the xz-plane. Big crosses show the positions of Abell clusters A1367 and A1656.

from the SBF distance moduli given in West & Blakeslee (2000) and Neilsen & Tsvetanov (2000). The scale of the plot has been augmented to include the positions (big crosses) obtained from the Hubble law and mean redshifts of the rich Abell clusters A1367 and A1656 located behind the Virgo cluster. The figure shows that the upper branch of the spiral distribution is pretty well aligned with the chain of bright elliptical galaxies that defines the principal axis of Virgo, producing a pronounced finger about 60 Mpc long which points in the approximate direction of A1367. Hence, our data give additional support to the proposition that this upper filament constitutes the backbone of the Virgo cluster region.

To complete our description of the three-dimensional distribution of the gaseous deficiency, we show in figure 3.11 the surfaces of iso-H I deficiency corresponding to 1, 2, and 3 standard deviations from normalcy. These surfaces have been generated by a straightforward extension of the adaptive kernel method described in Silverman (1986) for smoothing galaxy number density distributions, also used in the determination of the H I deficiency contours depicted in figure 3.1. We observe in the panel corresponding to the 1σ-level surface the presence of two disconnected

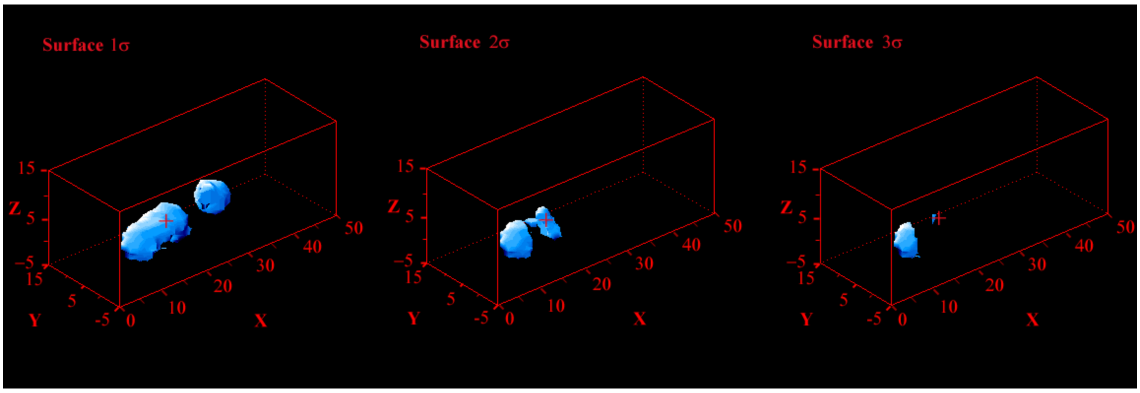

Figure 3.11: *Left to right:* Surfaces of iso-H I deficiency corresponding to 1, 2, and 3 standard deviations from normalcy. All plots are in rectangular equatorial coordinates as in figure 3.9 with distances given in Mpc. The crosses mark the position of M87. Our position is at the origin of the coordinate system.

condensations of H I deficiency: the elongated one in the front encompasses most of the H I-deficient galaxies associated with the main body of the cluster and the gas-poor objects nearest to us, while the most distant surface is related to the group of strongly gas-deficient galaxies that we have tentatively identified in the background of the Virgo cluster (compare this panel with figures 3.4 and 3.8). The remaining two panels illustrate the already commented fact that the highest gas deficiencies in the Virgo region are found in the front of the cluster. As explained in Section 3.3.1, little bias seems to be caused by H I deficiency in the TF distances, even for extreme gas depletions, so the abundance of gas-poor objects at short radial distances from our position appears to be a real effect.

3.6 Summary and conclusions

In this chapter, we have used the distances and H I contents of 161 spiral galaxies in the region of Virgo cluster to gain insight into the complicated structure of this galaxy system. Specially, we have examined in more detail the suggestion presented in Solanes et al. (2001) that, in addition to the main galaxy concentration around M87, some of the well-known peripheral Virgo groups also contain strongly gas-deficient spirals. The overall distribution of H I deficiency in the Virgo region has been compared with the three-dimensional galaxy distribution. The following conclusions have been reached:

(1) Our data seems to confirm that the distribution of the spirals in the Virgo I cluster region is very elongated along the line-of-sight; the galaxies associated with this region have LOS distances raging from less than 10 to more than 50 Mpc. The projected sky distribution of the Virgo spirals, however, looks (lumpy but) relatively compact, with a typical extent of only about 10 Mpc. The overall width-to-depth ratio is approximately 1 : 4, although with a strong east-west variability. The most distant objects concentrate in the western quadrant, while in the eastern half few spirals are seen at LOS distances larger than 25 Mpc. The Virgo filamentary structure appears to split into two branches around the W′ cloud region.

(2) The distribution of spiral galaxies with significant H I deficiency is also characterized by great depth along the line-of-sight. The highly gas-deficient spirals tend to concentrate along the upper branch of the spiral galaxy distribution, which is roughly aligned with the principal axis of the Virgo cluster.

(3) Within 4 Mpc of M87, the measured H I deficiency is essentially a monotonically decreasing function of the distance from that galaxy, in agreement with the behavior observed in other H I-deficient clusters. Moreover, in the Virgo region, significant H I deficiency enhancements are also identified at large distances from the Virgo core, well beyond the typical distance where the hot X-ray emitting ICM is concentrated. Tests of whether locally-high peripheral gas deficiencies are a rather common feature in cluster regions must await the equally-careful tracing of the H I deficiency, incorporating quality 3D distance measures around other clusters.

(4) While the principal peak in the distribution of H I deficiency arises from numerous gas-poor galaxies coincident with the core and with distances ranging from ~ 16 to 22 Mpc, other important enhancements of the gas deficiency are associated with several nearby galaxies ($d \lesssim 15$ Mpc) moving away from the cluster with large relative velocities, and with what appears to be a compact background group of galaxies between ~ 25–30 Mpc, most with roughly the same systemic velocities as the cluster mean, which matches the original definition of the W′ cloud. In addition, we have demonstrated that the localized enhancement in DEF observed in the Virgo sky map around the M cloud position actually arises from several galaxies at very different distances aligned along the line-of-sight and without any physical connection. In agreement with results presented by Dale et al. (2001), nothing in our analysis suggests that TF distance measurements are unreliable in objects with severe gas depletion.

Confirmation and further progress in these conclusions would need a careful revision of TF distances —at least until Cepheid distance measurements in Virgo galaxies become more commonplace. Even after the elimination of systematic differences among published Virgo catalogs, a few galaxies still exhibit strongly inconsistent distance measurements: 16 of the 161 members of the 21-cm sample have 1σ uncertainties larger than 5 Mpc. Nevertheless, although the details may be questioned, the general picture reporting the elongated structure of the distribution of both the spirals and their H I deficiency, as well as the clumped nature of the latter, should be correct. We can make a simple estimate of the typical elongation introduced by the uncertainty in the distances. From figure 3.1 we can see that the cluster typically extends up to 9° in the plane of the sky. If one assumes the center of the cluster to be at the position of M87 (lying at the peak of the X-ray emission), i.e. at $\sim$17Mpc, this angular distance represents 2.7 Mpc. Thus, if the cluster were spherical, it would extend from 14.3 to 19.7 Mpc. The standard deviation of individual distances (0.29 mag, i.e, 13% in relative distance) is likely responsible for an increase of the extension of the cluster. However, applying a 3σ error in relative distance would lead objects at the far edge of the spherical cluster (at 19.7 Mpc) to 27.4 Mpc, which is not enough to account for the huge number of galaxies observed at distances beyond 30 Mpc and up to 50 Mpc. In the opposite sense, objects at the near edge of the spherical cluster (at 14.3 Mpc) would arrive, after the inclusion of a 3σ error, at 8.7 Mpc. This low distance would encompass almost every object in the near side of the cluster, although it is not probable that this is the case for the 7 objects we find at roughly 10 Mpc or below. Moreover, the clumpiness of the radial H I deficiency pattern as well as of the three-dimensional distribution of this quantity (see figures 3.5 and 3.11) suggests that these concentrations of deficient spirals are a real effect and not a consequence of distance errors. In this latter case, one would expect a continuous distribution, just broadened by the dispersion in the position of the galaxies caused by distance errors.

If confirmed, results (3) and (4) could have profound implications on our understanding of the gas removal events and the influence of the environment on the life of the galaxies. While the characteristics exhibited by the H I deficiency in cluster centers tend to support the interaction between the galaxies and the hot intracluster gas as the main cause of their gas depletion, our finding that a number of spirals with substantial H I deficiencies lie at large radial distances from the Virgo cluster center is hard to reconcile with the proposition that this environmental process is also the cause. Nevertheless, for the ram pressure stripping to be responsible for the

H I deficiency of these objects, there is still the possibility that the galaxies at large Virgocentric distances are deficient from having traversed the cluster core earlier. The feasibility of this scenario will be explored in the next chapters.

4 Dynamical model of the Virgo region

4.1 Introduction

The characterization of the large-scale 3D distribution of the neutral gas deficiency around the Virgo I Cluster (VIC) region in Chapter 3 has shown that there is a significant number of galaxies with a dearth of atomic hydrogen at large Virgocentric distances. These peripheral gas-deficient objects, which can be observed both in the cluster front and in a probable background group well behind the cluster core, show gaseous deficiencies comparable in strength to those measured in the centers of Virgo and other rich galaxy clusters.

One of the mechanisms that can most naturally account for the observed reduction in the interstellar gas content of cluster galaxies is the ram pressure ablation caused by the rapid motion of galaxies through the dense intracluster medium. There is now compelling evidence for the decisive participation of this process in the gaseous deficiencies of spirals located in the centers of rich clusters, either directly from observations (Giovanelli & Haynes 1985; Gavazzi & Jaffe 1987; Dickey & Gavazzi 1991) —including the discovery of shrunken gaseous disks (Cayatte et al. 1994; Bravo-Alfaro et al. 2000) and the finding that H I-deficient spirals are on very eccentric orbits (Solanes et al. 2001)— or from theoretical studies that have checked the efficiency of this mechanism (Stevens et al. 1999; Quilis et al. 2000; Vollmer et al. 2001, to name only a few).

In the outer cluster regions the low density of the intergalactic medium calls, in principle, for alternative gas removal mechanisms, such as gravitational tidal interactions. Indeed, observational evidence suggests that processes of this kind might have played an important role in the evolution of the galactic population in distant clusters (e.g., van Dokkum et al. 1999) due to favorable conditions for frequent low-relative velocity encounters among the galaxies in early epochs. Although in the VIC region low-relative-velocity galaxy-galaxy interactions may also be responsible for the gaseous deficiencies observed in some of the peripheral galaxies, it should not be forgotten that the dynamics of the Virgo region is dominated by large-scale non-Hubble radial streaming motions. In this context, it is plausible that some galaxies at large Virgocentric distances are on very eccentric orbits that carry them right through the cluster center with high relative velocities and are therefore liable to have suffered a strong interaction with the ICM.

One of the most influential studies of the Local Supercluster based on dynamical model calculations is the analysis by Tully & Shaya (1984) of the infall of galaxies in the Virgo Southern Extension (or Virgo II cloud) toward the VIC. The lumpy distribution of galaxies in space led these authors to predict a very irregular infall rate which would be responsible for the secular evolution of the mix of morphological types in the cluster. It was suggested that the formation of the cluster took place at an early epoch —when the universe was about one fourth of its present age (R. B. Tully 2002, private communication)— by a first generation of, probably, early-type galaxies. Afterwards, infall was reduced until very recently when the large spiral-rich Virgo II cloud has begun to fall into the cluster diluting the fraction of early-type systems. The fact that Tully & Shaya saw very few outwardly moving galaxies outside the 6° VIC circle supported their argument that most, or perhaps all, spirals and irregulars in Virgo, mostly supplied by the Virgo II cloud, were recent arrivals.

All the findings of Tully & Shaya (1984) were based on a data set that contained a limited number of galaxies with relatively uncertain distance estimates. Now, with a much larger sample and more accurate distances, we provide evidence that a substantial number of galaxies, with a wide range of clustercentric distances, are expanding away from Virgo. This suggests that these galaxies are probably reemerging after infall. If our interpretation of the situation is correct, then there is a more continuous influx of galaxies into Virgo than previously anticipated, so the hypothesis that the strong gaseous deficiencies currently seen in some peripheral objects were originated in a previous infall episode is worth exploring.

4.2 The main H I deficiency enhancements of the Virgo cluster

A continuous representation in rectangular equatorial coordinates of the spatial distribution of H I deficiency in the VIC region is shown in figure 4.1. This image is like a radiography in which the shade intensity informs on the average H I deficiency of the galaxy distribution observed from a given viewing angle. Three bright spots indicating the accumulation of galaxies with a dearth of neutral hydrogen are easily identified aligned along the line-of-sight (LOS). In Chapter 3 it was demonstrated that the central enhancement of the H I deficiency, which is essentially coincident with the cluster core, arises from numerous gas-poor galaxies with distances from the Local Group ranging from ~ 16 to 22 Mpc. Another region with important H I deficiency is associated with several nearby galaxies at distances ~ 10–15 Mpc, preferentially located to the north of M87, and moving away from the cluster with large relative velocities. Finally, there is a tentative background group of galaxies at distances ~ 25–30 Mpc, most with systemic velocities close to the cluster mean, lying in the region dominated by the southern edge of the classical M49 subcluster, and clouds W′ and W.

While the frontside enhancement of the H I deficiency is produced by gas-poor galaxies that appear relatively clustered in 3D space simply because they are nearby objects, the gas-deficient enhancement in the background arises from a tight aggregation of galaxies segregated in the four-dimensional position-radial velocity phase space. Up to 14 of the galaxies listed in the data set in table A.2 can be identified as probable members of this group, since they all share similar positions on the sky ($12^{\rm h}15^{\rm m} \leq$ R.A. $\leq 12^{\rm h}30^{\rm m}$ and $+6^\circ \leq$ Decl. $\leq +10^\circ$). In addition, 11 of these objects have distances from the Local Group between 27 and 30 Mpc, and 9 of them (12 out of the initial 14) have systemic velocities between ~ 600–1300 km s^{-1}. Certainly, the lack of good resolution in the radial direction prevents us for claiming that we have identified a true group on a sufficiently safe basis. Yet, the fact that one third of its potential members have gas deficiencies that deviate more than 2σ from normalcy and that two of them have H I masses less than 10% of the expectation values for their morphology —characteristics that are both typical of rich cluster interiors— reinforces the impression that it is not a fortuitous feature. Table 4.1 summarizes the properties of the possible members of this suggested group.

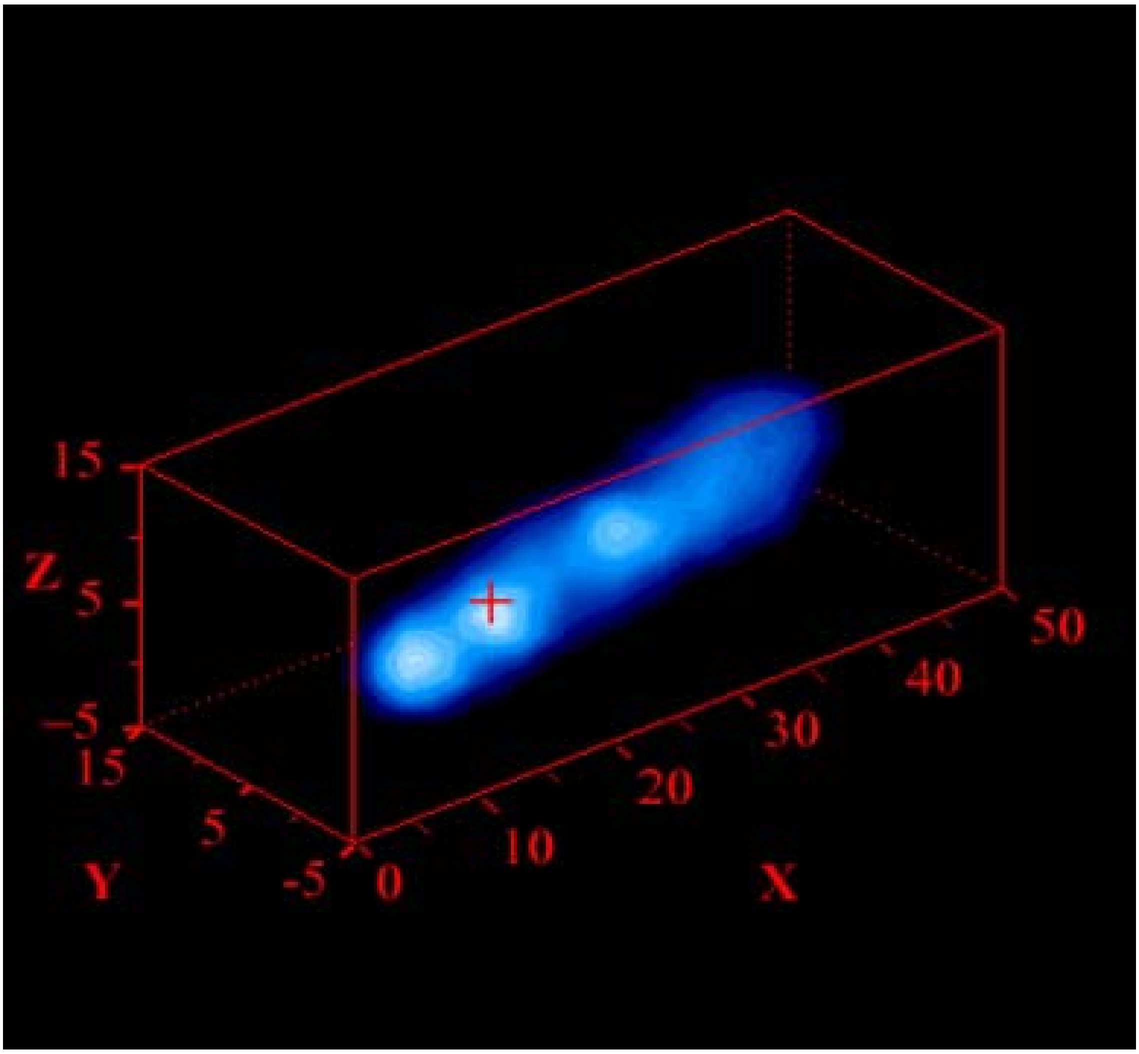

Figure 4.1: Voxel projection of the 3D distribution of H I deficiency in the VIC region. The plot is in rectangular equatorial coordinates with distances given in Mpc. The xy-plane corresponds to $\mathrm{Decl.} = 0°$, the x- and y-axis point to $\mathrm{R.A.} = 12$ and 18 hr, respectively, and the z-axis points to the north. The central bright spot is associated with the cluster, with M87 (marked as a cross) being at its center. The other two enhancements are peripheral regions of H I deficiency in the frontside and backside of the VIC. Our position is at the origin of the coordinate system.

Table 4.1: Possible members of the group in the background

Galaxy	R.A.	Dec.	T	v_{sys}	d	DEF
Name	(B1950)			(km s^{-1})	(Mpc)	
V0667	$12^{h}21^{m}16^{s}.2$	$+07^\circ27'49''$	8	1279	$25.59^{+0.96}_{-0.89}$	0.54
V0566	$12^{h}20^{m}05^{s}.0$	$+08^\circ34'24''$	9	1267	$25.82^{+1.34}_{-1.17}$	−0.20
V1002	$12^{h}24^{m}53^{s}.6$	$+06^\circ32'23''$	3	1301	$26.79^{+8.04}_{-6.12}$	0.29
V0737	$12^{h}22^{m}06^{s}.6$	$+04^\circ16'36''$	8	1566	27.16	0.00
V0453	$12^{h}18^{m}33^{s}.0$	$+11^\circ52'24''$	6	785	$27.29^{+6.75}_{-5.41}$	0.51
V0524	$12^{h}19^{m}33^{s}.0$	$+09^\circ19'06''$	3	913	$27.42^{+3.49}_{-3.07}$	1.24
V1193	$12^{h}26^{m}58^{s}.0$	$+07^\circ58'20''$	2	616	$27.67^{+3.52}_{-3.12}$	−0.12
V0939	$12^{h}24^{m}15^{s}.0$	$+09^\circ09'42''$	6	1135	$27.93^{+0.65}_{-0.57}$	0.63
V0267	$12^{h}15^{m}26^{s}.0$	$+06^\circ55'53''$	6	584	$27.93^{+0.65}_{-0.64}$	0.00
V1330	$12^{h}28^{m}27^{s}.4$	$+08^\circ21'13''$	1	1638	$27.93^{+8.72}_{-6.71}$	0.78
V0656	$12^{h}21^{m}05^{s}.0$	$+07^\circ13'58''$	3	868	$28.44^{+4.52}_{-3.92}$	0.40
V1118	$12^{h}26^{m}08^{s}.4$	$+09^\circ32'06''$	3	725	$28.71^{+0.94}_{-0.85}$	0.25
V0576	$12^{h}20^{m}10^{s}.2$	$+09^\circ36'36''$	6	1117	$28.84^{+3.08}_{-2.80}$	0.26
V0713	$12^{h}21^{m}42^{s}.1$	$+08^\circ48'48''$	6	998	$29.38^{+3.74}_{-3.25}$	1.35

4.3 The Tolman-Bondi model

In a homegeneous universe, the so called Tolman-Bondi Model (Tolman 1934; Bondi 1947) provides the full general-relativistic solution for the velocity field drawn by a spherically symmetric pressure-free density excess. The general features of this model can be found in Olson & Silk (1979). Nevertheless, to model the virgocentric velocity field only the equations of motion in the Newtonian limit of a thin mass-shell are necessary. Following the formulation of Ekholm et al. (1999) and references therein, the velocity relative to the center of Virgo, v, for shells of radius r in a universe with null cosmological constant is given by the pair of parametric equations

$$\frac{\eta-\sin\eta}{(1-\cos\eta)^{3/2}} = \frac{\sqrt{GM(r)}t_0}{r^{3/2}}, \qquad v = \frac{r}{t_0}\frac{\sin\eta(\eta-\sin\eta)}{(1-\cos\eta)^2} \tag{4.1}$$

for the bound shell case, and by

$$\frac{\sinh\eta-\eta}{(\cosh\eta-1)^{3/2}}=\frac{\sqrt{GM(r)}t_0}{r^{3/2}},\quad v=\frac{r}{t_0}\frac{\sinh\eta(\sinh\eta-\eta)}{(\cosh\eta-1)^2} \tag{4.2}$$

for the unbound case.

In these expressions, $M(r)$ is the mass enclosed within the shell of radius r, t_0 is the current age of the universe, and G is the gravitational constant. Given t_0, for each r, we can estimate

$$A(r,t_0)=\frac{\sqrt{GM(r)}t_0}{r^{3/2}}, \tag{4.3}$$

calculate the corresponding development angle η and thus obtain the velocity of each shell.

Teerikorpi et al. (1992) and subsequent works (e.g. Ekholm & Teerikorpi 1994, Ekholm 1996, Ekholm et al. 1999, 2000) assumed a $M(r)$ following

$$M(r)=\frac{H_0^2q_0}{G}r^3(1+kr^{-\alpha}) \tag{4.4}$$

where H_0 is the Hubble constant and q_0 the deceleration parameter of the Universe. For the case of the Virgo cluster, if instead of the variable r, we use $R=r/R_{\rm VIC}$, i.e., the ratio between r and the distance of the VIC to the Local Group, we obtain

$$M(R)=\frac{H_0^2q_0}{G}R_{\rm VIC}^3R^3(1+k'R^{-\alpha}) \tag{4.5}$$

With this radial behaviour of mass, we thus have

$$A(R,t_0)=H_0t_0\sqrt{q_0(1+k'R^{-\alpha})} \tag{4.6}$$

Given that the factor H_0t_0 depends only on q_0, the equations of motion depend on k', α (characteristic of the density perturbation) and q_0 (characteristic of the chosen universe).

In order to determine the parameters related to the density perturbation, one can use the cosmic recession velocity of Virgo $V_{\mathrm{VIC}}^{\mathrm{cosm}}$ as well as the observed velocity of the Virgo cluster with respect to the Local Group V_{VIC}. As shown in equations 4.1 and 4.2, the velocity field caused by the density excess can be written as

$$v = \frac{R\ R_{\mathrm{VIC}}^3}{t_0} f(\eta) = \frac{R V_{\mathrm{VIC}}^{\mathrm{cosm}} V_{\mathrm{VIC}}}{H_0 t_0} f(\eta) \tag{4.7}$$

For $R = 1$ the velocity must be equal to the observed velocity of the Virgo cluster with respect to the Local Group V_{VIC}, so we can obtain from this equation the development angle corresponding to $R = 1$ and from equation 4.6, the value of k', which happens to be independent of the density perturbation and depends only on the universe chosen. Presuming Virgo to be at rest with cosmological background (i.e. $V_{\mathrm{VIC}}^{\mathrm{cosm}} = V_{\mathrm{VIC}} + V_{\mathrm{LG}}$), for $V_{\mathrm{VIC}} = 980$ km s^{-1} (Teerikorpi et al. 1992) and a Virgocentric infall velocity of the Local Group $V_{\mathrm{LG}} = 220$ km s^{-1}(Tamman & Sandage 1985), the previous procedure results in $k' = 0.606$ for an Einstein - de Sitter Universe ($q_0 = 0.5$).

Once k' is known, in order to obtain the value of the slope of the mass distribution, α, it is necessary to have accurate positions and velocities of galaxies whose dynamics is governed by the Virgocentric potential. Ekholm et al. (1999) used 32 galaxies whose distances were known using their Cepheids, generally measured with the HST, through the PL-relation. Thus, minimizing the average difference between the velocities observed for these galaxies and predicted by equations 4.1 and 4.2 for different values of the mass slope, they obtained $\alpha = 2.85$.

4.4 Infall model with rebound

As we are interested in modeling the velocity of galaxies that have already crossed once the center of the cluster, we cannot use the Tolman-Bondi model as it was presented in Section 4.3. That approach only accounts for the motion of galaxies falling into the cluster for the first time and their parameters were derived neglecting other possible components in the cluster.

To be able to model the virgocentric velocity field including rebound orbits, we implemented a simple point mass model for the spherical collapse of a zero-pressure fluid. In this way, the solution of the problem is not limited to the classical deduction of the velocity field of objects until a singularity first develops. The calculations can be extended beyond that time until galaxies recollapse again by allowing that the spherical shells of matter reaching the singularity pass through themselves and reemerge.

In the present section, we take the, admittedly crude, point of view of treating galaxies as test particles moving in a constant point-mass potential well, which allows us to ignore the effects of shell crossing on their first orbit. Shell crossing is most important inside the previously relaxed cluster body, but galaxies on first infall spend little time in this region because of their radial trajectories and high pericentric velocities. Hence, the gravitational acceleration they undergo during their first crossing of the cluster core is not expected to differ substantially from that exerted if all the mass were concentrated at the center.

Under the point mass approximation, equations 4.1 and 4.2 become

$$\frac{\eta - \sin\eta}{(1-\cos\eta)^{3/2}} = \frac{\sqrt{GM_{\rm VIC}}t_0}{r^{3/2}}, \quad v = \frac{r}{t_0}\frac{\sin\eta(\eta-\sin\eta)}{(1-\cos\eta)^2} \tag{4.8}$$

for the bound shell case, and by

$$\frac{\sinh\eta - \eta}{(\cosh\eta-1)^{3/2}} = \frac{\sqrt{GM_{\rm VIC}}t_0}{r^{3/2}}, \quad v = \frac{r}{t_0}\frac{\sinh\eta(\sinh\eta-\eta)}{(\cosh\eta-1)^2} \tag{4.9}$$

for the unbound case. In these expressions, $M_{\rm VIC}$ is the *effective* total mass of the VIC region (strictly speaking, the point mass representative of the region under consideration around the VIC center). In our double-infall model bound shells reach maximum expansion for development angles $\eta = \pi$ and 3π, whereas full collapse is achieved when $\eta = 2\pi$ and 4π.

The predicted radial velocity, V, of a galaxy at a distance d from the Local Group and observed at an angular distance θ from the Virgo center can be evaluated from

$$V(d) = V_{\rm VIC}\cos\theta \pm v\sqrt{1 - R_{\rm VIC}^2\sin^2\theta/r^2}\ , \tag{4.10}$$

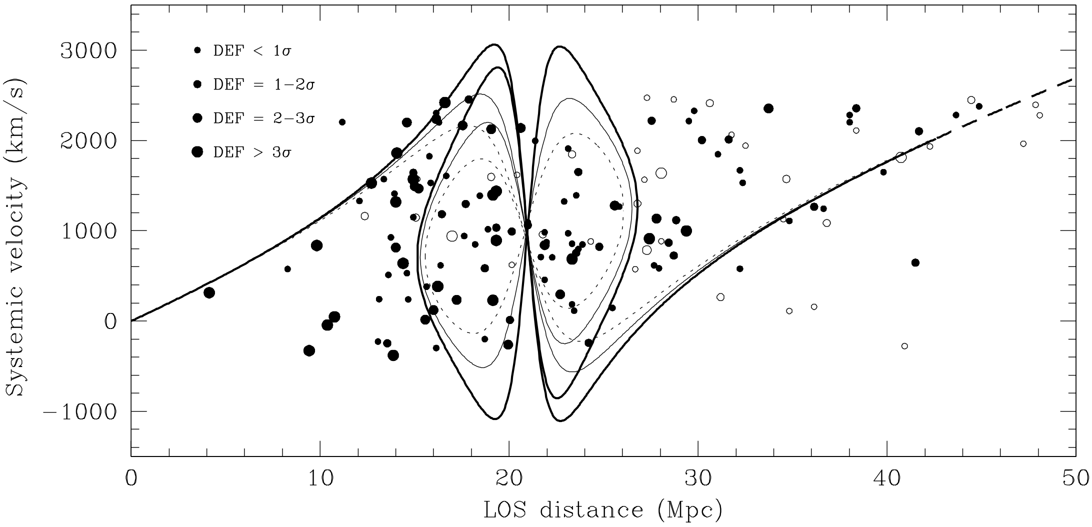

Figure 4.2: Systemic velocity vs. distance from the Local Group (LOS distance) for Virgo spirals. The curves demonstrate the predicted velocities for $\theta = 4°$ (thick solid), $\theta = 6°$ (thin solid), and $\theta = 8°$ (dotted). The dashed portion at large Virgocentric distances is for unbound shells. Galaxies with uncertain distances (open symbols) have been excluded from the fit. Parameter DEF measures H I deficiency in units of the mean standard deviation for field objects ($= 0.24$).

The linear and angular distances of the galaxy are related through the cosine law

$$R^2 = 1 + D^2 - 2D\cos\theta \ , \tag{4.11}$$

where $R = r/R_{\rm VIC}$ and $D = d/R_{\rm VIC}$ are the linear distances to the center of the cluster and to the LG, respectively, expressed in Virgo's distance units. The $(-)$-sign applies for galaxies with $D < \cos\theta$, while the $(+)$-sign is for $D \geq \cos\theta$.

4.5 Model predictions vs. observations

As shown in the previous section, our simple dynamical model describing the velocity field in the VIC region involves parameterization in terms of t_0, $M_{\rm VIC}$, $R_{\rm VIC}$, and $V_{\rm VIC}$ —the systemic velocity can be replaced by the cosmological velocity of Virgo for a given infall velocity of the Local Group. In spite of the fact that only three of these

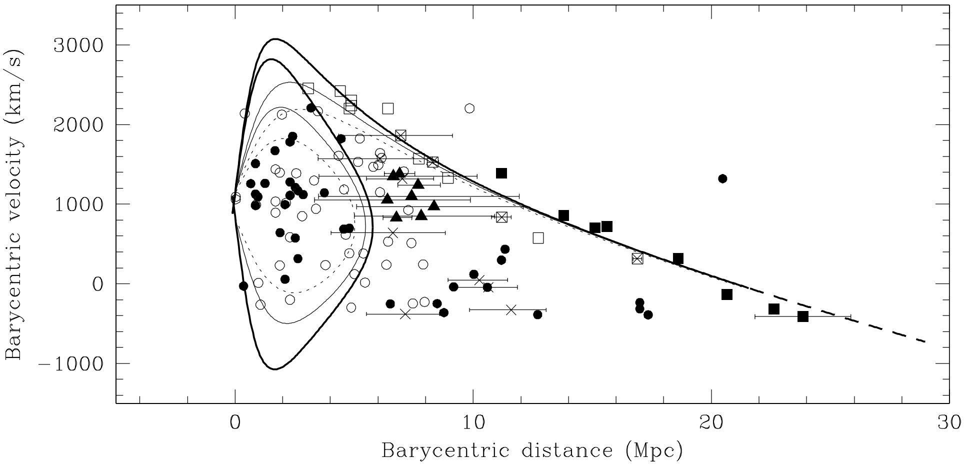

Figure 4.3: Barycentric velocity vs. barycentric distance for spirals with reliable distances. Open and filled symbols are, respectively, for galaxies closer and more distant than the barycenter. Squares identify the galaxies used to define the two asymptotic branches, triangles are for members of the H I-deficient background group, and crosses for galaxies with DEF $\geq 3\sigma$ and LOS distance ≤ 15 Mpc. Error bars in distance are shown for the last two subsets of galaxies and for one (representative) of the galaxies within the asymptotic regime. The curves are the same solutions depicted in figure 4.2.

parameters are independent, it is advisable to work with no more than two free parameters, as the current velocity-distance data on the VIC are still insufficient to constrain models with so much freedom. For this reason, we allow the Virgo mass and distance to vary freely while keeping $V_{\rm VIC}$ fixed to 980 km s^{-1}. We have, nonetheless, checked that the range of values of $V_{\rm VIC}$ allowed by the observations does not lead to significantly different results. The viability of the solutions will be cross-checked by comparing the value of t_0 predicted by the best fits to the observations with the cosmological age of 13.7 Gyr obtained recently from the WMAP CMB experiment (Spergel et al. 2003).

The systemic velocity-distance diagram for the VIC region plotted in figure 4.2 shows the basic expected features: an initial steeply rising velocity-distance relation at the cluster front, a central broad region with the maximum observed velocity amplitudes, and a final ascending part of the relation, expected to approach the local Hubble law asymptotically. The difficulties inherent to the modeling of the motions in the innermost cluster region —where multiple rebounds are expected to occur— prompted us to restrict the acceptable range of models by putting all the weight of the fits on the envelope to the streaming velocities *within the asymptotic*

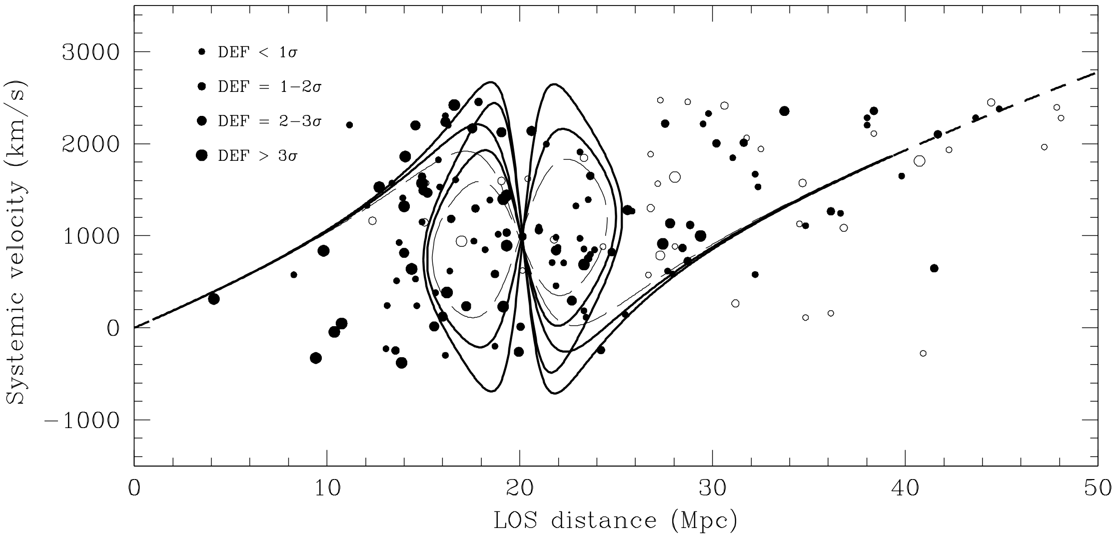

Figure 4.4: Same as figure 4.4 for the model parameters $M_{\rm VIC} = 1.8 \times 10^{15}$ M$_\odot$ and $R_{\rm VIC} = 20.2$ Mpc obtained when assuming galaxies in table 4.1 to be on first infall.

regime . This is indeed the fitting procedure adopted by first-infall models and has the advantages of: (1) relying on the subset of observations that offer the highest constraining power; (2) being unaffected by shell crossing; and (3) being barely sensitive to the angular distance from the VIC center.

The three solid curves in figure 4.2 demonstrate the locus of the optimum model, with parameters $M_{\rm VIC} = 3.2 \times 10^{15}$ M$_\odot$ and $R_{\rm VIC} = 21.0$ Mpc, leading to $t_0 = 13.5$ Gyr, for lines-of-sight corresponding to angular separations of 4°, 6°, and 8°. We find it compelling that, in spite of the fact that the minimization relies on a fraction of the data, our best solution explains a large number of the galaxy motions around the VIC region. The good accordance between the observations and the prediction of the double-infall model is reinforced by the remarkable symmetry of the motions with respect to the local Hubble flow defined by the imaginary straight line passing through the position of the Local Group and that of the predicted VIC barycenter, as shown in figure 4.3.

We have also explored the possibility that the gas-deficient group in the background would also be on first infall. When we used galaxies on the asymptotic branch as well as galaxies in the background group as tracers for fitting our model, we obtained $M_{\rm VIC} = 1.8 \times 10^{15}$ M$_\odot$ and $R_{\rm VIC} = 20.2$ Mpc, leading to $t_0 = 14.0$ Gyr. We show the results of the fitted model in figure 4.4, where we used the same symbols as in figure 4.2.

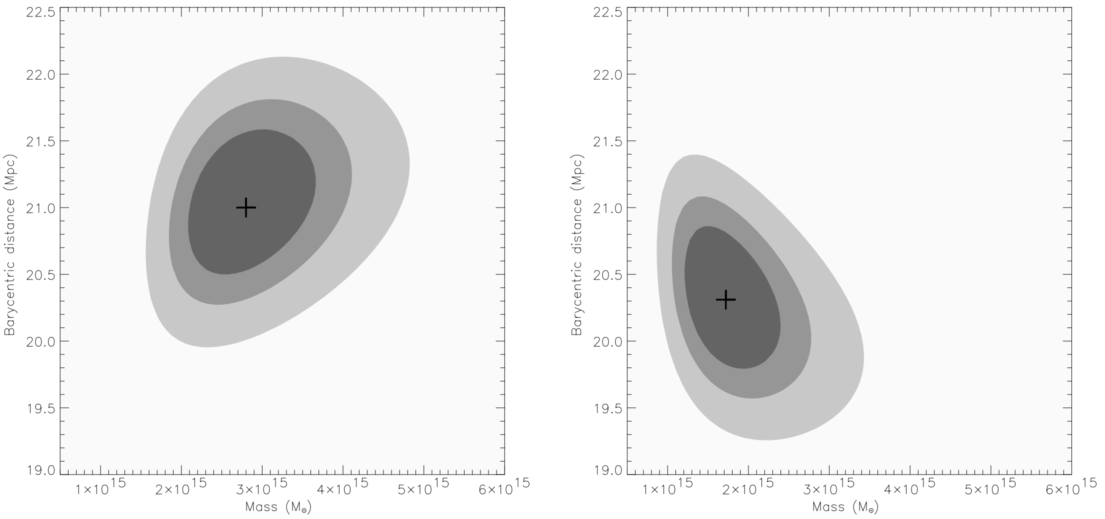

Figure 4.5: 1, 2, and 3σ confidence limits on $M_{\rm VIC}$ and $R_{\rm VIC}$ obtained from our dynamical model of the VIC region for the background group on a rebound (*left* panel) or on a first infall trajectory (*right* panel). The crosses indicate the best estimates of these parameters for each scenario.

In both scenarios (galaxies in the background group on first infall or already passed through the centre of the cluster), the error contours in the $(M_{\rm VIC}, R_{\rm VIC})$ plane drawn in figure 4.5 show that our predictions are in reasonable agreement with previous estimates of the values of these parameters. As seen in Section 4.3, for a given distance to the Virgo cluster, we can obtain an estimate of the dynamical mass of the cluster applying equation 4.5, which can be written in terms of the cosmic recession velocity of Virgo $V_{\rm VIC}^{\rm cosm}$ as

$$M(R) = \frac{(V_{\rm VIC}^{\rm cosm})^2 q_0}{G} R_{\rm VIC} R^3 (1 + k' R^{-\alpha}) \tag{4.12}$$

If we take the values of k' and α from Ekholm et al. (1999) for $q_0 = 0.5$, $V_{\rm VIC}^{\rm cosm} = 1200$ km s^{-1} and consider the mass enclosed within 8 degrees, we obtain $M \sim 2 \times 10^{15}$ M$_\odot$ for both estimates of $R_{\rm VIC}$ obtained in this chapter. Thus, while mass calculations of the central cluster region based on the X-ray emission or the virial theorem amount to about several times 10^{14} M$_\odot$, our best estimates $M_{\rm VIC} = 2.8 \times 10^{15}$ M$_\odot$ or $M_{\rm VIC} = 1.8 \times 10^{15}$ M$_\odot$ approach the values $\lesssim 2 \times 10^{15}$ M$_\odot$ inferred from modelings of the velocity field of the Local Supercluster (Tully & Shaya 1984; Fouqué et al. 2001, and the above calculation). The acceptable barycentric distances are also well within the very poorly constrained range ($\sim$

14–21 Mpc) of VIC distances reported in the literature (see e.g. Ciardullo et al. 1998; Ekholm et al. 2000), although our most likely values $R_{\rm VIC} = 21.0$ Mpc and $R_{\rm VIC} = 20.2$ Mpc advocate a large-distance scale which, for a cosmological VIC velocity of 1200 km s^{-1}, brings the *local* value of the Hubble constant to about 60 km s^{-1} Mpc^{-1}. Furthermore, our best solutions lead to $t_0 \sim 14.0$ Gyr, in excellent agreement with the expansion age advocated in Spergel et al. (2003). Finally, note from equation (4.10) that the constraint provided by the motion of the Local Group with respect to the VIC (i.e., a null systemic velocity at our position) is automatically satisfied by the models.

4.6 Summary and conclusions

The presence on the Virgo cluster outskirts of spiral galaxies with gas deficiencies as strong as those of the inner galaxies stripped by the intracluster medium has led us to explore the possibility that some of these peripheral objects are not newcomers. A dynamical model for the collapse and rebound of spherical shells under the point mass and radial flow approximations has been developed to account for the amplitude of the motions in the Virgo I cluster region.

One of the most striking predictions, illustrated in figure 4.3, is that various H I-deficient galaxies in the frontside and backside of Virgo could be accommodated in the same way on an orbit following rebound and on a first infall trajectory. We conclude that these galaxies might not be recent arrivals but have already plunged into the VIC center in the past. Especially interesting is the case of the H I-deficient background group observed at $d \sim 28$ Mpc and $v_{\rm sys} \sim 1000$ km s^{-1}, whose near turnaround position in the Hubble diagram and the assumed standard harmonic oscillation movement of the galaxies around the cluster center, together with a cosmic age presumably close to 13.5 Gyr, indicate that it might have passed through the Virgo core about 4.5 Gyr ago. The fit to the observed velocity field also indicates that a significant number of galaxies in the VIC region might be currently falling towards the cluster from the frontside —perhaps not for the first time either—, so it does not substantiate former claims of a paucity of objects of this sort (Fouqué et al. 2001).

We do not claim, however, that this is the only possible solution satisfying the observations. The alternative model based on the assumption that the gas-deficient group in the background is also on first infall gives similarly reasonable best values of the assumed parameters. Nor are we endorsing the argument that *all* H I-deficient galaxies in the VIC region have passed through the cluster core. It is clear from figures 4.2 and 4.3 that the positions of some gas-poor galaxies, especially in the front cluster side, are best explained according to our model if they are on first infall. In any event, our dynamical modeling of the VIC region has shown that characteristics such as a large Virgocentric distance or a near turnaround position are not by themselves conclusive indications of a recent arrival. The substantial H I deficiency of the background subclump found in Chapter 3 may well have originated in an earlier passage of this entity through the Virgo core.

Even if our suggestion that the H I-deficient group on the backside of the VIC might not be a recent arrival is finally proven well-founded, it is still necessary to find an explanation for the apparently long time ($\sim$4.5 Gyr) along which these galaxies have maintained a substantial dearth of gas without noticeable consequences on their morphologies: 8 of its 14 probable members are late-type spirals, whereas the 5 with the largest gaseous deficiencies have types Sb or later. Moreover, the magnitudes of these latter galaxies do not show any evidence of a substantial dimming. Yet, the details and chronology of the evolution of galactic properties triggered by the sweeping of the atomic hydrogen, as well as its repercussions on the star formation rate, are still poorly understood. For instance, estimates for gas consumption time scales in the absence of gas replenishment from a sample of 36 spiral galaxies of various morphologies by Larson, Tinsley, & Caldwell (1980) produced values ranging from 0.9 to 15 Gyr, with a median of 3.9 Gyr. These authors also discussed the color evolution of disk galaxies whose star formation has been truncated at various past times and concluded that substantial reddening in the latest spiral types requires that most of their star formation ceased about 5 Gyr ago. On the other hand, recent observational studies of the galaxy populations in clusters at different redshifts (e.g., Fasano et al. 2000) indicate that while the quenching of star formation induced by the removal of the gas appears to be rapid ($\sim$1 Gyr), the morphological evolution of disk galaxies takes several billion years. Perhaps evolution is still slower for objects, such as the members of the gas-deficient cloud detected in the background of Virgo, that spent most of their time out of the aggressive cluster environment.

On the other hand, the fact that, for both scenarios considered in this chapter, there is still a significant number of galaxies which do not fit in our dynamical model of the cluster, makes us wonder about its applicability. In order to be able to model the trajectory of galaxies after a passage through the center of the cluster, we had to make some approximations, such as the point mass assumption and the negligence of shell crossing during collapse, which could have led to incorrect results. In addition, our model does not consider the interactions of galaxies among them, which could eject galaxies at high speeds to high clustercentric distances (Solanes et al. 2001; Vollmer et al. 2001). Moreover, although we have rejected for our fit galaxies with the highest distance errors (i.e. errors greater than 5 Mpc), there could also be the possibility that distance errors would be greater than our *estimated* mean error (i.e. 13%, see Chapter 3). This could also explain the discordant position in the phase space diagram of galaxies with small *estimated* distance errors. In order to study these discrepant galaxies it is necessary to rely on numerical simulations, which follow in a realistic way the dynamical evolution of clusters and whose analysis is not hinted by the presence of observational errors.

5 Numerical approach to halos: implications for the Virgo cluster

5.1 Introduction

We have seen in Chapter 4 that it is statistically plausible that some of the gas deficient galaxies in the periphery of the Virgo cluster found in Chapter 3 could have passed through the cluster core and in the process had their interstellar gas swept out by the ram pressure of the intracluster hot diffuse gas. However, our data did not allow us to rule out either the alternative possibility that these peripheral galaxies, especially the background group identified at a distance of ~ 28 Mpc, were on first infall towards the cluster.

In this chapter, we further investigate whether these H I-deficient galaxies on the outskirts of the Virgo cluster (with several objects over 5 Mpc in front or behind the cluster core) have previously passed through its core, using both analytical arguments and the output of cosmological N-body simulations. In Section 5.2, we describe the N-body simulations. Next, in Section 5.3, we study the structure in radial phase space of dark matter halos of the simulations. In Section 5.4, we compute the maximum rebound radius, both analytically, making use of the turnaround radius of cosmological structures, whose calculation is shown in Appendix B, and by studying the structure of our simulated halos in radial phase space, as well as analyzing the orbital evolution of particles in the cosmological simulations of Fukushige & Makino (2001). In order to link this *rebound radius* with the Virgo case, we measure in Section 5.5, from the parameters obtained from X-ray observations, the virial radius of the Virgo cluster as well as the enclosed mass and circular velocity at this radius. In Section 5.6, we use the N-body simulations to check the results of the point mass model developed in Chapter 4. Finally, we discuss our results in Section 5.7.

5.2 N-body simulations

The N-body simulations used here were carried out by Hatton et al. (2003) using their GALICS hybrid N-body/semi-analytic model of hierarchical galaxy formation. The outlines of this model can be found in Hatton et al. (2003). Here we are basically interested in the density and velocity fields directly traced by dark matter particles. The N-body simulation contains 256^3 particles of mass $8.3 \times 10^9 M_\odot$ in a box of 150 Mpc size and it is run with a softening length amounting to a spatial resolution of 29 kpc. The simulation was run for a flat universe with cosmological parameters $\Omega_0 = 0.333, \Omega_\Lambda = 0.667$, $H_0 = 66.7\,\mathrm{km\,s^{-1}\,Mpc^{-1}}$, and $\sigma_8 = 0.88$. Once the simulation is run, halos of dark matter are detected with a 'Friends-of-Friends' (FoF) algorithm (Davis et al. 1985), with a variable linking length such that the minimum mass of the FoF groups is $1.65 \times 10^{11} M_\odot$ (20 particles) at any time step. With this method, over 2×10^4 halos are detected at the final timestep, corresponding to the present-day ($z = 0$) Universe. The GALICS halo finder does not allow halos within halos, so that a cluster, to which is assigned a massive halo, cannot contain smaller halos within it.

5.3 Halo structure in radial phase space

Figure 5.1 shows the radial phase space diagrams, i.e. radial velocity vs. radial distance, both relative to the halo center, for 4 massive halos. We have studied the final output of the simulation at $z = 0$. The centers of the isolated halos shown in figure 5.1 are provided by the simulation output and correspond to the barycenter of the FoF groups of particles. Radial distances are normalized to the virial radius r_{100}, corresponding to the radius where the mean density is 100 times the critical density of the Universe. We use r_{100} instead of r_{200} because the former represents better the virial radius in universes with non zero cosmological constant (Kitayama & Suto 1996; Łokas & Hoffman 2001). Velocities are normalized to the respective circular velocities at r_{100}.

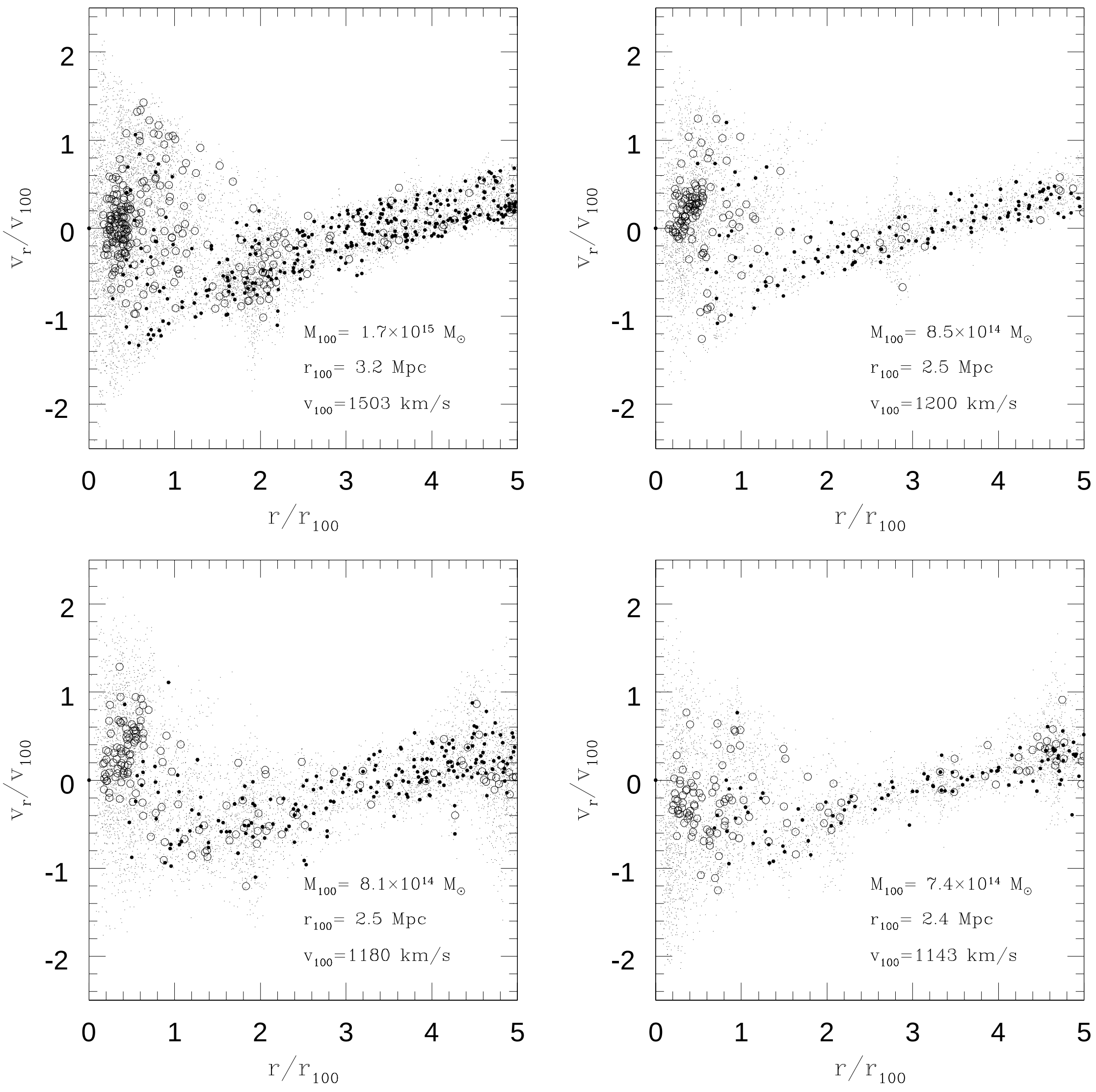

Figure 5.1: 3D radial phase space plots of dark matter particles in a ΛCDM cosmological N-body simulation for the four most massive halos at redshift $z = 0$. The virial radius, mass and circular velocity at virial radius are listed on the right corner of each plot. The *open* and *small closed circles* are the identified halos in the cosmological simulation respectively without and with galaxies within them.

Most of the massive halos in the simulation have a phase space diagram similar to those for the 4 halos shown in figure 5.1, once scaled to the virial radius and circular velocity at the virial radius, v_{100}. In particular, all plots show a virialized region for radii smaller than r_{100} (although this virialization is not perfect, for example see the excess of positive velocity particles in the lower left plot, presumably caused by a large group that is bouncing out of the cluster), and an infalling region with velocity increasing with radius and asymptotically reaching the (linear) Hubble flow. One clearly notices groups or small clusters of particles in the outer regions (e.g. at $r = 3\,r_{100}$ in the upper right plot), which display *Fingers of God* patterns in phase space. The material within 1 or $2\,r_{100}$ that bounces out of the cluster should form a pattern symmetric to the infalling pattern relative to the zero velocity line. It is smeared out by numerical two-body relaxation (S. Colombi informed us that the rebounding region is seen more sharply when simulations are run with increased potential softening lengths that reduce the numerical relaxation). The global aspect of these phase space plots is similar to those shown by Fukushige & Makino (2001, figure 21), at various epochs of their cosmological simulations (run with a standard — $\Omega_m = 1$, $\Omega_\Lambda = 0$ — CDM cosmology).

5.4 Maximum rebound radius

An inspection of figure 5.1 shows that dark matter particles beyond the virialized core and outside the infalling/expanding zone of phase space can reach 2 or 2.5 times the virial radius, but not any further, and moreover come in groups of particles which appear to be tidally shredded in phase space. In other words, particles that cross through the core of a cluster cannot bounce out beyond 2.5 virial radii.

Now galaxies are not just particles, but develop within particle condensations known as dark matter halos, which should arise as vertically-elongated (Fingers of God) particle condensations in phase space, and therefore ought to avoid the fairly sparse regions of phase space where the outermost outgoing particles are seen. The open circles in figure 5.1 indicate the halos without galaxies within them in GALICS. The absence of galaxies within halos is a feature of GALICS for halos that cross a larger one (its galaxies become part of the larger halo). Empty halos can also occur in GALICS for isolated halos in which galaxies have not yet had time to form. The empty halos outside the infalling/expanding region do not extend beyond $1.7\,r_{100}$

(upper left and lower right panels, with the former possibly a member of the group at $1.9\, r_{100}$). In contrast, the normal halos (filled circles in figure 5.1) outside the infalling/expanding region do not extend as far from the main halo. The positions of the empty circles in figure 5.1 therefore suggests that halos crossing the main halo do not bounce out further than $1.7\, r_{100}$.

This maximum rebound radius is consistent with a close inspection of the right panel of figure 20 from Fukushige & Makino (2001) (a copy of which we reproduce in figure 5.2), which shows that the largest rebound radii in one of their cosmological simulations, i.e. the largest radii of a particle that has experienced at least one pericenter, is 2 Mpc, occurring at the present epoch, for a cluster whose present-day virial radius (r_{200}) is at 1.7 Mpc (see their table 2). Hence for that particular shell, the rebound radius is only 1.2 times r_{200} and an even smaller factor times r_{178} (the canonical radius for the cosmology used). Given the $\Omega_m = 1$ cosmology used, for which the spherical infall model yields scale-free growth, the rebound radius should be proportional to the turnaround radius, which itself should be proportional to the virial radius, with a time growth of $r \sim t^{8/9}$ (Gott 1975). We checked that the other rebound radii occurring earlier were even smaller than the scaled expectation of a 2 Mpc radius today.

One can confirm this result through simple analytical arguments. First, if one identifies the virial radius to the radius where infalling shells meet the rebounding shells, this will be very close to the rebound radius itself, defined as the radius where a shell reaches its second apocenter (see figure 1 of Mamon 1992), so that the rebound radius will be very close to r_{100}.

Moreover, one can estimate the rebound radius for a flat cosmology in the following manner. To begin, assume that the rebound radius is $\widetilde{r}$ times smaller than the turnaround radius (the first apocenter of the shell), and occurs at a time equal to $\widetilde{t}$ times the epoch of turnaround. The mass within a shell that has reached its second apocenter will be close to but greater than the mass M within the same shell at turnaround, since some additional matter will be infalling for the first time. We write this as

$$\rho_{\rm reb}(t_0) \gtrsim \widetilde{r}^3\, \rho_{\rm ta}(T_{\rm ta}) \ , \tag{5.1}$$

where the rebound density is for the present epoch, while the turnaround density is for the epoch of a shell's first apocenter given that its second apocenter is today.

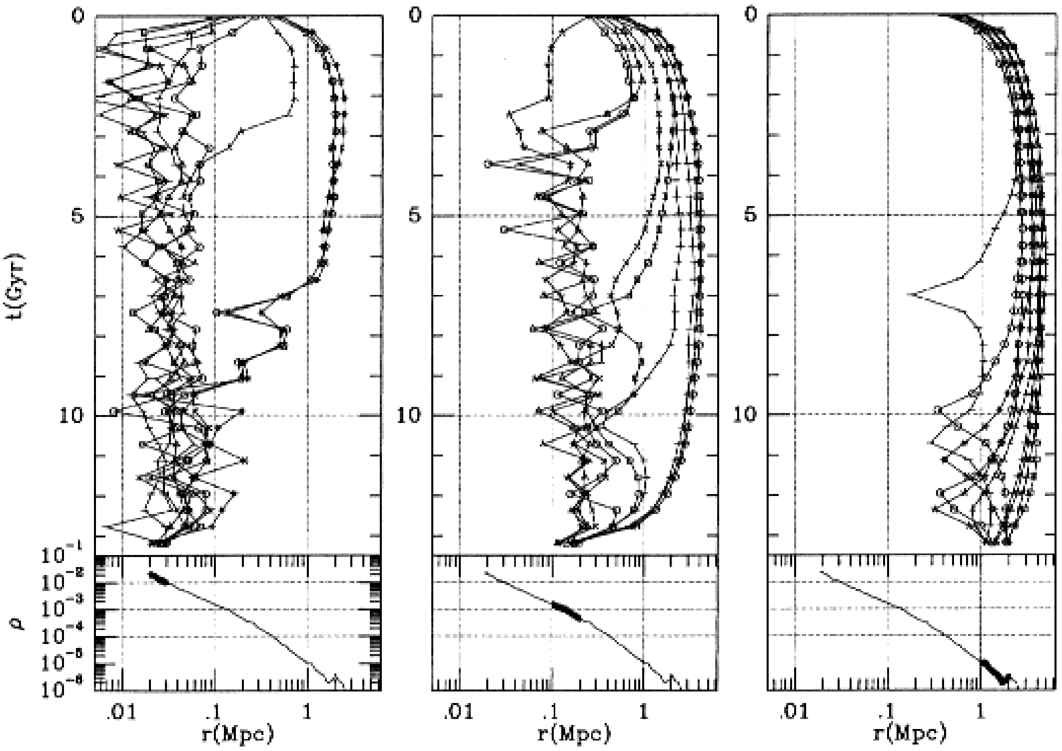

Figure 5.2: One-dimensional trajectories of 10 randomly selected particles for a halo of $M_{200} = 2.6 \times 10^{14}$ M$_\odot$ and $r_{200} = 1.7$ Mpc at $z = 0$. Distance from the center of the halo is plotted as a function of time, together with the density profile at $z = 0$. Region indicated by thick curve in density profile indicates where the selected particles exist at $z = 0$. *Note:* Taken from Fukushige & Makino (2001)

Given that the mass within the shell at turnaround is

$$\begin{aligned} M &= \frac{4\pi}{3}(1+\delta_i)\,\rho_i\,r_i^3 \\ &= \frac{4\pi}{3}\left(1+\frac{\delta_0}{1+z_i}\right)\rho_0\,r_0^3\ , \end{aligned} \tag{5.2}$$

where we used equations B.10 and B.17, We then obtain a mean density within the turnaround radius that satisfies

$$\frac{\rho_{\rm ta}}{\rho_0} = \left(1+\frac{\delta_0}{1+z_i}\right)\frac{1}{y_{\rm ta}^3} \simeq \frac{1}{y_{\rm ta}^3}\ . \tag{5.3}$$

Equations 5.1 and 5.3 lead to

$$\rho_{\rm reb} \gtrsim \left(\frac{\widetilde{r}}{y_{\rm ta}}\right)^3 \Omega_0\,\rho_{\rm c,0}\ , \tag{5.4}$$

where $\rho_{c,0}$ is the present day critical density. Inverting mean density into mass, assuming $d\ln\rho/d\ln r = -\alpha$, leads to

$$\frac{r_{\rm reb}}{r_{\rm vir}} \lesssim \left(\frac{\Omega_0}{\Delta}\right)^{-1/\alpha} \left(\frac{\widetilde{r}}{y_{\rm ta}}\right)^{-3/\alpha} , \tag{5.5}$$

where the virial radius $r_{\rm vir}$ is defined such that the mean density within it is Δ times the critical density. For Navarro, Frenk, & White (1995, hereafter NFW) density profiles, with concentration parameters $c \simeq 6$, as found by Bullock et al. (2001) in recent ΛCDM cosmological simulations, using $\Delta \simeq 100$, we obtain a slope $\alpha = 2.4$ at the virial radius.

There are two ways one can reach a large rebound radius today: either with a large ratio of rebound to turnaround radius for a given shell (i.e. $\widetilde{r}$ as small as possible, but it cannot be smaller than unity), or with a turnaround as late as possible (i.e. $\widetilde{t}$ as small as possible), which implies a lower turnaround density, hence a lower rebound density (for given $\widetilde{r}$).

In the first case, the rebound radius could be equal to the initial turnaround radius, i.e. $\widetilde{r} = 1$. One then expects that a shell that is presently at its second apocenter, should have reached turnaround at epoch $t_0/3$, i.e. $\widetilde{t} = 3$. We make use of the reasonably simple expression for the turnaround radius versus time obtained in the Appendix B. Solving equation B.21 for δ_0, using equations B.18 and B.19 for $y_{\rm ta}$ and $(\Omega_0 = 0.3, \lambda_0 = 0.7)$, yields $\delta_0 = 2.69$ and $y_{\rm ta} = 0.229$. Equation 5.5 and $\alpha = 2.4$ then lead to $r_{\rm reb} \lesssim 1.8\, r_{100}$.

Second, in the spirit of the shell rapidly virializing through violent relaxation at full collapse, one can assume that the shell reaches its second apocenter right after its first pericenter (full collapse), i.e. $\widetilde{t} \gtrsim 2$, with a radius near half its turnaround radius ($\widetilde{r} = 2$). This yields (not surprisingly) $r_{\rm reb} = 1.03\, r_{100}$. The very best case requires $\widetilde{r} = 1$ and $\widetilde{t} = 2$, and leads to $r_{\rm reb} = 2.46\, r_{100}$. Table 5.1 summarizes these estimates of the rebound radius, where δ_0 and $y_{\rm ta}$ come from equations B.18, B.19 and B.21 and $r_{\rm reb}/r_{100}$ from equation 5.5. The last four lines are for the four particle orbits from the simulations of Fukushige & Makino (2001) that rebound within the last 7 Gyr, and for these δ_0 is computed so that the epoch of the second apocenter is the present time, hence the epoch of turnaround is $t_0/(t_{\rm reb}/t_{\rm ta})$.

Although the uncertain effects of relaxation as the shell crosses through the virialized region lead to uncertain values of the ratios of rebound to turnaround radius

Table 5.1: Rebound radius in different scenarios

$\widetilde{r}$	$\widetilde{t}$	δ_0	$y_{\rm ta}$	$r_{\rm reb}/r_{100}$
1.0	3.00	2.69	0.229	1.78
2.0	2.50	2.42	0.258	0.87
2.0	2.00	2.15	0.296	1.03
1.0	2.00	2.15	0.296	2.46
1.5	2.50	2.42	0.258	1.25
2.3	2.50	2.42	0.258	0.73
2.4	2.17	2.24	0.282	0.77
2.3	3.58	2.99	0.205	0.55

($\widetilde{r}$) and time ($\widetilde{t}$), in the most favorable spherical infall model, the rebound radius cannot be greater than 2.5 times the virial radius. The cosmological simulations of Fukushige & Makino suggest rebound radii of order of r_{100}, but recall that they are for a different cosmology ($\Omega_0 = 1, \lambda_0 = 0$). The use of real simulations has the added advantage of incorporating the effects of two-body encounters that can push material beyond the theoretical rebound radius. However, it is not always easy to distinguish in a given snapshot the material that is bouncing out of a structure with material that is infalling for the first time (except that the former particles are in halos without galaxies), and the analysis of particle histories, done for the simulations of Fukushige & Makino, is beyond the scope of this work for the GALICS simulations.

5.5 Virial radius, mass and velocity of the Virgo cluster

For the application of results of Section 5.4 to the Virgo cluster, we require an estimate of the virial radius of the cluster. We estimate r_{100} through the large-scale X-ray observations of the Virgo cluster obtained with the ROSAT All-Sky Survey by Schindler et al. (1999). The peak of the X-ray emission in Virgo coincides with the position of the giant elliptical M87, and we use the integrated mass profile around M87 obtained by Schindler et al. to derive the virial radius. With their isothermal approximation for the total mass profile (their figure 11a), $M(r)/r$ is independent of radius for $r \gg r_c$ and also of the assumed distance to Virgo, yielding

$$\frac{G\,M(r)}{r} = 3\,\beta\,\frac{kT}{\mu m_p}\ , \tag{5.6}$$

where $\beta = 0.47$ is the shape parameter of the X-ray gas density profile, $kT = 2.7\,\mathrm{keV}$ and μm_p is the mean particle mass, generally assumed for a hot plasma to be roughly $0.6\,m_p$, where m_p is the proton mass. The virial radius, r_{100}, is then obtained through

$$\overline{\rho} = \frac{3M_{100}}{4\pi r_{100}^3} = \Delta\,\frac{3\,H_0^2}{8\,\pi\,G}\ , \tag{5.7}$$

where $\Delta = 100$ is the spherical overdensity at the virial radius. Solving equations 5.6 and 5.7, one obtains

$$\begin{aligned} r_{100} &= \frac{1}{H_0}\sqrt{\frac{2}{\Delta}}\sqrt{\frac{3\,\beta\,kT}{\mu m_p}} = 1.65\,h_{2/3}^{-1}\,\mathrm{Mpc}\ , && (5.8)\\ M_{100} &= \frac{1}{G\,H_0}\sqrt{\frac{2}{\Delta}}\left(\frac{3\,\beta\,kT}{\mu m_p}\right)^{3/2} = 2.30\times10^{14}\,h_{2/3}^{-1}\,\mathrm{M}_\odot\ , && (5.9)\\ v_{100} &= \sqrt{\frac{G\,M_{100}}{r_{100}}} = \sqrt{\frac{3\,\beta\,kT}{\mu m_p}} = 780\,\mathrm{km\,s^{-1}}\ , && (5.10) \end{aligned}$$

where $h_{2/3} = H_0/(66.7\,\mathrm{km\,s^{-1}\,Mpc^{-1}})$.

The Virgo cluster is believed to have a complex structure, as it may be composed of several subclusters (Binggeli et al. 1987) around the elliptical galaxies M87 (NGC 4486), M86 (NGC 4406), and M49 (NGC 4472). The virial radius of $1.65\,h_{2/3}^{-1}$ Mpc is such that the important substructure surrounding M86 is well within it, at a distance of 0.23 (projected) and 0.44 (3D) times r_{100} (converted to $H_0 = 70\,\mathrm{km\,s^{-1}\,Mpc^{-1}}$) of M87. Similarly, the important substructure around M49 lies just within the virial radius, at a distance of 0.82 (projected) and 0.88 (3D) times the virial radius of M87. Among the other Messier galaxies in Virgo, which all have fairly secure distances, M60 is well within the virial radius, M89 lies just at the virial radius, while M59 is outside (see table A.3).

Analyzing the X-ray emission of the intra-cluster gas, Schindler et al. (1999) found that the M49 subcluster is 2.4 times less massive than the M87 subcluster. The ratio of masses between the M87 and the M86 subclusters is even larger (Böhringer et al. 1994). It therefore appears that the structure surrounding M87 is by far the most massive component in the Virgo cluster, and it is not a bad approximation to choose a single halo to represent the cluster, so we can apply the results of Section 5.4.

5.6 Point mass model versus N-body simulations

The value obtained for the virial mass of the Virgo cluster ($\sim 10^{14}$ $M_\odot$) is one order of magnitude smaller than the mass obtained through the fit of the parameters of the dynamical model performed in Chapter 4 ($\sim 10^{15}$ $M_\odot$). In principle, the punctual mass does not have to coincide with the virial mass of the cluster, as the latter one represents only the virialized part of the cluster, while the former gives us an idea of the dynamical mass of the whole Virgo region. However, it is interesting to investigate, by means of the N-body simulations, the relation between the point mass creating the gravitational potential in that dynamical model and the virial mass of the cluster and, at the same time, to test the validity of the point mass approximation and the subsequent negligence of the effects of shell crossing, non-zero cosmological constant and interactions of galaxies among them.

In figure 5.3 we show the radial phase space diagram of the most massive halo of the simulations (at the top left panel in figure 5.1). Radial distances are normalized to the virial radius, while velocities are normalized to v_{100}. We show in the left panel of figure 5.3 the shape of the phase space diagram up to $20\,r_{100}$. This is approximately the maximum distance, normalized to the virial radius of the Virgo cluster, of the spiral sample used in Chapter 4 to fit the parameters of the dynamical model of the Virgo region. The right panel in figure 5.3 shows the same diagram up to a maximum distance of $5\,r_{100}$, plotted to see the details of the core envelope. Superposed to both diagrams, we find the results of the point mass model with a central mass of $1M_{100}$ (solid line), $2M_{100}$ (short dashed line) and $5M_{100}$ (long dashed line).

We can see from these plots that, at large distances from the cluster, the central punctual mass able to reproduce the mean velocity-distance relation would be between $\sim 2M_{100}$ and $5M_{100}$, although lower values would also be acceptable, while, at short distances, most of the particles of the dark matter halo fall inside the envelope defined by the model with a central mass of $1M_{100}$ (although there are several particles outside), which is also the best model following the mean infall pattern up to $\sim 5\,r_{100}$. The models with higher central masses are only valid at larger distances. Note that at very short distances, the velocity predicted by the point mass model diverges to infinity (see equation 4.8 for $\eta = n\,2\pi$), which is obviously not the case for real halos. Overall, we can conclude that a point mass model with a

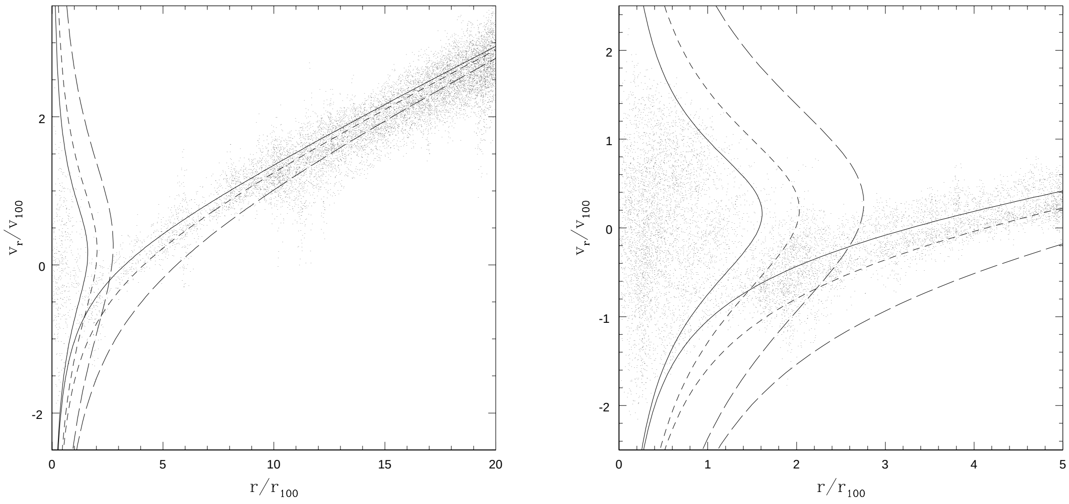

Figure 5.3: Radial phase space diagram of the most massive halo of the simulations (at the top left corner in figure 5.1. Radial distances are normalized to the virial radius r_{100}, while velocities are normalized to the respective circular velocities at r_{100}. The curves show the results of the point mass model with a central mass of $1M_{100}$ (*s*olid line), $2M_{100}$ (*s*hort dashed line) and $5M_{100}$ (*l*ong dashed line).

central mass between $\sim 1 - 2M_{100}$ is able to reproduce the main features of the radial phase space diagram of clusters up to a distance of $20\,r_{100}$, where the mean velocity-distance relation begins to grow slowlier than predicted by this model.

5.7 Summary and conclusions

In this chapter we have calculated the maximum distance that galaxies can bounce out of clusters. We computed this maximum rebound radius both analytically and using simulated dark matter halos. Our results indicate that the maximum rebound radius is between 1 and 2.5 times the virial radius. Given the virial radius of 1.65 Mpc for the Virgo cluster, which we derived in Section 5.5, and the maximum rebound radius derived in Section 5.4, galaxies passing through the Virgo cluster core in the past cannot lie further than $(1 - 2.5) \times 1.65 = 1.7 - 4.1$ Mpc from the cluster center.

An examination of figure 3.4 indicates $3\,\sigma$ H I-deficient galaxies lying between 9 and 30 Mpc from the Local Group, and in particular galaxies at 10 and 28 Mpc from the Local Group, whose distance error bars do not reach the wide range of distances to the Virgo cluster found in the literature (14 Mpc by Ciardullo et al. 1998 to 21 Mpc by Ekholm et al. 2000). Therefore, it appears very difficult to explain such H I-deficient galaxies over 5 Mpc in front or behind the cluster center as having crossed through the center of the cluster and bounced out if their distance estimates are accurate. This would suggest that the H I-deficient galaxies in the outskirts of the Virgo have not had their interstellar gas ram pressure stripped by the intracluster diffuse hot gas.

On the other hand, we have checked the applicability of the dynamical model developed in Chapter 4. We found that, considering its simplicity, this model is nevertheless consistent with the velocity field drawn by clusters if a central mass between 1 and 2 M_{100} is used.

Two questions remain still open. On one hand, the origin of the H I deficiency of the peripheral Virgo galaxies, if the lack of neutral hydrogen can not be attributed to the effects of ram pressure stripping. On the other hand, the origin of the difference between the point mass fitted in Chapter 4 and the virial mass of the Virgo cluster calculated in Section 5.5, as we have seen that the large difference between these two values is not explained by the simplifications adopted in the point mass model. These questions will be addressed in the next chapter.

6 The velocity field drawn by the Virgo cluster

6.1 Introduction

We have seen, in Chapter 5, that neither the difference between the virial mass of the Virgo cluster and the dynamical mass fitted by our Tolman-Bondi model, nor the position in the velocity-distance diagram of some galaxies that do not match the predictions of the model (see figures 4.2 and 4.4) can be attributed to an over-simplification of the point mass approximation as it reproduces fairly well the main features of the radial phase space diagram of clusters. Note that the amplitude of the core envelope decreases with mass (see figure 5.3), so with a central mass of $\sim 1 - 2M_{100} \sim 10^{14}$ $\mathrm{M}_{\odot}$, as suggested by the results of the previous chapter (see Section 5.6), instead of the fitted $M_{\mathrm{VIC}} \sim 10^{15}$ $\mathrm{M}_{\odot}$, there would be even more galaxies whose position in the velocity-distance diagram (figure 4.2) could not be accommodated on the predictions of the dynamical model.

For a better understanding of the kinematics of galaxies in the direction of the Virgo cluster, we simulate in this chapter an observation of the velocity-distance relation using the dark matter particles in the GALICS cosmological simulations carried out by Hatton et al. (2003) (see details of the simulations in Section 5.2). In Section 6.2, we present our compilation of the literature for elliptical Virgo galaxies, which will lead us to identify more precisely the velocity field around the cluster and estimate more accurately the distance to the center of Virgo, a crucial ingredient for the dynamical infall model. Next, in Section 6.3, we explain the adopted criteria to choose the halo used to represent the cluster. In Section 6.4, we show the procedure applied to pass from the simulation reference frame to the Virgo cluster reference frame. The mimicked velocity-distance relations with and without distance errors are provided in Section 6.5. Finally, in Section 6.6, we estimate the errors on the distance and mass of the Virgo cluster obtained by fitting a Tolman-Bondi model. Our conclusions are given in Section 6.7.

6.2 The inclusion of ellipticals into the Virgo galaxy sample

Using only late-type spirals, we have obtained in Chapter 4 two possible distances (20 and 21 Mpc) to the center of Virgo. Other distance estimates to the Virgo cluster, based upon spiral galaxies, produced distances in the range from 16 Mpc (Tully & Shaya 1984) to 21 Mpc (Ekholm et al. 2000).

An alternative way to estimate the cluster distance is by using the early-type components of the cluster, as they are thought to be better tracers of the center of the cluster due to morphological segregation (see e.g. Ferguson & Binggeli 1994). To do so, we have collected as many as possible early-type galaxies (E's, dE's and S0's) with redshift-independent distance measurements. Heliocentric velocities were extracted from the HyperLEDA database and converted to the Local Group reference frame, while the direct distant measurements are obtained from a variety of sources.

Table 6.1 summarizes the distance datasets on the early-type galaxies towards Virgo. Although different authors use different methods with different accuracy, we have not found systematic deviations between them, and furthermore found that the spread in differences of the distance moduli was consistent with the quoted errors, for all sets of early-type galaxies common to two authors. Therefore, we estimated a global distance modulus $\overline{d}$ for each galaxy, using the maximum likelihood estimator (e.g. Bevington & Robinson 1992)

$$\overline{d} = \frac{\sum_i d_i/\sigma_i^2}{\sum_i 1/\sigma_i^2} \ , \tag{6.1}$$

where d_i are the distance moduli and σ_i are the absolute errors on these distance moduli. Equation 6.1 supposes that the relative error on distance measurements is independent of distance and that the p.d.f. of the distance moduli (proportional to log distance) is Gaussian. The error on the global distance modulus is (e.g.

Table 6.1: Datasets contributing to elliptical sample

Method[a]	Authors	Band	rel. accuracy (rms)	Number
FP	Gavazzi et al. (1999)	H	0.41	41
$L-n$	Young & Currie (1995)	B_J	0.54	9
$R-n$	Young & Currie (1995)	B_J	0.54	14
SBF	Tonry et al. (2001)	I	0.18	31
SBF	Jensen, Tonry, & Luppino (1998)	I	0.07	6
SBF	Jensen, Tonry, & Luppino (1998)	K'	0.17	7
SBF	Neilsen & Tsvetanov (2000)	I	0.15	15
GCLF	Kundu & Whitmore (2001)	$V-I$	0.07	8

[a] FP = Fundamental Plane; $L-n, R-n$ = Luminosity / Sérsic shape and Radius / Sérsic shape relations; SBF = Surface Brightness Fluctuations; GCLF = Globular Cluster Luminosity Function.

Bevington & Robinson)

$$\sigma_d^2 = \frac{1}{\sum_i 1/\sigma_i^2} \ . \tag{6.2}$$

Table A.3 in Appendix A provides our final sample of 63 early-type galaxies.

Figure 6.1 shows a wedge diagram of the Virgo region with the early-types shown as circles and the spirals shown as triangles. One clearly notices the concentration of elliptical galaxies at a distance of $d \simeq 17\,\mathrm{Mpc}$, which is spread out in velocity space.

6.3 Picking isolated halos

Among the 12 halos that GALICS produces at $z = 0$ with $M_{\mathrm{FoF}} > 10^{14}\,M_\odot$, we wish to choose those that resemble the Virgo cluster, both in terms of mass and environment.

As we can see in the radial phase space diagrams of dark matter halos of the simulations (figure 5.1), it is quite common to find small groups around the main

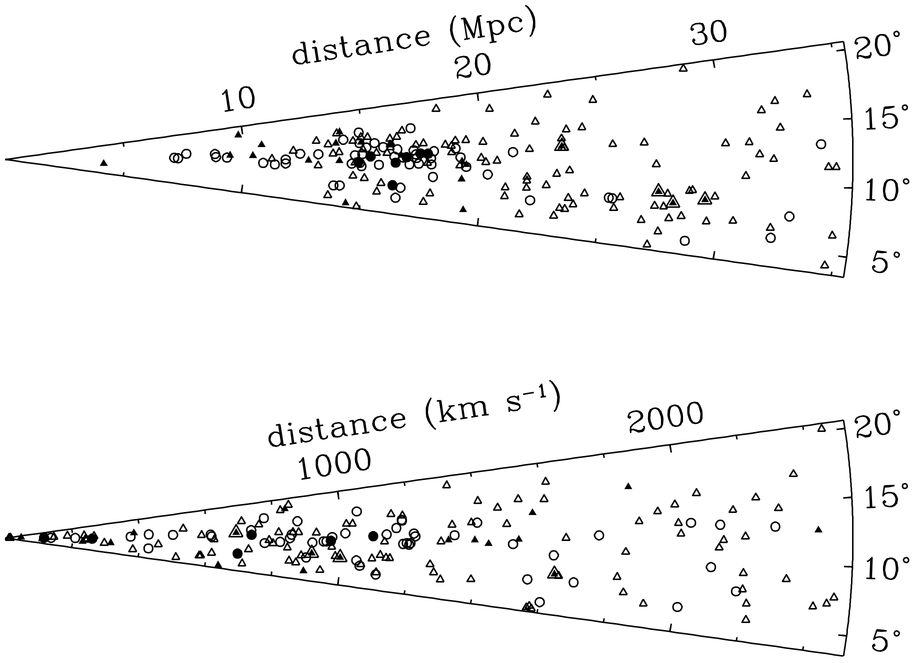

Figure 6.1: Positions of galaxies in Virgo field as a function of Declination and distance (assumed correct, *top*) and radial velocity (*bottom*). Spiral and elliptical galaxies are shown as *triangles* and *circles*, respectively. H I-deficient galaxies (deviating more than 3σ from normalcy) are shown as *filled triangles* — with the ones apparently behind the cluster shown as *surrounded filled triangles*, while Messier ellipticals (see table A.3) are shown as *filled circles*, with M49 to the South, and M59, M89, M60, M87, M86 and M84 at increasing distances (top plot) and M89, M59, M84, M60 and M87 at increasing radial velocities (bottom plot, M86 has $v < 0$).

cluster halo, whereas the Virgo cluster is not known to have massive neighbors, except for the M49 group just within the virial radius. Note that the size of the simulation box, $L = 150\,\mathrm{Mpc}$, implies, given the periodic boundary condition, a maximum separation between halos of $\sqrt{3}\,(L/2) = 130\,\mathrm{Mpc}$.

The effect of a neighboring halo will be from its tide on the test halo. The ratio of the tidal acceleration on a particle of the test halo at distance r from its center caused by a neighboring halo at distance R from the center of the first halo to the acceleration of this particle by the potential of its halo amounts to a mean density criterion:

$$a_{\rm tid} \approx \frac{G\,M_2(R)}{R^3}\,r \qquad (6.3)$$

and

$$a_{\rm halo} = \frac{G\,M_1(r)}{r^2} \qquad (6.4)$$

so that

$$\frac{a_{\rm tid}}{a_{\rm halo}} \approx \frac{\rho_2(R)}{\rho_1(r)} \ , \tag{6.5}$$

where the densities are average (and not local) and subscripts 1 and 2 stand for the central and the neighboring halo respectively. For clarity, we denote r_1, M_1, r_2 and M_2 the virial radii and masses for the test and neighboring halo, respectively (i.e. we drop the '100' subscript). Then, equating $r = r_1$, noting that the mean density at the virial radius is the same for each halo, i.e. 100 times the critical density of the Universe, and writing

$$\eta = \frac{R}{r_2} \ , \tag{6.6}$$

the influence of each neighbor is measured by the mean density of the neighbor measured at the center of the test halo

$$\begin{aligned} \rho_2(R) &= \frac{3\,M_2(R)}{4\,\pi\,R^3} \\ &\propto \frac{M_2(R)/M_2}{\eta^3} = \left\{\eta^3\left[\ln\eta - \eta/(1+\eta)\right]\right\}^{-1} \ , \end{aligned} \tag{6.7}$$

where we assumed Navarro, Frenk, & White (1997, hereafter NFW) density profiles and where the last equality is from Cole & Lacey (1996). Since the mean density is a monotonously decreasing function of radius (i.e. the function of η in equation 6.7 decreases with η), the most isolated halos will have the highest minimum values of η.

The output from GALICS includes the mass of each halo obtained from the FoF estimator, so that one can easily perform a first guess of which of the halos with mass close to that of Virgo are as isolated as the Virgo cluster appears to be. Table 6.2 lists for the 10 most massive halos in the simulation, the parameters of its most perturbing neighbor (that with the lowest value of η) using FoF quantities for radii and masses. Columns 2 to 4 list the virial radius, mass and circular velocity obtained using the more precise spherical overdensity (SO) method, which allow a direct comparison with the value we obtained for the Virgo cluster in Chapter 5.

As seen in table 6.2, the most perturbing halo is always inside $r_1^{\rm SO} \equiv r_{100}$. Therefore, it is not clear that we can easily estimate the exact virial radius and mass of each perturbing halo with the spherical overdensity method to produce a better estimate of isolated halos. As we expect $r_1^{\rm SO}$ to be approximately proportional to $r_1^{\rm FoF}$, we take the results of table 6.2 as good indicators of the degree of isolation of halos in the simulations.

Table 6.2: Most perturbing neighbors of 10 most massive halos in GALICS simulation

rank (FoF)	$r_1^{\rm SO}$ (Mpc)	$M_1^{\rm SO}$ ($10^{14}\,M_\odot$)	$v_1^{\rm SO}$ ($\rm km\,s^{-1}$)	$\frac{R}{r_1^{\rm SO}}$	$\frac{M_2^{\rm FoF}}{M_1^{\rm FoF}}$	$\eta_{\rm min}$
1	3.19	16.7	1503	0.55	0.011	3.7
2	2.42	7.4	1143	0.58	0.003	3.1
3	2.50	8.1	1180	0.55	0.020	2.4
4	2.54	8.5	1200	0.53	0.011	2.4
5	2.10	4.8	989	0.62	0.001	2.9
6	2.00	4.1	942	0.58	0.001	2.5
7	1.97	3.9	927	0.57	0.031	3.4
8	1.78	2.9	842	0.61	0.002	2.5
9	1.84	3.2	869	0.58	0.103	2.2
10	2.03	4.3	958	0.51	0.003	2.6

As shown in table 6.2, the most isolated halo in the simulations is halo 1, the most massive halo. Picking the most massive halo also ensures that no other massive halos will distort the mock velocity-distance relation.

6.4 Rescaling the simulations to the scales of the Virgo cluster

We now need to rescale the simulated clusters to Virgo. A reasonable way to put two halos in comparable units is to normalize distances with the virial radius, r_{100}, and velocities with the circular velocity of the halo at the virial radius, v_{100}. We therefore convert from the simulation frame to the Virgo cluster frame by rescaling the terms related to distance with the factor (omitting the '100' subscripts for clarity) $r_{\rm V}/r_{\rm s}$ and the terms related to velocities by the analogous factor $v_{\rm V}/v_{\rm s}$, where superscripts 's' and 'V' refer to the simulation and the Virgo cluster, respectively. We adopt the Virgo cluster virial radius and circular velocity derived in Chapter 5 from X-ray observations: $r_{\rm V} = 1.65\,h_{2/3}^{-1}\,{\rm Mpc}$, where $h_{2/3} = H_0/(66.7\,{\rm km\,s^{-1}\,Mpc^{-1}})$, and $v_{\rm V} = 780\,{\rm km\,s^{-1}}$.

Moreover, the N-body simulations give us comoving velocities $\mathbf{u}_\mathrm{s}$ of dark matter particles, to which we must add the Hubble flow. Therefore:

$$\begin{aligned} d &= d_\mathrm{s}\,\frac{r_\mathrm{V}}{r_\mathrm{s}} && (6.8) \\ v &= u_\mathrm{s}\,\frac{v_\mathrm{V}}{v_\mathrm{s}} + H_0\,d && (6.9) \end{aligned}$$

where u_s represents the comoving radial velocity of the particle in the simulation with respect to the observer in comoving units.

Inverting equation 6.8, we need to place the observer at a distance

$$d_\mathrm{obs} = d_\mathrm{V}\,\frac{r_\mathrm{s}}{r_\mathrm{V}} \qquad (6.10)$$

to the halo used to mimic the Virgo cluster (in simulation units). Once we have d_obs, we can select different observers by choosing different positions on a sphere of radius d_obs centered on the halo and assigning to each position, the mean velocity of the 10 nearest halos to the observer, so as to give the observer an appropriate peculiar velocity. As our galaxies in the Virgo cluster extend up to $d_\mathrm{max} = 50\,\mathrm{Mpc}$, we will need to use particles around the chosen dark matter halo up to a distance from the cluster of $d_\mathrm{max} - d_\mathrm{V} \simeq 20\,r_{100}$.

It is interesting to check the peculiar velocities (or equivalently the systemic velocities) found for the simulated observer relative to the simulated cluster and compare to that of our Local Group of galaxies relative to the Virgo cluster, after rescaling the simulation radial and velocity separations to the Virgo cluster attributes as in equations 6.8 and 6.9. For 500 observers placed at a given distance from the halo, but in different random directions, we find a systemic velocity between the halo and the observer (i.e. the mean of 10 nearest halos) in Virgo units of $998 \pm 118\,\mathrm{km\,s^{-1}}$ (errors are the $1\,\sigma$ dispersion) when we assume $d_\mathrm{V} = 16.8\,\mathrm{Mpc}$ (as suggested by the positions of the early-type galaxies in figure 6.1, and especially of M87, which lies at the center of the X-ray emission) and $1308 \pm 155\,\mathrm{km\,s^{-1}}$ when we assume $d_\mathrm{V} = 21\,\mathrm{Mpc}$, as obtained in Chapter 4. The values of the systemic velocity of the Virgo cluster in the literature range approximately between 900 and 1000 km $\mathrm{s^{-1}}$ (Teerikorpi et al. 1992). Therefore, putting the Virgo cluster at 16.8 Mpc, as indicated by the early type galaxies, gives a better match to the systemic velocity of the cluster. In addition, if we calculate the number of all galaxies (early-type and late-type ones) per distance bin, we find the maximum of the distribution between $16 - 18\,\mathrm{Mpc}$. Even if our sample lacks of completeness, this result, together with the previous ones, lead us to choose $d_{\rm V} = 16.8\,{\rm Mpc}$ for the comparison between the N-body simulations and the Virgo cluster.

6.5 Velocity-distance relation

We take all the objects lying within a cone of half-opening 9° aligned with the axis connecting the observer to the center of the halo.

Because observed galaxy catalogs, such as the VCC catalog of Virgo cluster galaxies (Binggeli et al. 1985), are magnitude-limited, we imposed upon our simulated catalog (of dark matter particles) the same magnitude limit as the VCC, namely $B < 18$. For this, we consider bins of distance to the observer, and, in each distance bin, we remove a fraction of dark matter particles equal to the predicted fraction of particles fainter than $B = 18$ given the distance and the Gaussian-shaped luminosity function of spiral galaxies derived by Sandage, Binggeli, & Tammann (1985). This method supposes that the luminosity function is independent of environment (i.e. distance to the center of the Virgo cluster) and that those VCC galaxies with redshift-independent distance measurements have the same magnitude limit as the VCC galaxies in general. This luminosity incompleteness is only noticeable at large distances, where it amounts to reducing less than 10%.

Figure 6.2 shows the velocity-distance plot of the simulated dark matter particles (*small points*), rescaled to Virgo units, and from which particles statistically fainter than the magnitude limit of the observed catalogs were removed. Superposed are the spiral galaxies (*triangles*) from table A.2 and the early-type galaxies (*circles*) compiled in table A.3. We have added to our sample the spiral galaxies compiled in Chapter 3 with reliable Tully-Fisher (Tully & Fisher 1977) distances but no H I data. We list these galaxies in table 6.3, with their coordinates, morphological type, systemic velocity and the final distance with errors assigned to it. We represent these objects as *squares* in figure 6.2.

Although figure 6.2 concerns a single observer and a single halo to represent the Virgo cluster (i.e. halo 1, which is the most isolated), the results are very similar for all halos studied as well as for any observer whose velocity with respect to the center of the main halo is similar to the mean of the 500 random trials. In other words, figure 6.2 provides a realistic general velocity-distance relation for a Virgo-

Table 6.3: Spiral galaxies without H I data

Galaxy		R.A.	Dec.	T	v_{sys}	d
VCC	NGC	(J2000)			(km s^{-1})	(Mpc)
132	—	$12^{\mathrm{h}}15^{\mathrm{m}}03\overset{\mathrm{s}}{.}9$	$+13^\circ01'55''$	8	1965	$10.76^{+2.60}_{-2.10}$
343	—	$12^{\mathrm{h}}19^{\mathrm{m}}22\overset{\mathrm{s}}{.}0$	$+07^\circ52'16''$	8	2336	23.77
912	4413	$12^{\mathrm{h}}26^{\mathrm{m}}32\overset{\mathrm{s}}{.}2$	$+12^\circ36'39''$	2	-13	$15.63^{+2.57}_{-2.20}$
952	—	$12^{\mathrm{h}}26^{\mathrm{m}}55\overset{\mathrm{s}}{.}5$	$+09^\circ52'58''$	5	853	$4.77^{+4.60}_{-3.88}$
1605	—	$12^{\mathrm{h}}35^{\mathrm{m}}14\overset{\mathrm{s}}{.}5$	$+10^\circ25'53''$	5	951	$24.66^{+6.82}_{-5.34}$
1673	4567	$12^{\mathrm{h}}36^{\mathrm{m}}32\overset{\mathrm{s}}{.}9$	$+11^\circ15'28''$	4	2133	26.30
1933	—	$12^{\mathrm{h}}42^{\mathrm{m}}44\overset{\mathrm{s}}{.}7$	$+07^\circ20'16''$	2	2271	$35.16^{+0.33}_{-0.32}$

like cluster in a flat Universe with a cosmological constant. Note that the groups visible in the 3D phase space plot (figure 5.1) are much less visible here and the projection places them at smaller distances from the center of the main cluster.

Figure 6.2 indicates that the velocity field drawn by the observed spirals is noticeably different from the one followed by the dark matter particles of the simulation. Nevertheless, the figure shows that 1) the center of the halo corresponds to the location of greater galaxy density (not only for the early-type galaxies used to mark the center of the Virgo cluster), 2) the thickness of the halo in velocity space (the velocity dispersion) corresponds to the corresponding thickness of the central observed galaxies, and 3) the majority of the elliptical galaxies outside the cluster also appear to fit well the location of the particles in the outer infalling/expanding locus. These three facts suggest that both the distance to the halo and the rescaling factors are well chosen and that the differences between the Virgo cluster and the halo in the simulation should be attributable to errors arising from the distance estimates (as the velocity errors are negligible). It appears unlikely that the galaxies that, for a given distance, lie within more than $1000\,\mathrm{km\,s^{-1}}$ from the locus of dark matter particles belong to the low- or high-velocity tails of large velocity dispersion groups near the cluster, since in our simulations, there are no such high velocity dispersion groups outside the main cluster.

Given that most of the galaxies outside the velocity field drawn by dark matter particles are spirals, we now build a new velocity-distance diagram of our simulated particles incorporating the mean relative distance error for the spiral galaxy sample.

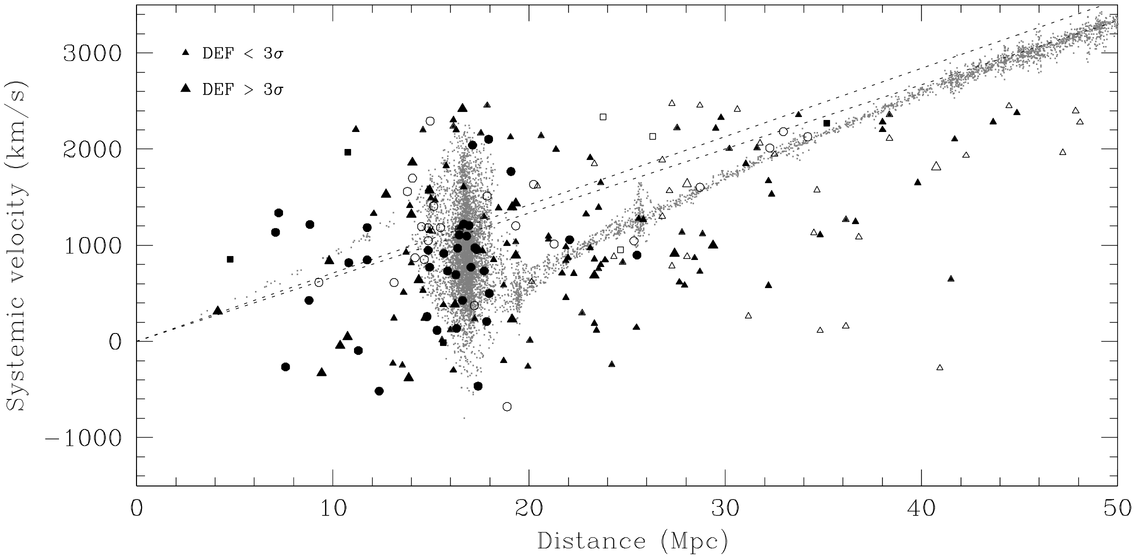

Figure 6.2: Simulated and observed velocity-distance diagrams. *Dots* represent the velocity field traced by the particles in the cosmological N-body simulation. Superposed are galaxies of the Virgo cluster. *Circles* and *triangles* represent early-type and late-type galaxies, respectively. The size of the triangles is proportional to the H I deficiency of the spiral galaxies measured in units of the mean standards deviation for field objects (= 0.24). *Squares* represent additional spiral galaxies with no H I deficiency data. *Open symbols* indicate galaxies with uncertain distances (with distance errors greater than 5 Mpc or spirals with only one distance estimate). *Dashed* lines show the unperturbed Hubble flow with $H_0 = 66.7$ and $70\,\mathrm{km\,s^{-1}\,Mpc^{-1}}$, respectively (going upwards).

In Chapter 3, we combined different studies of the TF relation to calculate the distances of spirals in the Virgo cluster. These studies give dispersions of the TF relation of roughly 0.4 mag., corresponding to an uncertainty of 18% in relative distance. Figure 6.3 shows the corresponding velocity-distance plot for our simulated Virgo line of sight, with inclusion of Gaussian relative distance errors with $\sigma(\ln d) = 0.20$ (a slightly more conservative value than 0.18). We omit particles beyond 40 Mpc, which corresponds to the distance (before folding in the distance errors) where the particles have a systemic velocity approximately equal to the maximum of the observed galaxy sample.

Figure 6.3 indicates that the inclusion of distance errors, at the 20% relative rms level, allows us to reproduce fairly well the observed velocity-distance diagram. There are still several galaxies that lie far outside the general locus of the dark matter particles. Among them are two galaxies (VCC 319, which is part of a

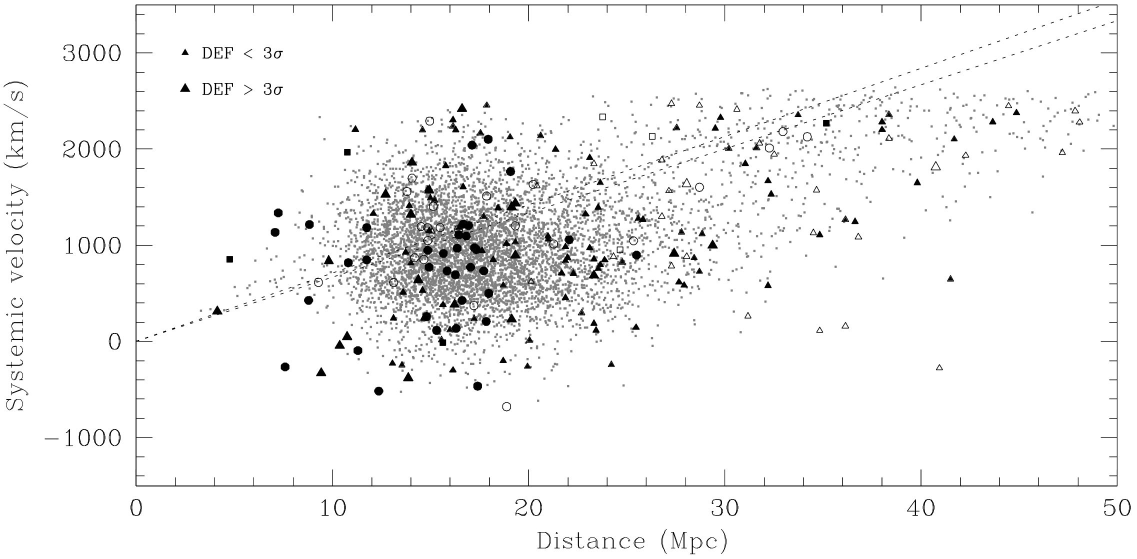

Figure 6.3: Same as figure 6.2, but incorporating Gaussian relative distance errors of $\sigma(\ln d) = 0.2$ for the dark matter particles.

galaxy pair and M90 = NGC 4569 = Arp 76, which is tidally perturbed by a close neighbor) apparently in the foreground of the cluster between 7 and 10 Mpc and with $v < -200\,\mathrm{km\,s^{-1}}$, and four galaxies (IC 3094, NGC 4299, which is part of a pair, NGC 4253 and VCC 1644) in the background between 34 and 42 Mpc and $v < 800\,\mathrm{km\,s^{-1}}$. Inspection of figure 6.2 indicates that these four galaxies are at more than $2000\,\mathrm{km\,s^{-1}}$ from the expected locus of the Tolman-Bondi pattern given negligible distance errors. It is highly unlikely that the peculiar velocities in interacting pairs can reach values as high as $2000\,\mathrm{km\,s^{-1}}$, hence the distances to these galaxies appear to be grossly incorrect.

We list the most discrepant galaxies in table 6.4. Most of these galaxies have a single distance measurement (the elliptical VCC 319 has a single Sérsic fit distance estimator, which is known to be inaccurate — see table A.3). However, it is a surprise to find a bright object such as M90 in this list, especially since it has 6 different Tully-Fisher distance measurements, 5 of which yield a distance between 7.9 and 10.2 Mpc and one (Gavazzi et al. 1999) giving $d = 16.1\,\mathrm{Mpc}$, which is what we expect from figure 6.2.

Since the 20% relative errors correctly reproduce the envelope of particles from the cosmological simulation, increasing the relative rms error to say 30% will not explain the distances to these discrepant spirals. We therefore conclude that the

Table 6.4: Grossly incorrect galaxy distances

Galaxy		R.A.	Dec.	T	v_{sys}	d
VCC	NGC	(J2000)			$(\mathrm{km\,s^{-1}})$	Mpc
213	—	$12^{\mathrm{h}}16^{\mathrm{m}}56.^{\mathrm{s}}0$	$+13^\circ37'33''$	5	-278	40.9
319	—	$12^{\mathrm{h}}19^{\mathrm{m}}01.^{\mathrm{s}}7$	$+13^\circ58'56''$	-4	-256	7.6
491	4299	$12^{\mathrm{h}}21^{\mathrm{m}}40.^{\mathrm{s}}9$	$+11^\circ30'03''$	8	112	34.8
1524	4523	$12^{\mathrm{h}}33^{\mathrm{m}}48.^{\mathrm{s}}0$	$+15^\circ10'05''$	9	158	36.1
1644		$12^{\mathrm{h}}35^{\mathrm{m}}51.^{\mathrm{s}}8$	$+13^\circ51'33''$	9	646	41.5
1690	4569	$12^{\mathrm{h}}36^{\mathrm{m}}49.^{\mathrm{s}}8$	$+13^\circ09'48''$	2	-328	9.4

VCC 1690 = NGC 4569 = M90 = Arp 76.

distances of the galaxies listed in table 6.4 must be highly inaccurate.

6.6 Tolman-Bondi estimates of the Virgo cluster mass and distance

In Chapter 4, we only used to fit the parameters of our dynamical model of the Virgo Region those spiral galaxies believed to trace the outer envelope of galaxies expanding out of the Virgo cluster. Figure 6.2 clearly indicates that the galaxies we used (roughly aligned between distances of 34 and 45 Mpc) lie at typically $600\,\mathrm{km\,s^{-1}}$ lower velocities for their distance than predicted by our simulated velocity-distance model. Figure 6.3 suggests that the alignment of these galaxies in the velocity-distance plot may be fortuitous, given the $\sim 20\%$ relative distance errors. This fortuitous alignment forced the fit of the parameters of the model to shift the center of the Virgo cluster to greater distances.

We now use the cosmological N-body simulations to quantify the errors on the distance and mass to the Virgo cluster obtained by fitting a Tolman-Bondi model to the velocity-distance data outside the cluster core. We construct simulated pseudo-galaxy samples by randomly selecting as many points from the cosmological N-body simulation as there are galaxies in the Virgo cluster sample. We apply fixed relative distance errors in the range 0%–30% and, for each relative distance error, we construct 50 realizations of the Virgo sample. We identify pseudo-galaxies presumably

Table 6.5: Best fitting parameters for each dataset

Error	$R_{\rm VIC}$ (Mpc)		$\log(M_{\rm VIC})$ ($\rm M_\odot$)		t_0 (Gyr)
	mean	σ	mean	σ	
0%	16.7	0.5	14.5	0.2	14.1
5%	16.8	0.5	14.6	0.3	13.9
10%	16.9	0.6	14.9	0.4	12.8
15%	17.0	0.8	15.1	0.5	12.1
20%	17.1	0.9	15.5	0.5	10.1
25%	17.1	1.0	15.7	0.4	9.0
30%	17.1	1.0	16.1	0.5	6.7

belonging to the core by building histograms of the number of pseudo-galaxies per 2 Mpc distance bin. Such histograms peak at the core of the halo, in a region of width ~ 4 Mpc for the no error set and up to ~ 12 Mpc for the 30% error set. We avoid the virialized core by only considering, for the fitting of the parameters of the model, pseudo-galaxies lying on the back side of the identified cluster core.

As in Chapter 4, we have fixed $V_{\rm VIC}$ to the mean velocity of the main halo for the 50 realizations (998 km s^{-1} for a distance of 16.8 Mpc, see Section 6.4) and we have allowed $M_{\rm VIC}$ and $R_{\rm VIC}$ to vary freely. The resulting t_0 will help us to see the viability of our results.

Table 6.5 shows the results of the fits to the point-mass Tolman-Bondi relation for the different sets. For zero distance errors, the model reproduces fairly well the input data of $R_{\rm VIC} \equiv d_{\rm V} = 16.8\,{\rm Mpc}$. With respect to $M_{\rm VIC}$, we obtain $M_{\rm VIC} = 1.4 M_{100}$, in agreement with the results of Section 5.6, where we showed that a point mass model with a central mass of $\sim 1 - 2M_{100}$ is able to reproduce the velocity field drawn by clusters. The values for $R_{\rm VIC}$ and $M_{\rm VIC}$ obtained result in an age of the Universe in agreement with the value $t_0 = 13.7\,{\rm Gyr}$ from the GALICS cosmological simulations (which happens to perfectly match the age recently obtained by Spergel et al. 2003 from the WMAP CMB experiment). The table also clearly indicates that the errors in distance contribute to a slightly larger distance to the cluster (by up to 2%), combined with a much larger mass for the cluster (up to a factor 40!). This dramatic rise in the mass decreases the resulting t_0 to unacceptably low values.

For the case of real data on the Virgo cluster, the same fitting procedure leads to $M_{\rm VIC} \sim 3 \times 10^{16}\, M_\odot$ and $R_{\rm VIC} \sim 17.4\,{\rm Mpc}$, which imply $t_0 = 5.2$ Gyr. Note that the present fitting procedure takes into account all galaxies beyond the identified core of the cluster, whereas in Chapter 4, we only used those galaxies that are aligned between distances of 34 and 45 Mpc in the velocity-distance plot, deducing a very different distance to the Virgo cluster (between 20 and 21 Mpc). The comparison of the values of t_0 from the real data and from the simulated data convolved with different relative distance errors, suggests that the TF distances may have up to 30% relative errors.

6.7 Summary and conclusions

In this chapter we have analyzed the structure of the Virgo velocity field drawn by both the early-type and the late-type population. We have used cosmological N-body simulations to mimic the velocity-distance relation around the cluster. Adding 20% relative distance errors to the dark matter particles, we have been able to reproduce the main features of the velocity-distance relation towards the Virgo cluster. In addition, we have shown that such distance errors can cause the fitting of Tolman-Bondi solutions to the velocity vs. distance of galaxies to yield incorrect cluster parameters. Nevertheless, the estimation of the distance to the cluster provided by the point mass model is relatively good even for appreciable errors in distances. Therefore, one could still obtain a reasonable value for the mass of the cluster by taking $R_{\rm VIC}$ from the fit (i.e., 17.4 Mpc), together with $V_{\rm VIC} = 980$ km s^{-1} (Teerikorpi et al. 1992) and $t_0 = 13.7$ Gyr (Spergel et al. 2003) as input parameters for the model and computing $M_{\rm VIC}$ as a result. In this way, we obtain a value of $M_{\rm VIC} = 7 \times 10^{14}\, M_\odot$ in good agreement with other studies.

7 On the origin of H I deficiency in galaxies on the outskirts of the Virgo cluster

7.1 Introduction

In Chapter 5, we have estimated the maximum radius out to where galaxies falling into a cluster can bounce out. We found that this maximum rebound radius goes from ~ 1 to ~ 2.5 cluster virial radii. After estimating the virial radius of the Virgo cluster using X-ray observations, we concluded that the H I-deficient galaxies located in the foreground or background of the cluster found in Chapter 3 appear to lie much farther from the center of the cluster, implying that ram pressure stripping cannot account for the H I deficiency of these outlying galaxies if their distances are correct.

In this chapter, we investigate in further detail the possible origin of the H I deficiency in the spiral galaxies that appear too far from the Virgo cluster to have suffered ram pressure stripping of their interstellar gas. Using our compilation of the literature for elliptical galaxies towards Virgo (see Section 6.2), which allows us to identify more precisely the density of the environment of the background deficient galaxies, and the results of the previous chapters, we examine different alternatives for the presence of these H I-deficient galaxies outside the core of Virgo:

1. very inaccurate distances (perhaps from the inadequacy of the Tully Fisher relation for galaxies undergoing ram pressure or tidal stripping) for galaxies that are in fact within the Virgo cluster (in the core or more probably coming

Table 7.1: H I-deficient galaxies possibly outside the Virgo cluster

Galaxy	R.A.	Dec.	T	D_{25}	θ	$v_{\rm sys}$	d	$< DEF >$	DEF	N	P_1	$P_{2.5}$
	(J2000)					(km s^{-1})	(Mpc)					
N4064	$12^{h}04^{m}11^{s}.8$	$18^{\circ}26'33''$	1	$4'.0$	$8^{\circ}.8$	837	9.8	1.39	1.19	942	0.00	0.81
N4305	$12^{h}22^{m}03^{s}.5$	$12^{\circ}44'27''$	1	$2'.0$	$2^{\circ}.2$	1814	40.7	0.92	0.95	200	0.00	0.00
N4307	$12^{h}22^{m}06^{s}.3$	$09^{\circ}02'27''$	3	$3'.5$	$4^{\circ}.0$	913	27.4	1.16	1.24	1846	0.41	0.48
N4312	$12^{h}22^{m}32^{s}.0$	$15^{\circ}32'20''$	2	$4'.7$	$3^{\circ}.7$	47	10.8	1.19	1.02	754	0.95	1.00
N4356	$12^{h}24^{m}15^{s}.9$	$08^{\circ}32'10''$	6	$2'.6$	$4^{\circ}.2$	998	29.4	1.28	1.35	1377	0.19	0.23
N4424	$12h27^{m}13^{s}.3$	$09^{\circ}25'13''$	1	$3'.4$	$3^{\circ}.1$	314	4.1	1.32	0.76	106	0.00	0.00
N4438	$12^{h}27^{m}46^{s}.3$	$13^{\circ}00'30''$	1	$8'.7$	$1^{\circ}.0$	–45	10.4	0.73	0.84	755	1.00	1.00
N4492	$12^{h}30^{m}58^{s}.9$	$08^{\circ}04'41''$	1	$1'.9$	$4^{\circ}.3$	1638	28.1	0.85	0.78	1261	0.08	0.11
V1569	$12^{h}34^{m}31^{s}.4$	$13^{\circ}30'23''$	6	$0'.8$	$1^{\circ}.4$	687	23.3	0.90	0.85	8967	0.72	0.94
N4569[a]	$12^{h}36^{m}50^{s}.5$	$13^{\circ}09'54''$	2	$10'.5$	$1^{\circ}.7$	–328	9.4	1.13	1.26	143	1.00	1.00
N4580	$12^{h}37^{m}49^{s}.5$	$05^{\circ}22'09''$	2	$2'.0$	$7^{\circ}.2$	893	19.3	1.17	1.05	8724	0.00	0.84
N4586	$12^{h}38^{m}28^{s}.1$	$04^{\circ}19'09''$	1	$3'.9$	$8^{\circ}.3$	639	14.4	1.15	1.06	4657	0.00	0.98
N4606	$12^{h}40^{m}57^{s}.7$	$11^{\circ}54'46''$	1	$2'.9$	$2^{\circ}.5$	1528	12.7	1.25	1.00	7648	0.95	1.00

[a] NGC 4569 is also M90.

out) and which would have lost some of their gas by ram pressure stripping from the intracluster gas;

2. tidal interactions from members of a same group;
3. tidal interactions from neighbors;
4. recent mergers;
5. overestimated H I deficiency in early-type spirals.

7.2 H I-deficient galaxies in the outskirts of the Virgo cluster

As mentioned above and clearly seen in figure 6.2, there is a non negligible number of H I-deficient galaxies distant from the cluster core, in particular at distances of 10 and 28 Mpc from the Local Group. In table 7.1 are listed all galaxies from the compilation of Chapter 3 (table A.2) with H I deficiencies deviating more than $3\,\sigma$ from normalcy (i.e. DEF > 0.72) which satisfy at least one of the following criteria:

- $d < 13\,\mathrm{Mpc}$,
- $21 < d < 50\,\mathrm{Mpc}$,
- $\theta/\theta_{100} > 1$,

where d is the distance to the Local Group, θ is the angular distance to M87 and $\theta_{100} = r_{100}/D_\mathrm{V} = 5\overset{\circ}{.}6$ is the angular virial radius of the Virgo cluster. Column (1) gives the galaxy name and the coordinates come in columns (2) and (3). The galaxy type is in column (4), the optical diameter in column (5), the projected distance to M87 in units of the virial radius of the cluster in column (6), and the velocity relative to the Local Group in column (7). Column (8) gives the adopted distance and columns (9) and (10) the H I deficiency measured with the two estimators described in Chapter 3. The last three columns of table 7.1 are explained in Section 7.3.

7.3 Inaccurate distances

If one wishes to explain the outlying H I-deficient galaxies as galaxies that have lost their interstellar gas by its stripping by ram pressure from the hot intracluster gas, then these galaxies must have passed through the core of the Virgo cluster where the intracluster gas is dense and the galaxy velocities large so that the ram pressure is largest.

We have found in Chapter 5 that objects that have passed through the core of a structure in the past cannot be at distances greater than 1–2.5 virial radii from the cluster today. With the estimate performed in Chapter 6 of the distance (16.8 Mpc) and the virial radius (1.65 Mpc) of Virgo, this means that galaxies that have passed through the core of Virgo cannot lie at a distance from the Local Group greater than 18.5 or 20.9 Mpc (for $r_\mathrm{reb}/r_{100} = 1$ or 2.5, respectively) nor can they lie closer than 15.1 or 12.7 Mpc from the Local Group.

For the 3 H I-deficient spirals at 28 Mpc to have passed through the core of Virgo, one would require that their distances be each overestimated by 52% (34%), which corresponds to $2.3\,\sigma$ ($1.6\,\sigma$) events for their distance moduli, for $r_{\rm reb}/r_{100} = 1$ (2.5), respectively. Such errors are possible, as shown in Chapter 6. Note that none of the distances of the 13 galaxies listed in table 7.1 are based upon Cepheid measurements, which are much more precise than Tully-Fisher estimates. On the other hand, given the presence in our sample of some spirals with grossly incorrect distances, one may wonder if the distances to the 3 spirals at 28 Mpc could also be grossly incorrect: they could lie at the cluster distance of 16.8 Mpc, thus leading in this case to distances overestimated by 66%, which for 20% rms relative errors correspond to three $2.8\,\sigma$ events for their distance moduli, which appears unlikely.

Similarly, the three foreground H I-deficient spirals at ~ 10 Mpc could have bounced out of the core of the Virgo cluster, as they lie on the outer edge of the envelope of the particles after inclusion of 20% rms distance errors in figure 6.3. Indeed, were they bouncing out of the Virgo cluster in the foreground at 15.1 (12.7) Mpc, one would then have three cases of 34% (21%) errors, each corresponding to $-2.3\,\sigma$ ($-1.3\,\sigma$) events for their distance moduli, for $r_{\rm reb}/r_{100} = 1$ (2.5), respectively. Alternatively, they could lie in the cluster proper, at 16.8 Mpc, which would correspond to three $-2.8\,\sigma$ events for their distance moduli, which again appears unlikely.

The offset of a galaxy relative to the Tolman-Bondi locus in figure 6.2 can be caused by a large distance error or a large peculiar velocity relative to the general flow at that distance, or a combination of both. To see which effect is more important, one can consider the N simulated particles with distance (with errors folded in) and velocity respectively within 3 Mpc and $200\,{\rm km\,s^{-1}}$ of each galaxy in table 7.1 , as well as angular distance to the halo center within $1\overset{\circ}{.}5$ of that of the galaxy relative to M87, and ask what fractions P_1 and $P_{2.5}$ of these particles were located (before the distance errors were folded in) within 1 or 2.5 times the virial radius of the halo, respectively. These fractions must be taken with caution, because the groups falling in or moving out of the Virgo cluster are at different distances and with different relative masses between the simulations and the observations. For example, a true group of galaxies in the background of the Virgo cluster will end up with too high values of P_1 and $P_{2.5}$ if there is no group at the same distance in the simulations, while a Virgo cluster galaxy with a measured distance of 10 Mpc or so beyond the cluster will have too low values of P_1 and $P_{2.5}$ if the simulations include a group at a distance close to this measured distance. Nevertheless, P_1 and $P_{2.5}$ should provide interesting first order constraints.

Of course, this method of locating galaxies, implies that galaxies NGC 4064, NGC 4580 and NGC 4586, at angular distances from M87 beyond $\theta_{100} = 5\overset{\circ}{.}6 + 1\overset{\circ}{.}5 = 7\overset{\circ}{.}1$ have $P_1 = 0$. Interestingly, all three galaxies are likely to be within $2.5\, r_{100}$.

Among the 5 foreground galaxies with $\theta < 7\overset{\circ}{.}1$, NGC 4312, NGC 4438, M90 and NGC 4606 are all likely to be in the Virgo cluster and all very likely to be close enough that they may have passed through its core. Only NGC 4424, apparently at distance 4.1 Mpc, is too close to the Local Group to actually be located within 2.5 virial radii from the Virgo cluster.

Among the 5 background galaxies with $\theta < 7\overset{\circ}{.}1$, all but NGC 4305, lying at 40 Mpc, have a non negligible probability of having crossed the cluster. Moreover, VCC 1569 measured at 23 Mpc is highly likely to be located within the virial radius of the Virgo cluster. Interestingly, the 3 galaxies at measured distances around 28 Mpc have very different values of P_1 and $P_{2.5}$. The closest one, NGC 4307, has one chance in two of being located near the cluster and 40% probability of being within the cluster itself. However, the furthest one, NGC 4356, has one chance in 5 of belonging to the Virgo cluster and less than one chance in four of being within 2.5 virial radii. The third one, NGC 4492, has only one chance in 9 of being within 2.5 virial radii of the Virgo cluster. This low probability is not surprising, given that it is located close to the infall/expansion zone of figure 6.2.

7.4 Interactions within small groups

Figure 7.1 shows the environment of the H I-deficient galaxies in three equal logarithm distance bins, $\pm 1.28 \times \sigma(\ln d) \equiv 1.28 \times 0.2$ wide, centered around 10 Mpc (the apparent distance to the foreground H I-deficient galaxies), 16.8 Mpc (the distance to the Virgo cluster) and 28 Mpc (the apparent distance to the background H I-deficient galaxies), as well as in three radial velocity bins, $\pm 1.28 \times \sigma_v$ wide (with a value for σ_v, which we took as the velocity dispersion of the elliptical sample, equal to 674 km s^{-1}). The log distance (velocity) bins are chosen wide enough that if the parent distribution function of the log distance (velocity) errors were Gaussian, one would have a probability $2\,\mathrm{erf}(1.28) - 1 = 0.86$ of having a galaxy with a true distance (velocity) within the interval appearing to lie at the center of the interval. Note that, among the outlying H I-deficient galaxies in table 7.1, neither NGC 4424, at $d = 4.1$ Mpc, nor NGC 4305, at $d = 40.7$ Mpc, appear in the left plots, as their distances are outside the explored distance range.

Among the 5 foreground H I-deficient spirals in the left plots, 4 (NGC 4312, NGC 4438, M90, which, as noted in Chapter 6, is far off the Tolman-Bondi relation, and NGC 4606), appear superposed (within the dotted circle in upper-left plot) with the galaxies at the distance of the main structure of the Virgo cluster, which suggests that their distances may be seriously underestimated, unless there happens to be a group of galaxies precisely along the line of sight to the center of Virgo lying at 10 Mpc.

One may be tempted to identify the 3 H I-deficient spirals close to M87 (NGC 4438, M90, and NGC 4606) with a group of ellipticals seen in the upper-left plot of figure 7.1. The velocity dispersion of this group would explain why these 3 galaxies are so far off the Tolman-Bondi solution given in figure 6.2. However, none of the ellipticals in this region have accurate ($< 38\%$) relative distance estimates (cf. table A.3) and some or all may actually belong to the Virgo cluster.

Interestingly, 3 of the 4 H I-deficient spirals at 28 Mpc (NGC 4307, NGC 4356 and NGC 4492) lie in a dense region, extending to the SSW of the position of M87 (lower-left plot), which is also seen in the middle distance bin (middle-left plot, corresponding to the distance to M87), but with 3 times fewer galaxies. Although the eastern edge of the region, and particularly the H I-deficient NGC 4492, coincide with the position of M49 (NGC 4472), it appears distinct from M49, which roughly lies at the middle of a group of galaxies (middle-left plot) that does not seem to be associated with the dense region at 28 Mpc (lower-left plot).

We now compare the Tully-Fisher distance estimator with the redshift distance estimator $d_v = v/H_0$. If a structure outside of the Virgo cluster lies at a distance d within a region with 1D velocity dispersion σ_v, the error on the distance estimator $d_v = v/H_0$ will be set by the dispersion of the peculiar velocities:

$$\delta d_v = \sigma_v/H_0 \ . \tag{7.1}$$

The redshift distance estimator d_v will be more accurate than the direct distance estimator when

$$H_0\, d > \frac{\sigma_v}{\delta d/d} \ , \tag{7.2}$$

where $\delta d/d$ is the relative error of the direct distance estimator. For Tully-Fisher distance measurements, $\delta d/d \simeq 20\%$ and a field velocity dispersion of $200-300\,\mathrm{km\,s^{-1}}$,

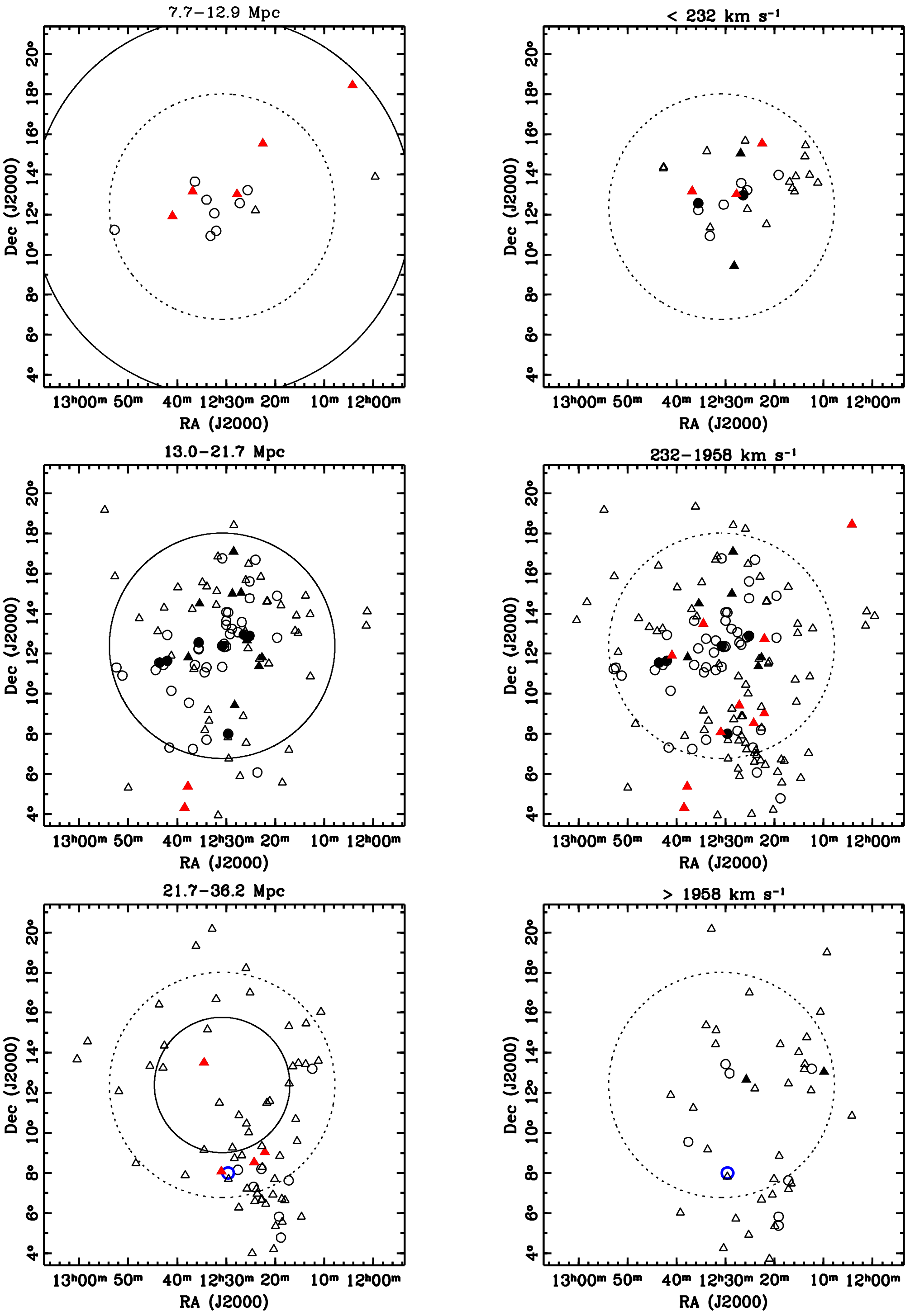

Figure 7.1: Positions of galaxies within 9° of M87 in 3 distance (*left*) and velocity (*right*) bins. Ellipticals and spirals are shown as *circles* and *triangles*, respectively. Messier ellipticals are shown as *filled circles*, while M49 (NGC 4472) is also highlighted as a *blue circle* (bottom plots). H I-deficient ($> 3\,\sigma$) spirals are shown as *filled symbols*, with outlying galaxies (table 7.1) in red. The *large solid circles* show the virial radius r_{100} at the different distance bins, while the *large dotted circles* indicates r_{100} at the distance to M87.

equation 7.2 yields a maximum distance for believing individual direct distances of 14 to 21 $h_{2/3}^{-1}$ Mpc, so that individual galaxy distances of 28 Mpc are less reliable than redshift distance estimators.

This change in optimal distance estimators is noticeable in figure 6.1, where only one of the background H I-deficient galaxies has a radial velocity much larger than the mean of the Virgo cluster. The three plots on the right of figure 7.1 show that the structure to the South-Southwest (SSW) of the Virgo cluster is present in the last two intervals of radial velocity. Of the 3 background H I-deficient galaxies to the SSW of M87, only one (NGC 4307) has a reasonably high chance of being located in or near the Virgo cluster, while one (NGC 4356) has only one chance in 4 of being in or near the cluster (from the analysis of Section 7.3), and one (NGC 4492) has a radial velocity indicative of a background object expanding away from the Virgo cluster (this galaxy shows up as the empty triangle in figure 6.2 very close to the Tolman-Bondi locus), and has only roughly one chance in 9 of being even close to the cluster. However, most of the projected neighbors to these 3 galaxies do lie at cluster radial velocities. But the analysis of P_1 and $P_{2.5}$ of Section 7.3 should be superior to the analysis of figure 7.1, because it takes into account the correlation of distance and velocity.

7.5 Interactions from companions or mergers

According to a search in SIMBAD, we find that (at least) 4 of the 13 H I-deficient galaxies in table 7.1 have companions whose mass and proximity may generate tides that could remove some of the neutral hydrogen, either by stripping the gas beyond the optical radius (without stripping the stars, thus leaving an H I deficiency) or by heating the gas. Of course, the presence of a companion in projection, even with a similar velocity, does not guarantee that this companion is in physical interaction with the galaxy in question, as projection effects are important in clusters.

Table 7.2 shows the properties of the companions to these 4 galaxies. Column 5 is the difference in velocity relative to the Local Group; column 6 is the difference in extinction-corrected total I-band magnitude; column 7 is the angular distance between the two components, in units of the optical radius ($D_{25}/2$) of the major member; columns 8 and 9 are indicators for morphological (see Section 7.6) and kinematical (Rubin, Waterman, & Kenney 1999) disturbances (R $\rightarrow$ regular, I $\rightarrow$

Table 7.2: Companions to H I-deficient galaxies in the outskirts of Virgo

Galaxy		Companion		Δv	Δm_T^c	$d/r_{\rm opt}$	M	K
VCC	NGC	VCC	NGC	(km s^{-1})				
522	4305	523	4306	−380	0.9[a]	2.8	R?	—
1043	4438[b]	1030	4435	−214	1.0	1.0	I	I
1690	4569[c]	1686[d]	—	1354	4.2	1.1	R	R
1859	4606	1868	4607	593	0.6	2.7	I?	—

[a] B-band; [b] also Arp 120; [c] also M90 and Arp 76; [d] also IC 3583.

irregular) for the major component.

Table 7.2 indicates that NGC 4438 has a very close major companion, which is likely to be responsible for its irregular morphology and internal kinematics. NGC 4305 and NGC 4606 have moderately close major companions. M90 has a close very minor ($\approx 1/50$ in mass) companion.

Moreover, NGC 4307 and NGC 4356 are close in 4D space: their projected separation (at the distance of M87) is 215 kpc and their velocity difference is 85 km s^{-1}, so they may constitute an interacting pair. Similarly, NGC 4580 and NGC 4586 are at a projected separation of 311 kpc with a velocity difference of 254 km s^{-1}, so they too may constitute an interacting pair.

Finally, two other galaxies in table 7.1 have unusually low inner rotation (Rubin et al. 1999): NGC 4064 and NGC 4424. Kenney et al. (1996) argue that NGC 4424 has undergone a merger with a galaxy 2 to 10 times less massive and presumably the same can be said for NGC 4064.

7.6 Errors in H I deficiency

As we saw in Chapter 3, the H I deficiency estimator has been defined by several authors (e.g. Chamaraux et al. 1980; Haynes & Giovanelli 1984; Solanes et al. 1996) as the hydrogen mass relative to the mean for field galaxies of the same morphological type and optical diameter. In Chapter 3, we applied a different H I deficiency estimator based on the hybrid mean surface brightness expected for each galaxy type independently of its diameter, which has the advantage of being independent of the distance to the galaxies.

Could the seemingly H I-deficient galaxies in the foreground and background of Virgo have normal gas content according to one definition but appear deficient with the other one? In Section 3.3 we checked the statistical agreement of these two H I deficiency estimators without finding any significant discrepancy (see figure 3.2). From table 7.1, we can confirm that the outlying galaxies present H I deficiencies larger than $3\,\sigma$ with both definitions of H I deficiency.

However, table 7.1 clearly shows that 7 out of our 13 H I-deficient possible outliers appear to be Sa galaxies ($T = 1$), some of which might be misclassified S0/a or even S0 galaxies, which are known to have little cold gas. The stronger H I deficiency of early-type spirals in the Virgo cluster has been already noticed by Guiderdoni & Rocca-Volmerange (1985). Some of these Sa galaxies may not be deficient relative to field S0/a or S0 galaxies. Indeed, the most recent study (Bettoni, Galletta, & García-Burillo 2003) of the H I content of galaxies as a function of morphological type indicates that the logarithm of the H I mass normalized to luminosity or to square optical diameter decreases increasingly faster for earlier galaxy types, therefore its slope for Sa's is considerably larger than for Sc's, and hence S0/a galaxies misclassified as Sa's will appear more H I-deficient than later-type galaxies misclassified by one-half of a morphological type within the Hubble sequence.

Moreover, independent estimates of morphological types by experts led to $\sigma(T) = 1.5$ (rms) for galaxies with optical diameters $> 2'$ (Naim et al. 1995). The galaxies listed in table 7.1 have optical diameters ranging from $2'$ to $10'$ plus one (VCC 1569) with $D = 0\overset{\prime}{.}8$. There are two galaxies (NGC 4305 and NGC 4492) with $T = 1$ and $D \leq 2'$, i.e. where the uncertainty on T is probably as high as 1.5.

On can see from table 7.1, that, for example, NGC 4424 and NGC 4492 are marginally H I-deficient and therefore prime candidates for losing their status of gas-deficient if they are misclassified lenticulars (by $\Delta T = 1$, the typical scatter given by HyperLEDA).

We must thus resort to visualizing the possibly misclassified galaxies. Figure 7.2 displays the snapshots of the 7 H I-deficient outliers classified as Sa ($T = 1$). We now discuss the morphologies of these 7 galaxies.

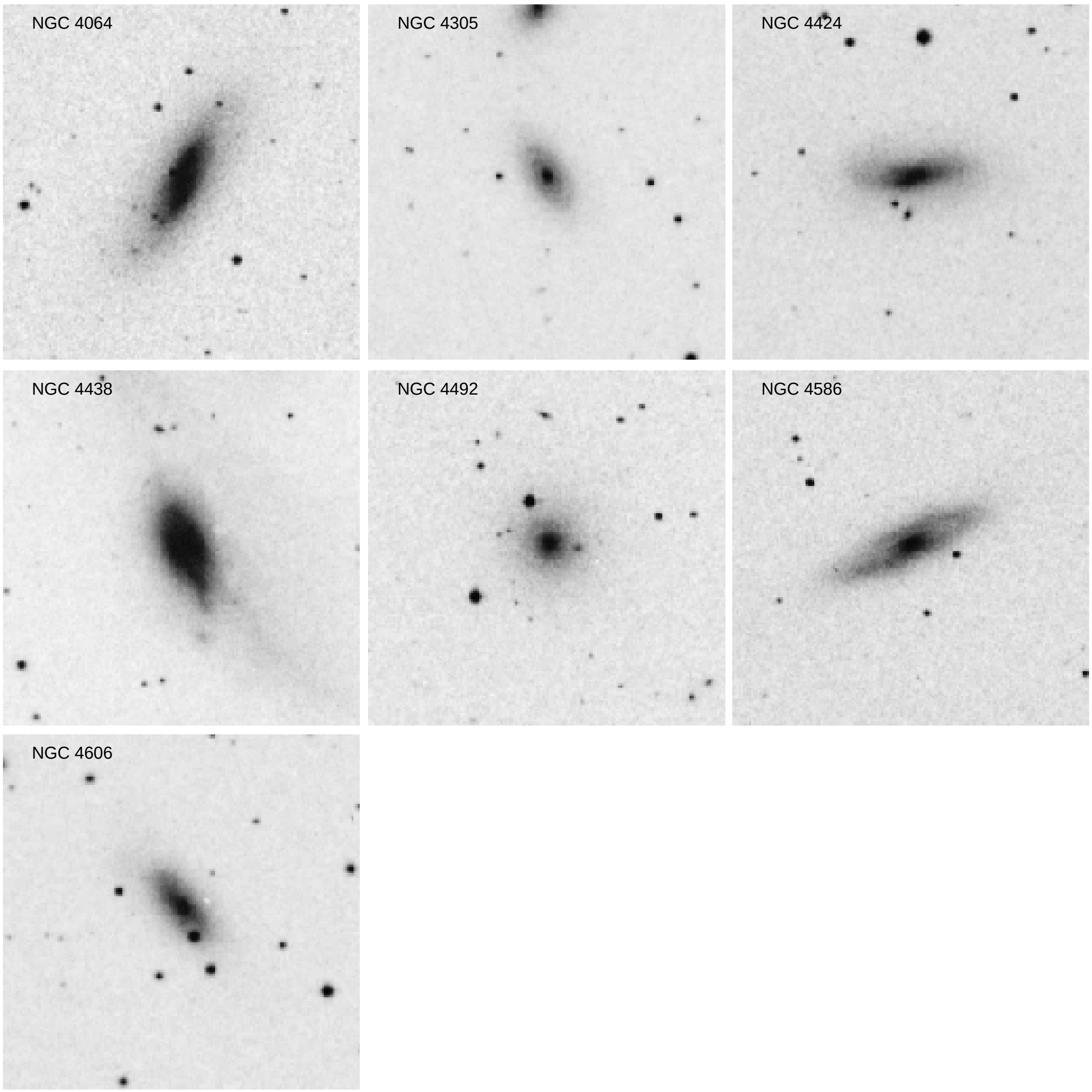

Figure 7.2: POSS I snapshots of the $T = 1$ H I-deficient galaxies of table 7.1. The box size is $6'$ and North points upwards.

NGC 4064 This galaxy has a very large high surface brightness inner disk or flattened bulge with little trace of spiral arms. NGC 4064 may lie between S0 and S0/a.

NGC 4305 This galaxy is of type Sa or later. It has a nearby major companion.

NGC 4424 This galaxy has an important bar and the size of the bulge is difficult to estimate. It shows little traces of spiral arms. Kenney et al. (1996) write "NGC 4424 is classified as an Sa rather than an S0 because the outer stellar disk is not structureless". It may well be an S0/a.

NGC 4438 This galaxy is tidally distorted by a companion just North of the frame.

NGC 4492 This galaxy is viewed face-on, hence the disk is not very visible. The bulge is relatively large and there are signs of a weak spiral arm. NGC 4492 may lie between S0/a and Sa.

NGC 4586 This galaxy shows spiral arms and a normal bulge for an Sa galaxy.

NGC 4606 This galaxy shows little traces of spiral arms and has an intermediate bulge. NGC 4606 appears between S0/a and Sa.

Altogether, aside from the obviously interacting galaxies NGC 4305 and NGC 4438, we suspect that 3 galaxies may be earlier than Sa: NGC 4064, NGC 4424, and NGC 4606. The first two of these appear to have recently ingested smaller galaxies, and significant amounts of cold gas may have been heated up during the merger.

Given that between types S0/a and Sa, the compilation of Bettoni et al. (2003) (left plots of their figure 2) indicates that the normalized H I content varies as $\log M_{\rm HI}^{\rm norm} \sim T/4 + {\rm cst}$, an overestimate of 1 (0.5) in T will lead to an underestimate in H I deficiency of 0.25 (0.125). The H I deficiency of NGC 4064 is sufficiently high that a correction of 0.25 will still keep it among the $3\,\sigma$ cases using both $< DEF >$ and DEF criteria. With respect to NGC 4424, if its morphological type corresponds to S0/a ($T = 0$), it would still be H I-deficient with criterion $< DEF >$, but no longer among the $3\,\sigma$ cases with DEF. Finally, given that NGC 4492 has DEF = 0.78 and $< DEF >= 0.85$, then if it were really an S0/a ($T = 0$), it would have DEF $\simeq 0.53$ and $< DEF >\simeq 0.6$, which places it out of the list of $3\,\sigma$ H I-deficient galaxies. On the other hand, if NGC 4492 has $T = 0.5$, it would have DEF $\simeq 0.655$ and $< DEF >\simeq 0.725$, so that it would be less than $3\,\sigma$ deficient according to DEF and just at $3\,\sigma$ deficiency with $< DEF >$.

Note, however, that if most H I-deficient outliers classified as Sa's were in fact S0/a's, we would find ourselves with the new problem of justifying the presence of S0/a's so far away from the cluster core and apparently not within groups (see Section 5.3). We also have to keep in mind that Koopmann & Kenney (1998) argued that spirals in the Virgo cluster could have also been misidentified as early-type objects, an opposite trend to the above suggested.

7.7 Case by case analysis

We now focus on each of the 13 galaxies, one by one.

NGC 4064 Although it lies outside the virial angular radius of the Virgo cluster, this galaxy probably lies close to the Virgo cluster. Its very low inner rotation (Rubin et al. 1999) suggests that it is a merger remnant (see NGC 4424 below).

NGC 4305 This galaxy, at 40 Mpc and with a large radial velocity, is almost certainly a background galaxy. It has a major tidal companion (table 7.2).

NGC 4307 The origin of the H I deficiency in this galaxy is difficult to ascertain, as it has 41% (48%) probability of lying within the sphere centered on the Virgo cluster with radius 1 (2.5) times the virial radius. Its proximity with NGC 4356 suggests that it may have interacted in the past with that galaxy.

NGC 4312 This galaxy is very likely within the Virgo cluster.

NGC 4356 The origin of the H I deficiency in this galaxy is difficult to ascertain, as it has 19% (23%) probability of lying within the sphere centered on the Virgo cluster with radius 1 (2.5) times the virial radius. Its proximity with NGC 4307 suggests that it may have interacted in the past with that galaxy.

NGC 4424 This galaxy is almost certainly lies in the foreground of the Virgo cluster. Its very low inner rotation suggests a merger remnant (Rubin et al. 1999).

NGC 4438 This seemingly foreground galaxy is very probably a member of the Virgo cluster. Kotanyi & Ekers (1983) suggest that the H I deficiency of this highly distorted galaxy is caused not by the tidal companion, which should increase the line-width, but by interaction with the intracluster medium of the Virgo cluster.

NGC 4492 This galaxy is probably in the background of the Virgo cluster. The analysis in Section 7.6 suggests that this galaxy may be an S0/a with $T = 0$ or 0.5, but also that $T = 0$ is required to remove NGC 4492 from the list of $3\,\sigma$ H I-deficient galaxies.

VCC 1569 This faint galaxy probably lies in or very close to the Virgo cluster.

M90 Among the 13 galaxies listed in table 7.1, this Sab LINER (e.g. Keel 1996) deviates the most significantly from the Tolman-Bondi locus. Its distance has been controversial. Stauffer, Kenney, & Young (1986) suggest that the Tully-Fisher estimate is an underestimate because the optical rotation curve is still rising to the limit of its measurement (see Rubin et al. 1999) and that similarly low distances derived by Cowley, Crampton, & McClure (1982) using their line index / bulge luminosity relation may be erroneous because the weakness of the nuclear lines is in contrast with the high metallicity expected from the stellar population of the bulge. Note that M90 is extremely isolated in projected phase space. Among the galaxies with $d < 13\,\mathrm{Mpc}$, it appears associated with a group of ellipticals, none of which has accurate distance measurements, with sky coordinates associated with the central ellipticals with accurate distance measurements in the center of the Virgo cluster. This suggests that M90 is a member of the cluster. Moreover, given its location in 4D phase space (especially in view of its negative velocity), it appears considerably more likely to lie within the Virgo cluster than outside of it ($P_1 = 1$ in table 7.1). But, if it were located in a group with velocity dispersion around $400\,\mathrm{km\,s^{-1}}$ at roughly 4 Mpc from the Local Group, it would only be a $-1.5\,\sigma$ outlier in velocity space for galaxies at that distance.

NGC 4580 This galaxy probably lies near the Virgo cluster, and may possibly be bouncing out of the cluster, therefore losing its neutral gas by ram pressure stripping. Its proximity with NGC 4586 suggests that it may have interacted in the past with that galaxy.

NGC 4586 This galaxy probably lies near the Virgo cluster and may possibly be bouncing out of the cluster, therefore losing its neutral gas by ram pressure stripping. Its proximity with NGC 4580 suggests that it may have interacted in the past with that galaxy.

NGC 4606 This galaxy is a very likely member of the Virgo cluster. It is likely to be tidally perturbed by its companion NGC 4607 (table 7.2), although it shows only modest signs of such tides.

7.8 Summary and conclusions

In this chapter, we have investigated the origin of the deficiency in neutral hydrogen of the spiral galaxies lying on the outskirts of the Virgo cluster. The H I-deficient galaxies apparently lying well in front and behind of the Virgo cluster must have passed through the core of the cluster to have shed their gas by stripping by the ram pressure of the intracluster gas. As shown in Chapter 5, galaxies cannot bounce out beyond 2.5 virial radii, which according to the estimate of the virial radius of Virgo, amounts to 4.1 Mpc.

One possibility, discussed in Section 7.3, is that the true 3D locations of the outlying H I-deficient galaxies are in fact within the Virgo cluster's virial radius or at most within 4 Mpc from its center, which is possible (although not likely) given the typical 20% relative distance errors for the spiral galaxies in Virgo, expected from the Tully-Fisher relation, and from our comparison of the observed velocity distance relation with that derived from cosmological N-body simulations. Indeed, of the 13 H I-deficient spirals appearing in the outskirts of the Virgo cluster, 4 to 5 (depending on how to place the distance to M90) are highly likely to be located in 3D within the virial radius of the Virgo cluster (table 7.1) and one other galaxy (NGC 4307) has one chance in two of being in the cluster or near it. Three others are at an angular radius $> \theta_{100}$ from M87, but appear to be within 2.5 virial radii of it in 3D. Finally, two galaxies (NGC 4356 and NGC 4492) in the direction of the cluster have low but non negligible probability of being in or near the cluster, while the last two are definitely foreground (NGC 4424) and background (NGC 4305) galaxies. Hence, between 4 and 11 of these 13 galaxies may have passed through the core of the Virgo cluster and seen their neutral gas ram pressure swept by the hot intracluster gas.

The presence of a few discrepant distance measurements suggests that the nearly Gaussian parent distribution function for measurement errors in the distance modulus (or relative distance) has extended non-Gaussian wings.

It is also possible that highly inaccurate (at the 30% level or more) Tully-Fisher distance measurements may arise from physical biases. If galaxies are H I-deficient because of strong interactions with the cluster (through ram pressure stripping or tides) or with neighboring galaxies (through collisional tides), their Tully-Fisher distances may be biased and/or inefficient. Indeed, our analysis of Section 7.5 indicates that, among the galaxies likely or possibly within the Virgo cluster, one (NGC 4438) shows clear tidal perturbations from a close major companion, while 2 others (M90 and NGC 4606) are probably tidally perturbed by close companions, and the one possible Virgo cluster member (NGC 4307) may have interacted with a fairly close major companion in the past.

Moreover, there are general arguments, independent of these case-study tidal effects, that suggest that abnormal Tully-Fisher distances may be caused by H I deficiency. For example, Stauffer et al. (1986) noted that H I-deficient spirals in the direction of the Virgo cluster tend to have smaller line-widths for their *H*-band luminosity, and, similarly, Rubin, Hunter, & Ford (1991) found that the maximum rotation velocity of spiral galaxies within compact groups of galaxies tend to be smaller for their luminosity than for normal spirals. Such small line-widths or maximum rotation velocities imply that distances are underestimated. Mendes de Oliveira et al. (2003) have refined the analysis of Rubin et al. using 2D (Fabry-Perot) spectroscopy and find that 20% of the galaxies (mainly of low luminosity) have lower maximum rotation velocities than field spirals of the same luminosity. Moreover, they find that compact group galaxies display a more scattered Tully-Fisher relation than that of field spirals.

Alternatively, the outlying H I-deficient galaxies may have lost their gas by the tides generated during close encounters with other galaxies within a group or small cluster of galaxies. Indeed, the efficiency of tidal perturbations of galaxies from close encounters with other galaxies is stronger in groups and small clusters than in rich clusters (see figure 5 of Mamon 2000), basically because the rapid motions in rich clusters decrease the efficiency of tides. But while three of the four H I-deficient galaxies at 28 Mpc lie within a significant concentration of galaxies (figures. 6.1 and 7.1) that ought to create such collisional tides, the estimates of distance using the more precise radial velocities (for these distant objects, see equation 7.2) shows no such concentration of galaxies.

Moreover, one may contest that tides will remove stars as well as gas from the disk of a spiral galaxy. However, the estimates of H I deficiency presented here are based upon single-dish (Arecibo) radio observations, which often do not have sufficient angular resolution to map the gas (the half-power beam of Arecibo subtends $3\overset{\prime}{.}3$, close to the typical optical angular diameters of the H I-deficient galaxies — see table 7.1). One can therefore easily imagine that fairly weak tidal effects will deplete the neutral hydrogen gas beyond the optical radius without affecting the stars in the spiral disk, thus leading to an H I deficiency when normalized relative to the size of the optical disk.

Two galaxies among our H I-deficient Virgo outliers listed in table 7.1 (NGC 4438 and M90) have been studied by Cayatte et al. (1994), who computed H I-deficiencies of Virgo spirals, based upon high resolution 21cm VLA observations. Both galaxies present very small 21cm to optical diameter ratios (see figure 2.1), indicating that the gas deficiency sets in at small radii and cannot be caused by tidal effects. Additional high-resolution 21 cm observations at the VLA of the other galaxies in table 7.1 will obviously allow confirmation of this result.

The 3 galaxies outside the virial angular radius (NGC 4064, NGC 4580 and NGC 4586) all probably lie closer than 2.5 virial radii from M87, and may be in the process of bouncing out of the cluster after having lost their H I gas through ram pressure stripping by the intracluster gas. Moreover, one of these galaxies (NGC 4064) is a candidate for a recent merger as witnessed by its very low inner rotation, while the other two (NGC 4580 and NGC 4586) may have interacted in the past, given their proximity in phase space. In the case of recent merging, the neutral gas may have been shock heated with that of the galaxy being swallowed up, and should shine in Hα or X-rays depending on its temperature.

Of the 4 galaxies likely or certainly far outside the Virgo cluster (in 3D), one (NGC 4305) may be tidally perturbed by a close major companion, one (NGC 4424) has suffered a recent merger (given its very low inner rotation velocity), one may have interacted with another galaxy (NGC 4307) in the past, and one (NGC 4492) may be a misclassified S0/a (with $T = 0$), implying a lower expected H I content, hence a lower H I deficiency (less than $3\,\sigma$ upon the estimator $< DEF >$ and just at $3\,\sigma$ with DEF).

Although we can provide at least one explanation for each case of H I deficiency in the 13 spiral galaxies of our dataset that 1) appear to be located in the foreground or background of the Virgo cluster or 2) lie just outside the projected virial radius of the cluster, there is certainly room for an improved analysis. In particular, accurate distances obtained with Cepheids would be most beneficial.

8 Inferring the kinematical properties of bound systems: the effects of non-sphericity, substructure and streaming motions

8.1 Introduction

We have corroborated in the previous chapters the importance of knowing the kinematical properties of galaxies in order to infer the mechanism(s) driving the removal of their neutral gas and leading ultimately galaxies to morphological changes. So far, we have drawn attention to infall motions on the outskirts of clusters. In this chapter we focus on the kinematics of the inner parts of these galaxy systems.

There is a long tradition of determining the internal kinematical properties of bound systems based on the Jeans equations, which are velocity moments of the collisionless Boltzmann equation, and which link the 3D velocity moments (e.g. velocity dispersion and kurtosis) to the gradient of the potential. The Jeans equations are thus used to model the mass and velocity distribution inside elliptical galaxies (e.g. Binney & Mamon 1982), clusters of galaxies (e.g. Kent & Gunn 1982; Merritt 1987), as well as globular clusters (e.g. Merrifield & Kent 1990). The standard Jeans approach for the determination of the mass and velocity distribution assumes equilibrium and sphericity of the system. However, even in the inner parts of an object, there is non-virialized matter, for example matter falling into a cluster for the first time or smaller clumps in the process of relaxation. Such non-virialized matter could produce misleading results when a cluster is studied through the Jeans analysis. Moreover, clusters of galaxies are not observed to be spherically symmetric (Binggeli 1982; Wang & Ulmer 1997), nor are simulated structures of dark matter particles with the masses of clusters of galaxies (Cole & Lacey 1996; Jing & Suto 2002).

One way to avoid non-virialized matter within a cluster is to restrict the Jeans analysis to the population of elliptical galaxies, which is thought to be dynamically relaxed (Tully & Shaya 1984; Biviano et al. 2003; Łokas & Mamon 2003). The question of how the existing substructure and non-sphericity may affect the results can only be fully addressed by cosmological N-body simulations including realistic galaxy formation, where all 3D information would be available.

The effect of incomplete virialization of structures of dark matter particles seen in cosmological N-body simulations on the estimates of the mass of a single cluster through the Jeans equation has been addressed by Tormen, Bouchet, & White (1997). They showed that even for significantly perturbed halos, the mass $M(r)$ at distances larger than 2% of the virial radius inferred by the proper Jeans analysis is within 30% (rms) of the true mass and departs from it by less than 20% (rms) for average or relaxed halos.

In this chapter, we use cosmological N-body simulations and analytical modeling to study the effect of departures from equilibrium and non-sphericity of dark matter halos on the inferred properties of the halo and velocity distribution of its particles. We measure the mass and velocity distribution in the halos and calculate the projected velocity moments as an observer would do. We then perform a kinematic analysis based on the Jeans equations to check to what extent we can reproduce the properties of the halos from the second-order (line-of-sight velocity dispersion) and fourth-order (line-of-sight kurtosis) velocity moments.

The chapter is organized as follows. In Section 8.2, we describe the N-body simulations used and calculate the properties of the halos chosen for analysis. In Section 8.3, we estimate the projected velocity moments of the halos. Section 8.4 is devoted to analytical modeling of those moments based on Jeans formalism and testing its reliability in reproducing the properties of the halos. The discussion follows in Section 8.5.

Table 8.1: Three-dimensional properties of the simulated halos

Halo	Axis ratio	M_{100} (10^{14} $M_{\odot}$)	r_{100} (Mpc)	c	$\langle\beta\rangle$	$\overline{v}_{\rm r}$ (v_{100})
1	2.3 : 1.3 : 1	16.7	3.2	5.6	0.40 ± 0.06	0.005
2	1.9 : 1.1 : 1	8.5	2.5	5.0	0.13 ± 0.03	0.103
3	2.8 : 2.0 : 1	8.1	2.5	4.5	0.24 ± 0.05	0.134
4	3.3 : 1.3 : 1	7.0	2.4	7.1	0.14 ± 0.06	-0.260
5	2.0 : 2.0 : 1	4.5	2.1	7.9	0.15 ± 0.07	0.065
6	2.6 : 1.4 : 1	4.3	2.0	5.0	0.36 ± 0.05	0.028
7	1.8 : 1.4 : 1	4.1	2.0	8.9	-0.03 ± 0.05	-0.079
8	2.4 : 1.6 : 1	3.9	2.0	10.0	0.44 ± 0.03	-0.018
9	2.2 : 1.5 : 1	3.2	1.8	7.1	0.08 ± 0.12	-0.012
10	1.8 : 1.3 : 1	2.9	1.8	10.0	-0.23 ± 0.08	-0.168

8.2 The simulated dark matter halos

We have used the N-body simulations carried out by Hatton et al. (2003) (see details of the simulations in Section 5.2). We restrict our analysis to dark matter particles. Although the GALICS simulations we use include galaxy formation and evolution, this part of the simulations is based on a semi-analytical approach, which for our purposes is not yet satisfactory. For example, the isotropic velocity distribution of GALICS galaxies is imposed and is not a result of virialization. We therefore conclude that the galaxies in these simulations are not reliable tracers of the overall dynamical properties of the halos and cannot be used to infer the density and velocity distributions from the 'observed' velocity moments.

For our analysis, we have chosen the ten most massive halos formed in the simulation box (labeled hereafter in order of decreasing virial mass as halo 1, halo 2 and so forth[1], see table 8.1). We estimated their virial radii, r_{100}, as the distances from the center where the mean density is 100 times the present critical density. The centers of the halos are determined as the local density maxima which turn out

---

[1] These labels differ from the FoF rank of table 6.2 because the former are based upon the virial mass of the halos, while the latter comes from the mass of the groups identified by the FoF algorithm.

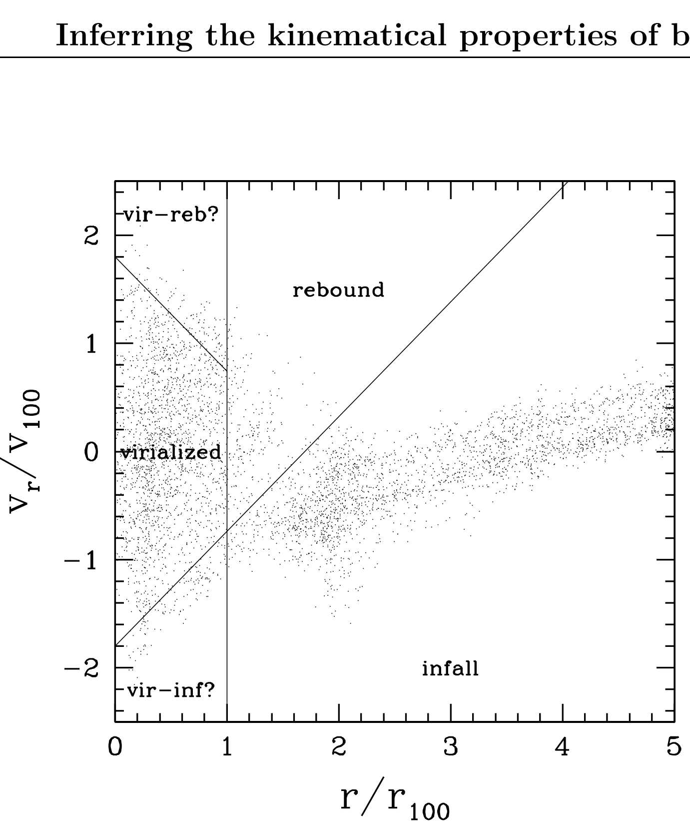

Figure 8.1: 3D radial phase space diagram (radial velocity, Hubble flow included, versus radial distance, both with respect to the cluster center and normalized to virial quantities v_{100} and r_{100}, respectively) for a random set of 1% of particles of the most massive of the simulated halos (halo 1). The oblique lines separating the dynamical regimes were drawn 'by eye' and correspond to $v_r/v_{100} = 1.8 - 1.06\,r/r_{100}$ (*bottom*) and $v_r/v_{100} = -1.8 + 1.06\,r/r_{100}$ (*top*)

to be slightly different than the centers of mass found using FoF algorithm. Within the virial radius, the halos have 2×10^5 particles for the most massive halo and 4×10^4 particles for the least massive one of the ten we have chosen. The virial radii and masses of the halos, $M_{100} = M(r_{100})$, are listed in table 8.1.

All halos have similar 3D radial phase space distributions (as it was already shown in Chapter 5). An example of such a distribution for the most massive halo is presented in figure 8.1. The figure shows the radial velocity (with respect to the center of the halo) of the particles in units of the circular velocity at r_{100} as a function of radial distance measured in units of r_{100}. We have divided the phase space into different regions corresponding to different dynamical states that we expect to find in a typical dark matter halo. Inside the virial radius, we can identify three regions. The region with low to moderate absolute velocities is likely to be populated by virialized particles, although there are indications of a group of particles at $r = 0.3\,r_{100}$ slowly moving into the halo core. On the outskirts of the velocity distribution we can find particles whose dynamical state is not clear, as they could be either high-velocity outliers of the virialized component or else infalling towards the cluster core or already in a rebound regime after a passage through the center. Beyond the virial radius, we can also find particles in a rebound trajectory and particles on the infalling branch (which includes particles expanding away from the cluster beyond the turnaround radius at 2.5–4 virial radii). In figure 8.1, these five different subsamples are denoted by `virialized`, `vir-inf?`, `vir-reb?`,`rebound` and `infall`, respectively, where the question marks indicate the uncertainty in the actual dynamical state of these subsamples.

It is important to note that when studying projected quantities we need to consider all five subsamples, as well as the whole sample (which will be marked hereafter by 'all'), because, as seen projected on the sky, there are particles belonging to each subsample that fall inside the 'virial' cylinder whose projected radius is the virial radius r_{100}, but there is no way of determining which of these particles are actually within the 'virial' sphere of radius r_{100} (inscribed in the virial cylinder).

Figure 8.2 shows the density distribution in the most massive halo 1 as a function of radial distance in units of r_{100}. We found that the measured density profile is well approximated by the NFW formula

$$\frac{\varrho(s)}{\varrho_{c,0}} = \frac{\Delta_c\, c^2 g(c)}{3\, s\, (1+cs)^2} \ , \tag{8.1}$$

where $s = r/r_{100}$, $\varrho_{c,0}$ is the present critical density, $\Delta_c = 100$, c is the concentration parameter and $g(c) = [\ln(1+c) - c/(1+c)]^{-1}$. The statistical errors are much smaller than the departures due to substructure in the halo, but the overall fit is satisfactory. We find that the best-fitting concentration parameter for halo 1 is $c = 5.6$. The virial mass of halo 1 is $M_{100} = 1.67 \times 10^{15}\ \mathrm{M}_\odot$ so the concentration we estimated is consistent with the dependence of c on mass inferred from N-body simulations by Bullock et al. (2001), also run with a ΛCDM cosmology:

$$c(M_{100}) = 5.95 \left(\frac{M_{100}}{10^{15} h^{-1} \mathrm{M}_\odot} \right)^{-0.122} \tag{8.2}$$

Similar results are obtained for the other halos. The fitted parameters are summarized in table 8.1.

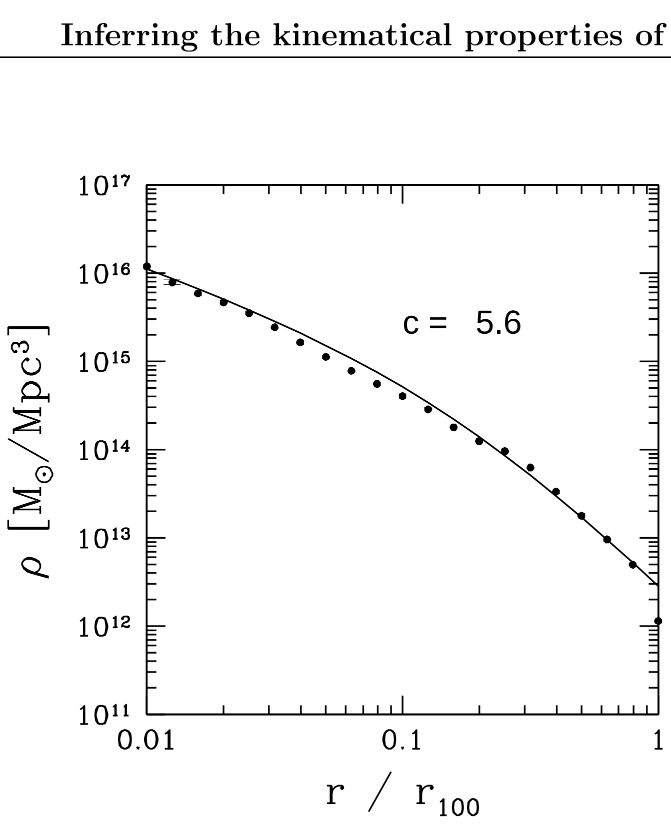

Figure 8.2: Density profile of halo 1. The measurements were done in radial bins of equal logarithmic length and errors were estimated as Poisson fluctuations. The errorbar in the second point shows the maximum error assigned to measurements. The *curve* is the best-fitting NFW profile with concentration $c = 5.6$.

In figure 8.3 we present radial profiles of the mean radial velocity in units of the circular velocity at r_{100} and the anisotropy parameter

$$\beta = 1 - \frac{\sigma_\theta^2(r)}{\sigma_r^2(r)} \tag{8.3}$$

for the ten halos, where σ_θ and σ_r are the velocity dispersions (with respect to the mean velocities) discussed in detail in the next sections. We show measurements for all particles inside the sphere of radius r_{100}. Each point represents the anisotropy or mean radial velocity of dark matter particles enclosed in shells of thickness $0.1r_{100}$ centered in each radius r. As we can see, the orbits of most of the halos are mildly radial, with positive mean β. We have calculated the unweighted mean anisotropy inside the virial radius. These values are listed in table 8.1, where the uncertainties are the dispersions of the values about the unweighted mean. The anisotropy does not vary strongly with radius so in the modeling which follows we will assume it to be constant and equal to the mean value inside the virial radius. However, it is interesting to note that the variation of β with distance from the center is very different for each of the analyzed halos. As for the mean radial velocity, we can see

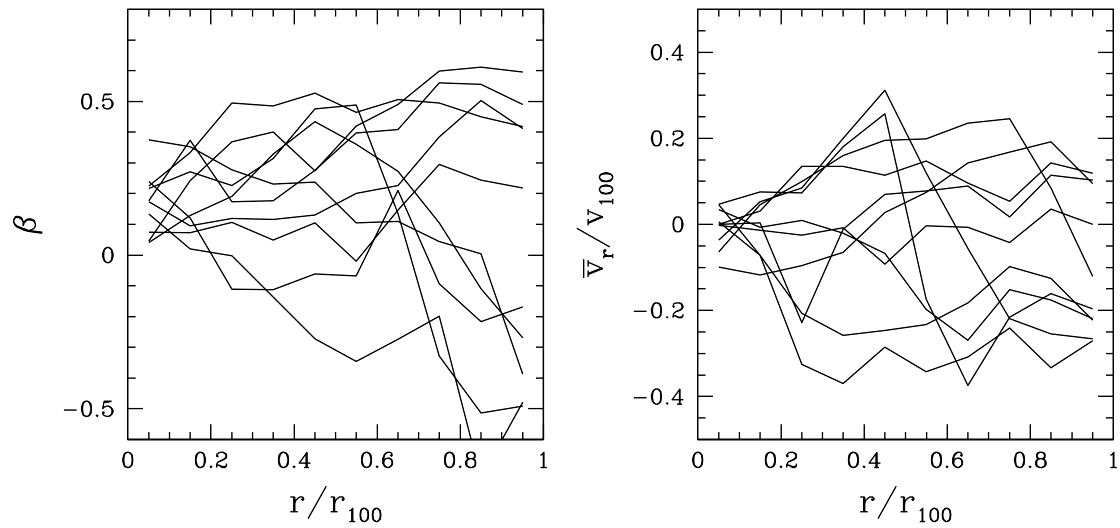

Figure 8.3: The radial profile of the anisotropy parameter β (*top panel*) and the mean radial velocity in units of the circular velocity at r_{100} (*bottom panel*) for all particles inside r_{100} for the 10 halos of table 8.1.

from figure 8.3 that it is consistent on average with zero inside r_{100} for most halos, albeit with non-negligible radial variations caused by internal streaming motions, including some abrupt variations suggesting the presence of smaller halos (akin to groups of galaxies) falling in or bouncing out of the halo. In table 8.1 we list this quantity in units of v_{100}. The negative sign indicates infall motion towards the center of the halo.

8.3 Velocity moments of dark matter particles

We now study the kinematical properties of halos as they would be seen by a distant observer. The quantities discussed are all projected along the line of sight. With the Jeans formalism, we can only model the projected velocity moments of objects in equilibrium, and thus we cannot make any prediction about the velocity moments of the regions of phase space called 'rebound', 'infall', 'vir-reb?' and 'vir-inf?' in figure 8.1. Moreover, not all particles inside r_{100} are virialized, as they could be falling into the core for the first time or be on a rebound orbit not yet in equilibrium. However, the division of the phase space into the 5 regions (figure 8.1) was made by eye, with no exact determination of the dynamical state of the particles, and it was only based on the radial component of the particle velocities. This could produce misleading results in the analysis of the velocity moments, which involve all components of the velocity. For these reasons, in what follows, we will restrict ourselves to the study of the velocity moments of all particles inside the virial sphere of radius r_{100} and all particles within the virial cylinder of projected radius smaller than r_{100}. The latter would be the ones used in the Jeans formalism by an observer unable to distinguish which particles actually lie in the virial sphere of radius r_{100}.

We mimic the observations as follows. For each halo, we place an observer at either 0°, 45° or 90° with respect to the major axis (see table 8.1) so that the three chosen directions are in the same plane defined by the major axis and the sum of the other two axes. The choice of axes is dictated by the non-sphericity of the set of particles within the virial sphere, but also of the filaments of groups and other matter falling into the virial sphere out to scales $\simeq 10\,r_{100}$. It turns out that the principal axes on scales of $\simeq 10\,r_{100}$ are very similar to those computed for $r < r_{100}$, so we restrict ourselves to the principal axes obtained from the tensor of inertia of the particles within the virial sphere. We then project all the particle velocities along the line of sight and the distances on the surface of the sky. In figure 8.4 we show line-of-sight velocities of dark matter particles in halo 1 projected along the major axis as a function of projected distance from the center in units of r_{100}.

Observers remove a fraction of the interlopers of a cluster by excluding the high-velocity outliers. Here, we remove the high-velocity outliers from our mock samples in a similar way as done by Kent & Gunn (1982) and Łokas & Mamon (2003) for clusters of galaxies. The velocity cuts are shown as solid curves in figure 8.4. Less than 2% of all particles within the virial cylinder were removed in this fashion. Although the main body of the halo is quite well defined in velocity space, with much more particles than there are galaxies in a cluster, the gaps between the halo and the background are not as visible as found by Łokas & Mamon (2003) for the Coma cluster. After applying this selection procedure, the fraction of particles lying inside the cylinder of projected radius r_{100} that are actually outside the sphere of radius r_{100} is between 6% and 35%, with a mean of 15%.

We divide the projected radius in ten bins and calculate, in each bin of projected radius, the mean, dispersion, skewness, and kurtosis of the line-of-sight velocities, v_i, according to the following formulae

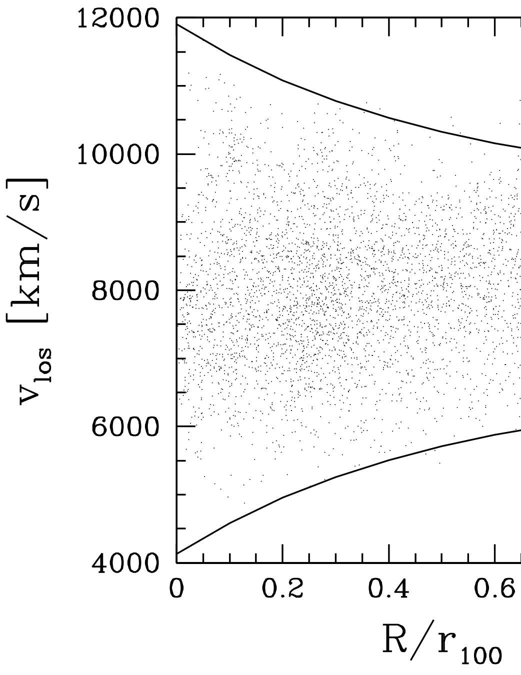

Figure 8.4: Line-of-sight velocities of a random set of 2% of the dark matter particles in halo 1 projected along the major axis as a function of projected distance from the center in units of r_{100}. The *curves* indicate the cuts used to distinguish between particles belonging to the halo from the background. The vertical clumps indicate groups of particles (nearly all within the virial sphere).

$$\begin{aligned}
\overline{v}_{\rm los} &= \frac{1}{N}\sum_{i=1}^{N} v_i && (8.4)\\
\sigma_{\rm los}^2 &= \frac{1}{N-1}\sum_{i=1}^{N}(v_i-\overline{v}_{\rm los})^2 && (8.5)\\
s_{\rm los} &= \frac{1}{N}\sum_{i=1}^{N}\left(\frac{v_i-\overline{v}_{\rm los}}{\sigma_{\rm los}}\right)^3 && (8.6)\\
\kappa_{\rm los} &= \frac{1}{N}\sum_{i=1}^{N}\left(\frac{v_i-\overline{v}_{\rm los}}{\sigma_{\rm los}}\right)^4 - 3 && (8.7)\\
& && (8.8)
\end{aligned}$$

where N represents the number of particles per bin.

To see the effects of non-sphericity, we show the results for halos 1, 4 and 5,

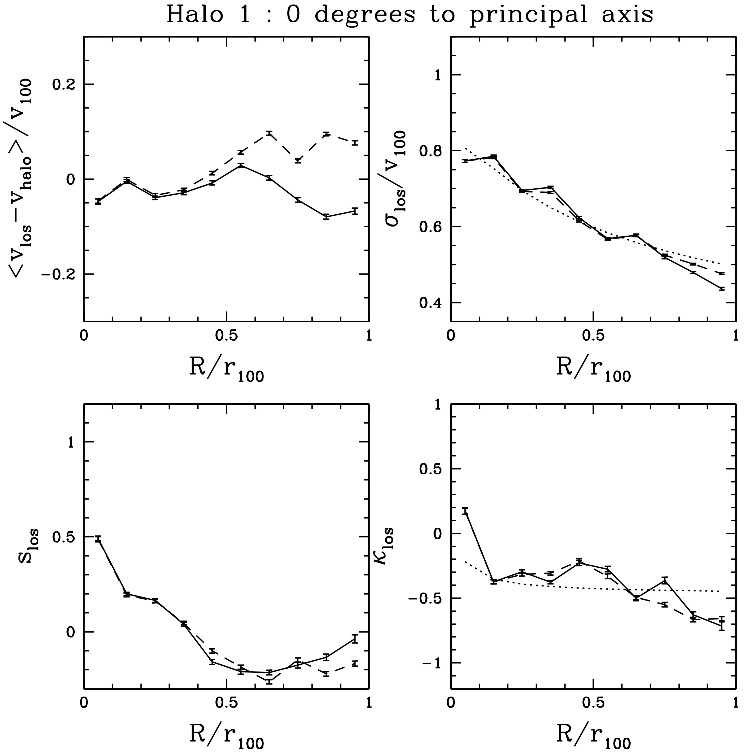

Figure 8.5: Projected velocity moments of the dark matter particles in halo 1 measured at 0° to the principal axis. The *upper left panel* shows the mean line-of-sight velocity with respect to the velocity of the center of the halo in units of the circular velocity at r_{100}. The *upper right panel* gives the line-of-sight velocity dispersion in the same units. The two *lower panels* give the skewness *(left)* and kurtosis *(right)*. In each panel the *solid line* shows results for particles lying inside the sphere of radius r_{100}, while the *dashed line* is for all particles. The *dotted curve* shows the fits obtained from the Jeans equations.

which have three different shapes: halo 5 is oblate, halo 4 is roughly prolate and halo 1 is triaxial. The results for halo 1 are shown in figures 8.5 and 8.6 for observers situated at 0°, 45° and 90° with respect to the major axis. The errors were estimated using bootstraps, but since the number of particles in each bin is very large (of the order of 10^4), the errors are small and do not account for the variability of the profiles, which is mainly due to substructure. In each panel, the dashed line shows results for all particles that in projection end up with a projected radius smaller than the virial radius, whether or not they are actually within the virial radius in 3D space. The solid line shows results for the particles really lying inside r_{100}. In the right-hand panels presenting even moments (velocity dispersion and kurtosis)

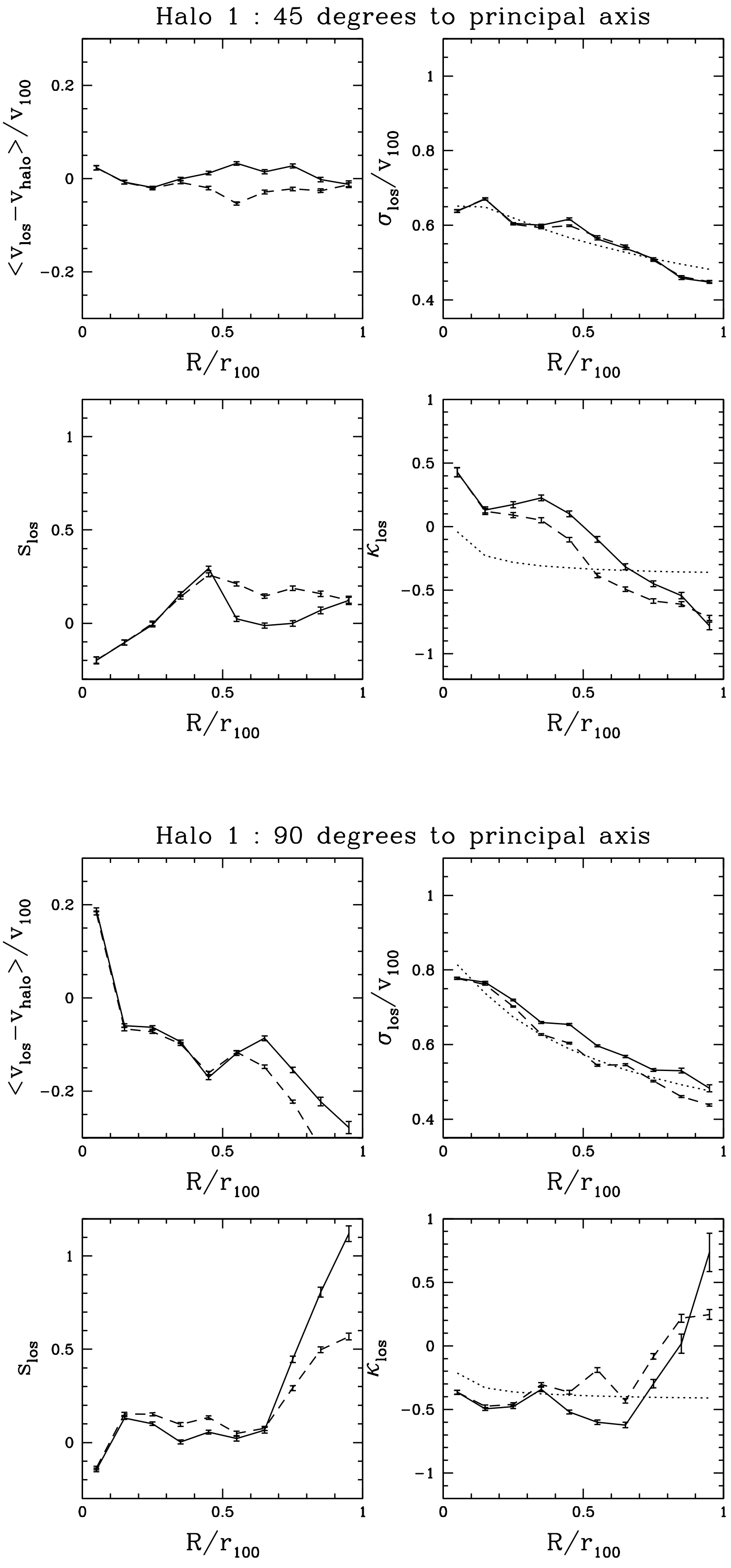

Figure 8.6: Same as figure 8.5, but measured at 45° (*top* panel) and 90° (*bottom* panel) to the principal axis.

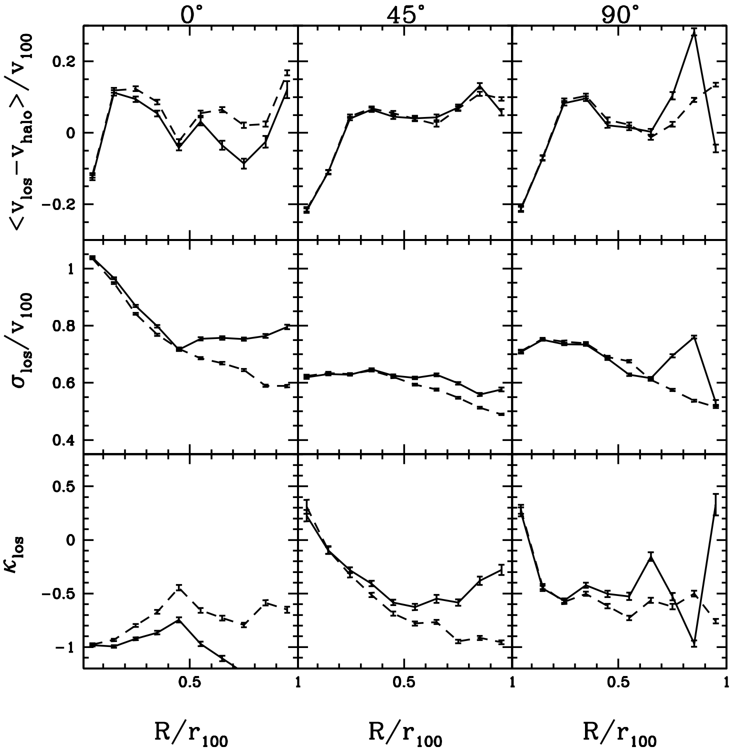

Figure 8.7: Same as figures 8.5-8.6 but for halo 4. Line-of-sight skewness is not plotted. No theoretical predictions are shown.

in figures 8.5 and 8.6 we also show dotted lines resulting from the fitting procedure based on the Jeans formalism presented in Section 8.4.

The variation of the mean velocity with projected radius provides an indication of the amount of substructure present in the halo. For observers at 0° and 45° with respect to the major axis, the mean velocity with respect to the center of the halo is approximately zero for every radial bin, indicating, if not the lack of substructure, at least the compensation of effects of different substructures. This is true for the two subsets of particles studied, especially for particles actually within the virial sphere. For an observer at 90° with respect to the major axis, we find a departure of the mean velocity from the velocity of the center of the halo, which indicates presence of substructure. As could be expected, this radial variation of the mean velocity is more pronounced for the particles we find in projection inside r_{100} that are not necessarily within the virial sphere of radius r_{100}.

Contrary to the case of elliptical galaxies, where velocity moments are measured from spectra obtained in slits, e.g. along the major axis, and thus do not involve

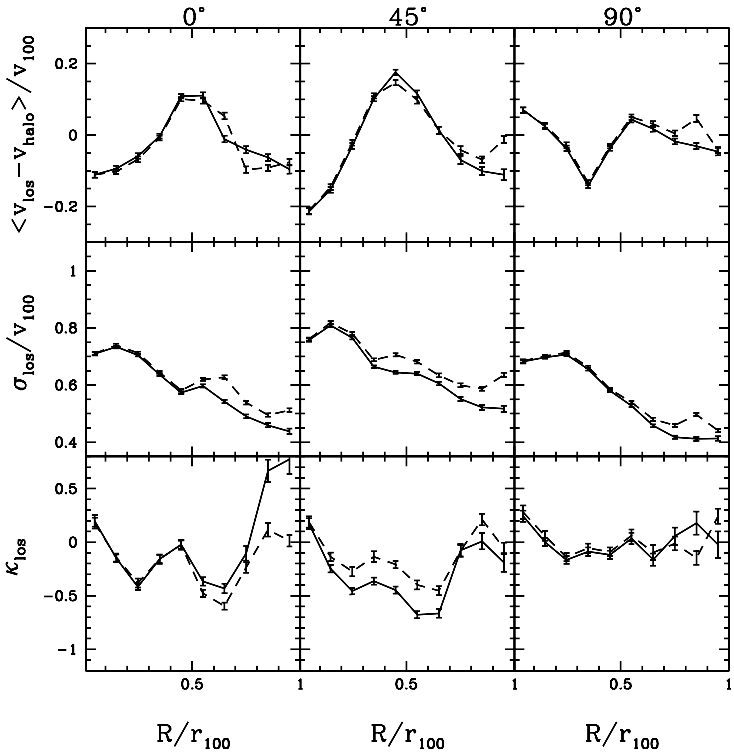

Figure 8.8: Same as figure 8.7, but for halo 5.

averaging in shells of similar projected radius, here and in the analysis of galaxy motions in clusters the mean projected velocity is less affected by the presence of global motions like rotation or infall. Therefore, the estimation of the bulk velocities requires the 3D information. We find that the mean velocities in the radial and tangential directions inside the virial radius are typically of the order of few percent of v_{100}, except for halos 4 and 10 where significant net radial infall seems to be present (see table 8.1).

Figures 8.7 and 8.8 illustrate how the velocity moments depend on the given halo. To save space, we only show the even moments that we will model in the next section and the mean line-of-sight velocity with respect to the velocity of the center to test the relaxation of the halos. For the sake of clarity of the plots, we do not show the fits based on the Jeans equations, although we will discuss them in the following section.

Even with significant noise from substructure, such as the trend for high mean velocity at $R \simeq 0.5\, r_{100}$ for halo 5 (figure 8.8) probably arising from a group bouncing out of the halo, we can see some common trends in figures 8.5–8.8. First, the line-of-sight velocity dispersion and kurtosis profiles can differ substantially for a given halo seen along three different axes (especially in halo 4). Moreover, the velocity moments are not strongly affected by the presence of particles outside the virial radius, i.e. the solid and dashed lines typically do not differ significantly. This is understandable as the virial sample is a subsample of the 'all' sample and the mean difference in the number of particles is less than 20% as previously noted. The discrepancies between the velocity moments are more important for larger projected distances from the center of a halo, as the surface density of the 3D halos decreases faster than that of the surrounding material.

In appendix C we show the velocity moments of the rest of the halos measured with all particles (which will be modeled in the next section).

8.4 Modeling of the velocity moments

We now describe the Jeans formalism for modeling the projected velocity moments of virialized objects and apply it to recover the properties of the halos. A detailed description of the calculations involved in the Jeans formalism can be found in Łokas (2002) and Łokas & Mamon (2003) (see also Merrifield & Kent 1990; van der Marel et al. 2000).

Our purpose here is to reproduce the projected velocity moments discussed in the previous section by solving the Jeans equations for the second and fourth velocity moments and adjusting the parameters describing the mass and velocity distribution in the halos. We will then verify whether the fitted parameters match the real properties of the halos. The Jeans analysis assumes that the system is spherically symmetric and in equilibrium, that there are no net streaming motions (no infall and no rotation) so that the odd velocity moments vanish. As we have seen in the previous section, none of these is exactly the case for dark matter halos. We want to check to what extent violating these assumptions affects the recovered properties of the halos.

One difference with respect to the analysis of galaxies is that the dark matter particles are very numerous in our simulations (of order 10^5 per halo) while the number of galaxies in a cluster usually does not exceed a thousand. This is another reason why the errors due to substructure will be more significant here than sampling errors which are the dominant ones in measured velocity moments of galaxies.

The second order velocity moments are $\overline{v_r^2}$ and $\overline{v_\theta^2} = \overline{v_\phi^2}$ and we will denote them hereafter by σ_r^2 and σ_θ^2 respectively. They can be calculated from the lowest order Jeans equation (e.g. Binney & Mamon 1982)

$$\frac{\mathrm{d}}{\mathrm{d}r}(\nu\sigma_r^2) + \frac{2\beta}{r}\nu\sigma_r^2 = -\nu\frac{\mathrm{d}\Phi}{\mathrm{d}r} \ , \tag{8.9}$$

where ν is the 3D density distribution of the tracer population and Φ is the gravitational potential. Since in our case dark matter particles trace their own gravitational potential, we have $\nu(r) = \varrho(r)$. We assume that the dark matter distribution is given by the NFW profile (8.1) characterized by its virial mass M_{100} and concentration c. We solve equation 8.9 assuming the anisotropy parameter of equation 8.3 to be constant with $-\infty < \beta \leq 1$. This model covers all interesting possibilities from radial orbits ($\beta = 1$) to isotropy ($\beta = 0$) and circular orbits ($\beta \rightarrow -\infty$).

The solution of the lowest order Jeans equation with the boundary condition $\sigma_r \rightarrow 0$ at $r \rightarrow \infty$ for $\beta = \mathrm{const}$ is (e.g. Łokas & Mamon 2003)

$$\nu\sigma_r^2(\beta = \mathrm{const}) = r^{-2\beta}\int_r^\infty r^{2\beta}\nu\frac{\mathrm{d}\Phi}{\mathrm{d}r}\ \mathrm{d}r \ . \tag{8.10}$$

As discussed in the previous section, the quantity an observer would measure is the line-of-sight velocity dispersion obtained from the 3D velocity dispersion by integrating along the line of sight (Binney & Mamon 1982)

$$\sigma_{\mathrm{los}}^2(R) = \frac{2}{I(R)}\int_R^\infty \left(1 - \beta\frac{R^2}{r^2}\right)\frac{\nu\,\sigma_r^2\,r}{\sqrt{r^2 - R^2}}\,\mathrm{d}r \ , \tag{8.11}$$

where $I(R)$ is the surface distribution of the tracer and R is the projected radius. In our case $I(R)$ is given by the projection of the NFW profile (see Łokas & Mamon 2001) . Introducing equation 8.10 into equation 8.11 and inverting the order of integration, the calculation of σ_{los} can be reduced to one-dimensional numerical integration of a formula involving special functions for arbitrary $\beta = \mathrm{const}$:

$$\sigma^2_{\rm los}(R) = \frac{2G}{I(R)} \int_R^\infty {\rm d}x \ \nu(x) M(x) x^{2\beta-2} \times \int_R^x {\rm d}y \left(1 - \beta \frac{R^2}{r^2}\right) \frac{y^{-2\beta+1}}{\sqrt{y^2 - R^2}} \qquad (8.12)$$

where $M(x)$ is the mass distribution and variables x and y are used instead of r to avoid confusion.

It has been established that systems with different densities and velocity anisotropies can produce identical $\sigma_{\rm los}(R)$ profiles (see e.g. Merrifield & Kent 1990; Merritt 1987). This degeneracy can be partially lifted through the modeling of the fourth-order moment. With $\beta = $ const, the solution of the Jeans equation for the fourth-order moment

$$\frac{\rm d}{{\rm d}r}(\nu \overline{v_r^4}) + \frac{2\beta}{r} \nu \overline{v_r^4} + 3\nu\sigma_r^2 \frac{{\rm d}\Phi}{{\rm d}r} = 0 \ , \qquad (8.13)$$

is (see Łokas 2002; Łokas & Mamon 2003)

$$\nu \overline{v_r^4}(\beta = {\rm const}) = 3 r^{-2\beta} \int_r^\infty r^{2\beta} \nu \sigma_r^2(r) \frac{{\rm d}\Phi}{{\rm d}r} \ {\rm d}r \ . \qquad (8.14)$$

By projection, we obtain the line-of-sight fourth moment

$$\overline{v^4_{\rm los}}(R) = \frac{2}{I(R)} \int_R^\infty \frac{\nu \, \overline{v_r^4} \, r}{\sqrt{r^2 - R^2}} \, g(r, R, \beta) \, {\rm d}r \ , \qquad (8.15)$$

where

$$g(r, R, \beta) = 1 - 2\beta \frac{R^2}{r^2} + \frac{\beta(1+\beta)R^4}{2r^4}. \qquad (8.16)$$

Introducing equations 8.10 and 8.14 into equation 8.15 and inverting the order of integration, the calculation can be reduced to a double integral:

$$\overline{v^4_{\rm los}} = \frac{6G^2}{I(R)} \int_R^\infty \frac{r^{-2\beta+1}}{\sqrt{r^2 - R^2}} g(r, R, \beta) {\rm d}r \times \int_r^\infty \frac{\nu(q) M(q)}{q^{2-2\beta}} {\rm d}q \int_r^q \frac{M(p)}{p^2} {\rm d}p \qquad (8.17)$$

In the following, we use the fourth projected moment scaled with $\sigma^4_{\rm los}$ in the form of projected kurtosis

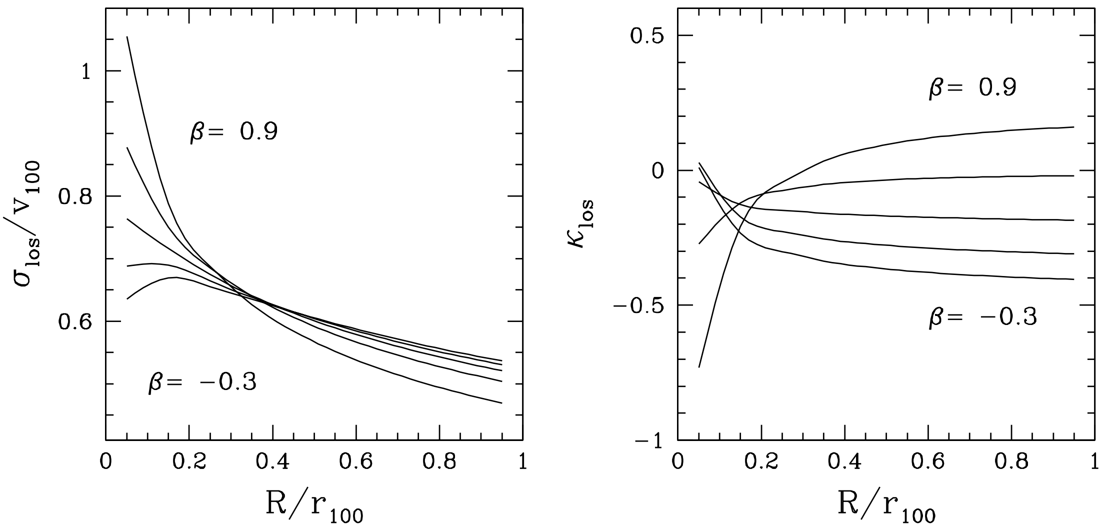

Figure 8.9: Predicted profiles of $\sigma_{\rm los}(R)$ and $\kappa_{\rm los}(R)$ for dark matter halo with concentration $c = 5.6$ and different values of $\beta = -0.3, 0, 0.3, 0.6$ and 0.9. The values of $\sigma_{\rm los}$ are scaled with circular velocity at r_{100} and distances are in units of r_{100}. These theoretical profiles are independent of the virial mass M_{100}.

$$\kappa_{\rm los}(R) = \frac{\overline{v_{\rm los}^4}(R)}{\sigma_{\rm los}^4(R)} - 3, \tag{8.18}$$

where the value of $\kappa_{\rm los}(R) = 3$ valid for a Gaussian distribution has been subtracted.

We can now calculate the predictions of equations 8.11 and 8.15 for a given mass distribution and velocity anisotropy β. As already discussed, we assume that the mass is given by the NFW distribution. For halo 1 we found the concentration of $c = 5.6$. For this value and different β we obtain the profiles of $\sigma_{\rm los}(R)$ and $\kappa_{\rm los}(R)$ shown in figure 8.9. The values of $\sigma_{\rm los}$ are expressed in units of v_{100} and distances are in units of r_{100}. With these scalings, the predictions do not explicitly depend on the mass of the halo. The lines show results for different values of $\beta = -0.3, 0, 0.3, 0.6$ and 0.9, as indicated.

We see that for increasingly radial orbits (increasing β), the profile of $\sigma_{\rm los}$ turns steeper (e.g. Tonry 1983). Moreover, the kurtosis profile becomes more convex for increasingly radial orbits as opposed to the concave shapes in the case of isotropic and circular orbits. Since our measured kurtosis profiles in the previous section have a concave shape and are slightly negative we do not expect the orbits to depart significantly from isotropic, which is consistent with the measured anisotropy parameter (see table 8.1).

Mimicking the procedure used by observers to infer the mass and anisotropy profiles of galaxies and clusters, we fit the measured profiles of $\sigma_{\rm los}$ and $\kappa_{\rm los}$ of the three halos (shown as dashed lines in figures 8.5–8.8) by solving equations 8.11 and (8.15) and adjusting the parameters M_{100}, c and β, assuming that the objects are spherical and that their dark matter distribution is given by the NFW density profile. The fit is done by minimizing χ^2 for the 20 'data points' of $\sigma_{\rm los}$ and $\kappa_{\rm los}$ together (the data points are independent because the number of particles in each radial bin is very large, see the discussion in the Appendix of Łokas & Mamon 2003). The data points were weighted by the assigned bootstrap errors although they do not account for the real variability of the data and therefore the quality of the fits in terms of χ^2 is very bad. In reality, when dealing with real galaxy data for clusters, the bins would include a few tens of objects instead of thousands, resulting in errors larger by at least an order of magnitude. The best-fitting velocity moments found for halo 1 are shown as dotted lines in figures 8.5 and 8.6. In reality, when dealing with real galaxy data for clusters, the bins would include a few tens of objects instead of thousands, resulting in errors larger by at least an order of magnitude. To see how the sampling errors affect the determination of the dynamical parameters of clusters, we have also measured for each halo the velocity moments for a set of 40 randomly chosen particles per distance bin. This number of particles is chosen to be similar to the usual number of galaxies used in real clusters (e.g. by Łokas & Mamon 2003). Errors were assigned as described in the Appendix of Łokas & Mamon (2003). We have then performed the same fitting procedure as described above.

The best-fitting parameters for the halos estimated with all dark matter particles are shown in the left column of figure 8.10 as different symbols depending on the direction of observation with respect to the major axis: 0° (circles), 45° (triangles) and 90° (squares). The crosses mark the 'real' values of the parameters listed in table 8.1. In the right column of figure 8.10, we show the best-fitting parameters estimated with 400 particles (40 particles per bin).

Due to a rather time-consuming integration involved in the calculation of kurtosis, we restricted our analysis to the ten most massive halos. The general conclusion is that when taking into account all three fitting parameters, for all halos their best-fitting virial mass M_{100} is reasonably well recovered: the discrepancy between the best-fitting value and the real M_{100} (measured using 3D information) is smaller

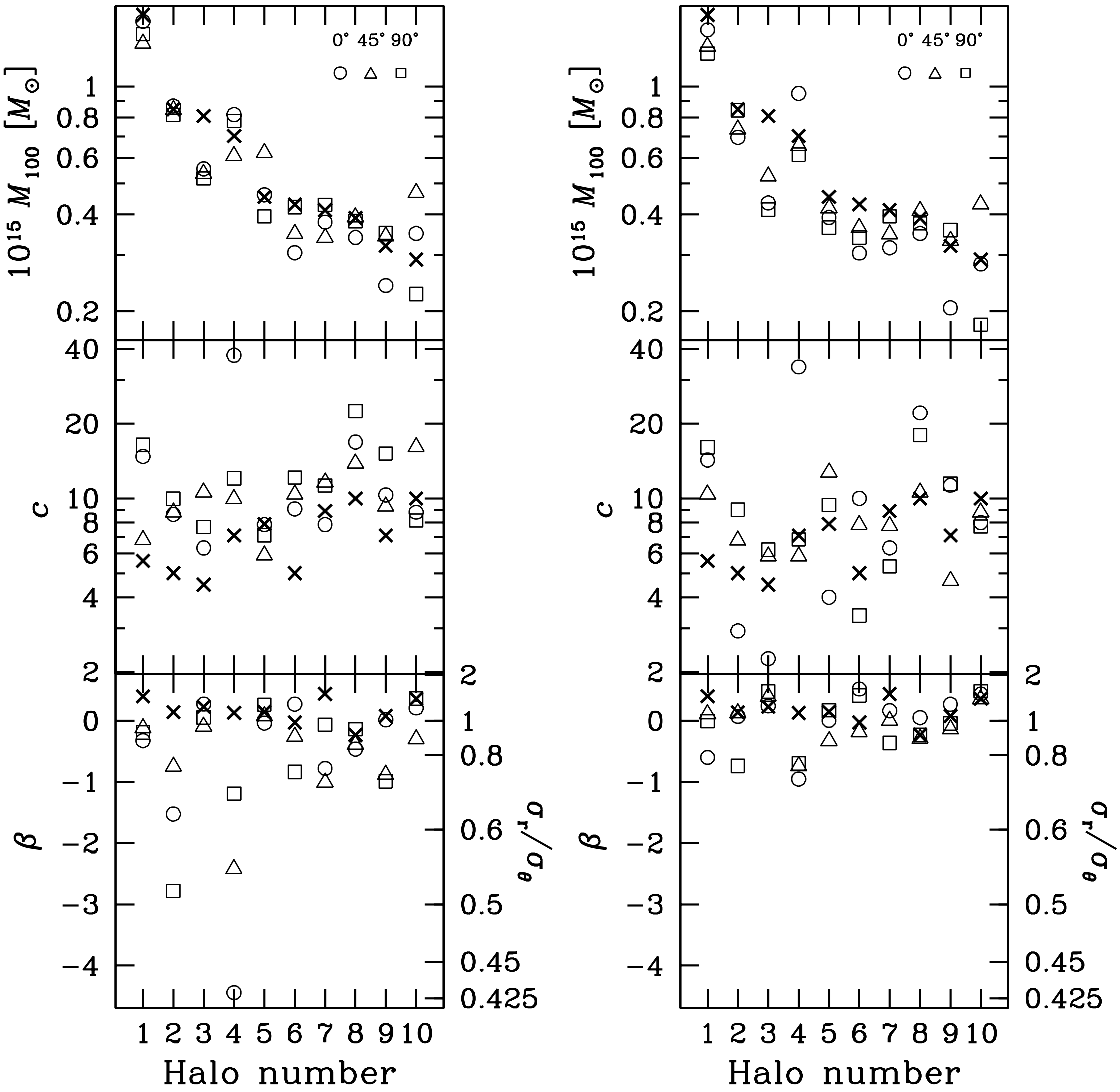

Figure 8.10: Fitted (on projected data) values of virial mass M_{100}, concentration parameter c and anisotropy β of the ten halos for the three directions of observation with respect to the major axis of each halo: $0°$ (*circles*), $45°$ (*triangles*) and $90°$ (*squares*). The values measured on 3D data are shown with *crosses*. *Left:* Fitted parameters obtained with all particles. *Right:* Fitted parameters obtained with 40 particles per bin.

Table 8.2: Results of the fitting procedure

Particles	$\Delta \log M_{100}$		$\Delta \log c$		$\Delta\beta$		$\Delta \log(\sigma_r/\sigma_\theta)$	
per bin	mean	σ	mean	σ	mean	σ	mean	σ
All	–0.03	0.09	0.20	0.18	–0.78	1.04	–0.12	0.12
40	–0.07	0.10	0.08	0.24	–0.20	0.48	–0.04	0.11

than 62% (this large discrepancy is obtained for halo 10 when observed at 45° with respect to the major axis). The next biggest error was obtained for halo 5 (37% when observed at 45° with respect to the major axis).

In the case of the two remaining parameters, concentration c and anisotropy β, all halos show common trend in the discrepancies: β is underestimated while c overestimated, especially for the fitting including all dark matter particles. The discrepancies can be traced to the specific behaviour of the $\sigma_{\rm los}$ and $\kappa_{\rm los}$ profiles. For example, in the case of halo 1 the three kurtosis profiles (see figures 8.5-8.6) give similar β values, however the $\sigma_{\rm los}$ is much shallower for the observation angle of 45° than in the two remaining cases. As already mentioned, $\kappa_{\rm los}$ is mainly sensitive to the velocity anisotropy. Since the line-of-sight velocity dispersion profile can be made steeper in the center either with a steeper density profile or with more radial orbits, and since the anisotropy parameter is almost the same in all three directions, we can expect the inferred concentration to be somewhat lower for the 45° direction, which is indeed the case. The situation is similar for halo 4. The kurtosis forces the anisotropy to be very tangential, so the very steep $\sigma_{\rm los}$ profile at 0° (the leftmost middle panel of figure 8.7) requires a very large concentration of the density profile.

We have calculated the means and standard deviations of the differences between the fitted parameters ($\log M_{100}$, $\log c$, and β or $\log[\sigma_r/\sigma_\theta]$) and their values measured from the full 6D particle phase space. As expected from figure 8.10, we have found no significant dependence on the viewing angle. We show these quantities in table 8.2 for the 30 cases studied (3 for each of the 10 halos). We can see from this table that, with 40 particles per bin, the virial mass is a little more underestimated, while the concentration parameter is less overestimated and the anisotropy less underestimated. This behaviour of c and β can be understood by recalling that in the case of using only 40 particles per bin the sampling errors of the moments are much larger. For very negative kurtosis, small errors may enforce

Table 8.3: Statistical significances in the biases of the fitting procedure

Particles	$\log M_{100}$		$\log c$		β		$\log(\sigma_r/\sigma_\theta)$	
per bin	P_t	$P_{\rm b}$	P_t	$P_{\rm b}$	P_t	$P_{\rm b}$	P_t	$P_{\rm b}$
All	0.96	0.90	1	1	1	1	1	1
40	1	1	0.96	0.71	0.96	0.82	0.99	0.82

Notes: P_t and $P_{\rm b}$ are the probabilities for bias using the Student's t and binomial statistics, respectively.

low β estimates, which have to be made up by high c values (to reproduce velocity dispersion). Moreover, we find that the error bars listed in table 8.2 are similar in both cases, which indicates that the physical variations due to substructure and to the different shapes of halos dominate over the statistical noise or sampling errors.

Table 8.3 shows the statistical significance of the biases on the parameters, using the Student's t-statistic, which assumes Gaussian distributions of the parameters ($\log M_{100}$, $\log c$, β and $\log[\sigma_r/\sigma_\theta]$), and the binomial statistic testing the distribution of the signs of these parameters. The two statistical tests lead to different conclusions about the bias of the parameters: the Student's t-statistic always leads to significant biases, while the binomial statistic indicates no significant bias in concentration parameter and velocity anisotropy when only 40 particles are used per radial bin. This difference is caused by the skewed distributions of $\Delta \log c$, $\Delta\beta$ and $\Delta \log(\sigma_r/\sigma_\theta)$. Although the Student's t-statistic has the advantage of being more sensitive to the outliers in the distribution, it has the disadvantage of only being valid for Gaussian parent distributions, which is not the case here. In summary, in the case of 40 particles per radial bin, while the virial mass is biased towards lower values, we cannot conclude that the concentration parameter and velocity anisotropy are biased with the data we have.

Given the range of $\Delta \log c$ seen in the right plots of figure 8.10 (see also table 8.2), the discrepancies noted by Łokas & Mamon (2003) between their concentration parameter for Coma and the lower values obtained by Biviano & Girardi (2003) and Biviano et al. (2003) in their kinematical analysis of stacked clusters are reduced. Assuming that the departures in $\log c$ are independent of c and M_{100}, we deduce that the difference in $\log c$ between the measurement for the Coma cluster ($c = 9.4$) by Łokas & Mamon and the smaller concentration ($c = 5.5$) found by Biviano et al. can be accounted for in 27% of our 30 projected halos. On the other hand, the larger difference in $\log c$ between the Coma measurement and the concentration found by Biviano & Girardi (2003) can be accounted for in only 10% of our projected halos. Similarly, the difference in $\log c$ between Coma and the value ($c = 6$) extrapolated from the values found by Bullock et al. (2001) in their cosmological simulations, can be accounted for in 10 out of our 30 projected halos. Moreover, there is a non-negligible scatter in the relation between halo concentration and mass (Jing 2000; Bullock et al. 2001), which reduces even more any discrepancy with high concentration found for Coma.

8.5 Summary and conclusions

We studied the dynamical and kinematical properties of dark matter halos obtained in cosmological N-body simulations. First, using all the 3D information available, we calculated their virial masses, radii, anisotropy parameters and estimated their density profiles. Next, we obtained projected velocity moments, standard observables used to estimate the dark matter content of virialized objects. We then fitted those 'data' with spherical models based on Jeans equations in order to reproduce the 'observed' velocity moments.

Our approach was similar to the one of Tormen et al. (1997) who used lowest order Jeans equation to model the velocity dispersion and find the masses of simulated halos and compared them to the real masses of those halos. In addition to velocity dispersion, we used the projected kurtosis profiles in a similar way to that applied recently by Łokas & Mamon (2003) to infer the properties of the Coma cluster. The use of kurtosis allows us to estimate the anisotropy of the velocity distribution. Besides the virial mass and anisotropy parameter, we fitted the concentration of the density profiles of the halos.

Our results emphasize the difficulties in the use of the higher velocity moments to infer the properties of dark matter halos. The kurtosis seems to be very sensitive to the substructure and local matter flows. The discrepancies in the fitted properties of halo 4 can be traced to its peculiar mean radial velocity inside the virial radius which amounts to $0.26\, v_{100}$, while it is smaller than $0.1\, v_{100}$ for most of the remaining halos (also in the tangential directions). We therefore confirm the necessity of using only elliptical galaxies as tracers in the analysis of single clusters in order to minimize the effects of infall. Another source of problems lies in our very simple modeling

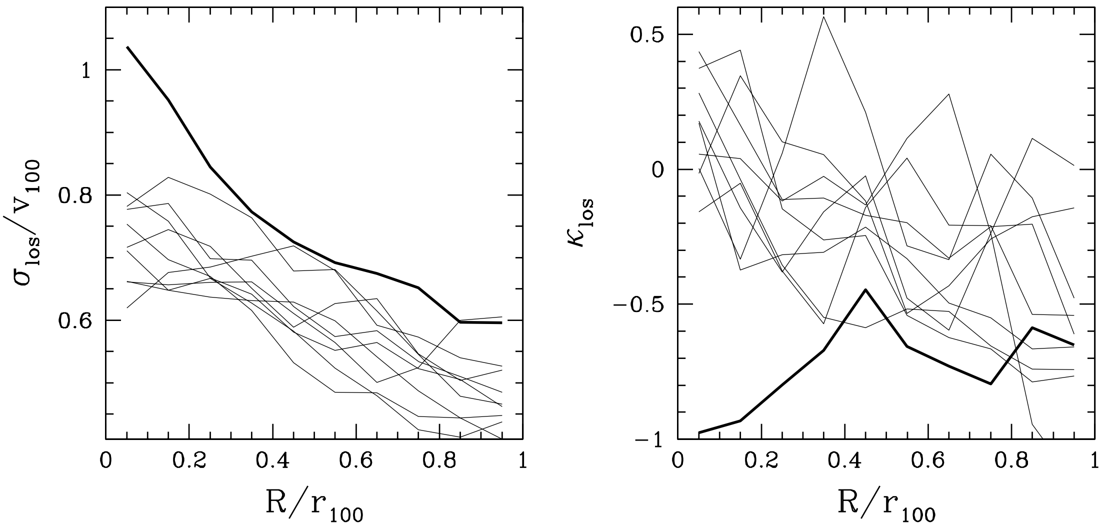

Figure 8.11: Line-of-sight velocity dispersion (*top*) and kurtosis (*bottom*) vs. projected distance to the center measured at 0° to the principal axis of the ten most massive halos in the simulation box. The *thick line* shows the results for halo 4, while the *thin lines* show the other nine halos.

of velocity anisotropy with constant β, while this quantity really shows some radial dependence. Again, in the case of halo 4 this dependence is rather unexpected, departing from isotropy in the very center of the halo.

In order to check to what extent the rather discrepant results for halo 4 are an exception or commonplace, we show, in figure 8.11, the line-of-sight velocity dispersion and kurtosis of the ten most massive halos in the simulation box for a observer placed along the major axis of each halo. The thick line shows the results for halo 4, while for the rest of the halos thin lines are used. We infer from figure 8.11 that the velocity moments of halo 4 follow an uncharacteristic pattern, probably caused by the unusually large mean radial velocity of this halo. We have also checked the pattern of the even velocity moments for the other two directions of observation used in Sections 8.3 and 8.4. In these cases, we found that the halo departing most from the general trend was halo 10, which has the highest mean velocity inside the virial radius with respect to v_{100} (with a smaller ratio than halo 4). Therefore, local matter flows, as witnessed by non-zero mean velocity profiles, produce perturbed line-of-sight velocity dispersion and/or kurtosis profiles, which themselves can lead to an inaccurate estimation of the mass, concentration and/or velocity anisotropy of a cluster of galaxies. It is important to note, however, that concentration and anisotropy seem to be more affected than the mass estimation, which is quite robust.

Figure 8.11 also shows a general trend of the behaviour of the kurtosis of the simulated halos. We notice that the kurtosis tends to be positive near the center of the halo and negative at large distances. This means that the velocity distribution is more peaked at the center and more flattened outside than the purely Gaussian distribution in agreement with a recent finding of Kazantzidis, Magorrian, & Moore (2003). But in spite of these departures from Maxwellian velocities at all radii, the Jeans analysis used here and in Łokas & Mamon (2003) produces fairly accurate measurements of the virial mass and concentration parameter (see figure 8.10 and table 8.2).

Although obvious interlopers to the halos have been removed in a similar fashion as in Łokas & Mamon (2003, see also Kent & Gunn 1982), our results could depend on the neighborhood of the analyzed halos. This would be the case if other halos with similar velocity were present in the direction of observation, so that their particles would not be removed by the procedure described in Section 8.3. To estimate the plausibility of such a case, we have calculated for every halo with mass up to one tenth of the mass of the most massive halo in the simulations (that makes a total of 40 halos) the probability that choosing an observer at a random position around it, there would be one or more perturbing halos with a mass greater than 25% of the mass of the studied halo, at a projected distance from the halo smaller than r_{100} and with a mean line-of-sight velocity within the interval $[\overline{v}_{\rm los} - 3v_{100}, \overline{v}_{\rm los} + 3v_{100}]$, where $\overline{v}_{\rm los}$ and v_{100} are the mean line-of-sight velocity and circular velocity at r_{100} of the analyzed halo. Choosing randomly 100 observers for each halo, we found that the probability of not finding any perturbing neighbouring halo was higher than 95% for 93% of the halos, while for two of the analyzed halos this probability was 88% and only one among the 40 halos had this probability smaller than 80% (77%). We can conclude from these numbers that it is quite unlikely that the results of the Jeans analysis are affected by neighbouring clusters. Moreover, the least isolated, i.e. the halo with the highest probability of having a perturbing halo around, among the top 10, halo 10, shows no specific bias in the parameter estimates (see figure 8.10).

Therefore, on one hand, the observed cosmic variance of the inner structure and internal kinematics of the massive halos in the cosmological simulations suggests that the typical properties of dark matter halos are best obtained through the analysis of stacked observations as performed by Carlberg et al. (1997a), Biviano & Girardi

(2003) and Biviano et al. (2003). But, on the other hand, in structures (clusters of galaxies) with near zero mean velocity profiles, this cosmic variance is much reduced. Therefore, it is well worth analyzing a single cluster with a large number of velocities and a near zero mean velocity, such as was done by Łokas & Mamon (2003) for the Coma cluster.

9 Summary and future perspectives

This thesis is focused on the implications of the dynamics of clusters on the H I content of galaxies. On one hand, we have analyzed the effects of infall motions on the amount of neutral gas in galaxies on the outskirts of clusters. The main target of this study has been the Virgo cluster region. Special attention has been paid to the role played by errors in galaxy distance estimates in the analysis of the infall pattern on the periphery of clusters. In addition, we have also studied the dynamics of the inner parts of these systems, analyzing the effects of an incomplete virialization on the determination of the internal kinematics of clusters, which is an essential factor in the investigation of the mechanism(s) behind the removal of neutral gas.

We have first inferred, in Chapter 3, the three-dimensional galaxy distribution of the Virgo cluster using quality distance estimates obtained by averaging distance moduli based upon the Tully-Fisher relationship taken from eight published datasets. Previous findings that the spiral distribution is substantially more elongated along the line-of-sight than in the plane of the sky were confirmed by our data even when taking into account the possible elongation introduced by estimated errors in distance measurements. In addition, an important east-west disparity in this effect has been detected, with the most distant objects concentrated in the western half. The filamentary structure of the spiral population and its orientation are also reflected by the H I-deficient objects alone. We found a central enhancement in the H I distribution extending from ~ 16 to 22 Mpc in distance from the Local Group. Most of this enhancement arises from galaxies that belong to the Virgo cluster proper. However, significant gas deficiencies were also detected outside the main body of the cluster in a probable group of galaxies at distances ~ 25–30 Mpc, lying in the region dominated by the southern edge of the M49 subcluster and clouds W′

and W, as well as in various foreground galaxies. Our results suggest that, in the Virgo region, the H I content of the galaxies is not a straightforward indicator of cluster membership.

The presence on the Virgo cluster outskirts of spiral galaxies with gas deficiencies as strong as those of the inner galaxies likely stripped by the intracluster medium has led us to explore, in Chapter 4, the possibility that some of these peripheral objects were not newcomers. A dynamical model for the collapse and rebound of spherical shells under the point mass and radial flow approximations was developed to account for the amplitude of the motions in the Virgo I cluster region. According to our analysis, it is not unfeasible that galaxies far from the cluster, including those in a gas-deficient group well to its background, went through its core a few Gyr ago. If confirmed, the implications of this finding would be: (1) that the majority of the H I-deficient spirals in the Virgo region might have been deprived of their neutral hydrogen by interactions with the hot intracluster medium; and (2) that objects spending a long time outside the cluster cores might keep their gas deficient status without altering their morphology.

In order to further investigate the possibility that the H I-deficient galaxies on the outskirts of the Virgo cluster have crossed already the cluster core, we have estimated, in Chapter 5, the maximum radius out to which galaxies can bounce out of a virialized system, using both cosmological N-body simulations and analytical arguments. We have shown that material that falls into a cosmological structure cannot bounce out beyond ~ 2.5 virial radii. After estimating the virial radius and mass of the Virgo cluster from X-ray observations, these peripheral H I-deficient galaxies appear to lie significantly farther away from the cluster center. Therefore, it does not seem plausible that these galaxies have crossed the cluster core if their distance estimates are accurate. In addition, we have used the N-body simulations to study the validity of the point mass model developed in Chapter 4. We have found that a model with a central mass between $\sim 1 - 2M_{100}$ is able to reproduce the main features of the radial phase space diagram of clusters.

In Chapter 6, the velocity field drawn by the Virgo cluster has been further studied by comparing the positions of both spiral and elliptical galaxies in velocity-distance plots with simulated diagrams obtained from cosmological N-body simulations. We have found that $\sim 20\%$ relative Tully-Fisher distance error is consistent with the great majority of the galaxies, except for a small fraction of them, whose positions in the velocity-distance diagram suggest grossly incorrect distances. We have shown, moreover, that distance errors may lead to an incorrect fitting of infall models that can generate significant errors in the distance and, especially, in the mass estimates of clusters.

In Chapter 7, we have investigated in detail the feasibility of four possibilities for the origin of the dearth of neutral gas in the outlying H I-deficient Virgo spirals: 1) that they have large relative distance errors and are in fact close enough to the cluster to have passed through its core and seen their gas removed by ram pressure stripping; 2) that their outer gas had been tidally stripped during interactions with other galaxies; 3) that their gas had been heated during recent mergers with smaller galaxies; and 4) an erroneous determination of their gas content, so that these galaxies were actually not H I-deficient (e.g. S0/a's misclassified as Sa's). We found that up to 11 among the 13 H I-deficient galaxies analyzed may have suffered the effects of ram pressure stripping, while possible evidences of tidal perturbations or recent mergers were found for up to 6 of these galaxies. Moreover, we checked that only in one case there could be a significant erroneous determination of the H I deficiency of the galaxies.

Finally, the cosmological N-body simulations of dark matter halos have also been used in Chapter 8 to study the effects of non-sphericity, substructure and streaming motions on the structure and internal kinematics of the inner region of clusters of galaxies recovered from the Jeans analysis. This method, contrary to the dynamical model used in Chapter 4, does not rely on (the relatively inaccurate) distance measurements, although is affected by uncertainties arising from the implicit assumption of sphericity and steady-state of clusters. To study the effect of these error sources, we have analyzed the kinematics of the ten most massive halos in the simulations. Fitting an NFW model to the 3D density profile, we determined the virial mass M_{100}, concentration parameter c and velocity anisotropy β of ten chosen halos, and then calculated the profiles of projected velocity moments, as they would be measured by a distant observer. Using these mock data, we applied a Jeans analysis for spherical objects to reproduce the line-of-sight velocity dispersion and kurtosis and fitted the three parameters (M_{100}, c and β). We found that the line-of-sight velocity dispersion and kurtosis profiles of a given halo can vary considerably with the angle of view of the observer. We showed that the virial mass, concentration parameter and velocity anisotropy of the halos can be reproduced satisfactorily independently of the halo shape, although the virial mass tends to be underestimated, the concentration parameter overestimated, while the recovered anisotropy is typically more tangential than the true one. The mass, concentration and velocity anisotropy of halos are recovered with better precision when their mean velocity profiles are near zero.

In summary, the determination of the origin of H I deficiency in cluster galaxies requires reliable values of their three-dimensional position and kinematics. With current uncertainties in the distance estimation of galaxies in the Virgo cluster region, the nearest rich galaxy aggregation and thus the easiest to study, it has been possible to draw only a general picture of the three-dimensional galaxy distribution of this cluster. The latter suggests the presence of H I-deficient galaxies on the outskirts of the cluster, with some of them likely at the turnaround radius after a passage through the cluster core. This would explain the presence of stripped galaxies up to $\sim 2r_{100}$, our estimation of the maximum rebound radius, which is more than twice the extension of the ICM revealed by the X-ray maps. Moreover, we have shown that, taking errors in distance properly into account, masses and distances to clusters can be estimated reliably from dynamical infall models. Besides, while the presence of deviations from sphericity, substructure and streaming motions do not allow an unambiguous determination of the internal structure and kinematics of clusters, we have shown that it is possible to obtain an acceptable estimate of their virial mass, concentration parameter and velocity anisotropy.

The topics developed in this work warrant further investigation: despite the evidences found suggesting that some H I-deficient galaxies apparently away from the Virgo cluster core could have lost their gas by interactions with the hot intracluster medium in an earlier passage through the core, we have neither been able to unambiguously confirm this hypothesis, nor to rule out other mechanisms of gas removal. For instance, these peripheral deficient objects may have been produced *in situ* by galaxy-galaxy interactions, predicted to operate in galaxy groups. In this sense, it would be desirable to perform multi-wavelength observations of the H I-deficient subclump detected in the Virgo background. Model calculations show that tidal stresses in disks generate extended tail structures in the stellar and neutral hydrogen distributions, the latter with surface densities well above the detection threshold of the most sensitive aperture-synthesis radio observations. In contrast, gas depletion arising from the ram pressure sweeping of the interstellar medium should produce a noticeable sharp drop in the surface density of atomic gas in the outer portions of the disks, as well as bow shocks and dense gaseous tails observable in X-rays.

Although we have been able to constrain considerably the maximum rebound radius out to which galaxies can bounce out of a virialized system, further constrains could be obtained by the analysis of the dynamical histories of dark matter particles from the output of the N-body simulations at different redshifts, i.e. following the secular variations of the positions of the dark matter particles with respect to the center of the cluster to check which of them have *really* crossed it.

With respect to our analysis of the reliability of the Jeans approach for characterizing the dynamics of clusters, it would be desirable to increment the number of studied dark matter halos to have a more statistically significant sample that allow us to put on a safer basis our conclusions about the effects of non-sphericity and substructure on the determination of the dynamical parameters of clusters. Moreover, it could also be interesting to investigate the sensitivity of our results to the adopted density profile (we have restricted ourselves to the NFW profile) by extending our analysis to other radial dark matter distributions, such as the steeper profile proposed by the simulations of Moore et al. (1998) or the core profile suggested by Burkert (1995).

As it has been already pointed out, the formation and evolution of galaxies can only be fully understood in a cosmological context within the hierarchical scenario for structure formation. The observed properties of the galaxies that nowadays populate the universe are set by the distribution of initial density fluctuations, the growth of dark matter halos and the physical processes affecting the baryons inside them. For that reason, the next logical step in our investigation of the processes leading to morphological changes would be the combination of all these ingredients into the analytical model of galaxy formation that we are currently developing.

A Additional tables

- Table A.1. Distance moduli for spiral galaxies in the Virgo cluster.

  In this table we show, in columns (1) to (3), different names for the spiral galaxies, and their coordinates, in columns (4) and (5). The morphological type comes in column (6) and in column (7), the membership given in Binggeli et al. (1993). Columns (8) to (15) contain the distance moduli to each galaxy given in the eight TF studies used for the spiral sample (see table 3.1). For seven of these galaxies, we list in column (16) their Cepheid distances given in Freedman et al. (2001) corrected for the effects of metallicity. Finally, in column (17), we list the distance moduli assigned to each galaxy, after the homogenization procedure, and their associated 1σ uncertainties.

- Table A.2. Parameters for the members of the 21-cm sample of spiral galaxies.

  We list in this table the parameters of the spiral sample defined in Chapter 3. Column (1) shows the name of the galaxy. Column (2), the systemic velocity of the galaxy and column (3) the distance to the galaxy with its associated errors. Columns (4) and (5) contain two different measurements of the H I deficiency (equations 3.1 and 3.3), while column (6) the H I line width. In column (7) we list the flags assigned to each galaxy (see footnotes) and finally, in column (8), the absolute B-magnitude of the galaxies, $M^{\mathrm{c}}_{B_{\mathrm{T}}}$, calculated from their total apparent corrected B-magnitude listed in LEDA and the distance estimate shown in column (3).

- Table A.3 Final sample of early-type galaxies in the Virgo cluster.

  We list in this table the parameters of the early-type sample defined in Chapter 6. Columns (1), (2) and (3) give the name of the galaxy, with its coordinates in columns (4) and (5). In column (6), we give the distance and its relative error in column (7). Column (8) gives the velocity relative to the Local Group and column (9) provides the sources for the distance (see footnote).

Table A.1: Distance moduli for spiral galaxies in the Virgo cluster

VCC (1)	NGC/ IC (2)	UGC/ CGCG (3)	R.A. (1950) (4)	Dec. (1950) (5)	T (6)	Mem. (7)	YFO97 (8)	MAH80 (9)	PT88 (10)	KCT88 (11)	Fou90 (12)	FTS98 (13)	Gav99 (14)	Ekh00 (15)	Ceph. (16)	Distance modulus (17)
...	...	CG69-10	$11^h57^m00^s.8$	$+14^\circ09'51''$	7	...	30.82	...	...	...	29.83	...	...	...	...	30.41 ± 0.37
...	I0755	U7001	$11^h58^m37^s.3$	$+14^\circ23'13''$	3	...	31.63	...	...	...	31.03	31.20	...	...	...	31.33 ± 0.18
...	N4037	U7002	$11^h58^m50^s.6$	$+13^\circ40'41''$	3	...	30.68	...	...	...	30.61	...	...	...	...	30.73 ± 0.09
...	N4064	U7054	$12^h01^m37^s.3$	$+18^\circ43'16''$	1	...	29.94	...	...	30.18	...	29.97	...	...	...	29.96 ± 0.09
...	N4067	U7048	$12^h01^m38^s.2$	$+11^\circ08'13''$	3	...	33.39	...	...	...	32.70	33.29	...	...	...	33.20 ± 0.20
...	...	U7133	$12^h06^m46^s.7$	$+19^\circ16'31''$	7	...	...	...	...	...	...	33.99	...	...	...	34.07
V0015	I3021	U7149	$12^h07^m21^s.6$	$+13^\circ19'42''$	9	M	33.79	...	...	...	...	...	...	...	...	33.72
V0025	N4152	U7169	$12^h08^m03^s.8$	$+16^\circ18'45''$	5	...	32.27	...	...	...	32.00	...	32.85	33.05	...	32.52 ± 0.36
V0034	I3033	U7181	$12^h08^m37^s.2$	$+13^\circ51'54''$	7	A	32.12	...	...	31.99	31.88	32.04	...	...	...	32.03 ± 0.08
V0047	N4165	U7201	$12^h09^m39^s.0$	$+13^\circ31'30''$	2	M	33.80	...	...	...	...	...	...	...	...	33.73
V0058	I0769	U7209	$12^h09^m59^s.4$	$+12^\circ24'00''$	4	M	32.39	...	32.68	...	...	32.99	32.92	33.52	...	32.93 ± 0.30
V0066	N4178	U7215	$12^h10^m13^s.8$	$+11^\circ08'48''$	7	...	30.51	31.02	30.52	29.44	30.22	30.78	30.86	30.59	...	30.59 ± 0.40
V0067	I3044	U7216	$12^h10^m15^s.6$	$+14^\circ15'18''$	6	A	31.57	...	...	30.69	30.94	30.94	...	...	...	31.05 ± 0.34
V0073	N4180	U7219	$12^h10^m28^s.9$	$+07^\circ19'01''$	2	W	33.33	...	...	...	32.50	33.53	32.72	33.57	...	33.13 ± 0.29
V0081	...	U7223	$12^h10^m53^s.0$	$+15^\circ03'00''$	7	A	32.87	...	...	...	33.70	...	...	...	...	33.37 ± 0.55
V0087	...	...	$12^h11^m07^s.0$	$+15^\circ43'54''$	9	A	31.92	...	...	32.02	31.75	...	...	...	...	31.92 ± 0.04
V0089	N4189	U7235	$12^h11^m14^s.4$	$+13^\circ42'12''$	6	M	32.64	...	31.63	...	...	32.64	...	33.01	...	32.39 ± 0.31
V0092	N4192	U7231	$12^h11^m15^s.4$	$+15^\circ10'23''$	3	A	30.81	30.67	30.65	30.55	30.59	30.98	30.36	31.17	...	30.66 ± 0.19
V0097	N4193	U7234	$12^h11^m21^s.0$	$+13^\circ27'00''$	4	M	32.78	...	...	...	...	32.98	32.64	33.54	...	32.91 ± 0.13
V0105	...	U7239	$12^h11^m36^s.0$	$+08^\circ03'00''$	10	...	32.08	...	...	...	32.61	...	...	...	...	32.43 ± 0.40
V0119	...	U7249	$12^h12^m05^s.4$	$+13^\circ05'24''$	10	A	31.86	...	31.78	31.89	31.62	31.78	...	...	...	31.85 ± 0.10
V0120	N4197	U7247	$12^h12^m04^s.9$	$+06^\circ05'01''$	6	...	31.82	...	...	31.89	31.68	31.56	31.91	...	...	31.82 ± 0.18
V0126	I3059	U7254	$12^h12^m22^s.8$	$+13^\circ44'12''$	10	A	31.87	...	...	...	31.73	31.92	...	...	...	31.89 ± 0.05
V0131	I3061	U7255	$12^h12^m31^s.8$	$+14^\circ18'24''$	5	M	33.11	...	...	...	32.75	32.70	...	33.37	...	32.90 ± 0.12
V0132	...	...	$12^h12^m32^s.3$	$+13^\circ18'41''$	8	A	30.67	...	...	...	...	29.77	...	...	...	30.16 ± 0.47
V0143	I3066	U7262	$12^h12^m43^s.2$	$+13^\circ45'06''$	4	A	32.89	...	...	...	32.33	32.04	...	...	...	32.47 ± 0.33
V0145	N4206	U7260	$12^h12^m44^s.4$	$+13^\circ18'12''$	4	A	31.48	31.36	31.01	31.47	31.20	31.15	31.29	...	...	31.36 ± 0.15

Table A.1: continued

VCC (1)	NGC/ IC (2)	UGC/ CGCG (3)	R.A. (1950) (4)	Dec. (1950) (5)	T (6)	Mem. (7)	YFO97 (8)	MAH80 (9)	PT88 (10)	KCT88 (11)	Fou90 (12)	FTS98 (13)	Gav99 (14)	Ekh00 (15)	Ceph. (16)	Distance modulus (17)
V0152	N4207	U7268	$12^h12^m58^s.2$	$+09^\circ51'48''$	6	...	31.87	...	...	32.00	31.65	31.75	31.08	...	...	31.70 ± 0.27
V0157	N4212	U7275	$12^h13^m06^s.6$	$+14^\circ10'48''$	5	A	31.36	...	31.45	31.54	31.23	31.23	31.04	31.98	...	31.36 ± 0.17
V0162	I3074	U7279	$12^h13^m13^s.4$	$+10^\circ58'36''$	8	...	32.51	...	32.64	32.49	32.01	32.21	...	...	...	32.46 ± 0.28
V0167	N4216	U7284	$12^h13^m21^s.6$	$+13^\circ25'36''$	3	A	31.13	30.81	30.81	30.73	31.23	31.35	30.65	31.34	...	30.96 ± 0.29
V0187	N4222	U7291	$12^h13^m49^s.8$	$+13^\circ35'12''$	6	A	31.80	...	...	31.87	31.70	31.46	...	32.91	...	31.85 ± 0.30
V0199	N4224	U7292	$12^h14^m00^s.4$	$+07^\circ44'20''$	1	W	33.30	...	...	...	...	...	...	...	...	33.24
V0213	I3094	U7305	$12^h14^m23^s.4$	$+13^\circ54'12''$	5	A	33.37	...	...	...	32.60	...	...	...	...	33.06 ± 0.25
V0222	N4235	U7310	$12^h14^m35^s.7$	$+07^\circ28'11''$	1	W	31.48	...	...	...	...	...	...	31.76	...	31.27 ± 0.18
V0224	I3099	U7313	$12^h14^m37^s.2$	$+12^\circ44'54''$	6	M	32.39	...	...	...	32.55	32.37	...	...	...	32.50 ± 0.19
V0226	N4237	U7315	$12^h14^m38^s.2$	$+15^\circ36'08''$	4	A	31.63	...	...	32.15	31.80	31.95	31.48	32.52	...	31.86 ± 0.19
V0241	I3105	U7326	$12^h15^m01^s.2$	$+12^\circ40'00''$	10	A	30.48	...	...	30.56	30.74	30.69	...	...	...	30.62 ± 0.20
V0267	I3115	U7333	$12^h15^m26^s.4$	$+06^\circ55'53''$	6	...	34.92	...	...	...	31.96	...	32.08	...	...	32.23 ± 0.05
V0289	N4252	U7343	$12^h15^m57^s.6$	$+05^\circ50'18''$	3	...	31.81	...	...	...	...	31.62	...	...	...	31.68 ± 0.08
V0297	...	CG42-1	$12^h16^m05^s.4$	$+06^\circ59'06''$	5	...	...	...	...	...	...	31.85	...	...	...	31.84
V0307	N4254	U7345	$12^h16^m16^s.8$	$+14^\circ41'42''$	5	A	30.56	...	31.28	...	30.54	31.42	...	...	...	31.04 ± 0.41
V0318	I0776	U7352	$12^h16^m30^s.0$	$+09^\circ08'06''$	8	...	32.36	...	32.24	32.27	31.99	32.58	...	...	...	32.37 ± 0.17
V0341	N4260	U7361	$12^h16^m48^s.8$	$+06^\circ22'40''$	1	W	33.14	...	...	...	...	...	...	33.42	...	32.99 ± 0.09
V0343	I3148	...	$12^h16^m48^s.0$	$+08^\circ09'00''$	8	W	31.93	...	...	...	...	...	...	...	...	31.88
V0382	N4273	U7380	$12^h17^m22^s.3$	$+05^\circ37'27''$	5	W	31.83	...	...	...	...	32.27	32.19	32.91	...	32.20 ± 0.25
V0393	N4276	U7385	$12^h17^m34^s.7$	$+07^\circ58'10''$	6	W	32.23	...	...	...	...	...	...	...	...	32.18
V0404	...	U7387	$12^h17^m42^s.9$	$+04^\circ28'47''$	7	W	...	...	...	...	...	32.67	...	...	...	32.70
V0415	...	CG42-36	$12^h17^m52^s.8$	$+07^\circ11'12''$	5	W	33.31	...	...	...	...	31.63	...	...	...	32.43 ± 0.82
V0449	N4289	U7403	$12^h18^m30^s.0$	$+04^\circ00'00''$	6	W	...	...	...	...	...	33.20	...	33.75	...	33.26 ± 0.01
V0453	...	...	$12^h18^m33^s.0$	$+11^\circ52'24''$	6	A	32.74	...	...	32.42	31.31	...	...	...	...	32.18 ± 0.48
V0460	N4293	U7405	$12^h18^m41^s.1$	$+18^\circ39'36''$	0	A	31.14	...	...	30.81	30.91	...	30.53	31.03	...	30.76 ± 0.32
V0465	N4294	U7407	$12^h18^m45^s.0$	$+11^\circ47'24''$	6	A	30.66	31.15	...	30.85	30.55	30.66	30.86	...	...	30.83 ± 0.24
V0483	N4298	U7412	$12^h19^m00^s.6$	$+14^\circ53'06''$	5	A	31.03	...	...	32.22	31.04	31.19	...	...	...	31.38 ± 0.44

Table A.1: continued

VCC (1)	NGC/ IC (2)	UGC/ CGCG (3)	R.A. (1950) (4)	Dec. (1950) (5)	T (6)	Mem. (7)	YFO97 (8)	MAH80 (9)	PT88 (10)	KCT88 (11)	Fou90 (12)	FTS98 (13)	Gav99 (14)	Ekh00 (15)	Ceph. (16)	Distance modulus (17)
V0491	N4299	U7414	$12^h19^m07.^s8$	$+11^\circ46'48''$	8	A	...	...	...	...	32.49	...	...	...	...	32.71
V0497	N4302	U7418	$12^h19^m10.^s2$	$+14^\circ52'36''$	5	A	...	...	...	31.82	31.53	31.51	30.78	32.01	...	31.44 ± 0.33
V0509	...	U7423	$12^h19^m22.^s3$	$+06^\circ43'43''$	9	W'	32.67	...	...	32.67	32.27	33.13	...	...	...	32.71 ± 0.27
V0512	...	U7421	$12^h19^m23.^s0$	$+12^\circ14'35''$	10	A	32.05	...	...	32.02	31.30	...	...	...	...	31.82 ± 0.21
V0514	...	U7424	$12^h19^m25.^s2$	$+08^\circ57'06''$	10	B	32.00	...	...	...	30.70	...	...	...	...	31.43 ± 0.52
V0522	N4305	U7432	$12^h19^m31.^s2$	$+13^\circ01'06''$	1	A	...	...	...	33.15	...	...	...	...	...	33.05
V0524	N4307	U7431	$12^h19^m33.^s0$	$+09^\circ19'06''$	3	B	...	...	...	32.75	31.91	32.02	32.05	32.49	...	32.19 ± 0.26
V0534	N4309	U7435	$12^h19^m38.^s9$	$+07^\circ25'20''$	-1	W'	32.26	...	...	...	31.61	...	...	...	...	32.02 ± 0.19
V0559	N4312	U7442	$12^h19^m59.^s4$	$+15^\circ48'58''$	2	A	30.46	...	...	...	30.03	...	29.84	...	...	30.16 ± 0.25
V0566	...	...	$12^h20^m05.^s0$	$+08^\circ34'24''$	9	W'	32.17	...	...	32.25	31.68	...	...	...	...	32.06 ± 0.11
V0567	I3225	U7441	$12^h20^m06.^s5$	$+06^\circ57'14''$	8	W	32.33	...	...	...	...	32.40	...	...	...	32.34 ± 0.06
V0570	N4313	U7445	$12^h20^m06.^s6$	$+12^\circ04'54''$	2	A	30.79	...	...	30.72	30.82	30.91	30.34	...	...	30.73 ± 0.22
V0576	N4316	U7447	$12^h20^m10.^s2$	$+09^\circ36'36''$	6	B	32.42	...	...	32.55	32.30	32.28	31.70	32.88	...	32.30 ± 0.22
V0593	I3229	U7448	$12^h20^m18.^s0$	$+06^\circ57'00''$	4	W'	32.07	...	...	...	31.83	31.52	...	...	...	31.86 ± 0.25
V0596	N4321	U7450	$12^h20^m23.^s2$	$+16^\circ06'00''$	4	A	30.45	...	31.32	...	30.41	30.91	30.82	30.94	30.91	30.91 ± 0.07
V0613	N4324	U7451	$12^h20^m32.^s5$	$+05^\circ31'36''$	-1	W	31.81	...	...	...	...	...	31.19	...	...	31.53 ± 0.23
V0620	I3239	...	$12^h20^m37.^s8$	$+12^\circ00'18''$	9	A	32.36	...	...	31.49	30.63	...	...	...	...	31.52 ± 0.61
V0630	N4330	U7456	$12^h20^m45.^s0$	$+11^\circ38'42''$	6	A	31.21	...	...	31.76	31.30	31.38	31.31	...	...	31.43 ± 0.17
V0656	N4343	U7465	$12^h21^m05.^s0$	$+07^\circ13'58''$	3	W'	32.75	...	...	...	32.24	32.39	31.71	32.54	...	32.27 ± 0.32
V0664	I3258	U7470	$12^h21^m12.^s0$	$+12^\circ45'18''$	10	A	30.18	...	...	...	30.50	31.57	...	...	...	30.80 ± 0.58
V0667	I3259	U7469	$12^h21^m16.^s2$	$+07^\circ27'49''$	8	W'	32.00	...	...	...	31.80	32.14	...	...	...	32.04 ± 0.08
V0688	N4353	...	$12^h21^m24.^s0$	$+08^\circ04'00''$	10	B	32.84	...	...	...	32.05	32.68	...	...	...	32.59 ± 0.23
V0692	N4351	U7476	$12^h21^m29.^s4$	$+12^\circ28'54''$	2	A	30.16	...	...	...	30.18	30.01	30.48	...	...	30.24 ± 0.23
V0697	I3267	U7474	$12^h21^m33.^s0$	$+07^\circ19'12''$	6	W'	32.89	...	...	...	...	...	...	...	...	32.83
V0699	I3268	U7477	$12^h21^m34.^s7$	$+06^\circ53'00''$	5	B	32.81	...	...	...	32.11	...	...	...	...	32.54 ± 0.21
V0713	N4356	U7482	$12^h21^m42.^s1$	$+08^\circ48'48''$	6	B	31.96	...	...	32.56	32.37	32.36	...	...	...	32.34 ± 0.26
V0737	...	CG42-86	$12^h22^m06.^s6$	$+04^\circ16'36''$	8	W	...	...	...	...	...	32.17	...	...	...	32.17

Table A.1: continued

VCC (1)	NGC/ IC (2)	UGC/ CGCG (3)	R.A. (1950) (4)	Dec. (1950) (5)	T (6)	Mem. (7)	YFO97 (8)	MAH80 (9)	PT88 (10)	KCT88 (11)	Fou90 (12)	FTS98 (13)	Gav99 (14)	Ekh00 (15)	Ceph. (16)	Distance modulus (17)
V0740	...	...	$12^h22^m07^s.0$	$+08°46'47''$	10	B	33.22	...	...	32.75	32.21	...	...	...	...	32.75 ± 0.30
V0768	I3298	...	$12^h22^m36^s.0$	$+17°17'00''$	4	...	32.79	...	...	...	32.34	32.59	...	...	...	32.63 ± 0.07
V0785	N4378	U7497	$12^h22^m44^s.3$	$+05°12'13''$	1	W	33.46	...	...	...	...	...	...	...	...	33.40
V0787	N4376	U7498	$12^h22^m45^s.3$	$+06°01'06''$	10	...	31.49	...	...	31.31	31.13	31.55	31.89	...	...	31.52 ± 0.29
V0792	N4380	U7503	$12^h22^m49^s.8$	$+10°17'36''$	2	B	31.47	31.20	31.30	31.27	32.09	32.13	31.73	32.42	...	31.70 ± 0.37
V0801	N4383	U7507	$12^h22^m53^s.8$	$+16°44'48''$	1	A	30.90	...	...	...	30.95	...	31.19	...	...	31.11 ± 0.18
V0809	I3311	U7510	$12^h23^m00^s.6$	$+12°32'12''$	7	A	31.62	...	...	31.50	31.43	31.38	...	...	...	31.50 ± 0.12
V0827	I3322A	U7513	$12^h23^m09^s.9$	$+07°29'36''$	6	B	31.94	31.51	31.74	32.18	32.12	31.66	31.58	32.29	...	31.89 ± 0.23
V0836	N4388	U7520	$12^h23^m13^s.8$	$+12°56'18''$	3	A	31.11	31.09	30.75	30.84	30.89	31.13	31.13	32.05	...	31.10 ± 0.19
V0849	N4390	U7519	$12^h23^m19^s.8$	$+10°43'48''$	5	A	31.45	...	...	...	31.21	32.15	32.09	...	...	31.82 ± 0.40
V0851	I3322	U7518	$12^h23^m21^s.6$	$+07°50'00''$	6	B	31.72	...	...	31.67	31.57	31.43	...	...	...	31.61 ± 0.14
V0857	N4394	U7523	$12^h23^m24^s.7$	$+18°29'30''$	3	A	31.93	...	...	...	31.83	...	...	...	...	31.96 ± 0.08
V0859	...	U7522	$12^h23^m25^s.8$	$+03°42'30''$	6	W	...	...	...	...	...	32.69	...	33.37	...	32.79 ± 0.07
V0865	N4396	U7526	$12^h23^m27^s.5$	$+15°56'55''$	7	A	30.58	...	...	30.62	30.25	30.33	31.00	...	...	30.58 ± 0.28
V0873	N4402	U7528	$12^h23^m34^s.8$	$+13°23'24''$	3	A	31.13	...	...	31.31	30.81	31.06	30.29	32.07	...	31.02 ± 0.35
V0874	N4405	U7529	$12^h23^m35^s.8$	$+16°27'26''$	0	...	31.52	...	...	...	30.15	30.63	...	...	...	30.80 ± 0.49
V0905	N4411A	U7537	$12^h23^m56^s.4$	$+09°08'54''$	5	B	30.27	...	...	...	30.68	33.04	...	...	...	30.89 $^{(b)}$
V0912	N4413	U7538	$12^h24^m00^s.0$	$+12°53'18''$	2	A	30.95	...	...	30.45	31.01	31.29	31.01	...	...	30.97 ± 0.33
V0938	N4416	U7541	$12^h24^m14^s.5$	$+08°11'51''$	6	B	33.12	...	...	...	32.36	...	...	...	...	32.82 ± 0.24
V0939	N4411B	U7546	$12^h24^m15^s.0$	$+09°09'42''$	6	B	32.23	...	...	...	32.05	...	...	...	...	32.23 ± 0.05
V0950	I3356	U7547	$12^h24^m21^s.6$	$+11°50'18''$	10	A	31.71	...	30.70	...	30.12	...	...	...	...	30.94 ± 0.55
V0952	...	...	$12^h24^m22^s.7$	$+10°09'17''$	5	B	32.48	...	...	...	31.74	31.55	...	...	...	31.97 ± 0.37
V0957	N4420	U7549	$12^h24^m24^s.6$	$+02°46'15''$	5	W	...	...	...	...	...	31.03	30.93	...	...	31.00 ± 0.01
V0958	N4419	U7551	$12^h24^m25^s.1$	$+15°19'28''$	1	A	30.73	...	...	30.82	30.15	...	30.97	...	...	30.71 ± 0.24
V0971	N4423	U7556	$12^h24^m36^s.2$	$+06°09'23''$	8	...	31.09	...	...	...	31.17	30.84	31.55	...	...	31.23 ± 0.34
V0975	...	U7557	$12^h24^m36^s.0$	$+07°32'00''$	9	B	31.73	...	...	...	33.89	...	...	...	...	... $^{(a)}$
V0979	N4424	U7561	$12^h24^m40^s.2$	$+09°41'48''$	1	B	28.00	...	...	28.25	...	...	...	...	...	28.07 ± 0.09

Table A.1: continued

VCC (1)	NGC/ IC (2)	UGC/ CGCG (3)	R.A. (1950) (4)	Dec. (1950) (5)	T (6)	Mem. (7)	YFO97 (8)	MAH80 (9)	PT88 (10)	KCT88 (11)	Fou90 (12)	FTS98 (13)	Gav99 (14)	Ekh00 (15)	Ceph. (16)	Distance modulus (17)
V0980	I3365	U7563	$12^h24^m42.^s0$	+16°12′00″	10	A	31.05	...	...	31.25	30.76	30.71	...	...	...	30.95 ± 0.19
V0989	...	...	$12^h24^m45.^s0$	+07°56′54″	7	W'	34.35	...	...	...	...	...	...	...	...	34.28
V0995	I3371	U7565	$12^h24^m49.^s2$	+11°08′36″	6	A	32.16	...	...	31.99	31.95	31.33	...	...	...	31.87 ± 0.34
V1002	N4430	U7566	$12^h24^m53.^s6$	+06°32′23″	3	B	32.76	...	...	...	31.35	...	...	...	...	32.14 ± 0.57
V1011	...	U7567	$12^h24^m56.^s7$	+07°55′17″	10	B	32.53	...	...	32.31	31.70	...	...	...	...	32.21 ± 0.23
V1043	N4438	U7574	$12^h25^m13.^s8$	+13°17′06″	1	A	...	29.79	...	...	29.79	30.51	30.26	30.80	...	30.08 ± 0.27
V1048	...	U7579	$12^h25^m22.^s6$	+05°59′50″	8	W	33.03	...	...	...	33.07	33.01	...	...	...	33.10 ± 0.14
V1086	N4445	U7587	$12^h25^m43.^s8$	+09°42′48″	2	B	31.54	...	...	...	31.29	31.30	31.26	...	...	31.41 ± 0.10
V1091	...	U7590	$12^h25^m46.^s2$	+09°00′18″	4	B	31.79	...	...	32.03	31.67	31.25	...	...	...	31.70 ± 0.29
V1110	N4450	U7594	$12^h25^m58.^s0$	+17°21′40″	2	A	30.77	30.22	30.67	30.43	30.56	31.35	30.51	31.88	...	30.74 ± 0.37
...	I3391	U7595	$12^h25^m55.^s6$	+18°41′32″	6	...	31.07	...	...	...	31.86	...	...	...	...	31.55 ± 0.52
V1118	N4451	U7600	$12^h26^m08.^s4$	+09°32′06″	3	B	32.23	...	31.97	...	32.04	32.37	32.16	...	...	32.29 ± 0.07
V1126	I3392	U7602	$12^h26^m12.^s0$	+15°16′40″	2	A	31.00	...	...	...	31.13	30.82	30.36	...	...	30.87 ± 0.35
...	N4455	U7603	$12^h26^m14.^s1$	+23°06′01″	7	...	29.85	...	...	29.96	...	29.20	...	...	...	29.59 ± 0.36
V1189	I3414	U7621	$12^h26^m56.^s2$	+07°02′50″	8	B	31.24	...	...	31.01	30.58	31.01	...	...	...	30.97 ± 0.15
V1193	N4466	U7626	$12^h26^m58.^s0$	+07°58′20″	2	B	32.31	...	...	31.90	32.33	32.21	...	...	...	32.21 ± 0.26
V1205	N4470	U7627	$12^h27^m05.^s3$	+08°05′56″	1	...	30.82	...	...	...	30.77	31.13	31.26	...	...	31.05 ± 0.21
V1290	N4480	U7647	$12^h27^m53.^s4$	+04°31′27″	5	W	...	...	...	...	...	32.94	32.64	33.36	...	32.90 ± 0.06
V1330	N4492	U7656	$12^h28^m27.^s4$	+08°21′13″	1	B	31.69	...	...	...	32.61	...	...	...	...	32.23 ± 0.59
V1356	I3446	...	$12^h28^m51.^s6$	+11°46′00″	9	A	33.48	...	...	32.62	31.91	...	...	...	...	32.69 ± 0.54
V1375	N4496A	U7668A	$12^h29^m05.^s8$	+04°12′56″	8	W	...	...	...	...	...	...	...	...	30.86	30.86 ± 0.03
V1379	N4498	U7669	$12^h29^m08.^s8$	+17°07′46″	6	A	30.82	30.34	30.36	30.63	30.72	30.98	30.99	...	...	30.72 ± 0.26
V1393	I0797	U7676	$12^h29^m22.^s9$	+15°24′00″	6	...	31.49	...	...	...	31.60	31.37	31.83	...	...	31.65 ± 0.27
V1401	N4501	U7675	$12^h29^m27.^s6$	+14°41′42″	3	A	31.20	31.12	31.25	31.13	30.82	31.58	30.87	31.98	...	31.22 ± 0.20
V1410	N4502	U7677	$12^h29^m32.^s2$	+16°57′47″	6	A	32.53	...	...	32.80	32.25	...	...	...	...	32.55 ± 0.11
V1442	I3474	U7687	$12^h30^m04.^s0$	+02°56′18″	7	W	...	...	...	...	...	30.95	...	...	...	30.90
V1450	I3476	U7695	$12^h30^m10.^s8$	+14°19′30″	10	A	30.90	...	...	...	31.28	31.71	...	...	...	31.35 ± 0.36

Table A.1: continued

VCC (1)	NGC/ IC (2)	UGC/ CGCG (3)	R.A. (1950) (4)	Dec. (1950) (5)	T (6)	Mem. (7)	YFO97 (8)	MAH80 (9)	PT88 (10)	KCT88 (11)	Fou90 (12)	FTS98 (13)	Gav99 (14)	Ekh00 (15)	Ceph. (16)	Distance modulus (17)
...	...	U7697	$12^h30^m20.^s8$	$+20^\circ27'40''$	6	...	...	...	...	...	...	32.28	...	...	...	32.29
V1486	I3483	...	$12^h30^m39.^s0$	$+11^\circ37'12''$	3	A	32.30	...	...	...	33.63	33.73	...	...	...	33.83 ± 0.03
V1508	N4519	U7709	$12^h30^m57.^s6$	$+08^\circ55'48''$	7	B	31.27	31.82	31.25	31.28	31.38	31.84	31.33	32.57	...	31.61 ± 0.32
V1516	N4522	U7711	$12^h31^m07.^s8$	$+09^\circ27'00''$	6	B	31.06	30.48	30.67	31.23	30.45	30.92	30.71	...	...	30.82 ± 0.20
V1524	N4523	U7713	$12^h31^m18.^s0$	$+15^\circ26'00''$	9	A	32.16	...	...	...	33.25	...	...	...	...	32.79 ± 0.68
V1532	I0800	U7716	$12^h31^m25.^s8$	$+15^\circ37'51''$	5	...	30.66	...	...	...	31.29	31.05	30.93	...	...	31.04 ± 0.32
V1540	N4527	U7721	$12^h31^m35.^s5$	$+02^\circ55'45''$	4	W	...	...	...	...	...	31.21	30.03	31.38	...	30.62 ± 0.47
V1554	N4532	U7726	$12^h31^m46.^s7$	$+06^\circ44'43''$	10	B	29.94	31.10	30.65	31.01	30.01	...	30.23	...	...	30.55 ± 0.46
V1555	N4535	U7727	$12^h31^m47.^s9$	$+08^\circ28'25''$	5	B	30.47	31.19	30.60	30.51	30.16	30.78	30.67	31.68	30.99	30.99 ± 0.05
V1557	N4533	U7725	$12^h31^m48.^s7$	$+02^\circ36'10''$	7	W	...	...	...	...	...	31.43	...	...	...	31.40
V1562	N4536	U7732	$12^h31^m53.^s5$	$+02^\circ27'50''$	4	W	...	...	...	...	...	30.74	30.65	...	30.87	30.87 ± 0.04
V1566	I3517	U7733	$12^h31^m58.^s8$	$+09^\circ25'54''$	9	B	31.96	...	...	31.70	31.26	32.11	...	...	...	31.78 ± 0.25
V1569	I3520	...	$12^h32^m00.^s0$	$+13^\circ46'54''$	6	A	33.47	...	...	31.65	32.03	31.73	...	...	...	31.84 ± 0.29
V1575	I3521	U7736	$12^h32^m06.^s8$	$+07^\circ26'09''$	10	B	31.28	...	...	31.79	31.07	...	31.23	...	...	31.39 ± 0.18
V1581	...	U7739	$12^h32^m13.^s0$	$+06^\circ34'35''$	10	B	32.58	...	...	...	32.77	...	...	...	...	32.76 ± 0.23
V1588	N4540	U7742	$12^h32^m20.^s1$	$+15^\circ49'37''$	6	A	31.83	...	...	...	30.39	31.39	30.51	...	...	31.07 ± 0.52
V1605	...	...	$12^h32^m42.^s5$	$+10^\circ42'24''$	5	A	32.45	...	...	...	32.04	31.25	...	...	...	31.96 ± 0.53
V1615	N4548	U7753	$12^h32^m55.^s2$	$+14^\circ46'24''$	3	A	30.81	...	30.89	...	30.66	31.31	30.88	31.65	31.05	31.05 ± 0.05
V1624	N4544	U7756	$12^h33^m03.^s3$	$+03^\circ18'45''$	1	S	...	...	...	31.73	...	31.68	31.17	...	...	31.52 ± 0.18
V1644	...	...	$12^h33^m21.^s0$	$+14^\circ08'00''$	9	A	33.17	...	...	33.28	32.75	...	...	...	...	33.09 ± 0.09
...	N4561	U7768	$12^h33^m38.^s4$	$+19^\circ35'56''$	7	...	32.01	...	...	...	31.42	...	...	...	...	31.80 ± 0.16
V1673	N4567	U7777	$12^h34^m01.^s2$	$+11^\circ32'00''$	4	A	...	...	...	...	...	...	...	32.68	...	32.10
V1676	N4568	U7776	$12^h34^m02.^s4$	$+11^\circ30'54''$	4	A	...	...	...	...	...	31.36	...	32.10	...	31.39 ± 0.07
V1678	I3576	U7781	$12^h34^m06.^s0$	$+06^\circ54'00''$	9	B	33.30	...	...	...	30.41	...	...	...	...	... $^{(a)}$
V1686	I3583	U7784	$12^h34^m12.^s6$	$+13^\circ32'00''$	10	A	30.17	...	...	31.17	30.46	...	30.68	...	...	30.66 ± 0.34
V1690	N4569	U7786	$12^h34^m18.^s6$	$+13^\circ26'24''$	2	A	29.77	29.56	...	29.49	29.69	30.05	30.37	31.03	...	29.87 ± 0.37
V1696	N4571	U7788	$12^h34^m25.^s2$	$+14^\circ29'48''$	6	A	30.99	...	30.55	...	30.84	31.70	31.41	...	...	31.18 ± 0.38

Table A.1: continued

VCC (1)	NGC/ IC (2)	UGC/ CGCG (3)	R.A. (1950) (4)	Dec. (1950) (5)	T (6)	Mem. (7)	YFO97 (8)	MAH80 (9)	PT88 (10)	KCT88 (11)	Fou90 (12)	FTS98 (13)	Gav99 (14)	Ekh00 (15)	Ceph. (16)	Distance modulus (17)
V1699	I3591	U7790	$12^h34^m29^s.9$	$+07^\circ11'59''$	10	B	31.02	...	...	31.20	30.69	...	...	...	...	31.00 ± 0.09
V1725	...	...	$12^h35^m09^s.0$	$+08^\circ50'00''$	10	B	31.66	...	...	31.57	30.71	...	...	...	...	31.34 ± 0.30
V1726	...	U7795	$12^h35^m13^s.0$	$+07^\circ22'47''$	10	B	31.08	...	...	...	31.03	31.20	...	...	...	31.15 ± 0.09
V1727	N4579	U7796	$12^h35^m12^s.0$	$+12^\circ05'36''$	3	A	31.30	...	31.06	...	31.07	31.74	31.61	31.86	...	31.41 ± 0.24
V1730	N4580	U7794	$12^h35^m15^s.6$	$+05^\circ38'38''$	2	...	31.35	...	...	...	31.34	...	...	...	...	31.43 ± 0.12
V1758	...	U7802	$12^h35^m48^s.0$	$+08^\circ10'00''$	6	...	31.73	...	...	...	32.07	31.65	...	...	...	31.87 ± 0.30
V1760	N4586	U7804	$12^h35^m55^s.1$	$+04^\circ35'37''$	1	S	...	...	...	31.24	...	...	30.40	...	...	30.79 ± 0.36
V1780	N4591	U7821	$12^h36^m39^s.9$	$+06^\circ17'11''$	3	...	33.25	...	...	...	...	33.64	...	33.80	...	33.41 ± 0.22
V1791	I3617	U7822	$12^h36^m53^s.0$	$+08^\circ14'12''$	10	...	31.34	...	31.06	31.89	30.92	...	...	...	...	31.37 ± 0.26
V1811	N4595	U7826	$12^h37^m20^s.9$	$+15^\circ34'23''$	3	A	30.66	...	...	30.91	30.78	30.71	30.94	...	...	30.82 ± 0.17
V1859	N4606	U7839	$12^h38^m26^s.4$	$+12^\circ11'12''$	1	A	30.52	...	...	30.58	30.37	...	...	...	...	30.52 ± 0.04
V1868	N4607	U7843	$12^h38^m40^s.8$	$+12^\circ09'54''$	3	A	31.53	...	...	31.86	31.36	31.49	...	...	...	31.58 ± 0.12
V1923	N4630	U7871	$12^h39^m58^s.5$	$+04^\circ14'03''$	10	S	...	...	...	...	...	31.14	30.91	...	...	31.05 ± 0.06
V1929	N4633	U7874	$12^h40^m06^s.6$	$+14^\circ37'48''$	8	A	31.63	...	...	32.57	31.45	31.86	31.48	...	...	31.84 ± 0.33
V1932	N4634	U7875	$12^h40^m10^s.2$	$+14^\circ34'12''$	6	A	31.53	...	...	...	31.59	31.27	...	...	...	31.51 ± 0.23
V1933	...	...	$12^h40^m12^s.5$	$+07^\circ36'42''$	2	...	32.82	...	...	...	32.49	...	...	...	...	32.73 ± 0.02
V1943	N4639	U7884	$12^h40^m21^s.0$	$+13^\circ31'54''$	4	A	31.74	...	31.57	32.07	31.74	32.55	32.00	32.53	31.71	31.71 ± 0.08
V1955	N4641	U7889	$12^h40^m36^s.0$	$+12^\circ19'24''$	-2	A	29.64	...	...	...	29.17	...	...	...	...	29.50 ± 0.12
V1972	N4647	U7896	$12^h41^m01^s.2$	$+11^\circ51'12''$	5	A	...	...	30.65	...	31.09	31.57	31.19	31.95	...	31.25 ± 0.26
...	N4651	U7901	$12^h41^m12^s.5$	$+16^\circ40'05''$	5	...	31.57	31.45	31.58	31.46	31.46	32.16	...	32.57	...	31.74 ± 0.25
V1987	N4654	U7902	$12^h41^m26^s.4$	$+13^\circ24'00''$	6	A	30.56	30.79	30.43	30.74	30.51	30.74	30.75	31.41	...	30.69 ± 0.11
V2023	I3742	U7932	$12^h43^m01^s.2$	$+13^\circ36'24''$	5	A	31.69	...	...	31.90	31.37	31.73	32.25	...	...	31.84 ± 0.32
V2058	N4689	U7965	$12^h45^m15^s.0$	$+14^\circ02'06''$	5	A	30.75	...	30.64	...	30.64	31.06	...	31.74	...	30.88 ± 0.14
V2070	N4698	U7970	$12^h45^m51^s.8$	$+08^\circ45'37''$	1	...	32.80	31.28	31.77	31.73	32.03	...	31.53	32.35	...	31.93 ± 0.41
...	N4701	U7975	$12^h46^m39^s.0$	$+03^\circ39'45''$	6	...	...	...	...	...	...	...	...	32.71	...	32.13
...	N4713	U7985	$12^h47^m25^s.6$	$+05^\circ34'58''$	7	...	30.92	...	...	30.63	...	30.65	...	...	...	30.67 ± 0.15
...	N4725	U7989	$12^h47^m59^s.9$	$+25^\circ46'20''$	2	...	...	...	...	...	...	...	...	30.78	30.46	30.46 ± 0.06

Table A.1: continued

VCC (1)	NGC/ IC (2)	UGC/ CGCG (3)	R.A. (1950) (4)	Dec. (1950) (5)	T (6)	Mem. (7)	YFO97 (8)	MAH80 (9)	PT88 (10)	KCT88 (11)	Fou90 (12)	FTS98 (13)	Gav99 (14)	Ekh00 (15)	Ceph. (16)	Distance modulus (17)
...	N4746	U8007	$12^h49^m25\overset{s}{.}2$	$+12°21'18''$	3	...	32.43	...	...	...	32.34	32.59	...	33.15	...	32.54 ± 0.10
...	N4758	U8014	$12^h50^m14\overset{s}{.}8$	$+16°07'10''$	9	...	30.57	30.62	...	31.19	30.95	30.93	...	...	...	30.87 ± 0.24
...	N4771	U8020	$12^h50^m48\overset{s}{.}5$	$+01°32'30''$	6	...	...	...	...	...	...	...	...	32.31	...	31.69
...	N4772	U8021	$12^h50^m55\overset{s}{.}9$	$+02°26'27''$	1	...	...	...	...	...	...	...	...	32.81	...	32.24
...	I3881	U8036	$12^h52^m20\overset{s}{.}2$	$+19°26'55''$	6	...	31.90	...	...	31.08	...	31.11	...	...	...	31.30 ± 0.39
...	N4808	U8054	$12^h53^m17\overset{s}{.}0$	$+04°34'28''$	6	...	...	...	...	31.49	...	30.80	...	...	...	31.07 ± 0.32
...	N4845	U8078	$12^h55^m28\overset{s}{.}1$	$+01°50'42''$	2	...	...	...	...	...	...	...	...	31.81	...	31.15
...	...	U8085	$12^h55^m47\overset{s}{.}8$	$+14°49'52''$	6	...	...	...	...	...	...	32.54	...	...	...	32.56
...	...	U8114	$12^h57^m54\overset{s}{.}4$	$+13°56'35''$	3	...	...	...	...	...	...	32.14	...	...	...	32.14

Col. (1)−(3): Galaxy names according to VCC, NGC or IC, and UGC or CGCG.

Col. (4) & (5): Galaxy coordinates. Units of right ascension are hours, minutes, and seconds. Units of declination are degrees, arcminutes, and arcseconds.

Col. (6): Morphological type index defined in RC3.

Col. (7): Membership given in VCC and Binggeli et al. (1993). M: member; A/B: clusters A/B; W/W'/M: clouds W/W'/M; S: southern extension.

Col. (8)−(15): Distance modulus to each galaxy given in each of the data sets listed in Table 3.1.

Col. (16): Distance modulus from Cepheids given by Freedman et al. (2001).

Col. (17): Mean distance modulus and 1σ uncertainty resulting from the homogeneization of the data sets (see text).

(a) All individual measures of the distance modulus rejected in the homogenization procedure.

(b) All but one individual measure of the distance modulus rejected in the homogenization procedure.

Table A.2: Parameters for the members of the 21-cm sample of spiral galaxies

Galaxy Name (1)	$v_{\rm sys}$ (km s^{-1}) (2)	d (Mpc) (3)	$< DEF >$ (4)	DEF (5)	$W_{20}^{\rm c}$ (km s^{-1}) (6)	Flag (7)	$M_{B_{\rm T}}^{\rm c}$ (8)
Z69-10	1330	$12.08^{+2.24}_{-1.89}$	−0.19	−0.35	107	w	−15.83
I0755	1388	$18.45^{+1.59}_{-1.47}$	0.21	0.09	231	H	−17.69
N4037	814	$14.00^{+0.59}_{-0.57}$	0.88	0.67	190	i	−17.96
N4064	837	$9.82^{+0.42}_{-0.40}$	1.39	1.19	226	...	−18.15
N4067	2281	$43.65^{+4.21}_{-3.77}$	−0.08	−0.19	422	...	−20.56
U7133	2486	65.16	−0.05	0.07	260	o,W	−19.26
V0015	2406	55.46	0.77	0.88	227	o	−19.45
V0025	2062	$31.92^{+5.76}_{-4.80}$	−0.45	−0.47	379	i,s	−19.91
V0034	145	$25.47^{+0.96}_{-0.89}$	0.04	0.00	159	...	−17.46
V0047	1742	55.72	0.40	0.38	342	o	−19.74
V0058	2110	$38.55^{+5.71}_{-4.91}$	−0.19	−0.04	323	s	−20.00
V0066	242	$13.12^{+2.65}_{-2.24}$	0.02	0.08	296	...	−19.54
V0067	−299	$16.22^{+2.75}_{-2.31}$	0.23	0.20	171	...	−17.41
V0073	1933	$42.27^{+6.04}_{-5.21}$	0.05	0.06	460	s	−20.43
V0081	1963	$47.21^{+13.61}_{-10.46}$	0.01	0.10	209	i,s	−17.80
V0087	−242	$24.21^{+0.45}_{-0.48}$	0.36	0.36	151	...	−16.86
V0089	2004	$30.06^{+4.61}_{-4.04}$	0.20	0.28	438	...	−20.32
V0092	−246	$13.55^{+1.24}_{-1.14}$	0.26	0.45	479	...	−20.61
V0097	2356	$38.19^{+2.36}_{-2.31}$	0.20	0.32	388	...	−20.35
V0120	1910	$23.12^{+2.00}_{-1.82}$	−0.01	0.07	295	...	−19.52
V0131	2201	$38.02^{+2.16}_{-2.09}$	0.05	0.06	315	...	−19.86
V0143	264	$31.19^{+5.12}_{-4.45}$	0.54	0.30	177	H,s	−17.74
V0145	584	$18.71^{+1.34}_{-1.22}$	0.16	0.34	295	...	−19.76
V0152	456	$21.88^{+2.90}_{-2.60}$	0.00	−0.02	267	...	−18.71
V0157	−200	$18.71^{+1.52}_{-1.44}$	0.17	0.12	368	...	−19.98
V0162	1847	$31.05^{+4.27}_{-3.78}$	−0.22	−0.16	238	...	−18.17
V0167	16	$15.56^{+2.22}_{-1.94}$	0.53	0.71	533	...	−21.02
V0187	114	$23.44^{+3.47}_{-3.00}$	0.02	0.09	248	...	−19.46
V0199	2448	44.46	0.25	0.33	575	o	−20.74
V0213	−278	$40.93^{+5.00}_{-4.54}$	−0.12	−0.25	308	i,s	−18.98

Table A.2: continued

Galaxy Name (1)	$v_{\rm sys}$ (km s^{-1}) (2)	d (Mpc) (3)	$< DEF >$ (4)	DEF (5)	$W^{\rm c}_{20}$ (km s^{-1}) (6)	Flag (7)	$M^{\rm c}_{B_{\rm T}}$ (8)
V0222	2453	$17.95^{+1.55}_{-1.39}$	0.35	0.34	343	H	-19.23
V0224	2011	$31.62^{+2.89}_{-2.60}$	0.22	0.28	227	...	-18.89
V0226	756	$23.55^{+2.15}_{-1.95}$	0.54	0.47	330	...	-19.81
V0267	584	$27.93^{+0.65}_{-0.64}$	-0.01	0.00	644	...	-18.50
V0289	709	$21.68^{+0.81}_{-0.79}$	0.37	0.04	180	...	-17.37
V0297	1847	23.33	0.54	0.43	170	o,W	-17.04
V0307	2303	$16.14^{+3.35}_{-2.76}$	-0.04	-0.04	452	i	-20.90
V0318	2328	$29.79^{+2.43}_{-2.25}$	-0.09	-0.05	236	...	-18.28
V0341	1649	$39.63^{+1.68}_{-1.70}$	-0.03	0.04	536	H	-20.63
V0382	2219	$27.54^{+3.36}_{-2.99}$	0.32	0.29	365	...	-20.29
V0393	2473	27.29	0.13	0.14	273	i,o	-18.54
V0404	1574	34.67	0.32	0.38	268	o,W	-19.24
V0415	2413	$30.62^{+14.05}_{-9.63}$	0.49	0.41	200	s	-17.08
V0449	2377	$44.87^{+0.21}_{-0.20}$	0.06	0.23	371	W	-20.47
V0453	785	$27.29^{+6.75}_{-5.41}$	0.56	0.51	127	s,w	-16.14
V0465	239	$14.66^{+1.71}_{-1.54}$	-0.08	-0.08	244	...	-19.04
V0483	1016	$18.88^{+4.24}_{-3.48}$	0.08	0.03	318	...	-19.92
V0491	112	34.83	-0.40	-0.36	349	i,o,W	-19.91
V0497	1034	$19.41^{+3.19}_{-2.72}$	0.27	0.28	383	...	-20.39
V0509	1109	$34.83^{+4.61}_{-4.11}$	0.03	0.04	181	...	-17.53
V0522	1814	40.74	0.92	0.95	457	H,o,W	-20.13
V0524	913	$27.42^{+3.49}_{-3.07}$	1.16	1.24	490	W	-20.33
V0559	47	$10.76^{+1.31}_{-1.19}$	1.19	1.02	232	...	-18.39
V0566	1267	$25.82^{+1.34}_{-1.27}$	-0.14	-0.20	117	w	-16.79
V0567	2215	$29.38^{+0.82}_{-0.86}$	0.11	0.13	233	...	-18.12
V0570	1319	$14.00^{+1.49}_{-1.33}$	1.04	0.90	280	...	-18.94
V0576	1117	$28.84^{+3.08}_{-2.80}$	0.19	0.26	334	...	-19.84
V0593	1392	$23.55^{+2.87}_{-2.52}$	0.47	0.17	159	H	-17.31
V0596	1468	$15.21^{+0.50}_{-0.49}{}^{a}$	0.32	0.49	482	i	-21.12
V0620	622	$20.14^{+6.53}_{-4.90}$	-0.13	-0.28	130	s,w	-16.40

Table A.2: continued

Galaxy Name (1)	$v_{\rm sys}$ (km s^{-1}) (2)	d (Mpc) (3)	$< DEF >$ (4)	DEF (5)	$W_{20}^{\rm c}$ (km s^{-1}) (6)	Flag (7)	$M_{B_{\rm T}}^{\rm c}$ (8)
V0630	1438	$19.32^{+1.57}_{-1.44}$	0.65	0.73	279	...	-19.35
V0656	868	$28.44^{+4.52}_{-3.92}$	0.40	0.40	401	...	-19.92
V0667	1279	$25.59^{+0.96}_{-0.89}$	0.53	0.54	212	...	-18.39
V0692	2203	$11.17^{+1.25}_{-1.13}$	0.60	0.17	164	i	-17.47
V0697	1085	36.81	0.30	0.29	280	i,o	-18.68
V0699	579	$32.21^{+3.27}_{-2.97}$	-0.31	-0.46	295	i	-18.44
V0713	998	$29.38^{+3.74}_{-3.25}$	1.28	1.35	302	...	-19.42
V0737	1566	27.16	0.02	0.00	164	o,W	-17.95
V0768	2354	$33.57^{+1.10}_{-1.12}$	0.61	0.49	212	H	-18.71
V0785	2395	47.86	-0.17	0.11	624	i,o	-21.00
V0792	840	$21.88^{+4.06}_{-3.47}$	0.60	0.62	346	...	-19.51
V0801	1608	$16.67^{+1.44}_{-1.32}$	-0.42	-0.73	302	...	-18.84
V0809	-262	$19.95^{+1.13}_{-1.05}$	0.62	0.61	178	...	-17.89
V0827	847	$23.88^{+2.67}_{-2.36}$	0.07	0.15	306	...	-19.53
V0836	2420	$16.60^{+1.52}_{-1.36}$	1.14	1.24	401	...	-20.17
V0849	972	$23.12^{+4.68}_{-3.86}$	0.06	-0.02	236	i	-18.73
V0851	1061	$20.99^{+1.40}_{-1.31}$	0.46	0.48	216	...	-18.59
V0857	823	$24.66^{+0.93}_{-0.95}$	0.27	0.33	432	i	-20.41
V0859	1265	$36.14^{+1.18}_{-1.15}$	0.33	0.43	321	W	-19.94
V0865	-228	$13.06^{+1.80}_{-1.57}$	0.22	0.22	202	...	-18.54
V0873	121	$16.00^{+2.80}_{-2.35}$	0.57	0.50	298	...	-19.27
V0905	1146	15.07	0.52	0.41	147	i,w	-17.43
V0938	1244	$36.64^{+4.28}_{-3.83}$	0.15	0.20	417	i	-19.80
V0939	1135	$27.93^{+0.65}_{-0.57}$	0.53	0.63	328	i	-19.16
V0957	1530	$15.85^{+0.07}_{-0.07}$	0.07	-0.04	232	W	-18.76
V0958	-380	$13.87^{+1.62}_{-1.43}$	0.92	0.74	307	...	-19.19
V0971	942	$17.62^{+2.99}_{-2.55}$	-0.08	-0.10	191	...	-18.45
V0979	314	$4.11^{+0.17}_{-0.18}$	1.32	0.76	108	w	-15.99
V0989	1704	71.78	0.12	0.13	195	i,o	-18.52
V0995	797	$23.66^{+4.01}_{-3.43}$	-0.06	-0.06	172	...	-17.57

Table A.2: continued

Galaxy Name (1)	$v_{\rm sys}$ (km s^{-1}) (2)	d (Mpc) (3)	$< DEF >$ (4)	DEF (5)	$W_{20}^{\rm c}$ (km s^{-1}) (6)	Flag (7)	$M_{B_{\rm T}}^{\rm c}$ (8)
V1002	1301	$26.79^{+8.04}_{-6.12}$	0.27	0.29	420	i,s	-19.48
V1043	-45	$10.38^{+1.37}_{-1.23}$	0.73	0.84	398	W	-19.56
V1048	2102	$41.69^{+2.78}_{-2.67}$	0.23	0.27	251	...	-19.14
V1086	230	$19.14^{+0.90}_{-0.88}$	1.11	0.98	240	...	-18.61
V1091	983	$21.88^{+3.13}_{-2.71}$	-0.16	-0.39	203	...	-18.06
V1110	1861	$14.06^{+2.61}_{-2.18}$	1.06	1.08	405	...	-20.14
I3391	1618	$20.42^{+5.52}_{-4.39}$	0.29	0.22	183	i,s	-18.03
V1118	725	$28.71^{+0.94}_{-0.85}$	0.43	0.25	308	...	-19.35
V1126	1571	$14.93^{+2.61}_{-2.20}$	1.08	0.79	228	...	-18.44
N4455	576	$8.28^{+1.49}_{-1.27}$	-0.12	-0.20	160	...	-16.77
V1189	381	$15.63^{+1.12}_{-1.04}$	0.24	0.18	170	...	-17.31
V1193	616	$27.67^{+3.52}_{-3.12}$	0.15	-0.12	237	...	-18.24
V1205	2200	$16.22^{+1.65}_{-1.54}$	0.07	-0.34	206	...	-18.34
V1290	2281	$38.02^{+1.07}_{-1.10}$	-0.04	-0.03	366	W	-20.28
V1330	1638	$27.93^{+8.72}_{-6.71}$	0.85	0.78	297	i,s	-19.19
V1356	1129	$34.51^{+9.74}_{-7.65}$	-0.27	-0.32	228	s	-17.94
V1375	1581	$14.86^{+0.21}_{-0.20}$[a]	-0.11	-0.09	303	W	-19.09
V1379	1411	$13.93^{+1.77}_{-1.57}$	0.22	0.23	234	...	-18.58
V1393	1995	$21.38^{+2.83}_{-2.52}$	0.06	0.01	219	...	-18.37
V1401	2167	$17.54^{+1.69}_{-1.56}$	0.40	0.55	603	...	-21.55
V1410	1531	$32.36^{+1.68}_{-1.65}$	0.04	0.04	225	...	-18.58
V1442	1572	15.14	-0.06	-0.09	154	H,o,W	-17.71
U7697	2454	28.71	0.09	0.13	215	o,W	-17.10
V1486	6	$58.34^{+0.81}_{-0.67}$	0.65	0.65	180	H	-18.82
V1508	1093	$20.99^{+3.33}_{-2.83}$	-0.21	-0.14	287	i	-19.37
V1516	2199	$14.59^{+1.41}_{-1.30}$	0.65	0.69	257	...	-18.82
V1524	158	$36.14^{+13.29}_{-9.72}$	-0.13	-0.04	299	i,s	-18.98
V1532	2237	$16.14^{+2.56}_{-2.20}$	0.72	0.57	151	i	-17.29
V1540	1571	$13.30^{+3.22}_{-2.60}$	-0.14	-0.04	410	W	-19.99
V1555	1825	$15.78^{+0.37}_{-0.36}$[a]	0.16	0.19	397	i	-20.64

Table A.2: continued

Galaxy Name (1)	$v_{\rm sys}$ (km s^{-1}) (2)	d (Mpc) (3)	$< DEF >$ (4)	DEF (5)	$W_{20}^{\rm c}$ (km s^{-1}) (6)	Flag (7)	$M_{B_{\rm T}}^{\rm c}$ (8)
V1557	1596	19.05	0.34	0.35	187	o,W	−18.18
V1562	1641	$14.93^{+0.28}_{-0.27}$[a]	0.08	0.25	394	W	−20.43
V1566	295	$22.70^{+2.77}_{-2.44}$	0.61	0.58	133	w	−17.04
V1569	687	$23.33^{+3.33}_{-2.95}$	0.90	0.85	215	...	−16.50
V1588	1184	$16.37^{+4.43}_{-3.51}$	0.39	0.36	338	i	−18.82
V1615	383	$16.22^{+0.38}_{-0.37}$[a]	0.77	0.83	410	i	−20.38
V1624	992	$20.14^{+1.74}_{-1.63}$	0.57	0.43	212	W	−18.01
V1644	646	$41.50^{+1.76}_{-1.62}$	0.23	0.26	114	w	−16.26
N4561	1324	$22.91^{+1.75}_{-1.63}$	−0.67	−0.70	293	...	−19.23
V1676	2125	$18.97^{+0.62}_{-0.64}$	0.35	0.49	248	W	−20.43
V1690	−328	$9.42^{+1.75}_{-1.47}$	1.13	1.26	401	...	−20.28
V1696	235	$17.22^{+3.29}_{-2.75}$	0.48	0.55	311	i	−19.58
V1727	1397	$19.14^{+2.24}_{-2.02}$	0.75	0.89	594	i	−21.18
V1730	893	$19.32^{+1.10}_{-1.08}$	1.17	1.05	283	i	−18.84
V1758	1651	$23.66^{+3.51}_{-3.01}$	0.37	0.37	185	...	−18.03
V1760	639	$14.39^{+2.59}_{-2.20}$	1.15	1.06	292	W	−18.72
V1780	2279	$48.08^{+5.13}_{-4.63}$	0.17	0.23	399	s	−19.88
V1811	530	$14.59^{+1.19}_{-1.10}$	0.34	−0.02	204	...	−18.37
V1859	1528	$12.71^{+0.24}_{-0.24}$	1.25	1.00	224	...	−18.27
V1868	2138	$20.70^{+1.18}_{-1.09}$	0.73	0.69	245	...	−18.89
V1929	185	$23.33^{+3.83}_{-3.27}$	0.06	0.07	228	...	−18.83
V1932	11	$20.04^{+2.24}_{-2.05}$	0.28	0.30	291	...	−19.51
V1943	873	$21.98^{+0.82}_{-0.80}$[a]	0.09	0.12	375	...	−19.90
V1972	1297	$17.78^{+2.26}_{-1.97}$	0.42	0.36	345	i,W	−19.58
N4651	705	$22.28^{+2.72}_{-2.45}$	−0.29	−0.29	472	...	−20.81
V1987	926	$13.74^{+0.71}_{-0.67}$	0.06	0.12	365	...	−20.13
V2023	856	$23.33^{+3.71}_{-3.24}$	−0.17	−0.26	205	...	−18.44
V2058	1493	$15.00^{+1.00}_{-0.95}$	0.65	0.61	320	i	−19.55
V2070	882	$24.32^{+5.05}_{-4.23}$	−0.20	−0.14	663	s	−20.79
N4701	574	26.67	−0.30	−0.21	272	i,o,W	−19.55

Table A.2: continued

Galaxy Name (1)	$v_{\rm sys}$ (km s^{-1}) (2)	d (Mpc) (3)	$< DEF >$ (4)	DEF (5)	$W_{20}^{\rm c}$ (km s^{-1}) (6)	Flag (7)	$M_{B_{\rm T}}^{\rm c}$ (8)
N4713	511	$13.61^{+0.97}_{-0.90}$	−0.35	−0.35	280	i	−18.66
N4725	1163	$12.36^{+0.35}_{-0.34}$	0.21	0.45	510	W	−20.68
N4746	1669	$32.21^{+1.52}_{-1.49}$	−0.18	−0.19	365	...	−20.08
N4758	1150	$14.93^{+1.74}_{-1.56}$	0.21	0.21	207	...	−18.60
N4771	959	21.78	0.31	0.39	293	o,W	−19.88
N4772	883	28.05	−0.07	−0.03	510	o,W	−20.56
I3881	849	$18.20^{+3.58}_{-3.01}$	0.08	0.14	249	...	−18.77
N4808	616	$16.37^{+2.60}_{-2.28}$	−0.68	−0.69	265	W	−19.60
N4845	940	16.98	1.20	1.26	596	o,W	−19.90
U8085	1943	32.51	−0.14	−0.06	246	o,W	−19.16
U8114	1887	26.79	0.11	−0.06	157	o,W	−16.90

a Distance from Cepheids. Errors are those quoted by Freedman et al. (2001).

Col. (7): H: non-AGC flux or non-detection corrected only for internal H I self-absorption; i: $i < 45°$ (from LEDA); o: distance based on a single non-Cepheid measurement; s: 1σ uncertainties in the distance larger than 5 Mpc; W: corrected H I line width *not* from YFO97; w: $100 < W_{20}^{\rm c} < 150$ km s^{-1} (see text for further details).

Table A.3: Final sample of early type galaxies in the Virgo cluster

Galaxy			R.A.	Dec.	d	rel. error	v_{sys}	sources
VCC	NGC	Messier	(J2000)		(Mpc)		($\mathrm{km\,s^{-1}}$)	
49	4168	—	$12^{\mathrm{h}}12^{\mathrm{m}}17\overset{\mathrm{s}}{.}3$	$+13^\circ12'17''$	34.20	0.41	2128	G
220	4233	—	$12^{\mathrm{h}}17^{\mathrm{m}}07\overset{\mathrm{s}}{.}7$	$+07^\circ37'26''$	32.96	0.41	2181	G
312	4255	—	$12^{\mathrm{h}}18^{\mathrm{m}}56\overset{\mathrm{s}}{.}1$	$+04^\circ47'09''$	28.71	0.41	1603	G
319	—	—	$12^{\mathrm{h}}19^{\mathrm{m}}02\overset{\mathrm{s}}{.}0$	$+13^\circ58'48''$	7.59	0.38	−266	$\mathrm{Y}_L\mathrm{Y}_R$
342	4259	—	$12^{\mathrm{h}}19^{\mathrm{m}}22\overset{\mathrm{s}}{.}2$	$+05^\circ22'34''$	57.02	0.41	2306	G
345	4261	—	$12^{\mathrm{h}}19^{\mathrm{m}}23\overset{\mathrm{s}}{.}2$	$+05^\circ49'32''$	32.27	0.16	2012	GT
355	4262	—	$12^{\mathrm{h}}19^{\mathrm{m}}30\overset{\mathrm{s}}{.}6$	$+14^\circ52'38''$	14.86	0.41	1181	G
369	4267	—	$12^{\mathrm{h}}19^{\mathrm{m}}45\overset{\mathrm{s}}{.}4$	$+12^\circ47'53''$	14.66	0.41	852	G
575	4318	—	$12^{\mathrm{h}}22^{\mathrm{m}}43\overset{\mathrm{s}}{.}3$	$+08^\circ11'52''$	25.35	0.41	1047	G
648	4339	—	$12^{\mathrm{h}}23^{\mathrm{m}}34\overset{\mathrm{s}}{.}9$	$+06^\circ04'54''$	16.44	0.17	1108	T
685	4350	—	$12^{\mathrm{h}}23^{\mathrm{m}}57\overset{\mathrm{s}}{.}7$	$+16^\circ41'33''$	14.86	0.41	1049	G
731	4365	—	$12^{\mathrm{h}}24^{\mathrm{m}}28\overset{\mathrm{s}}{.}3$	$+07^\circ19'04''$	22.07	0.05	1058	$\mathrm{J}_I\mathrm{J}_K$NT
763	4374	84	$12^{\mathrm{h}}25^{\mathrm{m}}03\overset{\mathrm{s}}{.}7$	$+12^\circ53'13''$	17.71	0.07	733	GNT
778	4377	—	$12^{\mathrm{h}}25^{\mathrm{m}}12\overset{\mathrm{s}}{.}3$	$+14^\circ45'43''$	15.49	0.41	1182	G
784	4379	—	$12^{\mathrm{h}}25^{\mathrm{m}}14\overset{\mathrm{s}}{.}8$	$+15^\circ36'26''$	14.19	0.38	871	T
810	—	—	$12^{\mathrm{h}}25^{\mathrm{m}}33\overset{\mathrm{s}}{.}8$	$+13^\circ13'30''$	12.36	0.38	−516	$\mathrm{Y}_L\mathrm{Y}_R$
828	4387	—	$12^{\mathrm{h}}25^{\mathrm{m}}41\overset{\mathrm{s}}{.}8$	$+12^\circ48'35''$	17.21	0.35	373	GT
881	4406	86	$12^{\mathrm{h}}26^{\mathrm{m}}12\overset{\mathrm{s}}{.}2$	$+12^\circ56'44''$	17.40	0.04	−465	$\mathrm{J}_I\mathrm{J}_K$KNT
940	—	—	$12^{\mathrm{h}}26^{\mathrm{m}}47\overset{\mathrm{s}}{.}1$	$+12^\circ27'14''$	7.24	0.54	1337	Y_R
953	—	—	$12^{\mathrm{h}}26^{\mathrm{m}}54\overset{\mathrm{s}}{.}7$	$+13^\circ33'57''$	18.88	0.38	−678	$\mathrm{Y}_L\mathrm{Y}_R$
965	—	—	$12^{\mathrm{h}}27^{\mathrm{m}}03\overset{\mathrm{s}}{.}1$	$+12^\circ33'39''$	9.29	0.54	614	Y_R
1025	4434	—	$12^{\mathrm{h}}27^{\mathrm{m}}36\overset{\mathrm{s}}{.}7$	$+08^\circ09'14''$	25.50	0.15	897	GT
1030	4435	—	$12^{\mathrm{h}}27^{\mathrm{m}}40\overset{\mathrm{s}}{.}6$	$+13^\circ04'44''$	13.12	0.41	611	G
1146	4458	—	$12^{\mathrm{h}}28^{\mathrm{m}}57\overset{\mathrm{s}}{.}6$	$+13^\circ14'29''$	17.97	0.09	499	GKNT
1173	—	—	$12^{\mathrm{h}}29^{\mathrm{m}}14\overset{\mathrm{s}}{.}8$	$+12^\circ58'41''$	14.96	0.38	2292	$\mathrm{Y}_L\mathrm{Y}_R$
1196	4468	—	$12^{\mathrm{h}}29^{\mathrm{m}}30\overset{\mathrm{s}}{.}9$	$+14^\circ02'55''$	15.85	0.13	732	T
1226	4472	49	$12^{\mathrm{h}}29^{\mathrm{m}}46\overset{\mathrm{s}}{.}7$	$+07^\circ59'59''$	16.27	0.03	693	G$\mathrm{J}_I\mathrm{J}_K$KNT
1231	4473	—	$12^{\mathrm{h}}29^{\mathrm{m}}48\overset{\mathrm{s}}{.}9$	$+13^\circ25'46''$	17.12	0.05	2041	GKNT
1242	4474	—	$12^{\mathrm{h}}29^{\mathrm{m}}53\overset{\mathrm{s}}{.}7$	$+14^\circ04'06''$	15.14	0.41	1405	G
1250	4476	—	$12^{\mathrm{h}}29^{\mathrm{m}}59\overset{\mathrm{s}}{.}1$	$+12^\circ20'55''$	19.08	0.11	1767	NT
1253	4477	—	$12^{\mathrm{h}}30^{\mathrm{m}}02\overset{\mathrm{s}}{.}2$	$+13^\circ38'11''$	16.44	0.41	1164	G
1279	4478	—	$12^{\mathrm{h}}30^{\mathrm{m}}17\overset{\mathrm{s}}{.}5$	$+12^\circ19'40''$	16.68	0.09	1220	GNT

Table A.3: continued

	Galaxy		R.A.	Dec.	d	rel. error	$v_{\rm sys}$	sources
VCC	NGC	Messier	(J2000)		(Mpc)		(km s^{-1})	
1297	4486B	—	$12^{\rm h}30^{\rm m}32\overset{\rm s}{.}0$	$+12^\circ29'27''$	16.31	0.03	136	KN
1308	—	—	$12^{\rm h}30^{\rm m}45\overset{\rm s}{.}9$	$+11^\circ20'36''$	17.86	0.38	1511	$\rm Y_LY_R$
1316	4486	87	$12^{\rm h}30^{\rm m}49\overset{\rm s}{.}4$	$+12^\circ23'28''$	16.82	0.09	1095	GNT
1321	4489	—	$12^{\rm h}30^{\rm m}52\overset{\rm s}{.}3$	$+16^\circ45'30''$	17.04	0.13	772	$\rm J_KT$
1386	—	—	$12^{\rm h}31^{\rm m}51\overset{\rm s}{.}5$	$+12^\circ39'24''$	7.08	0.38	1135	$\rm Y_LY_R$
1412	4503	—	$12^{\rm h}32^{\rm m}06\overset{\rm s}{.}3$	$+11^\circ10'35''$	11.75	0.41	1184	G
1420	—	—	$12^{\rm h}32^{\rm m}12\overset{\rm s}{.}3$	$+12^\circ03'42''$	11.75	0.38	847	$\rm Y_LY_R$
1489	—	—	$12^{\rm h}33^{\rm m}14\overset{\rm s}{.}0$	$+10^\circ55'43''$	11.30	0.38	−94	$\rm Y_LY_R$
1535	4526	—	$12^{\rm h}34^{\rm m}03\overset{\rm s}{.}1$	$+07^\circ41'57''$	16.61	0.17	427	GT
1537	4528	—	$12^{\rm h}34^{\rm m}06\overset{\rm s}{.}2$	$+11^\circ19'15''$	14.52	0.41	1195	G
1539	—	—	$12^{\rm h}34^{\rm m}06\overset{\rm s}{.}3$	$+12^\circ44'40''$	8.83	0.54	1216	$\rm Y_R$
1549	—	—	$12^{\rm h}34^{\rm m}14\overset{\rm s}{.}9$	$+11^\circ04'16''$	19.32	0.54	1202	$\rm Y_R$
1619	4550	—	$12^{\rm h}35^{\rm m}30\overset{\rm s}{.}7$	$+12^\circ13'13''$	17.84	0.09	208	KNT
1630	4551	—	$12^{\rm h}35^{\rm m}38\overset{\rm s}{.}1$	$+12^\circ15'49''$	17.24	0.15	973	GT
1632	4552	89	$12^{\rm h}35^{\rm m}40\overset{\rm s}{.}0$	$+12^\circ33'22''$	15.31	0.04	115	$\rm GJ_IJ_KKNT$
1664	4564	—	$12^{\rm h}36^{\rm m}27\overset{\rm s}{.}0$	$+11^\circ26'18''$	14.86	0.15	947	GT
1669	—	—	$12^{\rm h}36^{\rm m}30\overset{\rm s}{.}6$	$+13^\circ38'18''$	8.79	0.54	427	$\rm Y_R$
1692	4570	—	$12^{\rm h}36^{\rm m}53\overset{\rm s}{.}5$	$+07^\circ14'46''$	13.80	0.41	1559	G
1720	4578	—	$12^{\rm h}37^{\rm m}30\overset{\rm s}{.}6$	$+09^\circ33'16''$	17.94	0.06	2102	$\rm GJ_IJ_KT$
1834	4600	—	$12^{\rm h}40^{\rm m}23\overset{\rm s}{.}0$	$+03^\circ07'02''$	7.35	0.20	615	T
1869	4608	—	$12^{\rm h}41^{\rm m}13\overset{\rm s}{.}4$	$+10^\circ09'18''$	20.23	0.41	1633	G
1883	4612	—	$12^{\rm h}41^{\rm m}32\overset{\rm s}{.}8$	$+07^\circ18'50''$	14.06	0.41	1697	G
1902	4620	—	$12^{\rm h}41^{\rm m}59\overset{\rm s}{.}4$	$+12^\circ56'32''$	21.28	0.28	1012	T
1903	4621	59	$12^{\rm h}42^{\rm m}02\overset{\rm s}{.}3$	$+11^\circ38'45''$	14.80	0.05	258	GKNT
1938	4638	—	$12^{\rm h}42^{\rm m}47\overset{\rm s}{.}5$	$+11^\circ26'32''$	17.33	0.21	956	GT
1939	4624	—	$12^{\rm h}42^{\rm m}50\overset{\rm s}{.}0$	$+02^\circ41'16''$	15.14	0.06	924	$\rm GJ_IJ_KT$
1978	4649	60	$12^{\rm h}43^{\rm m}40\overset{\rm s}{.}1$	$+11^\circ33'08''$	16.36	0.04	969	GKNT
2000	4660	—	$12^{\rm h}44^{\rm m}32\overset{\rm s}{.}0$	$+11^\circ11'24''$	15.66	0.11	914	GNT
2087	4733	—	$12^{\rm h}51^{\rm m}06\overset{\rm s}{.}8$	$+10^\circ54'43''$	14.93	0.18	772	T
2092	4754	—	$12^{\rm h}52^{\rm m}17\overset{\rm s}{.}5$	$+11^\circ18'50''$	16.94	0.12	1206	GT
2095	4762	—	$12^{\rm h}52^{\rm m}55\overset{\rm s}{.}9$	$+11^\circ13'49''$	10.81	0.41	818	G

G = Gavazzi et al. (1999); T = Tonry et al. (2001); $\rm J_I$,$\rm J_K$ = Jensen, Tonry, & Luppino (1998); N = Neilsen & Tsvetanov (2000); K = Kundu & Whitmore (2001); $\rm Y_L$,$\rm Y_R$ = Young & Currie (1995).

B Radius, time and density of turnaround in a flat ΛCDM cosmology

In this appendix, we compute the parameters of shells at *turnaround*, i.e. reaching their first apocenter, in a ΛCDM Universe without quintessence ($w_Q = -1$).

In a non-quintessential Universe with a cosmological constant, the equation of motion of a shell of matter is

$$\frac{\mathrm{d}^2 R}{\mathrm{d}t^2} = -\frac{GM(R,t)}{R^2} + \frac{\Lambda}{3} R \,, \tag{B.1}$$

where the first term on the right hand side is the gravitational force and the second term is the repulsive effect of the cosmological constant Λ. A given shell of matter that first expands with the Universe and then turns around and collapses will begin to cross shells that have already settled in a structure only slightly before its own collapse. Therefore, during the expansion phase, there is no shell crossing and hence $M(R,t) = \mathrm{cst}$.

The equation of motion can then be easily integrated to yield the energy equation

$$E = \frac{1}{2}\dot{r}^2 - \frac{GM}{r} - \frac{1}{6}\Lambda r^2 = \frac{1}{2}\dot{r}_i^2 - \frac{GM}{r_i} - \frac{1}{6}\Lambda r_i^2 \,, \tag{B.2}$$

where E is the energy per unit mass of the shell, and where the i subscript refers to a very early time t_i, corresponding to redshift $z_i \gg 1$ (e.g. $z_i = 1000$). It is convenient to use the quantities

$$\Omega \equiv \frac{8\pi G\rho}{3\,H^2} \,, \qquad \text{and} \qquad \lambda \equiv \frac{\Lambda}{3\,H^2} \,, \tag{B.3}$$

which represent the dimensionless mass density and dark energy of the Universe at any epoch, and we will use subscripts '0' to denote the present epoch ($z = 0$). In the case of a flat Universe ($\Omega_0+\lambda_0 = 1$), as confirmed with the WMAP CMB experiment by Spergel et al. (2003), mass and energy conservation applied to the Universe lead to (e.g. Richstone, Loeb, & Turner 1992)

$$H_i^2 = H_0^2 \, \left[\Omega_0 \, (1+z_i)^3 + \lambda_0\right] \tag{B.4}$$

At time t_i, the mass enclosed within radius r_i is

$$M = \frac{4\,\pi}{3} \, (1+\delta_i) \, \Omega_i \, \rho_{\rm c,i} \, r_i^3 = \frac{1}{2} \, (1+\delta_i) \, \Omega_i \, H_i^2 \, \frac{r_i^3}{G} \ , \tag{B.5}$$

where δ_i is the relative overdensity within radius r_i at time t_i (normalized to the density of the Universe at that epoch), and where we made use of the critical density of the Universe at t_i:

$$\rho_{\rm c,i} = \frac{3\,H_i^2}{8\,\pi\,G} \ . \tag{B.6}$$

With a dimensionless radial growth factor $u(r,t) = r/r_i$, the first energy equation can be expressed as

$$\dot u = H_i \, \sqrt{\frac{2\,E}{H_i^2 r_i^2} + \frac{(1+\delta_i)\,\Omega_i}{u} + \lambda_i \, u^2} \ , \tag{B.7}$$

where we made use of equations (B.2), (B.3), (B.4), and (B.5). The energy E of the shell is obtained by expressing equation (B.7) for the epoch t_i, yielding

$$\frac{2\,E}{H_i^2 r_i^2} = \frac{\dot{u_i}^2}{H_i^2} - \left[(1+\delta_i)\,\Omega_i + \lambda_i\right] \ . \tag{B.8}$$

The second equality of equation (B.3) yields

$$\begin{aligned} \lambda_i &= \left(\frac{H_0}{H_i}\right)^2 \lambda_0 = \left(\frac{\Omega_0}{\lambda_0}\,(1+z_i)^3 + 1\right)^{-1} \\ &= O\left((1+z_i)^{-3}\right) \ll 1 \ . \end{aligned} \tag{B.9}$$

Mass conservation amounts to a mean density of the Universe that varies as

$$\rho_i \equiv \rho(z_i) = \rho_0 \, (1+z_i)^3 \ , \tag{B.10}$$

where ρ_0 is the present-day mass density of the Universe. This then yields

$$\begin{aligned} \Omega_i &= \Omega_0 \, (1+z_i)^3 \, \left(\frac{H_0}{H_i}\right)^2 \\ &= \left[1 + \frac{\lambda_0}{\Omega_0} \, (1+z_i)^{-3}\right]^{-1} = 1 - \lambda_i \end{aligned} \tag{B.11}$$

Inserting equations (B.8), (B.9) and (B.11) into equation (B.7) yields

$$\dot{u} = H_i \sqrt{\frac{\dot{u_i}^2}{H_i^2} + \frac{1+\delta_i-\lambda_i}{u} + \lambda_i\, u^2 - (1+\delta_i)}\ , \tag{B.12}$$

where we discarded terms in $o(\lambda_i)$. Now, as pointed out by Chodorowski (1988), Bartelmann, Ehlers, & Schneider (1993) and Padmanabhan (1993), one should not assume that the initial flow is a pure Hubble flow ($\dot{u}_i = H_i$), but incorporate the peculiar motion acquired before z_i. Using the Zeldovich (1970) approximation, Chodorowski and Bartelmann et al. show that

$$\dot{u}_i = H_i \left(1 - \frac{\delta_i}{3}\right)\ . \tag{B.13}$$

Inserting equation (B.13) into equation (B.12) and discarding high order terms in $(1+z_i)^{-1}$ and λ_i — writing $\delta_i = O(1/(1+z_i)) = \delta_0/(1+z_i)$ — yields

$$\dot{u} = H_i \sqrt{-\frac{5}{3}\,\delta_i + \frac{1}{u} + \lambda_i\, u^2}\ . \tag{B.14}$$

The turnaround radius is obtained by solving for $\dot{u} = 0$, i.e. solving

$$\lambda_i\, u_{\rm ta}^3 - \frac{5}{3}\,\delta_i\, u_{\rm ta} + 1 = 0 \tag{B.15}$$

for $u_{\rm ta}$. Łokas & Hoffman (2001) found the same solution without the 5/3 term, as their δ_i refers to the total initial density, whereas our δ_i refers to the growing mode only. We can go further than Łokas & Hoffman by expressing and solving a cubic equation *in terms of present-day quantities*. With equation (B.9), equation (B.15) reduces to solving

$$\frac{1-\Omega_0}{\Omega_0}\, y_{\rm ta}^3 - \frac{5}{3}\,\delta_0\, y_{\rm ta} + 1 = 0 \tag{B.16}$$

for $y_{\rm ta} = u_{\rm ta}/(1+z_i) = r_{\rm ta}/r_0 < 1$, where

$$r_0 = r_i\,(1+z_i) \tag{B.17}$$

is the comoving radius of the initial perturbation. The smallest real positive solution of the cubic equation (B.16) is

$$y_{\rm ta} = \frac{2\sqrt{5}}{3} \sqrt{\frac{\delta_0\,\Omega_0}{1-\Omega_0}}\, \cos\left(\frac{\phi+\pi}{3}\right) \tag{B.18}$$

$$\phi = \cos^{-1} \sqrt{\frac{729}{500} \left[\frac{(1-\Omega_0)\,/\Omega_0}{\delta_0^3}\right]} \tag{B.19}$$

for $\delta_0 \geq 2^{1/3}\, 9/10\ \left[\left(1-\Omega_0\right)/\Omega_0\right]^{1/3}$.

The time of turnaround is then obtained by integrating equation (B.14) and writing $u = (1+z_i)\, y$, yielding

$$\frac{H_i\, T_{\rm ta}}{(1+z_i)^{3/2}} = \int_0^{y_{\rm ta}} \frac{\sqrt{y}\ {\rm d}y}{\sqrt{1-(5/3)\,\delta_0\, y + \left[\left(1-\Omega_0\right)/\Omega_0\right]\ y^3}}\ . \tag{B.20}$$

The starting point of the integration is taken at 0 instead of $1/(1+z_i)$, which corresponds to adding the negligible time between the $t=0$ and t_i. With equation (B.4), equation (B.20) becomes

$$H_0\, T_{\rm ta} = \int_0^{y_{\rm ta}} \frac{\sqrt{y}\ {\rm d}y}{\sqrt{\Omega_0 - (5/3)\,\delta_0\,\Omega_0\, y + (1-\Omega_0)\ y^3}}\ . \tag{B.21}$$

For $\Omega_0 = 1$, $\lambda_0 = 0$, we get $y_{\rm ta} = 3/(5\,\delta_0)$, $H_0\, T_{\rm ta} = (\pi/2)\, [3/(5\delta_0)]^{3/2}$, so that a shell that collapses today, hence turns around at $H_0\, T_{\rm ta} = H_0\, t_0/2 = 1/3$, requires a linearly extrapolated density contrast of $\delta_0 = (3/5)\, (3\,\pi/2)^{2/3} = 1.686$, as expected.

C Velocity moments of dark matter particles

In this appendix we show the projected velocity moments of the dark matter particles in the rest of the halos analyzed in Chapter 8 measured with all particles that in projection end up with a projected radius smaller than the virial radius, whether or not they are actually within the virial radius in 3D space. The upper panels show the mean line-of-sight velocity with respect to the velocity of the center of the halo in units of the circular velocity at r_{100}. The middle panels give the line-of-sight velocity dispersion in the same units. The lower panels give the kurtosis. Each column show the velocity moments measured by an observer situated at 0°, 45° and 90° with respect to the major axis of the halo.

Figure C.1: Projected velocity moments of the dark matter particles in halo 2

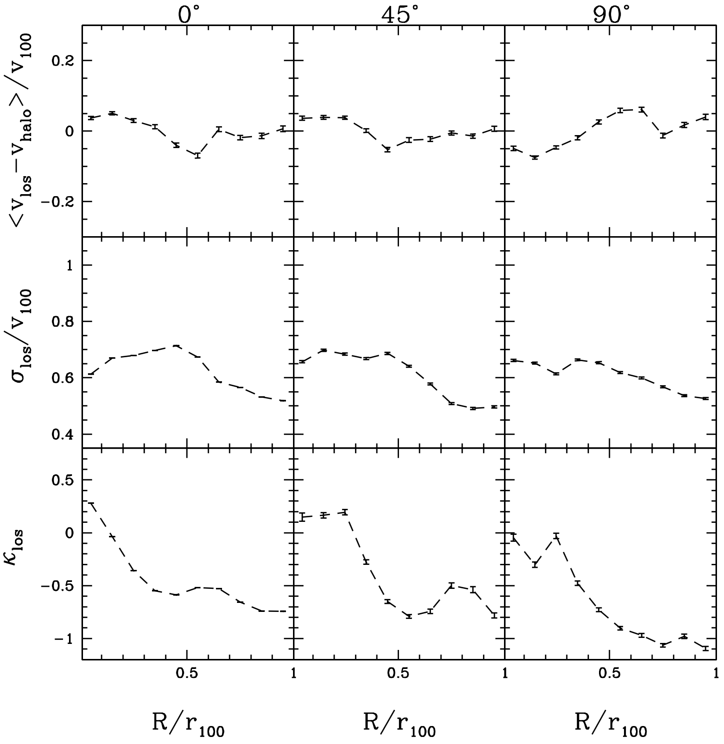

Figure C.2: Projected velocity moments of the dark matter particles in halo 3

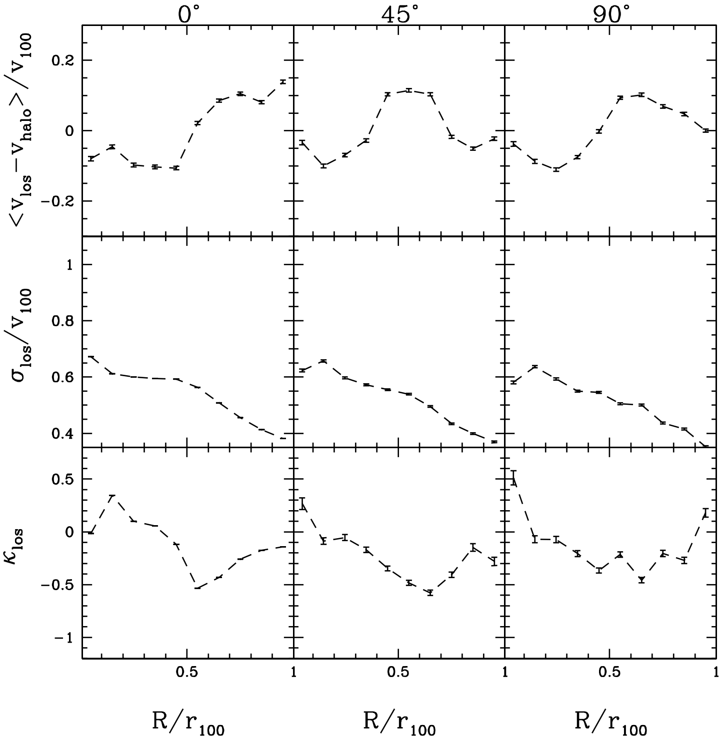

Figure C.3: Projected velocity moments of the dark matter particles in halo 6

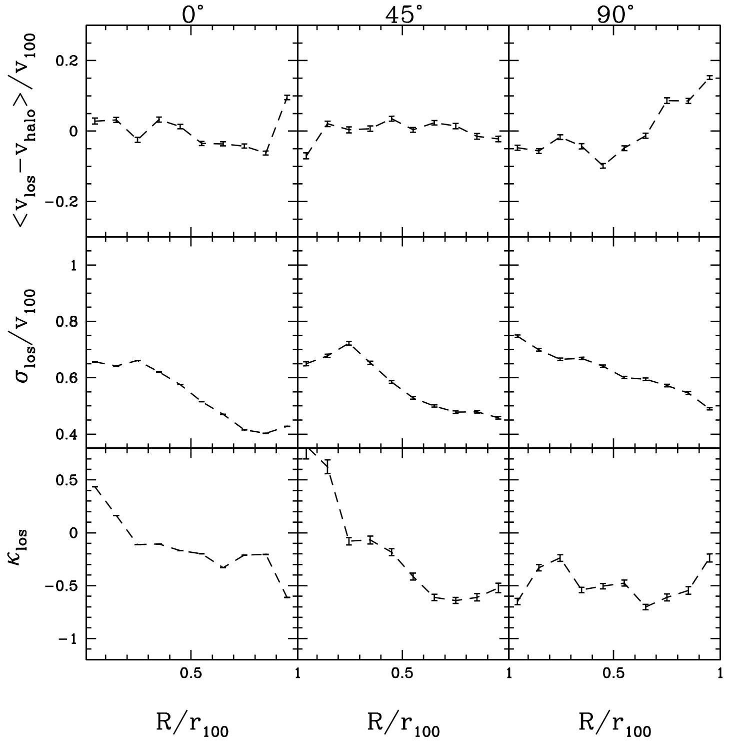

Figure C.4: Projected velocity moments of the dark matter particles in halo 7

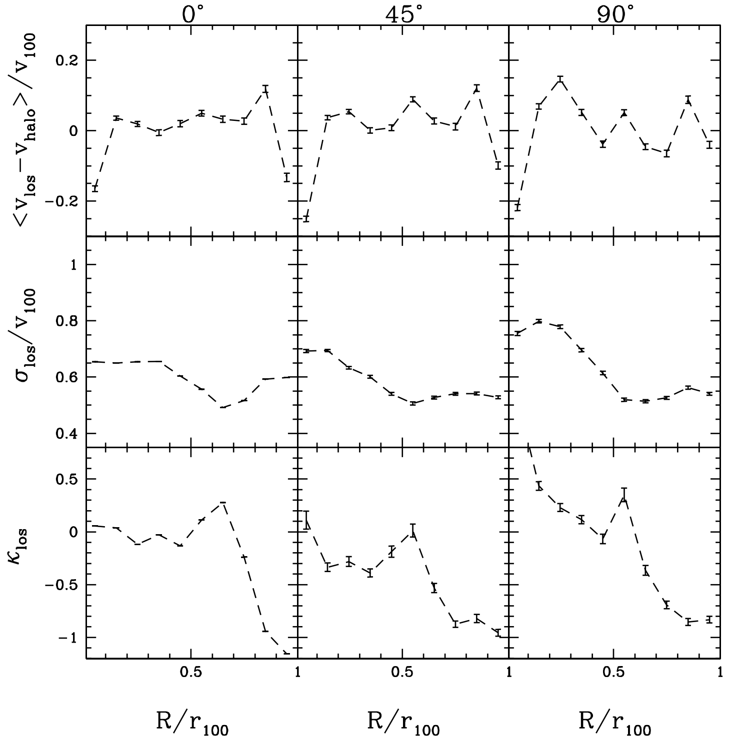

Figure C.5: Projected velocity moments of the dark matter particles in halo 8

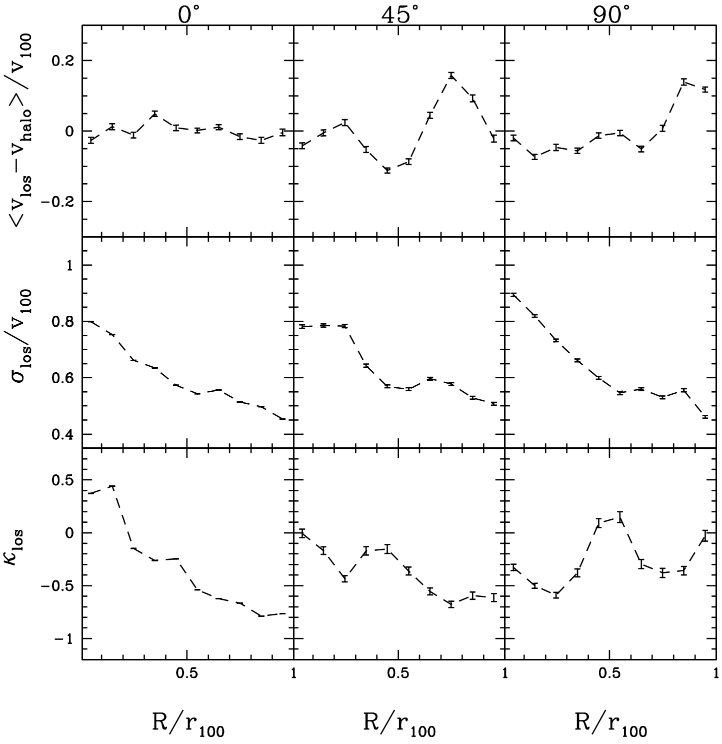

Figure C.6: Projected velocity moments of the dark matter particles in halo 9

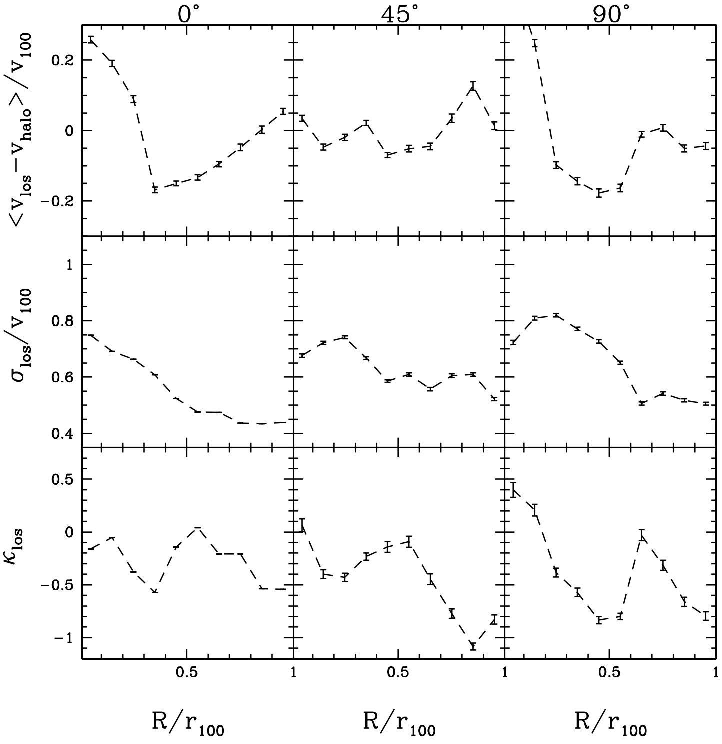

Figure C.7: Projected velocity moments of the dark matter particles in halo 10

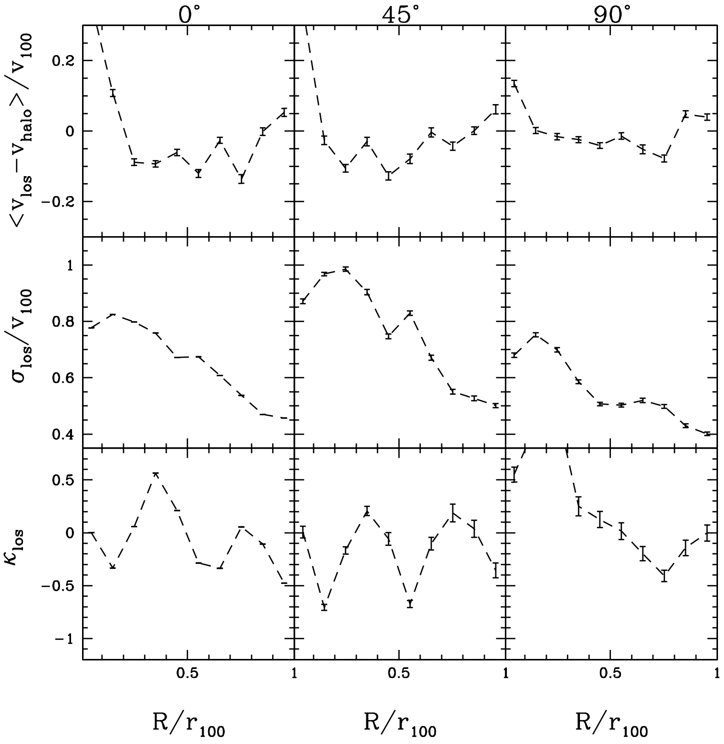

Bibliography

Abadi, M. G., Moore, B., & Bower, R. G. 1999, *Monthly Notices of the Royal Astronomical Society*, 308, 947

Abell, G. O. 1958, *Astrophysical Journal Supplement Series*, 50, 241

Andreon, S., Davoust, E., Michard, R., Nieto, J. L., & Poulain, P. 1996, *Astronomy & Astrophysics Supplement Series*, 116, 429

Arp, H. 1968, *Publications of the Astronomical Society of the Pacific*, 80, 129

Bailey, M. E. 1982, *Monthly Notices of the Royal Astronomical Society*, 201, 271

Balkowski, C. 1973, *Astronomy & Astrophysics*, 34, 43

Balogh, M. L., Morris, S. L., Yee, H. K. C., Carlberg, R. G., & Ellingson, E. 1999, *Astrophysical Journal*, 527, 54

Bardeen, J. M., Bond, J. R., Kaiser, N., & Szalay, A. S. 1986, *Astrophysical Journal*, 304, 15

Bartelmann, B., Ehlers, J., & Schneider, P. 1993, *Astronomy & Astrophysics*, 280, 351

Bettoni, D., Galletta, G., & García-Burillo. S. 2003, *Astronomy & Astrophysics*, 405, 5

Bevington, P. R., & Robinson, D. K. 1992, Data reduction and error analysis for the physical sciences (New York: McGraw-Hill, 2nd ed.)

Binggeli, B. 1982, *Astronomy & Astrophysics*, 107, 338

Binggeli, B., Popescu, C., & Tammann, G. A. 1993, *Astronomy & Astrophysics Supplement Series*, 98, 275

Binggeli, B., Sandage, A., & Tammann, G. A. 1985, *Astronomical Journal*, 90, 1681 (VCC)

Binggeli, B., Tammann, G. A., & Sandage, A. 1987, *Astronomical Journal*, 94, 251

Binney, J., & Mamon, G. A. 1982, *Monthly Notices of the Royal Astronomical Society*, 200, 361

Binney, J., & Tremaine, S. 1987, Galactic Dynamics (Princeton: Princeton University Press)

Biviano, A. 2002, in Tracing Cosmic Evolution with Galaxy Clusters, ed. S. Borgani, M. Mezzeti, & R. Valdarnini (San Francisco: ASP), 127

Biviano, A., & Girardi, M. 2003, *Astrophysical Journal*, 585, 205

Biviano, A., Durret, F., & Gerbal, D. 1996, *Astronomy & Astrophysics*, 311, 95

Biviano, A., Katgert, P., Thomas, T., & Mazure, A. 2003, in Proc. Cozumel Conference, Galaxy Evolution: Theory and Observations, ed. V. Avila-Reese, C. Firmani, C. S. Frenk, & C. Allen, RevMexAA (SC), 17, 191, astro-ph/0301343

Böhringer, H., Briel, U. G., Schwarz, R. A., Voges, W., Hartner, G., & Trümper, J. 1994, *Nature*, 368, 828

Bondi, H. 1947, *Monthly Notices of the Royal Astronomical Society*, 107, 410

Bothun, G. D., Schommer, R. A., & Sullivan, W. T. 1982a, *Astronomical Journal*, 87, 725

Bothun, G. D., Schommer, R. A., & Sullivan, W. T. 1982b, *Astronomical Journal*, 87, 731

Bottinelli, L., & Gouguenheim, L. 1974, *Astronomy & Astrophysics*, 36, 461

Bravo-Alfaro, H., Cayatte, V., van Gorkom, J. H., & Balkowski, C. 2000, *Astronomical Journal*, 119, 580

Bravo-Alfaro, H., Szomoru, A., Cayatte, V., Balkowski, C., & Sancisi, R. 1997, *Astronomy & Astrophysics Supplement Series*, 126, 537

Broeils, A., & van Woerden, H. 1994, *Astronomy & Astrophysics Supplement Series*, 107, 129

Bullock, J. S., Kolatt, T. S., Sigad, Y., Somerville, R. S., Kravtsov, A. V., Klypin, A. A., Primack, J. R., & Dekel, A. 2001, *Monthly Notices of the Royal Astronomical Society*, 321, 559

Burkert, A. 1995, *Astrophysical Journal*, 447, L25

Butcher, H., & Oemler, A. 1978, *Astrophysical Journal*, 219, 18

Butcher, H., & Oemler, A. 1984, *Astrophysical Journal*, 285, 426

Byrd, G., & Valtonen, M. 1990, *Astrophysical Journal*, 350, 89

Capelato, H. V., Gerbal, D., Mathez, G., Mazure, A., & Salvador-Solé, E. 1982, *Astrophysical Journal*, 252, 433

Carlberg, R. G. , Yee, H. K. C., & Ellingson, E. 1997a, *Astrophysical Journal*, 478, 462

Carlberg, R. G. , Yee, H. K. C., Ellingson, E., Morris, S. L., Abraham, R., Gravel, P., Pritchet, C. J., Smecker-Hane, T., Hartwick, F. D. A., Hesser, J. E., Hutchings, J. B., & Oke, J. B. 1997b, *Astrophysical Journal*, 485, L13

Carlberg, R. G. , Yee, H. K. C., Morris, S. L., Lin, H., Hall, P. B., Patton, D. R., Sawicki, M., & Shepherd, C. W. 2001, *Astrophysical Journal*, 552, 427

Cayatte, V., Kotanyi, C., Balkowski, C., & van Gorkom, J. H. 1994, *Astronomical Journal*, 107, 1003

Cayatte, V., Van Gorkom, J. H., Balkowski, C., & Kotanyi, C. 1990, *Astronomical Journal*, 100, 604

Chamaraux, P., Balkowski, C., & Gérard, E. 1980, *Astronomy & Astrophysics*, 83, 38

Chodorowski, M. 1988, Master's thesis, University of Warsaw

Ciardullo, R., Jacoby, G. H., Feldmeier, J. J., & Bartlett, R. E. 1998, *Astrophysical Journal*, 492, 62

Cole, S. 1991, *Astrophysical Journal*, 367, 41

Cole, S., & Lacey, C. 1996, *Monthly Notices of the Royal Astronomical Society*, 281, 716

Couch, W. J., Ellis, R. S., Sharples, R. M., & Smail, I. 1994, *Astrophysical Journal*, 430, 121

Cowie, L. L., & Songaila, A. 1977, *Nature*, 266, 501

Cowley, A. P., Crampton, D., & McClure, R. D. 1982, *Astrophysical Journal*, 263, 1

Dahle, H., Hannestad, S., & Sommer-Larsen, J. 2003, *Astrophysical Journal*, 588, L73

Dale, D. A., Giovanelli, R., Haynes, M. P., Campusano, L. E., & Hardy, E. 1999, *Astronomical Journal*, 118, 1489

Dale, D. A., Giovanelli, R., Haynes, M. P., Hardy, E., & Campusano, L. E. 2001, *Astronomical Journal*, 121, 1886

Davies, R. D. 1968, Herstmonceaux Conference Report, *Observatory*, 88, 196

Davies, R. D., & Lewis, B. M. 1973, *Monthly Notices of the Royal Astronomical Society*, 165, 231

Davis, M., Efstathiou, G., Frenk, C. S., & White, S. D. M. 1985, *Astrophysical Journal*, 292, 371

Dekel, A., & Rees, M. J. 1987, *Nature*, 326, 455

de Lapparent, V., Geller, M. J. & Huchra, J. P. 1986, *Astrophysical Journal*, 302, L1

Demarco, R., Magnard, F., Durret, F., & Márquez, I. 2003, *Astronomy & Astrophysics*, 407, 437

de Vaucouleurs, G. 1961, *Astrophysical Journal Supplement Series*, 6, 213

de Vaucouleurs, G., de Vaucouleurs, A., Corwin, H. G., Buta, R. J., Paturel, G., & Fouqué, P. 1991, Third Reference Catalogue of Bright Galaxies (New York: Springer) (RC3)

Diaferio, A. 1999, *Monthly Notices of the Royal Astronomical Society*, 309, 610

Diaferio, A., & Geller, M. J. 1997, *Astrophysical Journal*, 481, 633

Dickey, J. M. 1997, *Astronomical Journal*, 113, 1939

Dickey, J. M., & Gavazzi, G. 1991, *Astrophysical Journal*, 373, 347

Dressler, A. 1980, *Astrophysical Journal*, 236, 351

Dressler, A. 1986, *Astrophysical Journal*, 301, 35

Dressler, A., Oemler, A. J., Butcher, H., & Gunn, J. E. 1994, *Astrophysical Journal*, 430, 107

Dressler, A., Oemler, A. J., Couch, W. J., Smail, I., Ellis, R. S., Barger, A., Butcher, H., Poggianti, B. M., & Sharples, R. M. 1997, *Astrophysical Journal*, 490, 577

Drinkwater, M. J., Gregg, M., & Colless, M. 2001, *Astrophysical Journal*, 548, L139

Dupke, R. A., & Bregman, J. N. 2001, *Astrophysical Journal*, 547, 705

Ekholm, T. 1996, *Astronomy & Astrophysics*, 308, 7

Ekholm, T., & Teerikorpi, P. 1994, *Astronomy & Astrophysics*, 284, 369

Ekholm T., Lanoix, P., Teerikorpi, P., Fouqué, P., & Paturel, G. 2000, *Astronomy & Astrophysics*, 355, 835 (Ekh00)

Ekholm, T., Lanoix, P., Teerikorpi, P., Paturel, G., & Fouqué, P. 1999, *Astronomy & Astrophysics*, 351, 827

Ellis, R. S., Smail, I., Dressler, A., Couch, W. J., Oemler, A. J., Butcher, H., & Sharples, R. M. 1997, *Astrophysical Journal*, 483, 582

Ettori, S., De Grandi, S., & Molendi, S. 2002, *Astronomy & Astrophysics*, 391, 841

Evrard, A. E., Silk, J., & Szalay, A. S. 1990, *Astrophysical Journal*, 365, 13

Fasano, G., Poggianti, B. M., Couch, W. J., Bettoni, D., Kjærgaard, & P., Moles, M. 2000, *Astrophysical Journal*, 542, 673

Federspiel, M., Tammann, G. A., & Sandage, A. 1998, *Astrophysical Journal*, 495, 115 (FTS98)

Ferguson, H. C., & Binggeli, B. 1994, *Astronomy & Astrophysics Review*, 6, 67

Fouqué, P., Bottinelli, L., Gouguenheim, L., & Paturel, G. 1990, *Astrophysical Journal*, 349, 1 (Fou90)

Fouqué, P., Solanes, J. M., Sanchis, T., & Balkowski, C. 2001, *Astronomy & Astrophysics*, 375, 770

Freedman, W. L., Madore, B. F., Gibson, B. K., Ferrarese, L., Kelson, D. D., Sakai, S., Mould, J. R., Kennicutt, R. C., Ford, H. C., Graham, J. A., Huchra, J. P., Hughes, S. M. G., Illingworth, G. D., Macri, L. M., & Stetson, P. B. 2001, *Astrophysical Journal*, 553, 47

Ftclas, C., Struble, M. F., & Fanelli, M. N. 1984, *Astrophysical Journal*, 282, 19

Fukugita, M., Okamura, S., & Yasuda, N. 1993, *Astrophysical Journal*, 412, L13

Fukushige, T., & Makino, J. 2001, *Astrophysical Journal*, 557, 533

Gavazzi, G., & Jaffe, W. 1987, *Astronomy & Astrophysics*, 186, L1

Gavazzi, G., Boselli, A., Pedotti, P., Gallazzi, A., & Carrasco, L. 2002, *Astronomy & Astrophysics*, 396, 449

Gavazzi, G., Boselli, A., Scodeggio, M., Pierini, D., & Belsole, E. 1999, *Monthly Notices of the Royal Astronomical Society*, 304, 595 (Gav99)

Gavazzi, R., Fort, B., Mellier, Y., Pelló, R., & Dantel-Fort, M. 2003, *Astronomy & Astrophysics*, 403, 11

Geller, M. J., Diaferio, A., & Kurtz, M. J. 1999, *Astrophysical Journal*, 517, L23

Ghigna, S., Moore, B., Governato, F., Lake, G., Quinn, T., & Stadel, J. 1998, *Monthly Notices of the Royal Astronomical Society*, 300, 146

Giovanardi, C., Helou, G., Salpeter, E., & Krumm, N. 1983, *Astrophysical Journal*, 267, 35

Giovanelli, R., & Haynes, M. P. 1983, *Astronomical Journal*, 89, 1

Giovanelli, R., & Haynes, M. P. 1985, *Astrophysical Journal*, 292, 404

Giovanelli, R., Haynes, M. P., & Chincarini, G. L. 1986, *Astrophysical Journal*, 300, 77

Giovanelli, R., Haynes, M. P., Herter, T., Vogt, N. P., Da Costa, L. N., Freudling, W., Salzer, J. J., & Wegner, G. 1997, *Astronomical Journal*, 113, 53

Girardi, M., & Mezzetti, M. 2001, *Astrophysical Journal*, 548, 79

Girardi, M, Giuricin, G., Mardirossian, F., Mezzetti, M., & Boschin, W. 1998, *Astrophysical Journal*, 505, 74

Giraud, E. 1986, *Astronomy & Astrophysics*, 167, 25

Gott, J. R. 1975, *Astrophysical Journal*, 201, 296

Guhathakurta, P., van Gorkom, J. H., Kotanyi, C. G., & Balkowski, C. 1988, *Astronomical Journal*, 96, 851

Guiderdoni, B., & Rocca-Volmerange, B. 1985, *Astronomy & Astrophysics*, 151, 108

Gunn, J. E., & Gott, J. R. 1972, *Astrophysical Journal*, 176, 1

Hanski, M. O., Theureau, G., Ekholm, T., & Teerikorpi, P. 2001, *Astronomy & Astrophysics*, 378, 345

Hatton, S., Devriendt, J. E. G., Ninin, S., Bouchet F. R., Guiderdoni, B., & Vibert, D. 2003, *Monthly Notices of the Royal Astronomical Society*, 343, 75

Haynes, M. P., & Giovanelli, R. 1984, *Astronomical Journal*, 89, 758

Haynes, M. P., & Giovanelli, R. 1986, *Astrophysical Journal*, 306, 466

Haynes, M. P., Giovanelli, R, & Chincarini, G. L. 1984, *Annual Review of Astronomy and Astrophysics*, 22, 445

Helou, G., Hoffman, G. L., & Salpeter, E. E. 1984, *Astrophysical Journal Supplement Series*, 55, 433

Hoffman, G. L., & Salpeter, E. E. 1982, *Astrophysical Journal*, 263, 485

Hoffman, G. L., Olson, D. W., & Salpeter, E. E. 1980, *Astrophysical Journal*, 242, 861

Hubble, E. 1926, *Astrophysical Journal*, 64, 321

Hubble, E. 1927, *Observatory*, 50, 276

Hubble, E., & Humason, E. 1931, *Astrophysical Journal*, 74, 43

Huchtmeier, W. K., & Richter, O. G. 1989, A General Catalog of H I Observations of Galaxies (Berlin: Springer)

Huchtmeier, W. K., Tammann, G. A., & Wendker, H. J. 1976, *Astronomy & Astrophysics*, 46, 381

Jensen, J. B., Tonry, J. L., & Luppino, G. A. 1998, *Astrophysical Journal*, 505, 111 (JTL98)

Jing, Y. P. 2000, *Astrophysical Journal*, 535, 30

Jing, Y. P., & Suto, Y. 2002, *Astrophysical Journal*, 574, 538

Kaiser, N. 1987, *Monthly Notices of the Royal Astronomical Society*, 227, 1

Karachentseva, V. E. 1973, Astrofizicheskie Issledovaniia Izvestiya Spetsial'noj Astrofizicheskoj Observatorii, 8, 3 (Comm. Spec. Astrophys. Obs)

Kauffmann, G., White, S. D. M., & Guiderdoni, B. 1993, *Monthly Notices of the Royal Astronomical Society*, 264, 201

Kazantzidis, S., Magorrian, J., & Moore, B. 2003, *Astrophysical Journal*, in press, astro-ph/0309517

Keel, W. C. 1996, *Publications of the Astronomical Society of the Pacific*, 108, 917

Kenney, J. D. P., & Young, J. S. 1989, *Astrophysical Journal*, 344, 171

Kenney, J. D. P., Koopmann, R. A., Rubin, V. C., & Young, J. S. 1996, *Astronomical Journal*, 111, 152

Kennicutt, R. 1998, *Annual Review of Astronomy and Astrophysics*, 36, 189

Kent, S. M., & Gunn, J. E. 1982, *Astronomical Journal*, 87, 945

King, I. R. 1972, *Astrophysical Journal*, 174, L123

Kitayama, T., & Suto, Y. 1996, *Astrophysical Journal*, 469, 480

Koopmann, R. A., & Kenney, J. D. P. 1998, *Astrophysical Journal*, 497, L75

Koopmann, R. A., & Kenney, J. D. P. 2002, astro-ph/0209547

Kotanyi, C. G., & Ekers, R. D. 1983, *Astronomy & Astrophysics*, 122, 267

Kraan-Korteweg, R. C., Cameron, L. M., & Tammann, G. A. 1988, *Astrophysical Journal*, 331, 620 (KCT88)

Krumm, N., & Salpeter, E. E. 1979a, *Astronomical Journal*, 227, 776

Krumm, N., & Salpeter, E. E. 1979b, *Astronomical Journal*, 228, 64

Kundu, A., & Whitmore, B. C. 2001, *Astrophysical Journal*, 121, 2950 (KW01)

Lacey, C. G., & Silk, J. 1991, *Astrophysical Journal*, 381, 14

Lacey, C. G., Guiderdoni, B., Rocca-Volmerange, B., & Silk, J. 1993, *Astrophysical Journal*, 402, 15

Larson, R. B., Tinsley, B. M., & Caldwell, C. N. 1980, *Astrophysical Journal*, 237, 692

Lewis, I., Balogh, M., De Propris, R., Couch, W., Bower, R., Offer, A., Bland-Hawthorn, J., Baldry, I. K., Baugh, C., Bridges, T., Cannon, R., Cole, S., Colless, M., Collins, C., Cross, N., Dalton, G., Driver, S. P., Efstathiou, G., Ellis, R. S., Frenk, C. S., Glazebrook, K., Hawkins, E., Jackson, C., Lahav, O., Lumsden, S., Maddox, S., Madgwick, D., Norberg, P., Peacock, J. A., Percival, W., Peterson, B. A., Sutherland, W., & Taylor, K. 2002, *Monthly Notices of the Royal Astronomical Society*, 334, 673

Łokas, E. L. 2002, *Monthly Notices of the Royal Astronomical Society*, 333, 697

Łokas, E. L., & Hoffman, Y. 2001, in The Identification of Dark Matter, ed. N. J. C. Spooner & V. Kudryavtsev (Singapore: World Scientific), 121, astroph/0011295

Łokas, E. L., & Mamon, G. A. 2001, *Monthly Notices of the Royal Astronomical Society*, 321, 155

Łokas, E. L., & Mamon, G. A. 2003, *Monthly Notices of the Royal Astronomical Society*, 343, 401

Magri, C., Haynes, M. P., Forman, W., Jones, C., & Giovanelli, R. 1988, *Astrophysical Journal*, 333, 136

Mamon, G. A. 1992, *Astrophysical Journal*, 401, L3

Mamon, G. A. 2000, in 15th IAP Astrophys. Mtg., Dynamics of Galaxies: from the Early Universe to the Present, ed. F. Combes, G. A. Mamon, & V. Charmandaris, Vol. 197 (San Francisco: ASP), 377, astro-ph/9911333

Mazure, A., Biviano, A., Katgert, P., Thomas, T., & Adami, C. 2000, in Dynamics of Galaxies: from the Early Universe to the Present, ed. F. Combes, G. A. Mamon, & V. Charrmandaris (San Francisco: ASP), 373

McMahon, P. M. 1993, Ph. D. thesis. Columbia Univ.

Mendes de Oliveira, C., Amram, P., Plana, H., & Balkowski, C. 2003, in preparation

Merrifield, M. R., & Kent, S. M. 1990, *Astronomical Journal*, 99, 1548

Merritt, D. 1987, *Astrophysical Journal*, 313, 121

Merritt, D., & Saha, P. 1993, *Astrophysical Journal*, 409, 75

Moore, B., Governato, F., Quinn, T., Stadel, J., & Lake, G. 1998, *Astrophysical Journal*, 499, L5

Moore, B., Katz, N., & Lake, G. 1996, *Astrophysical Journal*, 457, 455

Moore, B., Quilis, V., & Bower, R. 1999, in ASP Conf. Ser. 197, Dynamics of Galaxies: From the Early Universe to the Present, ed. F. Combes, G. A. Mamon, & V. Charmandaris (San Francisco:ASP), 363

Morgan, W. W. 1961, Proceedings of the National Academy of Sciences of the USA, 47, 905

Mould, J., Aaronson, M., & Huchra, J. 1980, *Astrophysical Journal*, 238, 458 (MAH80)

Naim, A., Lahav, O., Buta, R. J., Corwin, H. G., de Vaucouleurs, G., Dressler, A., Huchra, J. P., van den Bergh, S., Raychaudhury, S., Sodre, L., & Storrie-Lombardi, M. C. 1995, *Monthly Notices of the Royal Astronomical Society*, 274, 1107

Navarro, J. F., Frenk, C. S., & White, S. D. M. 1995, *Monthly Notices of the Royal Astronomical Society*, 275, 720

Navarro, J. F., Frenk, C. S., & White, S. D. M. 1997, *Astrophysical Journal*, 490, 493

Neilsen, E. H., & Tsvetanov, Z. I. 2000, *Astrophysical Journal*, 536, 255

Nulsen, P. E. J. 1982, *Monthly Notices of the Royal Astronomical Society*, 198, 1007

Oemler, A. J. 1974, *Astrophysical Journal*, 194, 1

Oemler, A. J., Dressler, A., & Butcher, H. 1997, *Astrophysical Journal*, 474, 561

Olson, D. W., & Silk, J. 1979, *Astrophysical Journal*, 233, 395

Padmanabhan, T. 1993, Structure formation in the universe (New York: Cambridge University Press)

Peebles, P. J. E. 1976, *Astrophysical Journal*, 205, 318

Pierce, M. J., & Tully, R. B. 1988, *Astrophysical Journal*, 330, 579 (PT88)

Poggianti, B. M., Smail, I., Dressler, A., Couch, W. J., Barger, A. J., Butcher, H., Ellis, R. S., & Oemler, A. J. 1999, *Astrophysical Journal*, 518, 576

Quilis, V., Moore, B., & Bower, R. 2000, *Science*, 288, 1617

Regős, E., & Geller, M. J. 1989, *Astronomical Journal*, 98, 755

Richstone, D., Loeb, A, & Turner, E. L. 1992, *Astrophysical Journal*, 393, 477

Rines, K., Geller, M. J., Diaferio, A., Mahdavi, A., Mohr, J. J., & Wegner, G. 2002, *Astronomical Journal*, 124, 1266

Roberts, M. S. 1975, Galaxies and the Universe (Chicago: Univ. Chicago Press), 309

Roberts, M. S., & Haynes, M. P. 1994, *Annual Review of Astronomy and Astrophysics*, 32, 115

Robinson, B. J., & Koehler, J. A. 1965, *Nature*, 208, 993

Rubin, V. C., Hunter, D. A., & Ford, W. K. J. 1991, *Astrophysical Journal Supplement Series*, 76, 153

Rubin, V. C., Waterman, A. H., & Kenney, J. D. P. 1999, *Astronomical Journal*, 118, 236

Sakai, S., Mould, J. R., Hughes, S. M. G., Huchra, J. P., Macri, L. M., Kennicutt, R. C., Gibson, B. K., Ferrarese, L., Freedman, W. L., Han, M., Ford, H. C., Graham, J. A., Illingworth, G. D., Kelson, D. D., Madore, B. F., Sebo, K., Silbermann, N. A., & Stetson, P. B. 2000, *Astrophysical Journal*, 529, 698

Salvador-Solé, E., Sanromà, M., & Rdz. Jordana, J. J. 1989, *Astrophysical Journal*, 337, 636

Sandage, A., Binggeli, B., Tammann, G. A. 1985, *Astronomical Journal*, 90, 1759

Sandage, A., Freeman, K. C., & Stokes, N. R. 1970, *Astrophysical Journal*, 160, 831

Schindler, S., Binggeli, B., & Böhringer, H. 1999, *Astronomy & Astrophysics*, 343, 420

Schommer, R. A., Sullivan, W. T., & Bothun, G. D. 1981, *Astronomical Journal*, 86, 943

Schulz, S., & Struck, C. 2001, *Monthly Notices of the Royal Astronomical Society*, 328, 185

Silk, J. 1974, *Astrophysical Journal*, 193, 525

Silk, J. 1978, *Astrophysical Journal*, 220, 390

Silk, J., & Wilson, M. L. 1979a, *Astrophysical Journal*, 228, 641

Silk, J., & Wilson, M. L. 1979b, *Astrophysical Journal*, 233, 769

Silverman, B. W. 1986, Density Estimation for Statistics and Data Analysis (London: Chapman and Hall)

Smail, I., Dressler, A., Couch, W. J., Ellis, R. S., Oemler, A. J., Butcher, H., & Sharples, R. M. 1997, *Astrophysical Journal Supplement Series*, 110, 213

Smith, S. 1936, *Astrophysical Journal*, 83, 23

Solanes, J. M., & Salvador-Solé, E. 1990, *Astronomy & Astrophysics*, 234, 93

Solanes, J. M., & Salvador-Solé, E. 1992, *Astrophysical Journal*, 395, 91

Solanes, J. M., Giovanelli, R., & Haynes, M. P. 1996, *Astrophysical Journal*, 461, 609

Solanes, J. M., Manrique, A., González-Casado, G., García-Gómez, C., Giovanelli, R., & Haynes, M. P. 2001, *Astrophysical Journal*, 548, 97

Somerville, R. S., & Primack, J. R. 1999, *Monthly Notices of the Royal Astronomical Society*, 310, 1087

Spergel, D. N., Verde, L., Peiris, H. V., Komatsu, E., Nolta, M. R., Bennett, C. L., Halpern, M., Hinshaw, G., Jarosik, N., Kogut, A., Limon, M., Meyer, S. S., Page, L., Tucker, G. S., Weiland, J. L., Wollack, E., & Wright, E. L. 2003, *Astrophysical Journal Supplement Series*, 148, 175

Spitzer, L., & Baade, W. 1951, *Astrophysical Journal*, 113, 413

Stark, A. A., Knapp, G. R., Bally, J., Wilson, R. W., Penzias, A. A., & Rowe, A. E. 1986, *Astrophysical Journal*, 310, 660

Stauffer, J. R., Kenney, J. D., & Young, J. S. 1986, *Astronomical Journal*, 91, 6

Stevens, I. R., Acreman, D. M., & Ponman, T. J. 1999, *Monthly Notices of the Royal Astronomical Society*, 310, 663

Sullivan, W. T., Bates, B., Bothun, G. D., & Schommer, R. A. 1981, *Astronomical Journal*, 86, 919

Tammann, G. A., & Sandage, A. 1985, *Astrophysical Journal*, 294, 81

Teerikorpi, P., Bottinelli, L., Gouguenheim, L., & Paturel, G. 1992, *Astronomy & Astrophysics Supplement Series*, 260, 17

The, L. S., & White, S. D. M. 1986, *Astronomical Journal*, 92, 1248

Tolman, R. C. 1934, Proceedings of the National Academy of Science (Wash) 20, 169

Tonry, J. L. 1983, *Astrophysical Journal*, 266, 58

Tonry, J. L., Dressler, A., Blakeslee, J. P., Ajhar, E. A., Fletcher, A. B., Luppino, G. A., Metzger, M. R., & Moore, C. B. 2001, *Astrophysical Journal*, 546, 681 (Ton01)

Toomre, A. 1972, *Astrophysical Journal*, 178, 623

Tormen, G., Bouchet, F. R., & White, S. D. M. 1997, *Monthly Notices of the Royal Astronomical Society*, 286, 865

Tully, R. B. 1982, *Astrophysical Journal*, 257, 389

Tully, R. B., & Fisher, J. R. 1977, *Astronomy & Astrophysics Supplement Series*, 54, 661 (TF)

Tully, R. B., & Shaya, E. J. 1984, *Astrophysical Journal*, 281, 31

Valluri, M. 1993, *Astrophysical Journal*, 408, 57

Valluri, M., & Jog, C. J. 1990, *Astrophysical Journal*, 357, 367

Valluri, M., & Jog, C. J. 1991, *Astrophysical Journal*, 374, 103

van der Marel, R. P., Magorrian, J., Carlberg, R. G., Yee, H. K. C., & Ellingson, E. 2000, *Astronomical Journal*, 119, 2038

van Dokkum, P. G., Franx, M., Fabricant, D., Kelson, D. D., & Illingworth, G. D. 1999, *Astrophysical Journal*, 520, L95

van Gorkom, J. H. 1996, in ASP Conf. Series 106, Minnesota Lectures on Extragalactic H I, ed. E. D. Skillman (San Francisco:ASP), 293

van Haarlem, M. J., & van de Weygaert, R. 1993, *Astrophysical Journal*, 418, 544

van Haarlem, M. J., Cayón, L., de la Cruz, C. G., Martínez-González, E., & Rebolo, R. 1993, *Monthly Notices of the Royal Astronomical Society*, 264, 71

Vedel, H., & Hartwick, F. D. A. 1998, *Astrophysical Journal*, 501, 509

Verheijen, M. A. N. 1996, in Cold Gas at High Redshifts, ed. M. Bremer, P. van der Werf, & C. L. Carilli (Dordrecht: Kluwer), 165

Vollmer, B., Cayatte, V., Balkowski, C., & Duschl, W. J. 2001, *Astrophysical Journal*, 561, 708

Wang, Q. D., & Ulmer, M. P. 1997, *Monthly Notices of the Royal Astronomical Society*, 292, 920

Warmels, R. H. 1988, *Astronomy & Astrophysics Supplement Series*, 72,427

West, M. J., & Blakeslee, J. P. 2000, *Astrophysical Journal*, 543, L27

White, S. D. M., & Frenk, C. S. 1991, *Astrophysical Journal*, 379, 52

White, S. D. M., & Rees, M. J. 1978, *Monthly Notices of the Royal Astronomical Society*, 183, 341

Whitmore, B. C., & Gilmore, D. M. 1991, *Astrophysical Journal*, 367, 64

Wirth, G. D., Koo, D. C., & Kron, R. G. 1994, *Astrophysical Journal*, 435, L105

Yahil, A., Tammann, G. A., & Sandage, A. 1977, *Astrophysical Journal*, 207, 903

Yasuda, N., Fukugita, M., & Okamura, S. 1997, *Astrophysical Journal Supplement Series*, 108, 417 (YFO97)

Young, C. K., & Currie, M. J. 1995, *Monthly Notices of the Royal Astronomical Society*, 273, 1141 (YC95)

Zeldovich, Y. B. 1970, *Astronomy & Astrophysics*, 5, 84

Zwicky, F. 1933, *Helv. Phys. Acta*, 6, 10

Zwicky, F. 1937, *Astrophysical Journal*, 86, 217